MODELING AND INTERPRETATION OF DOWNHOLE TEMPERATURE IN A HORIZONTAL WELL WITH MULTIPLE FRACTURES

A Dissertation

by

NOZOMU YOSHIDA

Submitted to the Office of Graduate and Professional Studies of
Texas A&M University
in partial fulfillment of the requirements for the degree of

DOCTOR OF PHILOSOPHY

Chair of Committee,	Alfred Daniel Hill
Committee Members,	Ding Zhu
	Akhil Datta-Gupta
	Charles Glover
Head of Department,	Alfred Daniel Hill

August 2016

Major Subject: Petroleum Engineering

Copyright 2016 Nozomu Yoshida

ABSTRACT

Downhole temperature data obtained by either temperature logging or fiber-optic cables has been used to evaluate stimulation treatments and post-stimulation performance of horizontal wells with multiple fractures. Qualitative detection of transverse fractures, poor zonal isolation, and inflow locations is possible; however downhole temperature behavior in those wells is not fully understood from the theoretical modeling perspective.

In this study, comprehensive numerical flow and thermal models for a horizontal well with multiple fractures are presented. The well experiences single phase water flow during injection and shut-in, and gas-water two-phase flow during production. These models are formulated for reservoir and wellbore domains using mass, momentum and energy conservation in transient conditions. These models are coupled to obtain profiles of wellbore and sandface temperature as one of the solutions. These models enable us to simulate field operations in multistage fracturing treatments; injection and shut-in occur alternately for each stage from toe to heel with sufficient zonal isolation. Following the stimulation treatments, these models are used to simulate temperature behavior during production in gas-water two phase flow.

The developed model is applied for several synthetic cases. These case studies show capabilities of the developed model to simulate downhole temperature behavior during processes of injection, shut-in and production. A single fracture case shows injected fluid lowers temperature in the fracture below the geothermal temperature even after one month of shut-in. This affects the temperature interpretation during production. The initial

temperature is different than the geothermal temperature, as assumed by previously published work. A synthetic case with five fractures show capabilities of detection of fracture locations from the shut-in temperature profile. The temperature profiles obtained during production show different characteristics of the wellbore temperature and sandface temperature due to fluid mixing in the wellbore.

The developed model was also applied to field cases. One of the field cases shows possibility to evaluate relative fracture length based on the shut-in temperature behavior, and the results are consistent with other measurements qualitatively. The model was also applied for flow profiling of a field case. The estimated flow profile by this work is consistent with the interpretation by production logging tool and the temperature model by a single phase gas. These field cases show capabilities of the temperature interpretation to obtain further understanding of the downhole conditions in a horizontal well with multiple fractures.

ACKNOWLEDGEMENTS

I would like to express my gratitude to my advisor Dr. Alfred Daniel Hill and Dr. Ding Zhu for their continuous encouragement, guidance, and support. I will always remember their kindness. I would like to thank my committee members, Dr. Akhil Datta-Gupta and Dr. Charles Glover for serving as committee members. I appreciate their guidance and thoughtful discussions.

Thanks also go to my friends and colleagues to share their time with me at Texas A&M University.

Finally, thanks go to my family for their encouragement and support.

TABLE OF CONTENTS

LIST OF FIGURES

LIST OF TABLES

CHAPTER I

INTRODUCTION*

1.1 Background

Downhole temperature data has been used as one of the diagnostic methods in evaluation of stimulation design, completion effectiveness and wellbore performance. Detection of casing leaks, water/gas entry, and quantitative formation evaluation by estimating near wellbore permeability and skin factor are examples of the downhole temperature interpretation. Downhole temperature interpretations are enabled from distinct characteristics of the downhole temperature such as geothermal temperature gradient and Joule-Thomson effect. Anomalies in the temperature profile help interpret downhole conditions.

The downhole temperature is measured with production logging tools, permanent downhole gauges, and fiber-optic cables. Production logging provides spatial temperature distribution at certain times. The permanent downhole gauges measure temporal temperature behavior at certain points in a wellbore. And, the fiber-optic cables can measure real-time temperature behavior along a wellbore without any intervention after installation, and are called distributed temperature sensors (DTS). The spatial distribution and temporally continuous measurements make the DTS technology a useful method for local evaluations of wellbore performance (e.g. water/gas entry detection and near

* Part of this section is reproduced with permission from "Temperature-Prediction Model for a Horizontal Well with Multiple Fractures in a Shale Reservoir" by Yoshida, N., Zhu, D. and Hill, A.D. 2014. *SPE Production & Operations* **29** (4): 261-273. SPE-166241-PA. doi: 10.2118/166241-PA. Copyright 2014, Society of Petroleum Engineers. Further reproduction prohibited without permission.

wellbore formation evaluation) and stimulations (e.g. acidizing, acid fracturing and hydraulic fracturing).

Recently, multi-stage stimulation treatment has been widely applied in fields, and the fiber-optic cables are used to evaluate stimulation treatment and post-stimulation performance. Field observations in multi-stage fracturing treatments showed capabilities of detecting creation of transverse fractures and poor zonal isolation during the stimulation and the warm-back periods. In addition, temperature anomalies, driven by Joule-Thomson effects, during production period enables to detect inflow locations in a horizontal well with multiple fractures. These qualitative interpretations of the downhole temperature measurements give further possibilities of quantitative evaluation of completion effectiveness and post-stimulation performances of those horizontal wells with multiple fractures.

1.2 Literature Review

1.2.1 Downhole Temperature Measurement

Temperature data along a horizontal wellbore is measured with production logging tools, permanent downhole gauges, and fiber-optic cables. The temperature logs provides spatial temperature distribution at a single time point, and the permanent downhole gauges provide variant temporal temperature measurements at locations where the gauges are installed. Interpretation of the temperature logs offers detection of gas/water entry, casing leaks, fluid movement behind casing and so on (Hill 1990). On the other hand, the fiber-optic cables provide both spatial and temporal temperature distribution without any

intervention of interference with flow. The fiber-optic cables can measure not only the temperature data but also pressure and acoustics, which are called distributed pressure sensors (DPS) and distributed acoustic sensors (DAS).

The first installation of the fiber-optic sensors were by Shell in the Sleen field in the Netherlands in 1993 (Kragas et al. 2001). Those fiber-optic sensors have been installed in several fields for detection of early breakthrough of steam to producers (Carnahan et al. 1999), flow behind casing and cross flow during shut-in and water finger encroachment (Brown et al. 2000), zone production rate change in multi-layered reservoirs (Fryer et al. 2005). Johnson et al. (2006) and Huebsch et al. (2008) showed gas flow rate profiling in vertical wells using the DTS data, and they compared the temperature-estimated flow profile with the flow profile estimated by the production logging (spinner flowmeter). Real-time fluid distribution in matrix treatment was studied by Glasbergen et al. (2009) using DTS data for better understanding of placement and diversion of the injected fluid.

Sierra et al. (2008) and Huckabee (2009) applied the distributed temperature sensing technology to diagnose fracture stimulation and to evaluate well performance for several fields. They showed temperature profiles during multi-stage fracturing treatment with external casing perforating completion demonstrating capabilities of detecting locations of transverse fractures and poor zonal isolations during stimulation and warm-back periods. Huckabee (2009) pointed that the DTS can detect the flow path of the poor zonal isolation because different flow path shows different temperature characteristics between those zones. Sierra et al. (2008) discussed thermal coupling scenarios in DTS cables cemented behind casing; fluctuations in DTS measurement during injection are

results of poor thermal coupling of the fiber to the casing due to spatial location of the fiber relative to the bundle of instrumentation lines (Huckabee 2009). Those fluctuations are also observed in DTS data when openhole-packer completions are used in horizontal wells (Holley et al. 2013). Ugueto et al. (2015) showed, in their integrated interpretation with DAS, DTS temperature maps of multi-stage fracturing stimulation with several completion types. The 'stair-step' temperature distribution shows effective zonal isolations, and according to their plots, the created fracture locations seem to be identified by the early warm-back temperature data. Ugueto et al. (2016) further discussed perforation cluster efficiency in the cemented plug-and-perf completions investigating the DTS and the DAS responses during fracturing treatment, shut-in and production period. In their results, all of the cluster received some amounts of fracturing fluid during stimulation according to the DTS response, while efficiency of the treatment seems to be restricted as supported by insufficient DAS responses at some perforations. Their DTS/DAS responses during production also supported that, if a perforation showed cooling signal during treatment, both DTS and DAS showed no signals during production, and, even if there is a signal in the DTS response during production, the flow rate seemed to be small since the DAS response is quite small. They concluded, while all perforations received the injected fluid, only half or two-thirds of the perforation clusters are properly stimulated or produced at significant rates.

1.2.2 Temperature Modeling and Interpretation

For quantitative temperature interpretation, several temperature models have been developed in the past. Reservoir temperature models were proposed in the application of thermal recovery processes with considerations of the heat efficiency (Prats 1969, Prats 1992). For wellbores, one of the earliest works on temperature modeling was proposed by Ramey (1962). Ramey's model predicts temperature distribution for production or injection vertical wells of single phase incompressible liquid or ideal gas flow using steady-state wellbore model with transient formation model (Wang et al. 2008). Several authors relaxed the assumptions and extended the model to handle more complex situations. For vertical wells, the model is extended to multiphase transient flow with the coupling of wellbore and reservoir model (Kabir et al. 1996, Hasan et al. 1997, Izgec et al. 2007). Sui et al. (2008a) proposed a transient thermal coupled model for vertical wells, and they applied it for near wellbore formation evaluation by estimating permeability and skin factors of multiple layers with pressure and temperature transient measurements (Sui et al. 2008b, Sui et al. 2012). Duru and Horne (2010) presented a semi-analytical solution for reservoir thermal model under single phase and multi-phase condition coupled with the transient wellbore temperature model by Izgec et al. (2007), and they successfully estimated near wellbore porosity and thermal properties as well as permeability. For horizontal wells, Yoshioka et al. (2005b) presented a steady state wellbore temperature model coupled with a reservoir thermal model considering the variation of reservoir inflow temperature along the horizontal well. Because the geothermal temperature change is very small for horizontal wells, their reservoir thermal model took into account subtle thermal

effects caused by thermal expansion and viscous dissipation heating besides heat conduction and convection. They used the model to predict the temperature change in a deviated horizontal well, detection of water or gas entry in the horizontal direction and the vertical direction (water coning) (Yoshioka et al. 2005, Dawkrajai et al. 2006, Yoshioka et al. 2007). Sui (2009) showed that the transient wellbore model can be reduced to steady state condition if the measurement time is long enough, such as days. Based on this observation, Li and Zhu (2010b) presented a transient temperature model with a transient reservoir thermal model along with the steady state wellbore model proposed by Yoshioka et al. (2005b). Their work successfully captured the transient behavior of temperature along horizontal wells for a water coning case and a water injection case from the adjacent horizontal well (Li et al. 2011).

The temperature data has also been used in design and evaluation of the hydraulic fracturing treatment (Hannah et al. 1977, Harrington et al. 1978, Biot et al. 1987, Meyer 1989). Kamphuis et al. (1993) showed a numerical simulation model to estimate temperature profile inside of a fracture during injection and shut-in period. In their work, different temperature behavior is observed due to fracture geometry difference; radially shaped fractures are much cooler further away from the wellbore than rectilinear fracture are (Kamphuis et al. 1993). Davis et al. (1997) proposed a method to evaluate fracture height using temperature logs after fracturing treatment in a vertical well. Seth et al. (2010) presented a numerical model for interpretation of DTS data during fracturing treatment and shut-in period associated with fracture propagation model based on a simple volume balance. Hoang et al. (2012) presented the application to an injection fluid profile for

hydraulic fracturing in vertical wells with limited entry completions. While the above models are intended to apply for stimulations in vertical wells, as one of the theoretical studies on multi-stage fracturing treatment in horizontal wells, Tabatabaei and Zhu (2012) showed preliminary study of the temperature study during injection and warm-up periods by considering effects of injection rate allocation on wellbore temperature profile. Ribeiro and Horne (2013) discussed pressure and temperature behavior inside fracture during stimulation and shut-in (fracture closure) period for the fall-off analysis, and Ribeiro and Horne (2014) extended their model to consider multi-cluster fracturing treatment in horizontal wells by coupling previous model with wellbore flow and thermal model.

For production period, Yoshida et al. (2014) showed a temperature model in a horizontal wells with multiple fractures to predict wellbore fluid and sandface temperature along a nominally horizontal well by coupling of wellbore model and reservoir model. Their study concluded that the sandface temperature shows higher sensitivity to downhole conditions comparing wellbore fluid temperature, which is preferable for the interpretation. Cui et al. (2015b) presented a temperature model and applied it for several field cases to quantitatively estimate inflow rate profiles by matching estimated and observed temperature profiles using single phase gas model. Their work helps to evaluate actual inflow distribution along horizontal wells with multiple fractures, which can be comparable to interpretation results given by the analysis for injection and shut-in periods. Currently, effects of injected fluid and multiphase flow on temperature behaviors have not been fully investigated, and it is required to prove validity of the single phase assumption and to estimate possible estimation difference range in the quantitative inflow profiling.

According to App and Yoshioka (2013), sandface temperature changes in the ultra-tight reservoir such as shale gas reservoir will be minimal during production periods (less than 0.1 °C). Also, for hydraulically fractured wells, App (2013) concluded that the wellbore/sandface temperature change is reduced due to lower pressure gradients caused by linear flow regime compared with radial flow regime of non-hydraulically fractured wells. Further dimensionless analysis was performed to investigate effects on temperature profiled due to flow geometry differences (radial and linear) (App 2015). These analyses imply that the flow behavior in the fracture and in the vicinity of the fracture (secondary fracture or reactivated natural fractures created through the fracturing treatment (Fisher et al. 2005a, Fisher et al. 2004)) possibly affects inflow temperature into wellbores. Those network fractures and their enhancement effects have been modeled in several approaches: discrete fracture model (Mayerhofer et al. 2006), embedded discrete fracture model (Moinfar et al. 2014, Li and Lee 2008), dual/multiple continua model (Medeiros et al. 2008, Zhang et al. 2009, Moridis et al. 2010), and induced permeability field (Gildin et al. 2013, Yin et al. 2011). Recently, Cui et al. (2015a) adopted Fast Marching Method to quickly compute reservoir temperature distribution during production by explicitly expressing natural fractures with reservoir cells. The influences on sandface and inflow temperature by reservoir heterogeneity and natural fractures are demonstrated in their work. Yoshida et al. (2014) included the enhancement effects by network fractures using the induced permeability field or enhanced permeability region in the vicinity of the fracture. While the permeability contrast in their model setting gives the linear flow regime

in the reservoir, the influences on the temperature due to the difference in the network fracture modeling are not examined so far.

In addition, near wellbore modeling has also played an important role in downhole temperature interpretation. While downhole temperature is measured by several methods, basically, wellbore flowing temperature and temperature behind casing are possible locations of measurement. The wellbore flowing temperature is estimated by both of the reservoir inflow temperature and heat transfer against reservoir sandface. For vertical wells, inflow and sandface temperatures are estimated directly using cylindrical coordinate system (Sui et al. 2008a, Bahonar et al. 2011, App and Yoshioka 2013). However, for horizontal wells, the flow regime in the reservoir changes from linear to radial when fluid approaches to the near wellbore region. The radial flow regime offers larger pressure drop and leads to larger temperature changes due to Joule-Thomson effect compared to the linear flow regime. Yoshioka et al. (2005) obtained an analytical solution of the inflow temperature to a horizontal well under steady state condition. For a horizontal well with multiple fractures, while the additional pressure drop in the fracture due to the radial flow convergence can be estimated by the 'choke skin' concept (Mukherjee and Economides 1991), pressure and temperature distribution at near wellbore regions can be estimated directly by numerical simulations.

When reservoir simulation is adopted to solve reservoir flow/thermal problems, the productivity index concept is used to take care of the two flow regimes (Peaceman 1978). Recent work done by Livescu et al. (2010a), Livescu et al. (2010b), and Shirdel and Sepehrnoori (2012) used the productivity index with the wellbore grid pressure and

specific enthalpy to account for the mass and energy source to the wellbore system. In their work, the usage of the productivity index is reasonable because their main objective is to develop a general purpose wellbore-reservoir simulator or to apply the model for damage prediction and remediation, which does not require such a subtle temperature change at near wellbore regions. Li and Zhu (2010) used a simple steady state temperature model to calculate the inflow temperature analytically considering radial flow in the wellbore grid. While their approach can handle steady-state energy flow connection with wellbores, transient temperature characteristics are not modeled. Especially, a horizontal well with multiple fractures has two regions, perforated region and non-perforated region, and in the non-perforated regions transient temperature characteristics are critical during shut-in periods because heat conduction from surrounding formation is dominant. Yoshida et al. (2014) extended the simple model used by Li and Zhu (2010) at the wellbore grid to capture transient temperature change under steady-state flow condition by solving 1D transient energy balance equation. These methods enable to consider the transient temperature near wellbore, but require a model and procedure for coupling. As an alternate approach, a hybrid grid can be used; cylindrical grid system is used for near wellbore region while a Cartesian grid system is used for reservoir simulation (Pedrosa Jr. and Aziz 1986, Cheshire and Henriquez 1992). With use of simple radial grids in a Cartesian system, the coupled model is not required to consider, and simply both the radial and linear flow regimes can be included as solutions of the reservoir model under transient conditions.

Inclusion of observation data is also an essential part in diagnosis of wellbore performance and reservoir characterization as well as the development of theoretical modeling work. Production logging analysis is one of the methods to evaluate wellbore performance by matching the observed production logging data with the calculated data using theoretical model under certain assumed conditions. The history matching procedure can be automated through the so-called assisted history matching techniques. The matching procedure is regarded as the inverse problem by minimizing misfits of the simulator responses and observation data. For quantitative temperature interpretations, Yoshioka et al. (2009) and Sui et al. (2008b) used the Levenberg-Marquardt algorithm (Marquardt 1963) as one of the gradient based methods, and Li and Zhu (2010), Tabatabaei and Zhu (2012) and Tan et al. (2012) used Markov Chain Monte Carlo (MCMC) as one of the stochastic methods. The gradient based method requires computation of sensitivity matrix to update parameter vector. It needs smaller number of iterations to minimize the objective function comparing to the stochastic methods while it possibly falls into so-called 'local minimum' due to the non-linearity of the solution space. On the other hand, the MCMC is a sampling method, and it requires large samplings to converge to the solution. While it is computationally expensive to obtain large amount of samples, it avoids the 'local minimum' and provides uncertainty of the estimated parameters. It is difficult to prove the uniqueness of the estimated solution, but the uncertainty in the estimation provides reliability of the estimation.

Difficulties in the inverse modeling of horizontal wells with multiple fractures are mainly 1) a large amount of unknowns, 2) sensitivity of the unknowns and 3) non-

uniqueness of the solution. According to several field cases such as the Haynesville shale and Eagle Ford shale, more than 10 stages are completed in order to maximize the exposure to formations for the economic production from shale reservoirs (Thompson et al. 2011, Bazan et al. 2010, Pope et al. 2012). If we assume that there are four clusters per each stage, we have more than 40 fractures which have several parameters. Yoshida et al. (2014) examined the temperature sensitivity on the fracture length and fracture conductivity, and they concluded that fractures with longer half-length give lower inflow temperature while higher conductive fractures give higher inflow temperature after 30 days of production under constant bottom hole pressure constraint. Also, these complications in the sensitivity as well as large number of unknowns make the solution of inverse problem non-unique. Cui et al. (2014) successfully matched simulated temperature profile with field measured temperature data to estimate inflow profile, while it is difficult to prove the uniqueness of the estimated solution.

1.3 Objective and Organization of the Dissertation

The objective of this research is to interpret downhole temperature measured for injection, shut-in and production periods in a horizontal wells with multiple fractures. The interpretation is performed qualitatively and quantitatively. Qualitative insights are provided on the temperature behaviors on downhole conditions. Quantitative inflow profiling is another goal under multiphase conditions for temperature data during production. These objectives require the development of a temperature model for horizontal wells with multiple fractures under multiphase flow condition. The temperature

model needs to have the capabilities of simulating multiphase, non-isothermal fluid/thermal flow with consideration of the effect of well trajectory and inflow effect from the fractures along the wellbore. The entire model needs to have flexibility to account for situations occurring in actual fields such as multi-stage and multi-cluster fracturing treatment. Finally, the field observation data is integrated with the developed model for the diagnostics of the well performance and the characterization of the reservoir. It also requires consideration of the trade-off between the computational efficiency and the model complexity to account for the physical condition of the problem for practical applications.

In this research, we developed a comprehensive numerical simulation model for the entire system: wellbore and reservoir. These two systems are coupled together to simulate downhole temperature measurements such as temperature logs, permanent downhole gauges and DTS. In Chapter II, the development of the comprehensive numerical simulation model is discussed in detail. The drift-flux model and homogeneous model are implemented for the multiphase, non-isothermal wellbore simulation. In the reservoir domain, usage of local grid refinement of the cylindrical coordinate enables to integrate the non-isothermal reservoir simulation and the inflow temperature calculation with considerations of the radial flow convergence, which reduces one of the iterative procedures. The implemented model is verified against available analytical/semi-analytical solutions. In Chapter III, the developed model is used to simulate downhole temperature behavior considering actual field operations: injection, shut-in and production with several synthetic case studies. The case studies are intended to offer insights for better understandings of the downhole temperature qualitatively from the theoretical modeling

perspective. In Chapter IV, the developed model is applied to two field cases to justify qualitative interpretations and to estimate inflow profile quantitatively during production. In Chapter V, we summarize the entire work and suggest recommendations for future work.

CHAPTER II

MODELING OF DOWNHOLE TEMPERATURE BEHAVIOR IN A HORIZONTAL WELL WITH MULTIPLE FRACTURES

2.1 Chapter Summary

This chapter discusses development of a comprehensive numerical model to simulate downhole temperature in a horizontal well with multiple fractures. We start from discussions of prerequisites of the model, model domain (wellbore and reservoir), and governing equations for each domain. Then, we discuss implementation techniques used in this work to solve the governing equations and to couple the domains. The implemented model is verified through a series of simple cases which have analytical/semi-analytical solutions.

2.2 Introduction

A multi-stage fracturing treatment performs injection and shut-in repeatedly and sequentially from toe to heel for all stages with sufficient zonal isolations between the stages. Typically, fracture-sleeve completion or cemented plug-and-perforated completion is used. When the plug-and-perf completion is adopted for the target well, at first, a casing string is installed and cemented. Then, the casing is perforated for the first stage with single cluster or multiple clusters, fracturing fluid injection starts for the target stage, and, after pumping the fracture stage, a bridge plug is placed to isolate the target zone from successive treatments. The plug-and-perf completion limits the flow communication only

through the perforations, while the thermal communication occurs at both of the perforated and non-perforated regions. During injection period, the injected fluid makes formation temperature cooler via thermal conduction at the non-perforated regions. Once shut-in starts, the wellbore fluid and near wellbore formation temperature starts to increase since they are heated up by the surrounding formation. These cooling and heating cycles occur for each stage sequentially. The stages near the toe experiences longer shut-in period than the stages near the heel.

After the treatments of the all of the stages, the plugs are drilled out, and the well starts to produce fluids from the reservoir. During the production period, temperature anomalies are mainly caused by Joule-Thomson effect at perforated regions. For most of the real gases, the effect is cooling, while heating is observed for most of the liquids. In addition, if the injected fluids are not heated up to the original geothermal temperature, the temperature offsets to the original geothermal temperature after shut-in may also contribute to the temperature anomalies. These temperature anomalies, however, are relatively small, and it requires precise temperature measurements for interpretations.

In this work, we develop a comprehensive numerical model for downhole temperature profile in horizontal wells with multiple fractures. The model simulates wellbore flowing temperature and sandface temperature in those wells during injection, shut-in and production periods. The comprehensive model is formulated for wellbore and reservoir system under multi-phase and multi-component flow condition, which gives flexibility and capability to the model to account for situations occurring in actual field. Especially, the model needs to have capabilities to take care of the completion design and

the changing operational conditions with time for each zone. The developed model is applied to diagnose fracturing treatments and to evaluate post-stimulation production performance.

2.3 Model Description

The temperature model consists of two domains: the reservoir and the wellbore. Each domain has distinct governing equations for fluid flow and energy transport. **Figure 2.1** shows a schematic of the entire model domain. The reservoir model is described by mass balance equations of each component with Darcy's law, and a thermal energy balance equation. On the other hand, the wellbore model is described by mass balance equations of each component, a combined-phase momentum balance equation, and a total energy balance equation. With given reservoir properties (e.g. porosity, permeability etc.) and wellbore properties (e.g. wellbore diameter, overall heat transfer coefficient etc.), primary variables such as velocity, pressure, saturation/hold-up and temperature are obtained in both domains by solving the governing equations.

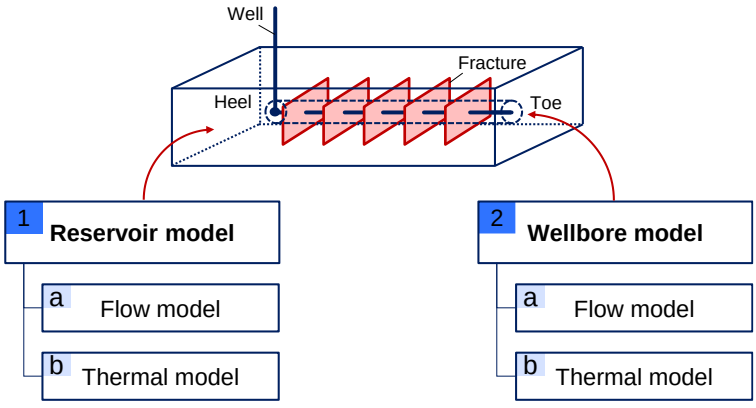

Figure 2.1—Model domains

2.3.1 Reservoir Model

The reservoir models are formulated for three-dimensional reservoir domain in transient condition with considerations of multiphase and multicomponent flow. The formulations in differential form are derived based on the work by Pruess et al. (1999) with the following assumptions similar to the work by Adenekan et al. (1993):

1) effects of molecular diffusion, adsorption and chemical reaction are ignored.
2) fluids and matrix are in thermal equilibrium locally.
3) thermal energy balance is used to depict energy balance in the reservoir.
4) enthalpy change due to phase transitions is ignored.

This section only shows final form of the reservoir models, and the detail derivations of these equations are summarized in Appendix A.

Flow Model

The reservoir flow model is derived from the conservation of mass with Darcy's law to depict the macroscopic volumetric flux in the reservoir. For a multiphase and multicomponent system, the conservation of component mass is expressed by

$$\frac{\partial}{\partial t}\left(\phi\sum_{\beta}S_{\beta}\rho_{\beta}X_{\beta}^{\kappa}\right)+\nabla\bullet\left[\sum_{\beta}\left(X_{\beta}^{\kappa}\rho_{\beta}\mathbf{v}_{\beta}\right)\right]=0 \quad \text{..... (2.1)}$$

where ϕ is porosity, S_β is saturation of phase β, ρ_β is density of phase β, $\mathbf{v}_\beta$ is volumetric flux vector of phase β and X_β^κ is mass fraction of component κ in phase β. The terms in the left-hand-side denote component mass accumulation and component mass flux, respectively. The volumetric flux of phase β is described by Darcy' law:

$$\mathbf{v}_\beta = -\frac{kk_{r\beta}}{\mu_\beta}\left(\nabla p_\beta - \rho_\beta \mathbf{g}\right) \quad \text{..... (2.2)}$$

where $k_{r\beta}$ is relative permeability of phase β, k is intrinsic permeability, p_β is pressure in phase β, and **g** is the acceleration of gravity. At contacts of the reservoir and the wellbore, mass interaction occurs by fluid movement between the domains. The mass sink/source at the wellbore position is expressed as:

$$q^\kappa = \sum_\beta X_\beta^\kappa q_\beta \quad \text{..... (2.3)}$$

where q^κ is mass transfer rate of component κ per unit volume and q_β is phase-mass flow rate of phase β per unit volume (injection is positive).

Thermal Model

The reservoir thermal model is derived from the conservation of thermal energy in the reservoir. For a multiphase and multicomponent system, it is expressed as

$$\frac{\partial}{\partial t}\left[\phi\sum_\beta \rho_\beta S_\beta U_\beta + (1-\phi)\rho_s U_s\right] = -\nabla\bullet\left(\sum_\beta \rho_\beta \mathbf{v}_\beta H_\beta\right) + \nabla\bullet\left(k_{Tt}\nabla T\right) \quad \text{... (2.4)}$$

where U_β is specific internal energy of phase β, U_s is specific internal energy of solid (matrix), H_β is specific enthalpy of phase β, k_{Tt} is total thermal conductivity and T is temperature of fluid/matrix (thermal equilibrium). The term in the left-hand-side denotes thermal accumulation. The first and second terms in the right-hand side are heat fluxes of advection and conduction, respectively. In a similar manner, at contacts of the reservoir and wellbore, energy interaction occurs. The thermal sink/source at the wellbore position consists of heat conduction and advective energy transport expressed as

$$q^{\theta} = q_{wb} + \sum_{\beta} H_{\beta} q_{\beta} \quad \text{..... (2.5)}$$

where q^{θ} is heat transfer rate per unit volume and q_{wb} is conductive heat transfer rate per unit volume due to temperature differences.

2.3.2 Wellbore Model

The wellbore models are formulated for one-dimensional wellbore domain in transient condition by considering conservation equations along measured depth of the well trajectory. This work adopted the models by Ishii and Hibiki (2011) and Brennen (2005).

Figure 2.2 shows a coordinate system considered in the wellbore model. The direction of the measured depth is expressed by *z*-coordinate and the direction of wellbore radius is denoted by *r*-coordinate. In this study, averaged properties over the cross-sectional area of the well segment are used by ignoring variations of properties in the *r*- and the θ-direction. The average over the cross-section is calculated by integration: (Ishii 1977)

$$\langle F \rangle = \frac{1}{\pi r_i^2} \int_0^{r_i} \int_0^{2\pi} F r d\theta dr \quad \text{..... (2.6)}$$

where F is a general property to be averaged (such as fluid density) and r_i is inner radius of wellbore. In the rest of this section, the area-averaging notation is omitted.

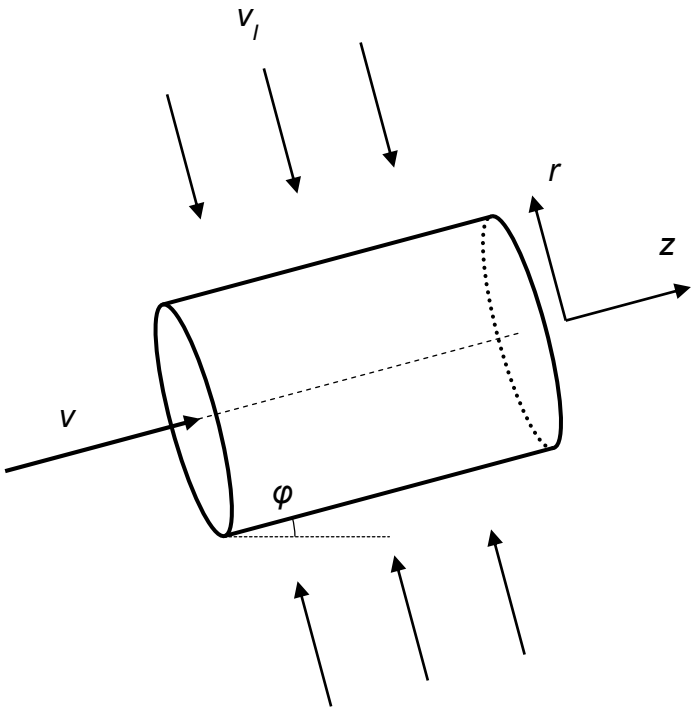

Figure 2.2—Differential volume element of wellbore segment

Flow Model

The wellbore flow model is derived from conservations of component mass and combined-phase momentum. With assumption of equilibrium of interphase mass transfer within a differential time, the component mass conservation can be expressed as

$$\frac{\partial}{\partial t}\left(\sum_{\beta}\alpha_{\beta}\rho_{\beta}X_{\beta}^{\kappa}\right)+\frac{\partial}{\partial z}\left(\sum_{\beta}\alpha_{\beta}\rho_{\beta}X_{\beta}^{\kappa}v_{\beta}\right)=\frac{2\gamma}{r_i}\left(\sum_{\beta}\alpha_{\beta,I}\rho_{\beta,I}X_{\beta,I}^{\kappa}v_{\beta,I}\right) \quad ..... \quad (2.7)$$

where α_β is volume fraction of phase β, v_β is fluid in-situ velocity of phase β, γ is pipe-open ratio and the subscript I denotes that the properties are evaluated at the inflow/outflow condition. The pipe-open ratio is introduced to consider the actual

inflow/outflow velocity with different completions (Yoshioka et al. 2005), and the pipe-open ratio is calculated as

$$\gamma = \frac{\text{Open pipe surface area}}{\text{Pipe total surface area}}. \ (0 \le \gamma \le 1) \quad \text{..... (2.8)}$$

The pipe-open ratio is considered over a certain length of the wellbore, and the value changes with position. For non-perforated region, the pipe-open ratio is zero. For perforated region, the value depends on the perforation density over the segment of the well (Yoshioka 2007). The pipe-open ratio gives a relationship of inflow/outflow velocity between open-hole ($v_{I,open}$) and cased-perforated completions (v_I) as

$$v_{I,open} = v_I \gamma . \quad \text{..... (2.9)}$$

This means the actual inflow velocity through cased-perforated completion is higher than the inflow velocity of open-hole wellbore (when γ = 1, the actual inflow velocity is same with that of open-hole completion).

The combined-phase momentum equation is given by adding phase momentum equations together for all the existing phases (Brennen 2005). The combined-phase momentum equation is expressed in one-dimensional form, ignoring the interfacial momentum transfer and axial stress terms (Pan et al. 2011d, Ishii 1977) as:

$$\frac{\partial}{\partial t}\left(\sum_{\beta}\alpha_{\beta}\rho_{\beta}v_{\beta}\right)+\frac{\partial p}{\partial z}+\frac{\partial}{\partial z}\left(\sum_{\beta}\alpha_{\beta}\rho_{\beta}v_{\beta}v_{\beta}\right)=-\frac{\Gamma}{2A}\rho_m v_m|v_m| f_m+\rho_m g_z \quad \text{.... (2.10)}$$

where v_m is mean mixture velocity of center of mass, Γ is perimeter of the well segment, A is cross-sectional area of the well segment and f_m is phase-mixture friction factor on the wellbore wall, respectively. The mean mixture velocity of center of mass is calculated by

$$v_m = \frac{\sum_\beta \alpha_\beta \rho_\beta v_\beta}{\sum_\beta \alpha_\beta \rho_\beta}. \quad \text{..... (2.11)}$$

Thermal Model

The wellbore thermal model is derived from the conservation of total energy in the wellbore. When we ignore effects of turbulence and viscous dissipation heating, the model is expressed in the form:

$$\begin{aligned} \frac{\partial}{\partial t}\left[\sum_\beta \alpha_\beta \rho_\beta \left(U_\beta + \frac{v_\beta^2}{2}\right)\right] &= -\frac{\partial}{\partial z}\left[\sum_\beta \alpha_\beta \rho_\beta \left(H_\beta + \frac{v_\beta^2}{2}\right) v_\beta\right] \\ &+ \frac{\partial}{\partial z}\left(k_f \frac{\partial T}{\partial z}\right) + \sum_\beta \alpha_\beta \rho_\beta g_{\beta,z} v_\beta \quad \text{..... (2.12)} \\ &+ \frac{2(1-\gamma)}{r_i} U_T\big|_{r=r_i}(T_{res} - T) + \frac{2\gamma}{r_i}\left\{\sum_\beta j_{\beta,I}\rho_{\beta,I}\left[H_{\beta,I} + \frac{v_{\beta,I}^2}{2}\right]\right\} \end{aligned}$$

where k_f is fluid thermal conductivity, j_β is volumetric flux of phase β, U_T is overall heat transfer coefficient, and T_{res} is reservoir sandface temperature. The left-hand-side term denotes the energy accumulation. The first, second and third terms in the right-hand-side are advective energy flux, conductive energy flux and work done by body force (gravity), respectively. The fourth and fifth terms express energy transport between the reservoir and wellbore: conduction and advection, respectively. These terms are corresponding to the terms in the sink/source term of the reservoir thermal model.

2.4 Constitutive Relations and Equations of State

The above governing equations are solved for primary variables such as pressure and temperature. The other variables need to be estimated by the primary variables, and they are described by constitutive relations and equations of state. This section lists the selected models used in this work, and full description of the listed models are in Appendix B.

2.4.1 Constitutive Relations

Capillary Pressure

Capillary pressure accounts for wettability differences between existing phases in porous medium. When gas-water two-phase system (aqueous and gaseous) is considered, the aqueous phase pressure, p_A, is expressed by

$$p_A = p_G + p_{cAG} \quad \text{..... (2.13)}$$

where p_{cAG} is aqueous-gaseous capillary pressure. While the capillary pressure value is estimated using models such as van Genuchten function (van Genuchten 1980), this work ignores the capillary pressure effect to simplify the problem.

Relative Permeability

Relative permeability is a function of saturations, and, in this work, Corey curve model and linear model are used. The Corey curve model is expressed as (Corey 1954):

$$k_{rA} = \bar{S}^4 \quad \text{..... (2.14)}$$

$$k_{rG} = \left(1 - \bar{S}\right)^2 \left(1 - \bar{S}^2\right) \quad \text{..... (2.15)}$$

where k_{rA} is aqueous phase relative permeability, k_{rG} is gaseous phase relative permeability, and the effective saturation $\bar{S}$ is expressed with residual water and gas saturation (S_{rA} and S_{rG}) as

$$\bar{S} = \frac{S_A - S_{rA}}{1 - S_{rA} - S_{rG}}. \quad \text{..... (2.16)}$$

The flow in the hydraulic fracture is described by the linear model when the pressure loss due to the interations between phases is negligible compared with the pressure loss due to the flow of each fluid (Chen et al. 2004):

$$k_{rA} = S_A \quad \text{..... (2.17)}$$

$$k_{rG} = S_G. \quad \text{..... (2.18)}$$

To incorporate reduction of the relative permeability from the linear model as discussed in some of the experimental work (Chen et al. 2004, Chen and Horne 2006), the Corey curve model can also be used in the fractures.

Total Thermal Conductivity

The total thermal conductivity, k_{Tt}, is estimated by a relation by Somerton et al. (1974):

$$k_{Tt} = k_{dry} + \sqrt{S_A}\left(k_{wet} - k_{dry}\right) \quad \text{..... (2.19)}$$

where S_A is aqueous phase saturation, k_{dry} is dry rock thermal conductivity (S_A = 0), and k_{wet} is water saturated rock thermal conductivity (S_A = 1).

In-situ Phase Velocity in Wellbore: Drift-flux Model and Homogeneous Model

The combined-phase momentum equation (Eq. 2.10) is formulated in terms of in-situ phase velocity and the mixture velocity of the center of mass (v_m). While the v_m is calculated by Eq. 2.11, we need a relationship between those in-situ phase velocities.

The drift-flux model for two-phase flow correlates the in-situ gaseous phase velocity with total volumetric flux of gas-liquid mixture using the drift-velocity. Zuber and Findlay (1965) proposed a kinematic relationship with consideration of effects of non-uniform flow/concentration profiles and local relative (slip) velocity. The in-situ gaseous phase velocity is expressed as

$$v_G = C_0 j + V_d . \quad \text{..... (2.20)}$$

where C_0 is the distribution parameter to account for the non-uniform flow and concentration profiles, j is the volumetric flux of gas-liquid mixture and V_d is the drift-velocity of gas phase to express the slip between the phases. With use of the drift-velocity and mixture volumetric flux, the in-situ liquid velocity is given by

$$v_L = \frac{1-\alpha_G C_0}{1-\alpha_G} j - \frac{\alpha_G}{1-\alpha_G} V_d \quad \text{..... (2.21)}$$

where α_G is the in-situ volume fraction of gaseous phase.

In this work, the distribution parameter and the drift-velocity are estimated by Shi et al. (2005b). Their work provides expressions for C_0 and V_d that are relatively simple, continuous and differentiable. It is noted that Shi et al. (2005b) used the experimental data from vertial to near horizontal (88°) because they considered the experimental holdup data for 90° and 92° display relatively large errors due to the end effect. Choi et al. (2012)

performed the comparison studies of the several modeling methods with a variety of dataset, and the model by Shi et al. (2005b) showed relatively higher error in the estimation of horizontal flow.

The homogeneous model assumes there is no slip between the two phases. Therefore, the in-situ phase velocities are mutually identical, and also they are same with mixture velocity of center of mass and mixture volumetric flux:

$$v_G = v_A = v_m = j. \quad \text{..... (2.22)}$$

Overall Heat Transfer Coefficient

The sandface temperature and wellbore temperature are related through the overall heat transfer coefficient. **Figure 2.3** shows temperature distribution near wellbore region for possible cases: tubing region, non-perforated region and perforated region. The overall heat transfer coefficients for these cases are given by

$$\frac{1}{U_T\big|_{r=r_{to}}} = r_{to}\left[\frac{1}{r_{ti}h_t} + \frac{\ln\frac{r_{to}}{r_{ti}}}{k_t} + \frac{1}{r_{to}h_{ann}} + \frac{\ln\frac{r_{co}}{r_{ci}}}{k_c} + \frac{\ln\frac{r_w}{r_{co}}}{k_{cem}}\right] \quad \text{..... (2.23)}$$

for tubing region, and

$$\frac{1}{U_T\big|_{r=r_{ci}}} = r_{ci}\left[\frac{1}{r_{ci}h_{ci}} + \frac{\ln\frac{r_{co}}{r_{ci}}}{k_c} + \frac{\ln\frac{r_w}{r_{co}}}{k_{cem}}\right] \quad \text{..... (2.24)}$$

for perforated/non-perforated regions. In these equations, h_t is heat transfer coefficient in the tubing, h_{ann} is heat transfer coefficient of annulus, h_c is heat transfer coefficient of

casing, *k* denotes the thermal conductivity, *r* denotes the radius, and subscripts *ti*, *to*, *ci*, *co*, *w*, *cem* denote inner tubing, outer tubing, inner casing, outer casing, wellbore and cement, respectively.

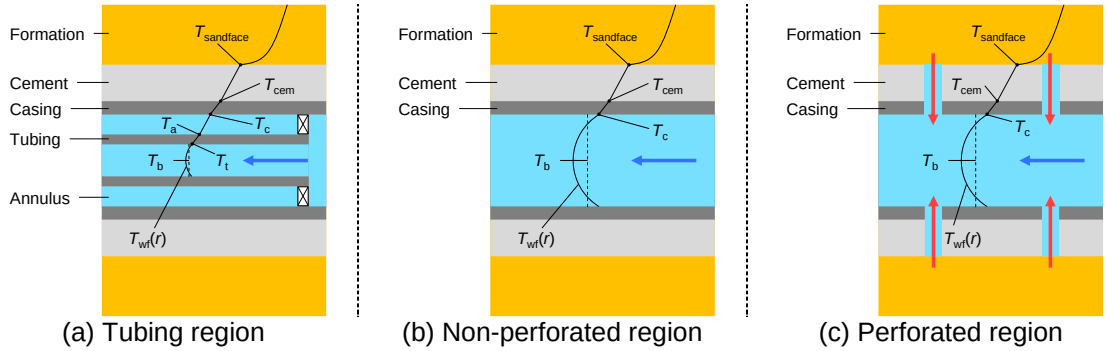

Figure 2.3—Temperature distribution near wellbore region for possible cases

2.4.2 Phase Transition and Thermophysical Properties

Suppose we know existing components in the system, possible and actual thermodynamic state of the system can be determined by pressure and temperature. This work assumes that the target system contains only two components: water (H_2O) and non-condensable gas (such as CH_4). The possible states are limited to combinations of two phases: Aqu (Aqueous), Gas (Gaseous) and AqG (Aqueous-Gaseous).

Mole Fractions

Those two components can exist in both of the aqueous phase and gaseous phase, and, in each phase, component mole fraction (Y_β^κ) and mass fraction (X_β^κ) have following constraints:

$$\sum_{\kappa} X_{\beta}^{\kappa} = 1 \quad (\beta = A \text{ or } G) \quad \text{..... (2.25)}$$

$$\sum_{\kappa} Y_{\beta}^{\kappa} = 1. \quad (\beta = A \text{ or } G) \quad \text{..... (2.26)}$$

In the gaseous phase, the component mixture is assumed to follow Dalton's law of partial pressures:

$$p_G = \sum_{\kappa} p_G^{\kappa} \quad \text{..... (2.27)}$$

where p_G is gaseous phase pressure, and the partial pressure of the gas component in the gaseous phase (p_G^g) is calculated by

$$p_G^g = Y_G^g p_G . \quad \text{..... (2.28)}$$

For single phase gaseous system, the gas component mole fraction in the gaseous phase (Y_G^g) is treated as one of the primary variables, and, then, the partial pressure of the water component and mole fraction of the water component in the gaseous phase can be calculated. For aqueous-gaseous two phase system (liquid water exists), the partial pressure of the water component in the gaseous phase is equal to the saturation pressure (p_{sat}^w). The mole fraction of the water component in the gaseous phase can be calculated as

$$Y_G^w = \frac{p_{sat}^w}{p_G} \quad \text{..... (2.29)}$$

The gas component mole fraction in the aqueous phase is calculated with Henry's law:

$$Y_A^g = \frac{p_G^g}{H^g} \quad \text{..... (2.30)}$$

where H^g is Henry's coefficient. The Henry's coefficient of the CH_4 in H_2O is estimated by a correlation in Fernández-Prini et al. (2003). For single phase aqueous system, the gas component mass fraction or mole fraction in the aqueous phase (X_A^g or Y_A^g) is treated as one of the primary variables.

Phase Transition Criteria

This work uses same phase transition criteria with the work by Class et al. (2002). For the aqueous-gaseous two phase system, diappearance of one of the phases is determined by a value of the phase saturation; when the saturation of a phase becomes lower than 0 during calculations, the state is switched to be single phase condition (either of single phase aqueous or single phase gaseous). For the single phase aqueous system, gaseous phase appears when sum of the water saturation pressure and the gas component partial pressure (given by Henry's law) exceeds the system pressure:

$$p < p_{sat}^w + Y_A^g H^g . \quad \text{..... (2.31)}$$

On the other hand, for the single phase gaseous system, aqueous phase appears when the water component partial pressure (p_G^w) exceeds water saturation pressure:

$$p_{sat}^w < Y_G^w p_G . \quad \text{..... (2.32)}$$

Fluid and Thermal Properties of Gas-water Mixture

Once the physical state is determined, thermophysical properties of each phase are calculated. At first, the saturation pressure of the water component is estimated with the model by Wagner et al. (2000). The aqueous phase density is calculated as mass fraction weighted average of the component density:

$$\rho_A = \sum_\kappa X_A^\kappa \rho_A^\kappa \quad \text{..... (2.33)}$$

where the component density of the ordinary water (H_2O) is estimated by a model by Wagner et al. (2000) and the gas component density is estimated by the Peng-Robinson equation of state (Peng and Robinson 1976). The calculated aqueous phase density is used in the calculation of the water viscosity by Huber et al. (2009). The aqueous phase specific enthalpy is also calculated as a mass fraction weighted average of the component specific enthalpy:

$$H_A = \sum_\kappa X_A^\kappa H_A^\kappa . \quad \text{..... (2.34)}$$

Once the specific enthalpy and density of the aqueous phase are given, the aqueous phase specific internal energy is computed by

$$U_A = H_A - \frac{p}{\rho_A} . \quad \text{..... (2.35)}$$

The aqueous phase thermal conductivity also uses the calculated aqueous phase density in the model by Huber et al. (2012).

The gas phase density is calculated as a sum of the water vapor density and gas component density evaluated with the partial pressure of each component. The gaseous

phase viscosity is estimated by Sun and Mohanty (2005) using the calculated gaseous phase density. The gaseous phase thermal conductivity is estimated by Yaws (1995). The specific enthalpy of the gaseous phase is computed as mass fraction weighted average based on the mole fractions of the enthalpy of the water vapor and the gas component (Adenekan et al. 1993):

$$H_G = \sum_{\kappa} X_G^{\kappa} H_G^{\kappa} \quad \text{..... (2.36)}$$

where the component specific enthalpy is evaluated with the partial pressure of each component. The specific enthalpy of the water vapor is estimated with the model by Wagner et al. (2000). The specific enthalpy of the gas component in the gaseous phase is computed with ideal gas specific enthalpy and departure function. The ideal gas specific enthalpy of a certain component is calculated by an empirical correlation in Poling et al. (2000). The departure function considers enthalpy differences of real fluid and ideal gas:

$$H_M(p,T) - H_M^{IG}(p,T) = \int_{p=0,T}^{p,T} \left[V_M - T\left(\frac{\partial V_M}{\partial T} \right)_p \right] dp \quad \text{..... (2.37)}$$

where the temperature is evaluated as absolute temperature, H_M is enthalpy per mole and V_M is molar volume. With use of the Peng-Robinson equation of state, the departure function is expressed in explicit form as (Sandler 2006, Peng and Robinson 1976)

$$H_M(p,T) - H_M^{IG}(p,T) = RT(Z-1) + \frac{T\left(\frac{da_T}{dT} \right) - a_T}{2\sqrt{2}b} \ln\left[\frac{Z + \left(1+\sqrt{2}\right)B}{Z + \left(1-\sqrt{2}\right)B} \right] \quad \text{.... (2.38)}$$

where R is gas constant, Z is compressibility factor, and a_T, b, and B are parameters in the Peng-Robinson equation of state described in Appendix B. The estimated molar enthalpy

is converted into the specific enthalpy with the molecular weight of the gas. Once the specific enthalpy and density of the gaseous phase are calculated, the gaseous phase specific internal energy is computed by

$$U_G = H_G - \frac{p}{\rho_G}. \quad \text{..... (2.39)}$$

2.5 Model Implementation

This section describes implementation techniques used in this work. This work employs the integral finite difference method to discretize the governing equations spatially (Narasimhan and Witherspoon 1976), and they are solved to obtain primary variables under fully-implicit scheme with Newton-Raphson iterations. Previous section discusses the possible physical states and their transition criteria within the ranges of pressure and temperature considered in this work. According to the phase transition, this work changes selection of the primary variables adaptively (Class et al. 2002, Pruess et al. 1999).

2.5.1 Primary Variables

Phase-transition criteria discussed in the previous section have a crucial role in the simulation; it triggers the switching of the primary variables. The primary variables are the variables used to determine the other parameters (secondary variables) with constitutive equations and models for thermophysical properties. This work considers three thermodynamic states: single phase aqueous, single phase gaseous, and two phase aqueous-gaseous. The pressure and temperature are commonly used as primary variables

for all of the three thermodynamic states, but the saturation is used only for the two-phase conditions since, under the single phase condition, the saturation is no longer an unknown parameter. Instead, under single phase condition, mass or mole fraction is used as one of the primary variables to account for the solubility of the gas component into the aqueous phase or the mixture of the water and gas component.

Figure 2.4 summarizes relationships of thermodynamic states, phase transition criteria and corresponding primary variables under gas-water two component system. The single phase aqueous conditions uses the gas component mass fraction in the aqueous phase (X_A^g), while the single phase gaseous condition uses the gas component mole fraction in the gaseous phase (Y_G^g). It is noted that, in the wellbore model, phase in-situ velocity (v_A, v_G) or mixture velocity of the mass center (v_m) is also one of the primary variables.

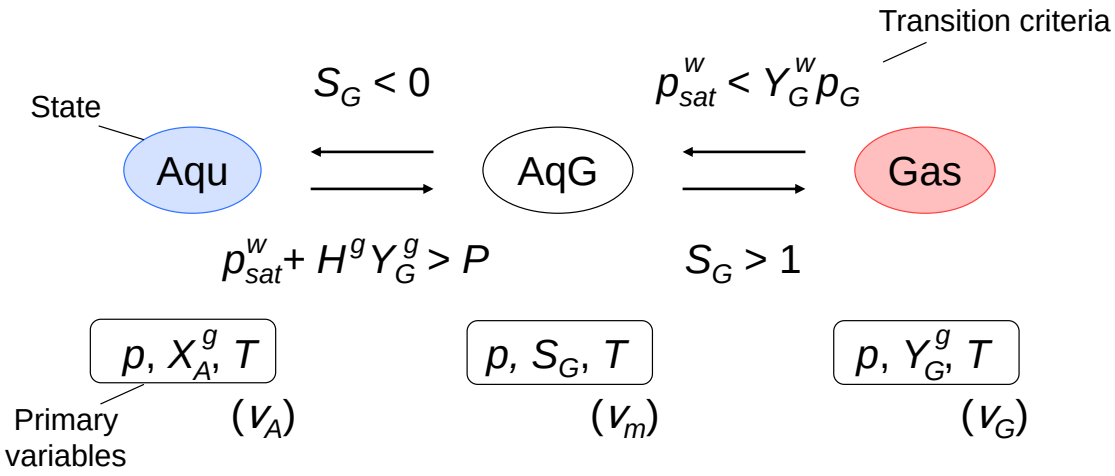

Figure 2.4—Primary variables and phase transition criteria

2.5.2 Numerical Method

The integral finite difference method discretizes the entire domain into conventionally small subdomains, and it formulates difference equations in integral form over each subdomain (Narasimhan and Witherspoon 1976). The reservoir domain is discretized into subdomains of small elements in the 2D or 3D spaces, and these elements are connected through connections. The wellbore model is also discretized into 1D elements along the measured depth of the wellbore with defined connections between the elements. The zonal isolation between the stages can be modeled by changing the condition of the wellbore connections: flowing connection or closed connection. The reservoir elements which contain wellbore elements have connections to the wellbore elements to define the sink/source terms. In order to obtain the discretized equations, because the above governing equations are in differential form, those equations are integrated over the subdomains in both reservoir and wellbore. Once the system of equations is obtained, the equations are solved in each domain under fully-implicit scheme with Newton-Raphson methods. This section shows final form of spatial and temporal discretization of the conservation equations, and details of the discretization are shown in Appendix C.

Reservoir Model

Reservoir flow model is expressed in the integral form (Pruess et al. 1999) as:

$$\frac{d}{dt}\int_{V_m} M^{\kappa} dV = \int_{\Gamma_m} \mathbf{F}^{\kappa} \bullet \mathbf{n} d\Gamma + \int_{V_m} q^{\kappa} dV \quad \text{..... (2.40)}$$

where M^{κ}, $\mathbf{F}^{\kappa}$ and q^{κ} are mass accumulation, mass flux, and mass sink/source of component κ, respectively, and V_m and Γ_m are control volume and the boundary of the element m, and **n** is the inward normal vector on the boundary. According to the Eq. 2.1, the terms in the integral form of the mass balance equations are expressed as:

$$M^{\kappa} = \phi \sum_{\beta} S_{\beta} \rho_{\beta} X_{\beta}^{\kappa} \quad \text{..... (2.41)}$$

$$\mathbf{F}^{\kappa} = \sum_{\beta} \left(X_{\beta}^{\kappa} \rho_{\beta} \mathbf{v}_{\beta} \right) \quad \text{..... (2.42)}$$

$$q^{\kappa} = \sum_{\beta} X_{\beta}^{\kappa} q_{\beta} \; . \quad \text{..... (2.43)}$$

The term q^{κ} is defined only at the wellbore positions, and in othr regions, the mass sink/source is zero. In similar manner, reservoir thermal model is also expressed in the integral form (Pruess et al. 1999) as:

$$\frac{d}{dt} \int_{V_m} M^{\theta} dV = \int_{\Gamma_m} \mathbf{F}^{\theta} \bullet \mathbf{n} d\Gamma + \int_{V_m} q^{\theta} dV \quad \text{..... (2.44)}$$

where M^{θ}, $\mathbf{F}^{\theta}$ and q^{θ} are heat accumulation, heat flux and thermal sink/source, respectively. According to the Eq. 2.4, the terms in the integral form of the energy balance equations are expressed as

$$M^{\theta} = \phi \sum_{\beta} \rho_{\beta} S_{\beta} U_{\beta} + (1 - \phi) \rho_s U_s \quad \text{..... (2.45)}$$

$$\mathbf{F}^{\theta} = -k_{\theta} \nabla T + \sum_{\beta} \rho_{\beta} \mathbf{v}_{\beta} H_{\beta} \quad \text{..... (2.46)}$$

$$q^{\theta} = q_{wb} + \sum_{\beta} H_{\beta} q_{\beta} \; . \quad \text{..... (2.47)}$$

These reservoir flow and thermal models are discretized in space and time under the fully

implicit scheme. Let Δt be timestep size, and current time be n-th timestep. Residual equations of the next timestep (n+1) are expressed as

$$R_m^{\kappa,n+1} = M_m^{\kappa,n+1} - M_m^{\kappa,n} - \frac{\Delta t}{V_m}\left(\sum_l A_{ml} F_{ml}^{\kappa,n+1} + V_m q_m^{\kappa,n+1}\right) = 0 \quad \text{..... (2.48)}$$

$$R_m^{\theta,n+1} = M_m^{\theta,n+1} - M_m^{\theta,n} - \frac{\Delta t}{V_m}\left(\sum_l A_{ml} F_{ml}^{\theta,n+1} + V_m q_m^{\theta,n+1}\right) = 0 \quad \text{..... (2.49)}$$

where R^{κ} is mass residual of component κ, R^{θ} is residual of energy, l is element adjacent to element m, A_{ml} is surface area between element m and element l, and superscript n and n+1 denote current and new timestep. This work considers two-component system, and, then, each element has three equations (two residual equations for component mass and one residual equation for thermal energy balance).

Wellbore Model

The wellbore model is also discretized through the integration of the equations over the control volume of the wellbore segment. Because the wellbore model is defined on the one-dimensional space, the flux terms are expressed for two adjacent points. **Figure 2.5** shows schematics of the wellbore segments and name of nodes and faces for the well segments, and these are used in following difference equations. In the wellbore model, a staggered-grid is adopted to solve velocity at the face of each control volume while other scalar quantities such as pressure and temperature are solved at the center of the control volume to avoid spurious pressure oscillations (Prosperetti 2007). In the following part, the element m is used to obtain difference equations of the mass balance and energy

balance, and the shifted element p ($m-1$ and m are faces of the element) to obtain the difference equation of the combined-phase momentum balance equation.

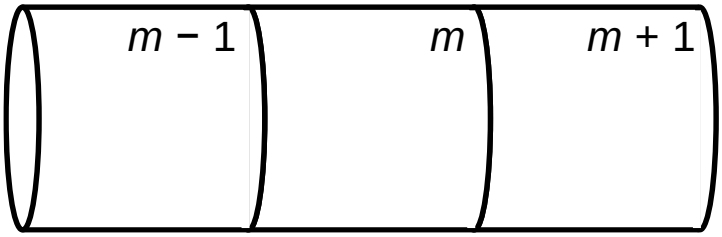

(a) Segmentation of the wellbore

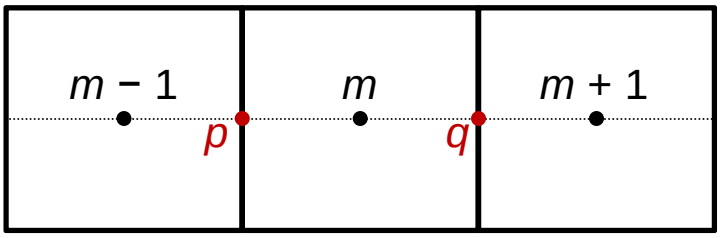

(b) Name of nodes and faces of segment

Figure 2.5—Discretization of the wellbore domain

The equations of the component mass balance and the total energy are integrated over the control volume of the element m. The final form of the residual equation of the component mass balance is expressed as

$$R_{v,m}^{\kappa,n+1} = \sum_{\beta} \alpha_{\beta,m}^{n+1} \rho_{\beta,m}^{n+1} X_{\beta,m}^{\kappa,n+1} - \sum_{\beta} \alpha_{\beta,m}^{n} \rho_{\beta,m}^{n} X_{\beta,m}^{\kappa,n} - \frac{\Delta t}{V_m} \left[\sum_{\beta} X_{\beta,I,m}^{\kappa,n+1} q_{\beta,I,m}^{n+1} \right] - \frac{\Delta t}{V_m} \left[\sum_{\beta} A_p \alpha_{\beta,p}^{n+1} X_{\beta,p}^{\kappa,n+1} \rho_{\beta,p}^{n+1} v_{\beta,p}^{n+1} - \sum_{\beta} A_q \alpha_{\beta,q}^{n+1} X_{\beta,q}^{\kappa,n+1} \rho_{\beta,q}^{n+1} v_{\beta,q}^{n+1} \right] = 0 \quad \text{..... (2.50)}$$

where A is cross-secitional area of the well segment, $q_{\beta,I,m}$ is mass inflow/outflow rate at the segment m and subscripts p and q denote faces of the well segment (**Figure 2.5b**). The final form of the residual equation of the total energy is expressed as

$$
\begin{aligned}
R_{T,m}^{\kappa,n+1} = & \sum_{\beta} \alpha_{\beta,m}^{n+1} \rho_{\beta,m}^{n+1} \left\{ U_{\beta,m}^{n+1} + \frac{\left(v_{\beta,m}^{n+1}\right)^2}{2} \right\} - \sum_{\beta} \alpha_{\beta,m}^{n} \rho_{\beta,m}^{n} \left\{ U_{\beta,m}^{n} + \frac{\left(v_{\beta,m}^{n}\right)^2}{2} \right\} \\
& - \frac{\Delta t}{V_m} \left[A_p \left\{ \left[\sum_{\beta} \alpha_{\beta,p}^{n+1} \rho_{\beta,p}^{n+1} \left(H_{\beta,p}^{n+1} + \frac{\left(v_{\beta,p}^{n+1}\right)^2}{2} \right) v_{\beta,p}^{n+1} \right] - k_{f,p}^{n+1} \frac{\partial T}{\partial z}\bigg|_{p}^{n+1} \right\} \right. \\
& \qquad \left. - A_q \left\{ \left[\sum_{\beta} \alpha_{\beta,q}^{n+1} \rho_{\beta,q}^{n+1} \left(H_{\beta,q}^{n+1} + \frac{\left(v_{\beta,q}^{n+1}\right)^2}{2} \right) v_{\beta,q}^{n+1} \right] - k_{f,q}^{n+1} \frac{\partial T}{\partial z}\bigg|_{q}^{n+1} \right\} \right] \quad \text{.....} \quad (2.51) \\
& - \Delta t \sum_{\beta} \left(\alpha_{\beta,m}^{n+1} \rho_{\beta,m}^{n+1} g_z v_{\beta,m}^{n+1} \right) - \frac{\Delta t}{V_m} \left\{ \sum_{\beta} q_{\beta,I,m}^{n+1} \left[H_{\beta,I,m}^{n+1} + \frac{\left(v_{\beta,I,m}^{n+1}\right)^2}{2} \right] \right\} \\
& - \frac{\Delta t}{V_m} A_{in,m} \left(1 - \gamma_m\right) U_{T,\mathrm{m}}^{n+1} \left(T_{res,m}^{n+1} - T_m^{n+1} \right) = 0
\end{aligned}
$$

where A_{in} is inner surface area of the well segment:

$$A_{in,m} = 2\pi r_{i,m} \Delta z_m , \quad \text{.....} \quad (2.52)$$

and Δz_m is the segment size in the axial direciton of the element m.

The momentum balance equation is integrated over the control volume between nodes $m-1$ and m, V_p. The final form of the residual equation of the component mass balance is expressed as

$$
\begin{aligned}
R_{P,p}^{n+1} = & \sum_{\beta} \alpha_{\beta,p}^{n+1} \rho_{\beta,p}^{n+1} v_{\beta,p}^{n+1} - \sum_{k} \alpha_{\beta,p}^{n} \rho_{\beta,p}^{n} v_{\beta,p}^{n} - \rho_{m,p}^{n+1} g_z \Delta t \\
& + \frac{\Gamma}{2A} \rho_{m,p}^{n+1} v_{m,p}^{n+1} \left| v_{m,p}^{n+1} \right| f_{m,p}^{n+1} \Delta t \\
& + \frac{\Delta t}{V_p} \left[A_m \left(\sum_{\beta} \alpha_{\beta,m}^{n+1} \rho_{\beta,m}^{n+1} v_{\beta,m}^{n+1} v_{\beta,m}^{n+1} \right) - A_{m-1} \left(\sum_{\beta} \alpha_{\beta,m-1}^{n+1} \rho_{\beta,m-1}^{n+1} v_{\beta,m-1}^{n+1} v_{\beta,m-1}^{n+1} \right) \right] \quad \text{..} \quad (2.53) \\
& + \frac{\Delta t}{V_p} \left[A_m p_m^{n+1} - A_{m-1} p_{m-1}^{n+1} \right] = 0
\end{aligned}
$$

When we have two components in the system, each element has three equations (two residual equations for component mass and one residual equation for total energy balance), and, at each interface between the nodes, one momentum balance equation exists.

Near Wellbore Treatment

In this work, temperature at the reservoir and wellbore contact needs to be estimated because of two reasons. Firstly, when DTS is deployed behind casing, the measured temperature should be close to the sandface temperature. **Figure 2.6** shows schematic of possible positions of the DTS deployment. The temperature measurements by the DTS deployed in the wellbore may provide similar measurement to production logging, and these measurements experience mixing effects at the inflow location. The estimated sandface temperature can be directly used as simulated DTS response when the cable is outside the casing. The sandface temperature is used as thermal sink/source term in both reservoir and wellbore model. At perforated regions, the temperature just outside the wellbore is the inflow temperature during production period, and, at non-perforated regions, the temperature leads to the wellbore-reservoir heat transfer through the overall heat transfer coefficient.

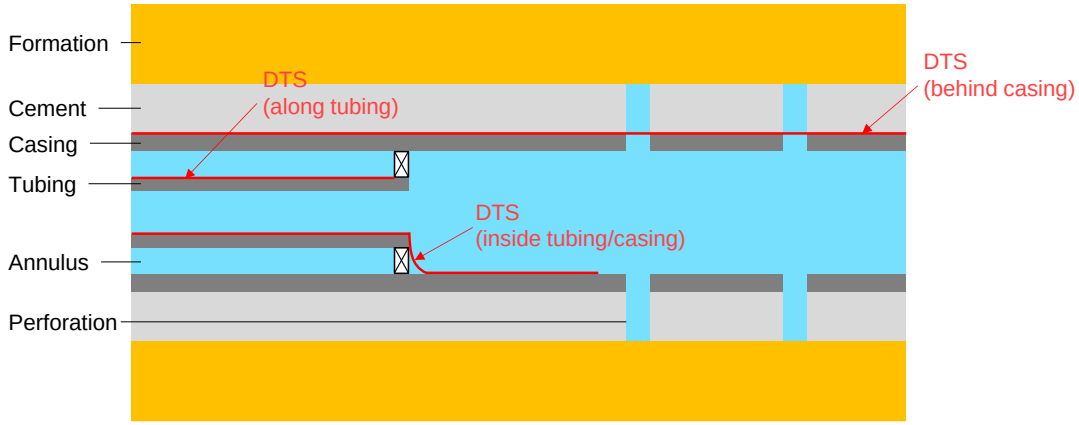

Figure 2.6—Near wellbore geometry and possible locations of DTSs

In order to compute the sandface temperature, this work uses cylindrical grids in the reservoir model near the wellbore region. We simply use the local grid refinement for the reservoir grid which contains the wellbore segment. When a transverse fracture is created along a horizontal well, the flow is radially converging into the wellbore (**Figure 2.7**). The radial converging flow characteristics near the wellbore can be modeled with the concentric cylinders of the local grid refinement (**Figure 2.8**).

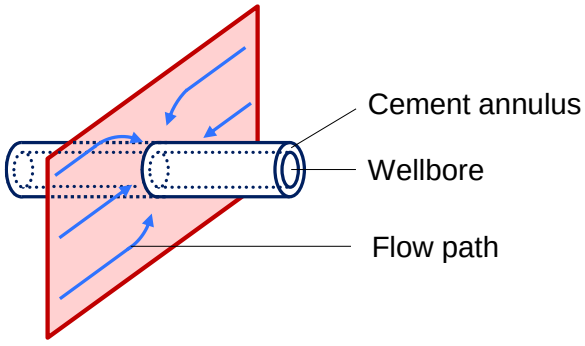

Figure 2.7—Schematic of flow path along a transverse fracture

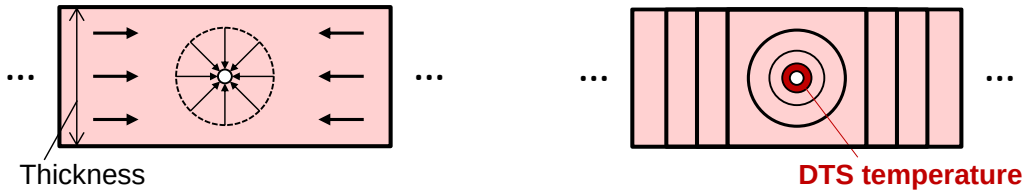

(a) flow directions along transverse fracture (b) Cartesian grids with cylindrical grids

Figure 2.8—Schematics of control volume for spatial discretization

Sink/Source Terms

The reservoir and wellbore mass balance equations are coupled through the mass sink/source in Eq. 2.3 and the inflow/outflow velocity term in Eq. 2.7. The mass flow rate at the reservoir/wellbore contact is given by a prescribed mass flow rate or calculated with a productivity index concept (Coats 1977):

$$\dot{q}_\beta = \rho_\beta \lambda PI\left(p_R - p_{wf}\right) \quad \text{.....} \quad (2.54)$$

where $\dot{q}_\beta$ is mass flow rate of phase β, λ is mobility, PI is the productivity index, p_R is reservoir pressure, and p_{wf} is fluid pressure of the wellbore segment. This equation is used for both the reservoir and wellbore model to compute mass sink/source. The selection of the mobility term depends on the pressure change between the reservoir and wellbore; for production case ($p_{wf} \leq p_R$), the reservoir fluid mobility of phase β is used, and, for injection case ($p_{wf} > p_R$), the total mobility is used.

The productivity index model depends on the near wellbore coordinate system used in the reservoir model. Let the well be penetrating into the x-direction. When the Cartesian coordinate system is used without using local grid refinement near the wellbore, the productivity index is calculated as (Peaceman 1983):

$$PI = \frac{2\pi \bar{k} \Delta x}{\ln \frac{r_o}{r_w} + s} \quad \text{..... (2.55)}$$

where Δx is size of the grid containing the wellbore segment, s is skin factor, r_o is equivalent wellbore radius:

$$r_o = 0.28 \frac{\left[\left(k_z/k_y\right)^{1/2} (\Delta y)^2 + \left(k_y/k_z\right)^{1/2} (\Delta z)^2 \right]^{1/2}}{\left(k_z/k_y\right)^{1/4} + \left(k_y/k_z\right)^{1/4}} \quad \text{..... (2.56)}$$

and $\bar{k}$ is effective permeability defined as

$$\bar{k} = \sqrt{k_y k_z} \,. \quad \text{..... (2.57)}$$

On the other hand, if the local grid refinement with cylindrical coordinate system is employed, the productivity index is simply calculated as the steady-state flow model:

$$PI = \frac{2\pi k_r \Delta x}{\ln \frac{r_{sand}}{r_w} + s} \quad \text{..... (2.58)}$$

where k_r is permeability in the radial direction, r_{sand} is radial coordinate of the reservoir cell which contacts to the wellbore segment.

Once the phase mass flow rate ($\dot{q}_\beta$) is obtained, the phase mass flow rate per unit volume (q_β) in the sink/source term of the reservoir model is calculated by dividing the $\dot{q}_\beta$ by volume of a reservoir element which contains the wellbore segment. Here, we consider a wellbore segment whose volume and surface area are $\pi r_{i2} \Delta z$ ($=V_w$) and $2\pi r_i \Delta z$ ($=A_r|_{r=ri}$), respectively. The sink/source term of the wellbore flow model (Eq. 2.7) is rearranged into

$$\frac{2\gamma}{r_i}\left(\sum_\beta \alpha_{\beta,I} \rho_{\beta,I} X^\kappa_{\beta,I} v_{\beta,I} \right) = \frac{1}{V_w}\left(\sum_\beta q_{\beta,I} X^\kappa_{\beta,I} \right) = \frac{1}{V_w}\left(\sum_\beta \dot{q}_\beta X^\kappa_{\beta,I} \right) \quad \text{..... (2.59)}$$

Therefore, the mass sink/source term in both reservoir and wellbore can be calculated with the phase mass flow rate ($\dot{q}_\beta$).

The reservoir and wellbore energy balance equations are coupled through the thermal sink/source (Eq. 2.5) and fourth and fifth terms in the right-hand-side of the Eq. 2.12. The advective energy interaction is simply associated with the mass transfer between the two systems. The conductive energy transport per unit volume, q_{wb}, is computed by considering heat conduction at the contact of the reservoir and the wellbore. At the contact, following boundary condition is considered:

$$-k_{Tt}\left.\frac{\partial T}{\partial r}\right|_{r=r_w} = U_T\big|_{r=r_w}\left(T_{wf} - T_R\big|_{r=r_w}\right) \quad \text{..... (2.60)}$$

where T_R is reservoir temperature and T_{wf} is wellbore fluid temperature. Let $A_r|_{r=rw}$ be surface area of the well segment at wellbore radius in the axial direction. The equation is rearranged into

$$\dot{q}_{wb} = -A\big|_{r=r_w} k_{Tt}\left.\frac{\partial T}{\partial r}\right|_{r=r_w} = A\big|_{r=r_w} U_T\big|_{r=r_w}\left(T_{wf} - T_R\big|_{r=r_w}\right) \quad \text{..... (2.61)}$$

where $\dot{q}_{wb}$ is heat transfer rate at the contact of reservoir and wellbore. The overall heat transfer coefficient at the wellbore radius is expressed as

$$U_T\big|_{r=r_w} = \frac{r_i}{r_w}U_T\big|_{r=r_i} = \frac{A\big|_{r=r_i}}{A\big|_{r=r_w}}U_T\big|_{r=r_i}. \quad \text{..... (2.62)}$$

Eventually, the heat transfer rate is rearranged into

$$\dot{q}_{wb} = A\big|_{r=r_i} U_T\big|_{r=r_i}\left(T_{wf} - T_R\big|_{r=r_w}\right). \quad \text{..... (2.63)}$$

When the cased-perforated completion is used, the heat conduction is assumed to occur

only through non-perforated zone, and, then, the heat transfer rate becomes

$$\dot{q}_{wb} = (1-\gamma)A\big|_{r=r_i} U_T\big|_{r=r_i} \left(T_{wf} - T_R\big|_{r=r_w}\right). \quad \text{..... (2.64)}$$

The term q_{wb} is calculated by dividing the heat transfer rate ($\dot{q}_{wb}$) by the reservoir grid volume which containts the well segment. For the wellbore model, the conductive energy transport term is also calculated by dividing the Eq. 2.64 by the segment volume (V_w) as

$$-\frac{A\big|_{r=r_i}}{V_w}(1-\gamma)U_T\big|_{r=r_i}\left(T_{wf} - T_R\big|_{r=r_w}\right) = \frac{2(1-\gamma)}{r_i}U_T\big|_{r=r_i}\left(T_R\big|_{r=r_w} - T_{wf}\right) \quad \text{..... (2.65)}$$

where the sign of the heat flow was switched. It is noted that the pipe-open ratio changes with position. At non-perforated regions, the value is set to 0 since over the regions we only considers conductive heat transport between the wellbore and the reservoir. On the other hand, at perforated regions, the pipe-open ratio becomes value between 0 and 1 depending on a local completion design of the well segment such as the perforation density.

From the above discussion, when we obtain the phase mass flow rate ($\dot{q}_\beta$) and the heat transfer rate ($\dot{q}_{wb}$), the sink/source terms can by calculated in both domains.

Newton-Raphson Method

For both domains of the reservoir and wellbore, residual equations are obtained, and they are connected mutually through the mass and thermal sink/source terms. In each domain, the system of equations are solved by the Newton-Raphson method. In the Newton-Raphson method, solutions of the primary variables are obtained through iterative procedures. Those residual equations are locally linearized by considering Taylor series

expansion at current guess of the solution during the Newton-Raphson iterations. Let p be the current iteration index, update vector of the primary variables is calculated by

$$\boldsymbol{\delta}\mathbf{x}_{p+1} = -\mathbf{J}^{-1}\mathbf{R} \quad \text{..... (2.66)}$$

where $\boldsymbol{\delta}\mathbf{x}_{p+1}$ is update vector of the primary variables for next Newton-Raphson iteration:

$$\boldsymbol{\delta}\mathbf{x}_{p+1} = \mathbf{x}_{p+1} - \mathbf{x}_p\,, \quad \text{..... (2.67)}$$

$\mathbf{x}_p$ is primary variable vector at the p-th Newton-Raphson iteration, $\mathbf{J}$ is a Jacobian matrix, and $\mathbf{R}$ is a residual vector. Let N be the amount of equations and primary variables, and the Jacobian matrix is expressed as

$$\mathbf{J} = \begin{bmatrix} J_{11} & \cdots & J_{1j} & \cdots & J_{NN} \\ \vdots & \ddots & & \ddots & \vdots \\ J_{i1} & & J_{ij} & & J_{iN} \\ \vdots & \ddots & & \ddots & \vdots \\ J_{N1} & \cdots & J_{Nj} & \cdots & J_{NN} \end{bmatrix} \quad \text{..... (2.68)}$$

where the component can be expressed as

$$J_{ij} = \frac{\partial R_i}{\partial x_j}\,. \quad \text{..... (2.69)}$$

Here, the R_i is the i-th element of the residual vector, and x_j is the j-th element of the primary variable vector. For each timestep, the update of the primary variable vectors is repeated until convergence.

2.5.3 Solution Procedure

In this work, the reservoir model and wellbore model are solved separately under fully-implicit condition. These models are coupled together iteratively. **Figure 2.9** shows a schematic of the solution procedure for the coupled model. At each time step, the wellbore models are solved to estimate pressure, temperature, holdup and velocity in the wellbore with the Newton-Raphson iterations. In the calculation of wellbore model, the reservoir conditions are fixed and used as boundary conditions. The phase mass flow rate ($\dot{q}_\beta$) and the heat transfer rate ($\dot{q}_{wb}$) are calculated with the fixed reservoir properties, and they are used as the sink/source terms in the wellbore flow and thermal model. Once the wellbore solutions are obtained, the reservoir model is solved to compute pressure, temperature and saturation distributions with use of wellbore conditions as boundary conditions. The phase mass flow rate ($\dot{q}_\beta$) and the heat transfer rate ($\dot{q}_{wb}$) are calculated with the fixed wellbore properties to estimate mass and thermal sink/source terms for the reservoir model. These calculations are repeated until changes of the phase-mass flow rate and heat flow rate are sufficiently small or the maximum number of coupling steps is attained. Once the convergence is attained, next time step is evaluated.

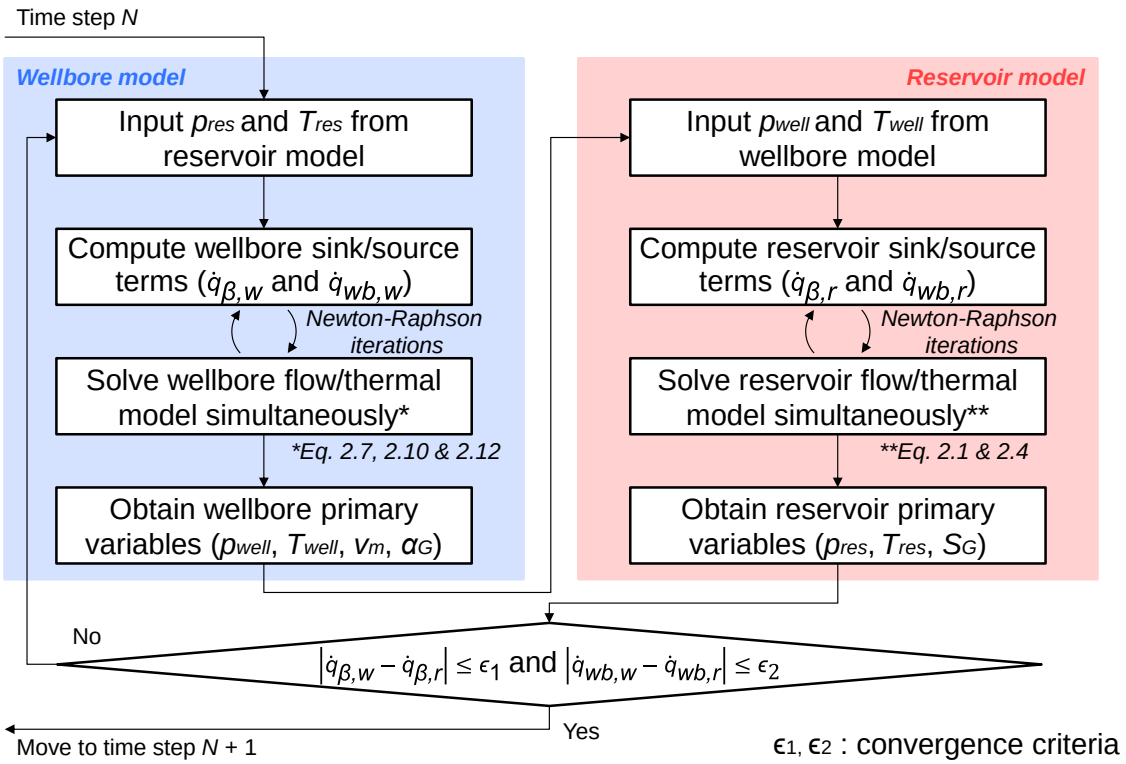

Figure 2.9—Solution procedure for coupled model

2.6 Model Verification

The models introduced and implemented in this work are verified against available analytical/semi-analytical solutions for simplified situations. The model verification is the processes to evaluate if an implemented model represents a conceptual/mathematical model within a specified accuracy (Schlesinger et al. 1979). It focuses on the identification and removal of errors in the implementation of the conceptual model (Thacker et al. 2004).

The verification study consists of three situations: single-phase gas production with a transverse fracture, water injection and warm-back with a transverse fracture, and gas-water two-phase production in a vertical well. The semi-analytical solutions of the first case were given by Cui et al. (2014). The analytical and semi-analytical solutions of

the second case can be given by Seth et al. (2010) and Han (2012). These two cases are for the verifications of the reservoir model. The last case is for the verification of the wellbore model, and the analytical solution was provided by Hasan and Kabir (1994, 2002). The implemented models were verified more in detail in the Appendix D.

2.6.1 Reservoir: Single Phase Gas Production

This first case considers single phase gas production from a horizontal well with a single transverse fracture. **Figure 2.10** shows geometries of the problem from top-view and in three-dimensional space. The fracture is perpendicular to the horizontal well. Properties of the reservoir and the fractures are summarized in **TABLE 2.1**. The reservoir is filled with single phase gas, and the well starts to produce the gas at constant bottom-hole pressure condition (2,600 psia) for 100 days.

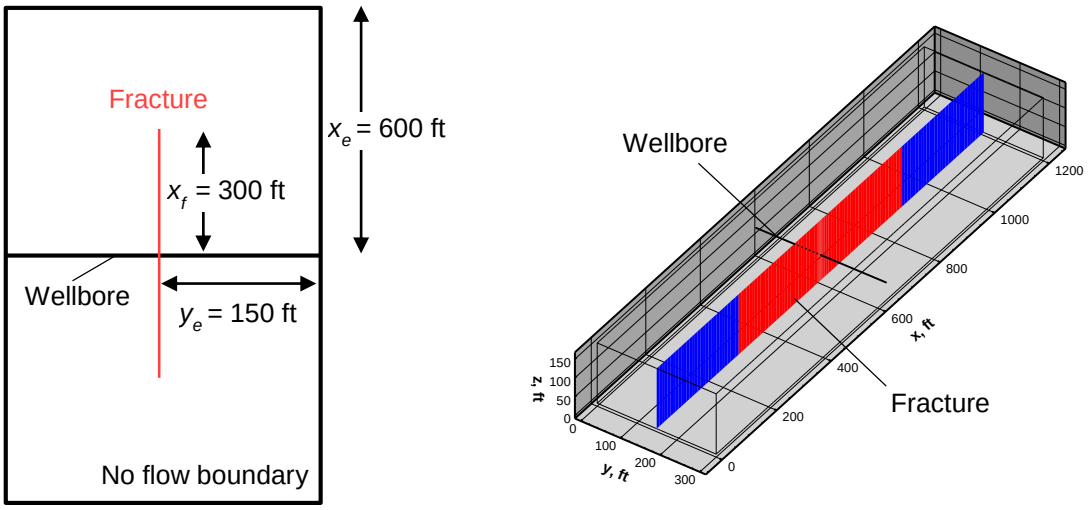

(a) *x-y* cross section (top view) (b) Slice of fracture position in 3D view

Figure 2.10—Geometry of the single phase gas production case

TABLE 2.1—RESERVOIR AND FRACTURE PROPERTIES (CASE 1)	
Parameter	Value
Reservoir	
Net pay thickness, ft	160
Matrix permeability, nD	583
Matrix porosity, %	4.2
Initial pressure, psi	4,500
Initial temperature, °F	238.37
Fracture	
Fracture width, in	0.24
Fracture permeability, mD	1,000
Fracture porosity, %	20
Fracture height, ft	160
Fracture half-length, ft	300

Cui et al. (2014) proposed a temperature model for this case by solving pressure semi-analytically and solving temperature numerically. In their work, the radial flow convergence near the wellbore in the fracture is not considered because the tri-linear model was used for their pressure solution. Therefore, we omitted the radial flow mesh near the wellbore region; the reservoir model is discretized into two-dimensions in Cartesian coordinate system. **Figure 2.11** shows the reservoir mesh used in this case (131 × 21 × 1). The fracture is represented as thin grid cells (at y = 150 ft), and logarithmic-spacing is employed in the direction perpendicular to the fracture face (y-direction) to account for the transient flow nature. In addition, finer mesh is used for near wellbore region in the x-direction to account for anticipated large pressure change near the wellbore region. The well is assumed to be completed with plug-and-perf, and the wellbore is only connected at the fracture position. This case ignores the wellbore heat transfer effect along the well.

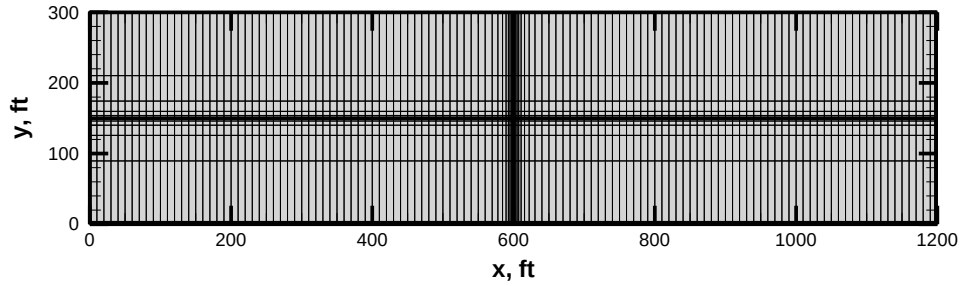

Figure 2.11—Reservoir mesh of the single phase gas production case (top-view)

Figure 2.12 shows results of gas flow rate by two methods, which shows satisfactory agreement for 100 days of production. **Figure 2.13** shows pressure and temperature distributions in the fracture direction. Steep changes of pressure and temperature can be seen at 300 ft, and this is the location of the fracture tip. These results show satisfactory agreements of both pressure and temperature along the fracture, while slight deviations can be seen in the matrix region (larger than 300 ft). **Figure 2.13a** shows that the pressure front by the semi-analytical method moves faster than that by fully numerical approach, which is caused by the assumption of the linear flow region in the outer formation in the semi-analytical model. In the numerical simulation, the flow regime near fracture tip is not linear flow; the flow converges into the fracture tip radially. It requires additional pressure difference, and leads to the slower frontal advance.

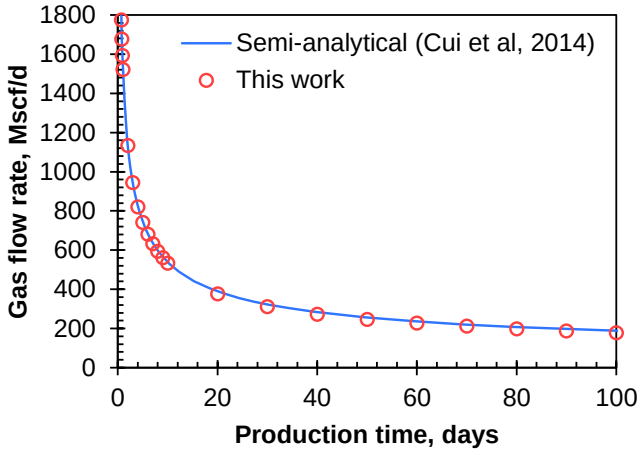

Figure 2.12—Comparison of gas production rate (single phase gas production)

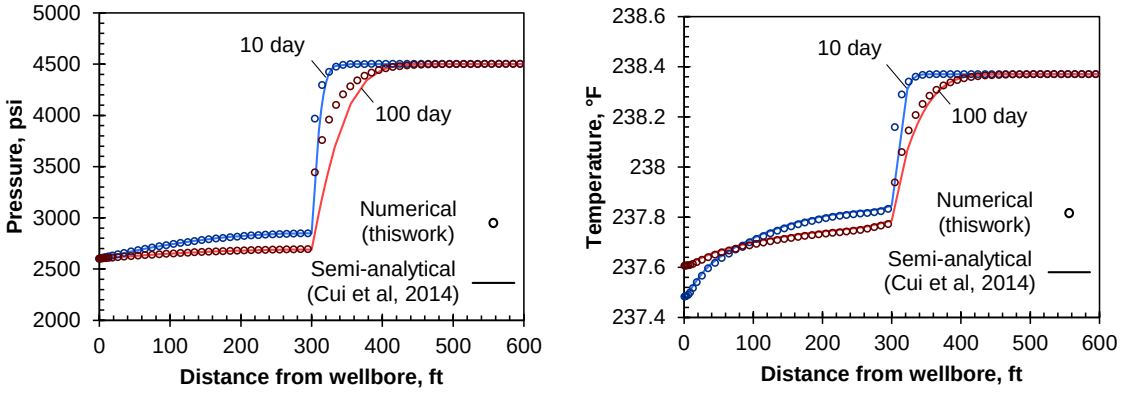

(a) Pressure (b) Temperature

Figure 2.13—Comparison of pressure and temperature distribution along fracture using different methods as model verification of the single phase gas production

2.6.2 Reservoir: Fracturing Treatment–Water Injection

The temperature behavior during the fracturing process has been studied in previous studies considering both a fracture propagation model and a temperature model. In this work, the problem is simplified by assuming a single transverse fracture is created instantaneously at the beginning of injection, and the geometry is fixed for the entire injection period.

Figure 2.14 shows geometries of the problem from top-view and in three-dimensional space. The entire reservoir is 4,600 ft × 4,600 ft × 160 ft with a single transverse fracture. During the fracturing, the fracture half-length is fixed at 1000 ft and the fracture conductivity is 1000 Darcy to mimic infinite conductivity fracture. **Figure 2.14b** shows the slice of the reservoir along the fracture direction. The fracture is expressed as the red region and the matrix region is expressed as the blue zone. A horizontal well is also placed at the center of the reservoir perpendicular to the transverse fracture. Properties of the reservoir, the fracture and the fluid are summarized in **TABLE 2.2**. It is noted that, in this verification case, the radial flow region near the wellbore and the wellbore-reservoir heat transfer effect are ignored to compare the simulation results against available analytical solutions.

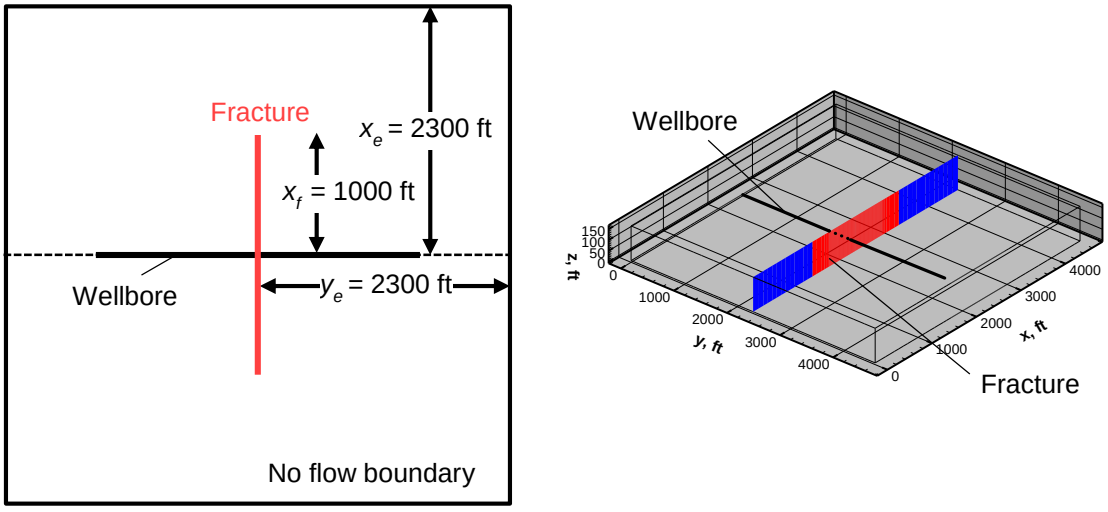

(a) *x-y* cross section (top view)

(b) Slice of fracture position in 3D view

Figure 2.14—Geometry of the case for injection and warm-up problem

TABLE 2.2—SUMMARY OF INPUT PROPERTIES (CASE 2)

Type	Property	Value
Reservoir	Reservoir size (*x*-dir) ft	4,600
	Reservoir size (*y*-dir) ft	4,600
	Net pay thickness, ft	160
	Matrix permeability, nD	583
	Matrix porosity, fraction	0.08
	Total thermal conductivity, Btu/(ft-hr-°F)	1.79
	Rock specific heat, Btu/(lbm-°F)	0.202
	Rock density, lbm/ft^3	148.58
	Initial pressure, psi	4,500
	Initial temperature, °F	238.37
Fracture	Fracture width, in	0.24
	Fracture permeability, D	1,000
	Fracture porosity, fraction	0.32
	Fracture height, ft	160
	Created fracture half-length, ft	1,000
	Enhanced permeability, mD	5.83×10^{-3}
Fluid	Water density, lbm/ft^3	61.5
	Water specific heat, Btu/(lbm-°F)	0.988

The fracturing treatment is performed for 100 min under 12 bbl/min injection rate with cold water (80 °F). This flow rate is based on a field case injection rate (60 bbl/min for 5 clusters).

Seth et al. (2010) presented a simple analytical solution for the fluid temperature along the fracture during fracturing process ignoring fluid leak-off to the formation. The governing equation they solved is

$$\rho_l C_{p,l} \frac{\partial T_{fr}}{\partial t} = -\rho_l v_{fr} C_{p,l} \frac{\partial T_{fr}}{\partial X} + \frac{2}{w}\left[h_l\left(T_r - T_{fr}\right)\right] \quad \text{..... (2.70)}$$

where X is a coordinate in the x-direction which origin is shifted to the reservoir center, w denotes fracture width, h_l is heat transfer coefficient on fracture face, and subscripts l, r and fr denote liquid phase, rock matrix, and fracture, respectively. This model can be rearranged using dimensionless variables into:

$$\frac{\partial T_D}{\partial t} + u_{fr}\frac{\partial T_{fr}}{\partial X} = -\eta T_D \quad \text{..... (2.71)}$$

with initial and boundary conditions:

$$T_D(X, t=0) = 0 \quad \text{..... (2.72)}$$

$$T_D(X=0, t) = 1 \quad \text{..... (2.73)}$$

where

$$\eta = \frac{2h_l}{\rho_l C_{p,l} w} \quad \text{..... (2.74)}$$

$$T_D = \frac{T_{init} - T_{fr}}{T_{init} - T_{inj}}. \quad \text{..... (2.75)}$$

T_{init} and T_{inj} denote initial temperature and injection fluid temperature, respectively. Hence, the analytical solution of the temperature distribution is given by

$$T_D = \begin{cases} 0 & X - v_{fr}t > 0 \\ e^{-X\frac{\eta}{v_{fr}}} & X - v_{fr}t < 0 \end{cases}. \quad \text{..... (2.76)}$$

The temperature profile itself does not change with time while the temperature front advanced with time. Then, the analytical solution is strongly dependent on the value of the heat transfer coefficient, h_l. To calculate the analytical solution, the heat transfer coefficient is estimated with a correlation (Zhao and Tso 1993):

$$h_l = (543 \pm 52)v^{0.90\pm0.03}. \quad \text{..... (2.77)}$$

The transient formation temperature distribution along the wellbore direction at the injection position (x = 2,300) can be estimated analytically by assuming that the temperature at x = 2,300 becomes injection fluid temperature at the beginning of the

injection. By ignoring advective heat transfer to the formation and conduction in the fracture direction (*x*-direction), the analytical solution is given as similarity solution. The governing equation can be simply expressed as one-dimensional heat conduction problem:

$$\frac{\partial T_Y(Y,t)}{\partial t} = \alpha \frac{\partial^2 T_Y(Y,t)}{\partial Y^2} \quad \left(0 \le t \le t_{inj}\right) \quad \text{..... (2.78)}$$

where *Y* denotes the *y*- coordinate which origin is shifted to the center of the reservoir (*y* = 2,300 ft) due to the symmetry of the problem. α is effective thermal diffusivity given by

$$\alpha = \frac{k_{Tt}}{\phi\rho_l C_{p,l} + (1-\phi)\rho_R C_{p,R}}. \quad \text{..... (2.79)}$$

The initial and boundary conditions are

$$T_Y(0,t) = T_{inj} \quad \text{..... (2.80)}$$

$$T_Y(Y=\infty,t) = T_{init} \quad \text{..... (2.81)}$$

$$T_Y(Y,0) = T_{init}. \quad \text{..... (2.82)}$$

The outer boundary condition is valid for the current problem since the injection continues only for 100 minutes. The analytical solution is given as similarity solution expressed as (Han 2012):

$$T_Y(Y,t) = T_{init} + (T_{inj} - T_{init})\,erfc\left(\frac{Y}{\sqrt{4\alpha t}}\right) \quad \left(0 \le t \le t_{inj}\right) \quad \text{..... (2.83)}$$

where *erfc*(·) denotes the complementary error function.

Figure 2.15 shows schematics of the two directions; the coordinate along fracture (*X*-dir) is used for the fracture temperature, and the coordinate along wellbore (*Y*-dir) is used for the transient formation temperature. **Figure 2.16** shows temperature profiles

along fracture direction in the middle of injection period (50 min) (**Figure 2.16a**) and temperature profiles along wellbore direction (**Figure 2.16b**) at the end of injection period (100 min) in semi-log scale to elevate the compressed near wellbore location. These results show satisfactory agreements.

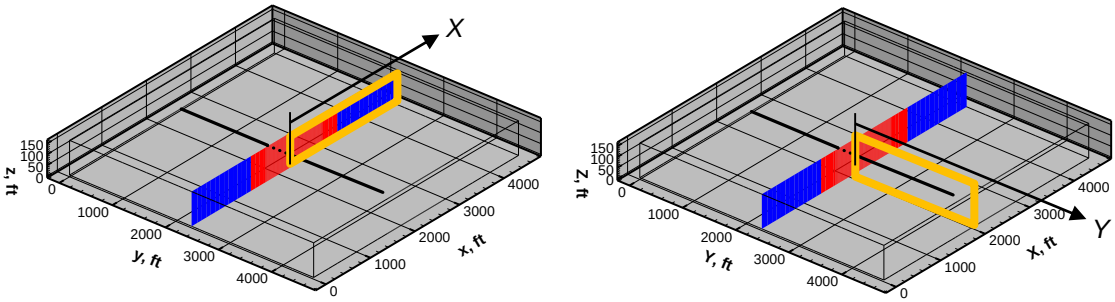

(a) Coordinates along fracture (*X*-dir) (b) Coordinates along wellbore (*Y*-dir)

Figure 2.15—Schematics of the coordinates for the two directions

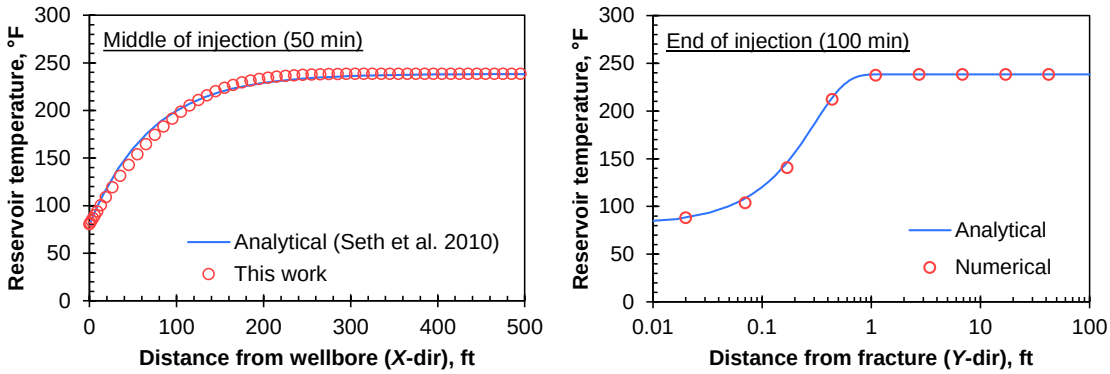

(a) Fracture temperature during injection (b) Formation temperature at the end of injection (semi-log scale)

Figure 2.16—Comparison of temperature profile in the fracture direction (*X*-dir.) and the well direction (*Y*-dir.)

2.6.3 Reservoir: Fracturing Treatment–Warm-back

After the fracturing treatment, the well is kept under shut-in condition. During the shut-in period, the injected cold fluid in the fracture experiences significant heating by the surrounding formation.

Seth et al. (2010) presented a semi-analytical solution for the temperature profile along the horizontal well direction by ignoring the heat conduction effect along the fracture direction. The governing equation is the same as for the formation temperature model during the injection period:

$$\frac{\partial T_Y(Y,t)}{\partial t} = \alpha \frac{\partial^2 T_Y(Y,t)}{\partial Y^2} \quad (t \geq t_{inj}) \quad \text{..... (2.84)}$$

with intial and boundary conditions:

$$T_Y(Y, t = t_{inj}) = g(Y) \quad \text{..... (2.85)}$$

$$\left.\frac{\partial T_Y}{\partial Y}\right|_{Y=0} = 0 \quad \text{..... (2.86)}$$

where $g(y)$ is the initial condition for the shut-in period.

In this verification, we compare the formation temperature profile at wellbore position (x = 2,300 ft) while ignoring wellbore-reservoir heat transfer effect. The function $g(Y)$ is given by the Eq. 2.83. The analytical soltion is expressed with Green's function as:

$$T_Y(Y,t) = \frac{1}{\sqrt{4\pi\alpha t}} \int_0^\infty \left\{ \exp\left[-\frac{(Y-s)^2}{4\alpha t} \right] + \exp\left[-\frac{(Y+s)^2}{4\alpha t} \right] \right\} g(s) ds \,. \quad (t > t_{inj}) \text{ .. (2.87)}$$

This solution requires the integration over the semi-infinite region, and the integration is conducted by numerical integration in this work.

All of the properties used in this case are the same with those used in the injection study. The well is shut-in for 30 days. **Figure 2.17a** shows the temperature profiles along wellbore direction (**Figure 2.15b**) at four different shut-in time with initial temperature profile in semi-log scale. These plots show satisfactory agreements between the analytical solution and numerical simulation. In addition, **Figure 2.17b** shows the comparison of elevated temperature profile at the end of shut-in. This confirms the validity of our implemented model, and also the near formation temperature does not become geothermal temperature within 30 days of shut-in.

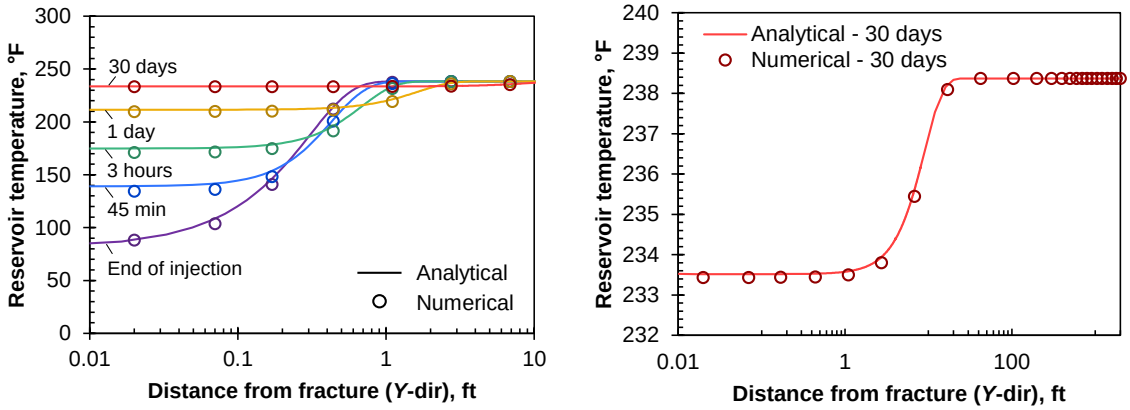

(a) Temperature profile during shut-in (b) Elevated temperature profile (30 days)

Figure 2.17—Comparison of temperature profile along horizontal well direction (*Y*-dir.) at injection location (*X* = 0) during shut-in period

2.6.4 Wellbore: Gas-Water Two Phase Production in a Vertical Well

Hasan and Kabir (1994) proposed a temperature model for production wells under multiphase flow (gas-liquid two phase flow), and it was simplified in the work of Hasan and Kabir (2002). In this work, their temperature model for compressible fluid is used as the analytical solution with averaged fluid properties for the gas-water mixture.

$$T_f = T_{eibh} - g_G(L-z)\sin\theta + \frac{1-e^{(z-L)L_R}}{L_R}\left[g_G\sin\theta - \frac{g\sin\theta}{C_{p,mix}}\right] \quad \text{..... (2.88)}$$

where $C_{p,\,mix}$ is mass-flow rate weighted specific heat of fluid mixture and L_R is

$$L_R = \frac{2\pi}{q_{mix}C_{p,mix}}\left[\frac{r_{ci}U_T\big|_{r=r_{ci}}k_{Tt}}{k_{Tt}+r_{ci}U_T\big|_{r=r_{ci}}T_D(t)}\right] \quad \text{..... (2.89)}$$

where q_{mix} is mass flow rate of the gas-water mixture, r_{ci} is casing inner radius and the U_T is evaluated at the casing inner radius. The dimensionless temperature T_D was derived in the work by Hasan and Kabir (1991), and it was extended to continuous expression in the form by Hasan and Kabir (2002):

$$T_D(t) = \ln\left[e^{-0.2t_D} + \left(1.5 - 0.3719e^{-t_D}\right)\sqrt{t_D}\right] \quad \text{..... (2.90)}$$

where the dimensionless time is given as

$$t_D = \frac{\alpha t}{r_w^2}. \quad \text{..... (2.91)}$$

Let us consider a cylindrical reservoir domain with large reservoir radius (r_e = 100,000 ft) to avoid effects by outer boundary. **Figure 2.18a** shows schematics of the reservoir/wellbore system. The target reservoir is located at 5,350 ft from the surface. The outer boundary of the reservoir is set to fixed pressure (constant pressure boundary). The *r*–*z* directional cross-sectional view of the entire domain with simulation mesh is shown in **Figure 2.18b**. The reservoir is discretized into logarithmically-spaced mesh in the *r*-direction to capture the diffusive nature of the thermal conduction in the reservoir, and, in the *z*-direction, the reservoir is uniformly discretized. The reference properties of each flowing fluid are summarized in **TABLE 2.3**. Properties of the completion and formation

are shown in **TABLE 2.4** and **TABLE 2.5**, respectively. It is noted that the gas fluid properties are estimated by the Peng-Robinson equation of state with critical properties of pure methane.

Figure 2.19 show results of pressure and temperature distribution by this work against the analytical solution. The numerical solutions are in satisfactory agreement with the analytical solutions.

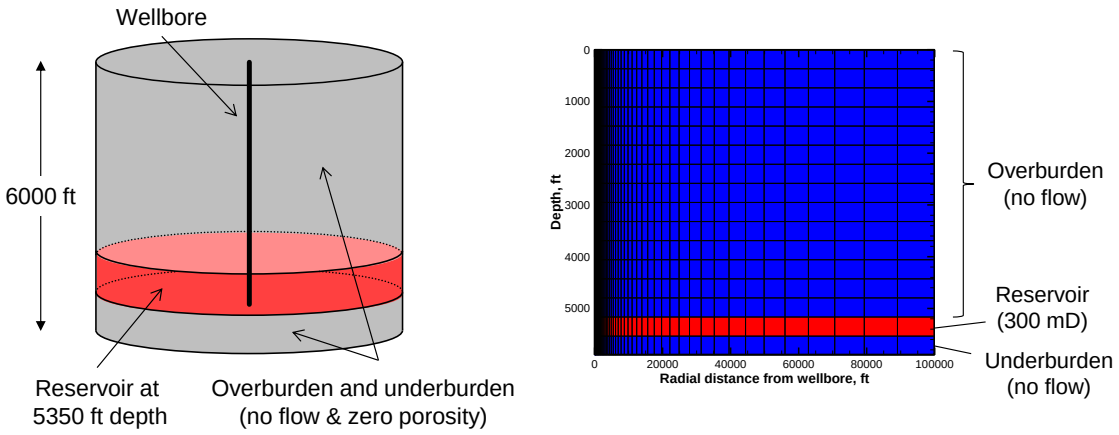

(a) Geometry of reservoir/wellbore (b) *r-z* cross section and simulation mesh

Figure 2.18—Schematics of the reservoir/wellbore system and simulation mesh

TABLE 2.3—REFERENCE PROPERTIES OF FLOWING FLUID

Fluid	Property	Value
Water	Density, lbm/ft^3	61.3
	Specific heat, Btu/(lbm-°F)	0.990
Gas	Density, lbm/ft^3	10.2
	Specific heat, Btu/(lbm-°F)	0.787

TABLE 2.4—COMPLETION PROPERTIES AND SURFACE FLOW RATE	
Parameters	Value
Wellbore radius, in	8.75
Casing inner radius, in	4.67
Overall heat transfer coefficient, Btu/(hr-ft^2-°F)	37.01
Friction factor, –	0.001
Water flow rate (two-phase), STB/d	403
Gas flow rate (two-phase), MSCF/d	1163

TABLE 2.5—FORMATION PROPERTIES		
Region	Properties	Value
Reservoir	Outer radius, ft	100,000
	Thickness, ft	350
	Permeability, mD	300
	Porosity, fraction	0.18
	Density, lbm/ft^3	162.313
	Total thermal conductivity, Btu/(ft-hr-°F)	1.79
	Rock heat capacity, Btu/(lbm-°F)	0.239
	Surface temperature, °F	76.0
	Geothermal gradient, °F/ft	0.02
Overburden & Underburden	Outer radius, ft	100,000
	Permeability, mD	0
	Porosity, fraction	0
	Density, lbm/ft^3	162.313
	Total thermal conductivity, Btu/(ft-hr-°F)	1.79
	Rock heat capacity, Btu/(lbm-°F)	0.239

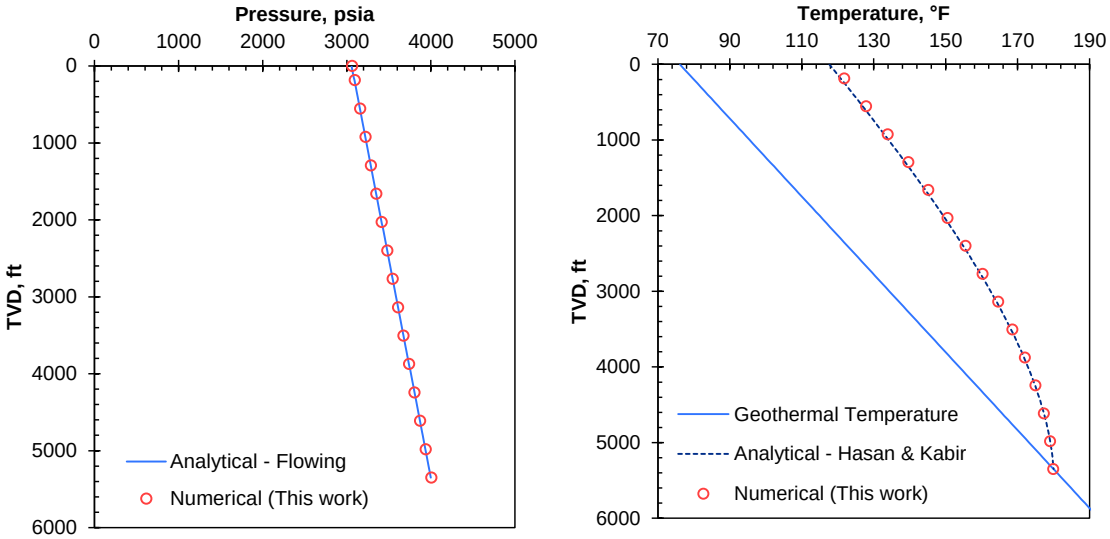

(a) Pressure (b) Temperature

Figure 2.19—Comparison of pressure and temperature distribution at 100 days of production with two-phase gas-water production

CHAPTER III

SYNTHETIC CASE STUDY

3.1 Chapter Summary

This chapter is dedicated to offer insights for better understanding of the downhole temperature behavior through several synthetic case studies. The first case study simulates temperature behavior in a single fracture during processes of injection, shut-in and production. It provides basic approaches and assumptions taken in this work to simulate those processes. The understandings of the single fracture study are applied to the second and the third case studies: a horizontal well with five fractures and a horizontal well with three stage treatment. These cases show different characteristics of the wellbore flowing temperature and the sandface temperature; the wellbore flowing temperature is less sensitive to the inflow temperature due to the mixing of the two streams (wellbore and fracture). Inflow temperature sensitivity on parameters related with fracture flow performance is also studied.

3.2 Case Studies

This section shows several case studies using the developed model for better understanding of downhole temperature behavior under various conditions demonstrating capabilities of the developed model. As the simplest case, temperature behavior of a well with a single fracture is presented. Second case simulates temperature behavior of a single-stage fractured well with five clusters. Finally, a horizontal well with three stage treatment

(five clusters per stage) is discussed. All these cases simulate processes of injection, shut-in and production. The temperature behaviors simulated by the gas-water model are compared with those by the single phase gas model to investigate effects of the injected water.

3.2.1 Horizontal Well with a Single Fracture

This example considers a horizontal well with a single transverse fracture at the center of the well. The fracture is created by injecting large amount of water and relevant additives with proppants to keep the created crack open. The created fracture length is thought to become more than one thousand feet in the field treatment inferred by some diagnostic techniques such as micro-seismic mapping (Fisher et al. 2005b). The actual propped fracture half-length, however, is thought to be shorter than the created fracture half-length because of several reasons such as closure stress and insufficient proppant transport along the fracture. The fracture conductivity can be considered as infinite conductivity during injection, while the conductivity seems to reduce during shut-in period due to closure. The fracture conductivity is affected by closure stress, proppant size/concentration, rock mineralogy (clay content) (Zhang et al. 2014, Zhang et al. 2015). The propped fracture half-length and conductivity are used to evaluate flow performance from the fracture during production period. In this case, to highlight effects by the fracture on temperature behavior, the heat transfer between the wellbore and reservoir are ignored; they are included in following two cases.

Injection and Shut-in

This study simplifies the injection process with an assumption that the hydraulic fracture is created at the time when injection starts, and the created fracture half-length and conductivity is fixed for the entire injection period. The created fracture is assumed to be highly conductive to mimic infinite conductive fracture during the injection period.

Figure 3.1 shows schematics of the geometry of the problem during injection and shut-in period. This case used the mixed coordinate system, and the cylindrical coordinate system is used for the near wellbore region. Water is injected for 100 minutes with injection rate at 18 bbl/min (equivalent to 90 bbl/min for five-cluster treatment). The injection fluid temperature is fixed at 80 °F. After the injection, the well is in shut-in for 30 days.

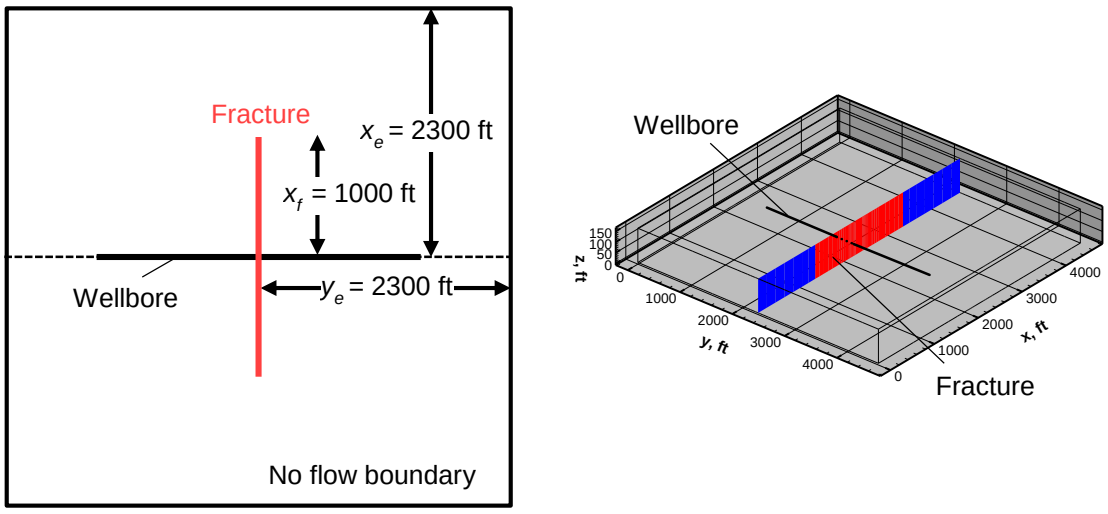

(a) *x-y* cross section (top view) (b) Slice of fracture position in 3D view

Figure 3.1—Geometry of the case for injection and warm-up problem

TABLE 3.1 summarizes input data for this case. The fracture conductivity during injection is 10 D-ft (1.0×10^4 mD-ft) and it is reduced to be 20 mD-ft for shut-in period. The enhanced permeability is introduced to account for flow contributions by re-activated natural fractures or fissures in the vicinity of the induced hydraulic fracture. This controls the leak-off from the fracture face during injection. The initial gas saturation is 0.9, and the gas is single component methane. The relative permeability in the fracture is modeled by the linear function with zero residual water and gas saturation. The relative permeability in the matrix is modeled by the Corey's model with irreducible water saturation = 0.1.

TABLE 3.1—INPUT DATA FOR INJECTION AND SHUT-IN (SINGLE FRACTURE CASE)

Type	Property	Value
Reservoir	Reservoir size (*x*-dir) ft	4,600
	Reservoir size (*y*-dir) ft	4,600
	Net pay thickness, ft	160
	Matrix permeability, nD	583
	Matrix porosity, fraction	0.042
	Total thermal conductivity, Btu/(ft-hr-°F)	0.924
	Rock specific heat, Btu/(lbm-°F)	0.202
	Rock density, lbm/ft^3	148.58
	Initial water saturation, fraction	0.1
	Initial pressure, psi	4500
	Initial temperature, °F	238.37
Fracture	Fracture width, in	0.24
	Fracture conductivity (injection), D-ft	10
	Fracture conductivity (shut-in), mD-ft	20
	Fracture porosity, fraction	0.2
	Fracture height, ft	160
	Created fracture half-length, ft	1,000
	Enhanced permeability, mD	5.83×10^{-3}

Figure 3.2 shows temperature and water saturation profiles along the fracture direction. In these plots, the fracture tip position is expressed as the dashed line. The injected fluid is heated up by the surrounding formation before it reaches the fracture tip (**Figure 3.2a**), while water saturation front has already reached the fracture tip (**Figure 3.2b**). The cold temperature signal disappears at around 500 ft away from the well. **Figure 3.3** shows temperature profile near the wellbore along the fracture during injection and shut-in. The dotted lines around 80 ft show transition position of the two flow regimes, radial flow and linear flow. Once injection is terminated, temperature in the fracture keep increasing as shown in **Figure 3.3b**. The temperature in the fracture is still lower than the initial geothermal temperature even after 30 days of shut-in.

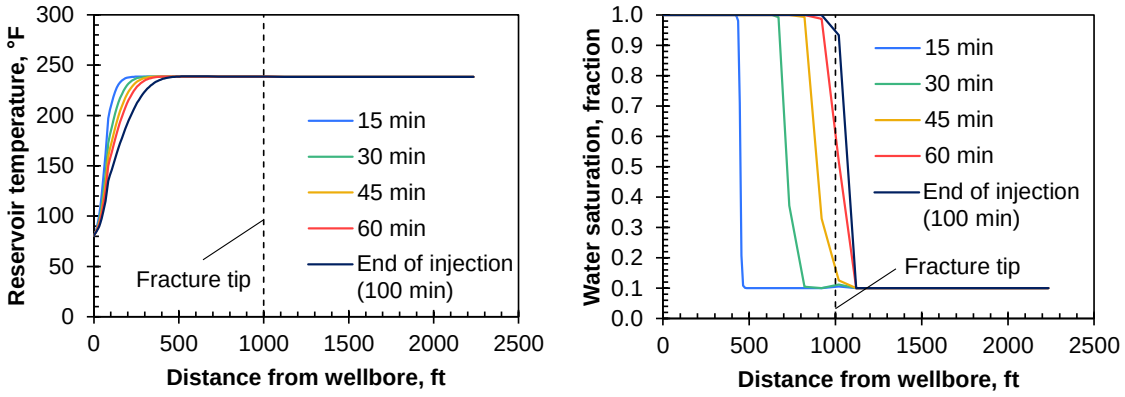

(a) Temperature (b) Water saturation

Figure 3.2—Temperature and water saturation profile in the fracture direction during injection

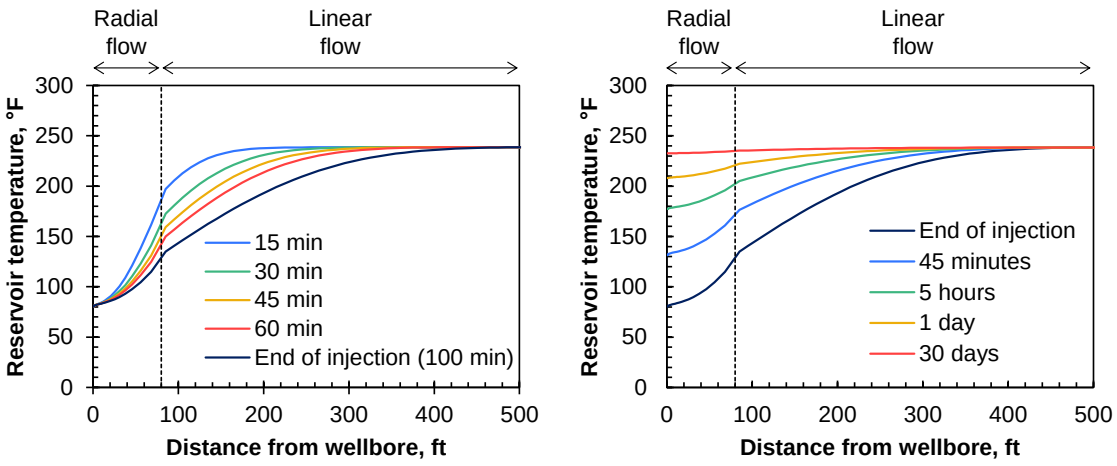

Figure 3.3—Temperature profile in the fracture direction near wellbore during injection and shut-in

Figure 3.4 further investigates effects of the radial flow on near wellbore temperature behavior. Temperature profiles given by the mixed coordinate (linear and radial) and linear coordinate system are compared in the plots. The radial flow region is highlighted as shaded zone to see their differences. The linear coordinate system overestimates the temperature profile near wellbore region in both injection and shut-in periods. While the deviation becomes smaller during the shut-in period, slight temperature difference exists even after 30 days of shut-in (**Figure 3.5**).

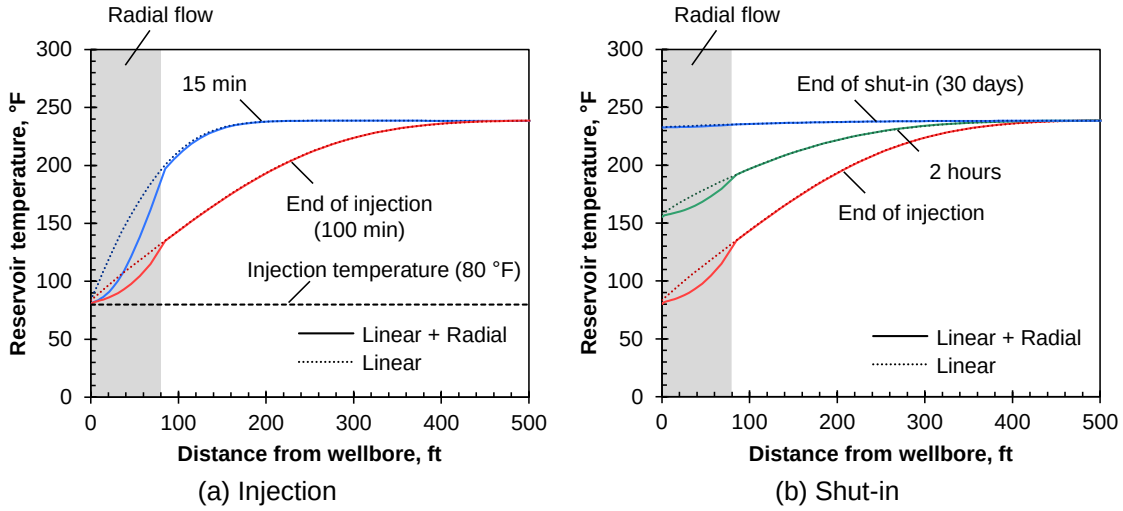

Figure 3.4—Radial flow effects on near wellbore temperature distribution during injection and shut-in

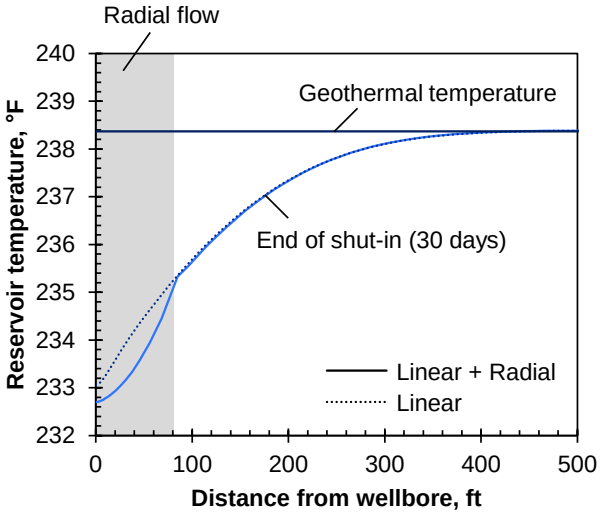

Figure 3.5—Elevated temperature profile along fracture at the end of shut-in

Figure 3.6 shows spatial temperature contours after the injection and shut-in viewed from the top of the reservoir. While the cold temperature region is limited along the fracture just after the injection, the low temperature region diffuses into the reservoir through the heat transfer between the cold fluid in the fracture and the warmer surrounding

formation. This temperature distribution after shut-in is used as the initial condition for the production period, and it means that usage of initial geothermal temperature for initial condition overestimates fracture temperature.

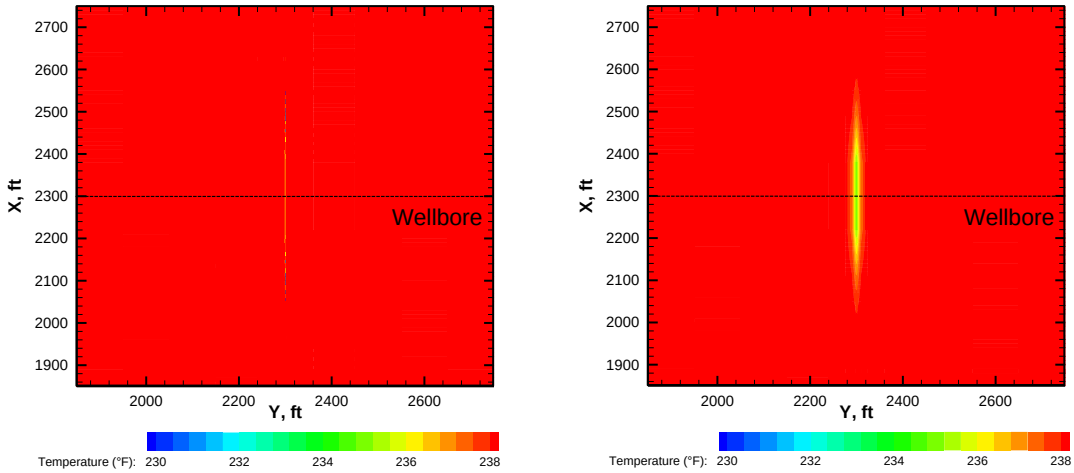

(a) After injection (100 min) (b) After shut-in (30 days)

Figure 3.6—Temperature distribution after injection and shut-in (top-view)

Production

The pressure, saturation and temperature profiles after shut-in are used as initial conditions for the production period. The well starts to produce with constant bottom-hole pressure condition (2,600 psi) for 100 days. While the created fracture length during treatment was 1,000 ft, the effective fracture half-length (propped fracture half-length) is assumed to be reduced to 300 ft as shown in **Figure 3.7**. The fracture conductivity is the same as the value during shut-in (20 mD-ft). The contribution of the induced fracture network is ignored ($k_{EPA} = k_M$).

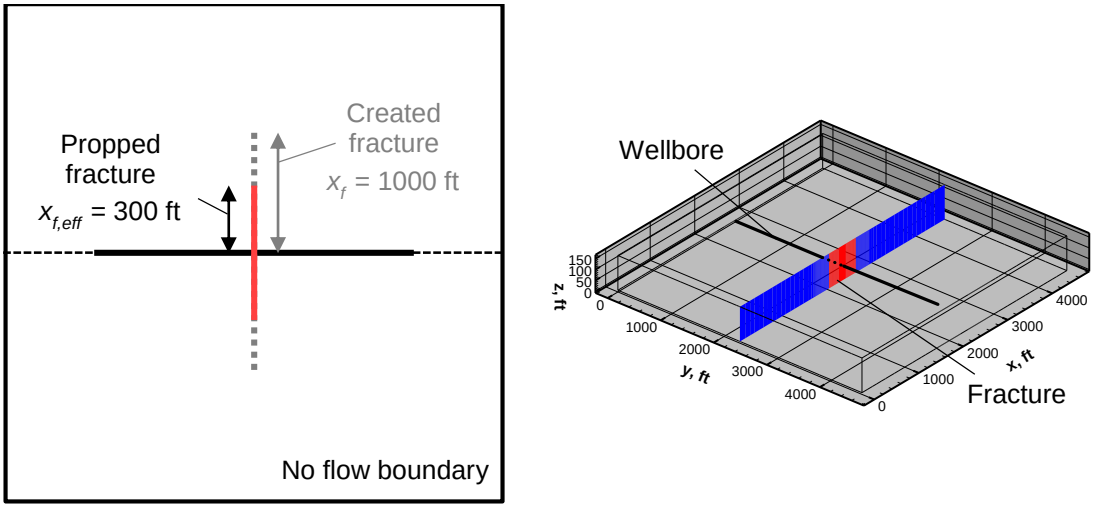

(a) *x-y* cross section (top view) (b) Slice of fracture position in 3D view

Figure 3.7—Geometry of the case for production problem

Figure 3.8a shows simulated gas and water flow rate with time for 100 days of production. Initially, water is dominant phase of the production (flow back water), and gradually gas production increases. The gas starts to produce at 0.1 day, and the gas production reaches a peak at around 5 days of production. **Figure 3.8b** shows simulated inflow temperature with time, overlain with the gas flow rate at the sandface. It is clearly seen that the lowest inflow temperature corresponds to the peak gas production rate. This is caused by the maximum gas cooling due to Joule-Thomson effect. After the peak gas production, the simulated inflow temperature increases because the gas cooling effect becomes smaller as the gas flow rate decreases.

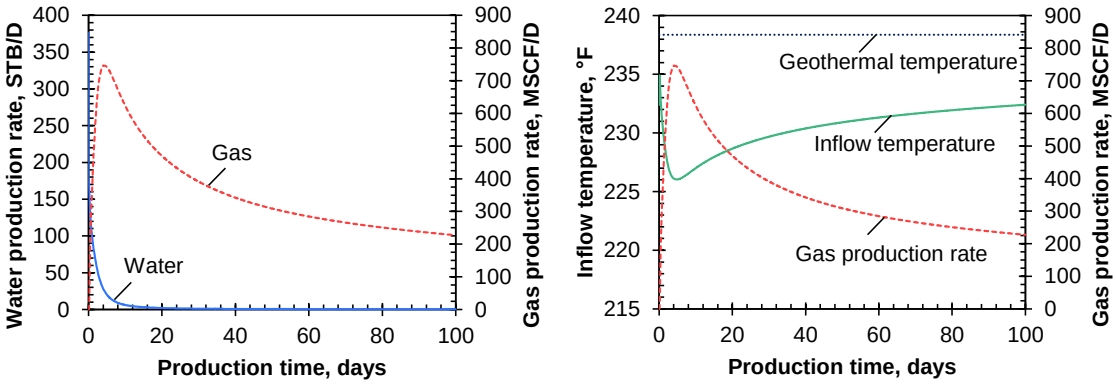

(a) Flow rate (b) Inflow temperature and gas flow rate

Figure 3.8—Production rate and inflow temperature during production

To further investigate early time temperature behavior, **Figure 3.9** shows same plots in semi-log time scale. Until 0.1 days of production, only the water phase produces, and it leads to a relative increase of the inflow temperature. Once the gas phase starts to produce, the inflow temperature starts to decrease due to the Joule-Thomson cooling effect.

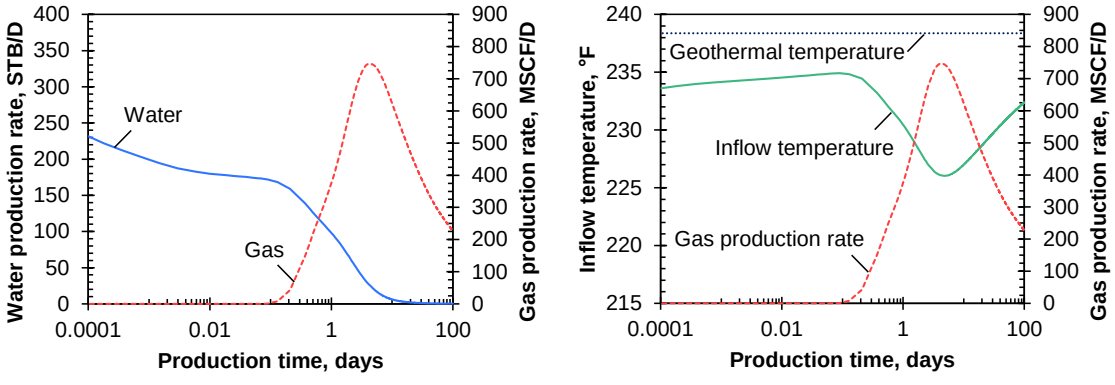

(a) Flow rate history (b) Inflow temperature and gas flow rate

Figure 3.9—Production history and inflow temperature during production (Semi-log time scale)

Figure 3.10 shows simulated temperature profile along fracture during production. The gray shaded zone denotes the region of radial flow, and the tip of the effective fracture is expressed by the dotted line at 300 ft away from the wellbore. It is clear that the deviation from the geothermal temperature is mainly occurring inside effective fracture while the temperature front propagates into the matrix region slightly. The gas cooling effect gets smaller spatially in the fracture with time due to decrease of the gas flow rate. In addition, the radial flow regime has significant effect on the near wellbore temperature. This is further investigated in **Figure 3.11** which shows comparison of the temperature profiles given by liner coordinate and mixed coordinate (linear and radial) at 10 days and 100 days of production. The deviations from the dotted lines (considering linear flow only) are significant even after 100 days of production with significant reduction of the gas flow rate.

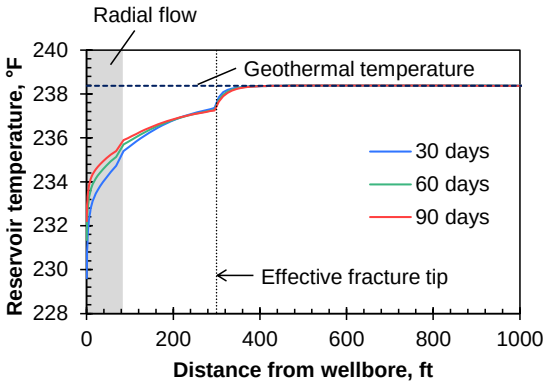

Figure 3.10—Temperature profile along fracture during production

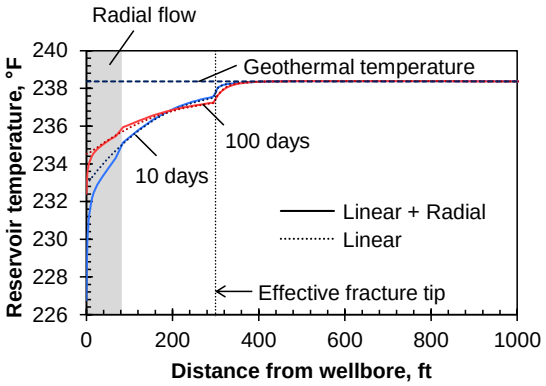

Figure 3.11—Radial flow effect on near wellbore temperature during production

Finally, the simulated flow rate and the simulated inflow temperature by the gas-water model are compared with those by the single-phase gas model. All of the input data

in the single phase gas model is the same as those in the gas-water case except for the saturation and temperature distribution. The single phase gas model considers gas-filled reservoir with original geothermal temperature distribution. **Figure 3.12** shows comparison of simulated inflow temperature and gas production rate by single phase gas (**Figure 3.12a**) and gas-water two-phase model (**Figure 3.12b**). The maximum temperature changes in both cases correspond to the time when the gas production reaches its peak. The single phase gas model gives maximum gas flow rate at the beginning of the production because the gas flow is not obstructed by the injected water. The delay of the gas peak production in the two-phase case results from the production of flow back water. In both cases, the gas cooling effect gets smaller as the gas production rate gets smaller showing similar trend. These plots are overlain in **Figure 3.13**. This plot shows the lower inflow temperature by the gas-water model even after 100 days of production while the simulated gas production rate is almost equal in both cases. The inflow temperature difference is around 2-3 °F in this case.

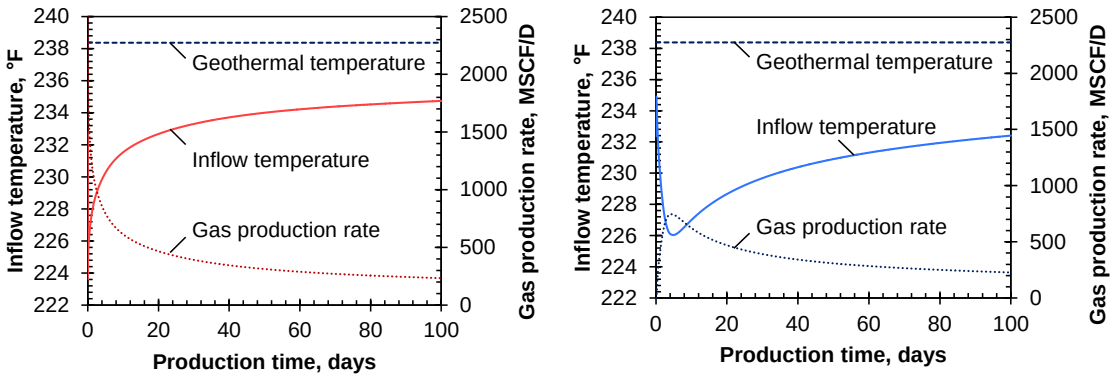

Figure 3.12—Comparison of inflow temperature and gas production rate (single-phase gas model and gas-water model)

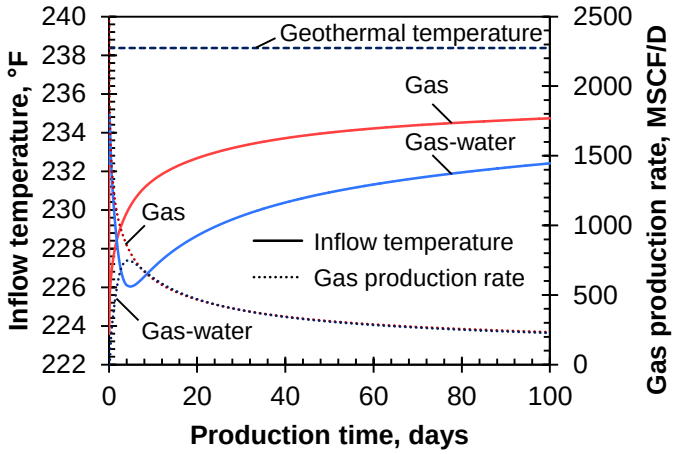

Figure 3.13—Comparison of simulated profiles of the inflow temperature and the gas production time by gas-water model and single phase gas model during production

In the above comparison, the gas-water model has two major differences in the initial condition at the onset of production: water saturation distribution and temperature distribution. To further investigate sources of the inflow temperature differences, effects by these two differences are considered separately. At first, we use a single phase gas model with the temperature distribution after shut-in. It removes the effects of the injected water for production. **Figure 3.14** compares the simulated inflow temperature and gas production rate with time considering only the temperature difference at the onset of production. With removal of the effects by the injected water, deviations can be seen at the early time (up to 10 days), but both simulated inflow temperature and gas production rate become identical at later time. The injected water only affects early time water gas production and corresponding early time gas cooling effect.

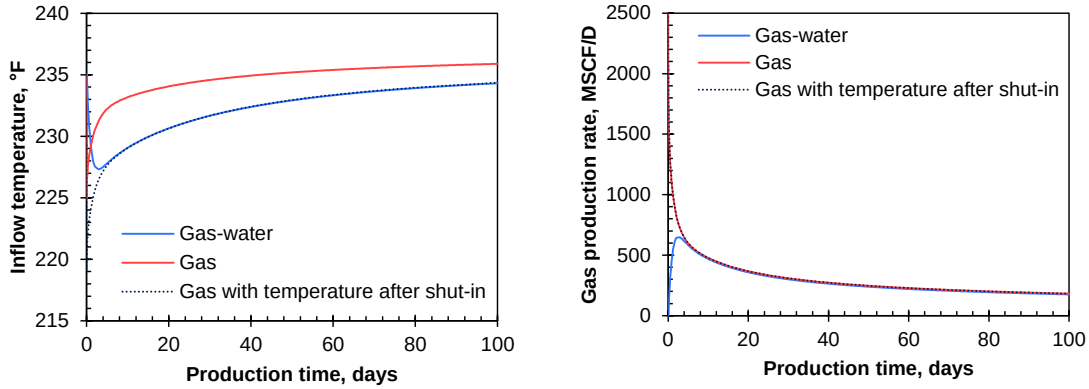

(a) Inflow temperature

(b) Gas production rate

Figure 3.14—Comparison of simulated inflow temperature and gas production with removal of effects by the injected water

On the other hand, we use the gas-water model with only the saturation differences at the onset of production. It removes the effects of the temperature difference at the onset of production **Figure 3.15** compares the simulated inflow temperature and gas production rate with time removing effects by the temperature differences at the onset of production. The shape of the simulated inflow temperature by the original gas-water model and the gas-water model with S_G = 1.0 are similar while there is off-set between these curves. Then, the temperature differences at the onset of production seem to lead to the off-set. It means that, if the initial temperature distribution is given, the use of the single phase gas model provides close results to the gas-water model.

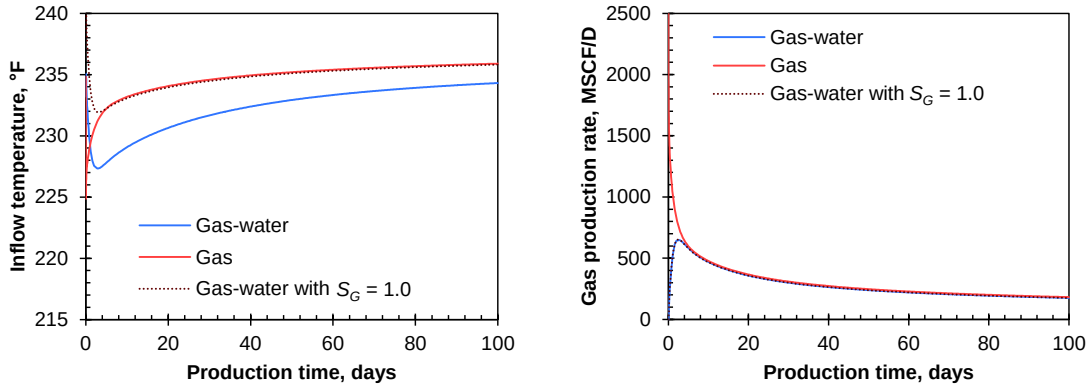

(a) Inflow temperature

(b) Gas production rate

Figure 3.15—Comparison of simulated inflow temperature and gas production with removal of effects by the temperature difference at the onset of production

This single fracture case went through the temperature behavior inside fracture during injection, shut-in and production period. It highlights the importance of the radial coordinate system near the wellbore in the interpretation of the sandface/inflow temperature just behind casing. And, it also highlights the importance of the estimation of temperature distribution at the onset of production in the temperature interpretation during production because it is the main reason for the significant difference in the inflow temperature.

The temperature behavior inside the fracture is not our main goal since the downhole temperature is not measured in the fracture but in the wellbore or behind casing. The better understanding of the fracture temperature behavior, however, helps interpret wellbore and sandface temperature distribution along the well with multiple fractures because those temperature changes occur at all of the created fractures separately.

3.2.2 Horizontal Well with Five Fractures

The second case considers a horizontal well with five fractures to simulate temperature behavior during a single-stage of fracturing of a horizontal well. The well is assumed to be completed by the plug-and-perf method. To investigate how the fracture heterogeneity affects the downhole temperature behavior, two examples are considered as fracture configurations: identical fractures and non-identical fractures. This case also simulates the processes of injection, shut-in and production.

During the injection period, the water is injected into one side of the horizontal well (heel side), and the injection rate is specified as mass flow rate with fixed temperature. This case assumes that the five fractures are created instantaneously at the beginning of injection. And, the velocity field in the wellbore is assumed to reach the steady-state condition with prescribed injection rates for each fractures. The total injection rate at the heel needs to be equal to the summation of the prescribed flow rate into the fractures (Ribeiro and Horne 2016):

$$q_{inj} = \sum_{i=1}^{N_f} q_i \quad \text{..... (3.1)}$$

where q_{inj} is the total injection mass flow rate, N_f is the number of fractures for the target stage, and q_i prescribed mass rate into the i-th fracture. The temperature of the fluid injected into the perforations is assumed to be the same as the wellbore temperature of the segment. In addition, at the beginning of the injection, the wellbore fluid temperature is also assumed to be the same as the prescribed injection fluid temperature. If the completion fluid is placed in the wellbore, the fluid temperature seems to be close to the reservoir

temperature, but, this study considers high rate injection such as 75 to 90 bpm and the effect can be ignored.

The fracturing treatment designs used in this study such as injection rate and time are based on a field case presented by Mayerhofer et al. (2011). The injection rate is 90 bpm for five clusters per stage. The injection continues for 100 min to get similar value of the total injected fluid volume (8,350 bbl of slick-water in their work).

After the injection, the well is shut-in for 30 days, and the production starts with constant bottom-hole pressure (2,600 psi) for 100 days. The shut-in period may be much longer than the actual field case, and the long term shut-in period is used to evaluate if the fracture temperature and wellbore temperature distribution get back to initial geothermal temperature during the period. Here, at the beginning of shut-in, the velocity field is assumed to become static. When the well is suddenly shut-in, the sudden change leads to a series of pressure pulses known as a water hammer by using the transient momentum balance equation (Carey et al. 2015). It makes the simulation time step size quite small, and takes long simulation time to get the static condition. While the water hammer effect itself can be useful method in the diagnostic fracture-injection test (McClure et al. 2016, Carey et al. 2015), this work ignores those effects. In addition, when fracture conductivity is quite high during shut-in period, the simulation time-step also becomes quite small because of the high rate flow interaction between the wellbore and the reservoir. To stabilize the process, lower productivity index multiplier is used until the flow interaction is stabilized. This seems to affect the pressure equilibration in the wellbore.

Identical Fractures

Figure 3.16 shows geometries used in this single stage fractured well with five identical fractures. **TABLE 3.2** summarizes input data used in this case. The reservoir and fracture properties are mostly the same with the single fracture case. The fracture spacing used in this study is 150 ft. The case assumes five identical fractures with half-length of 1,000 ft are created, and the propped fracture half-length is 300 ft. The treatment pressure is 7,500 psi in this case during injection.

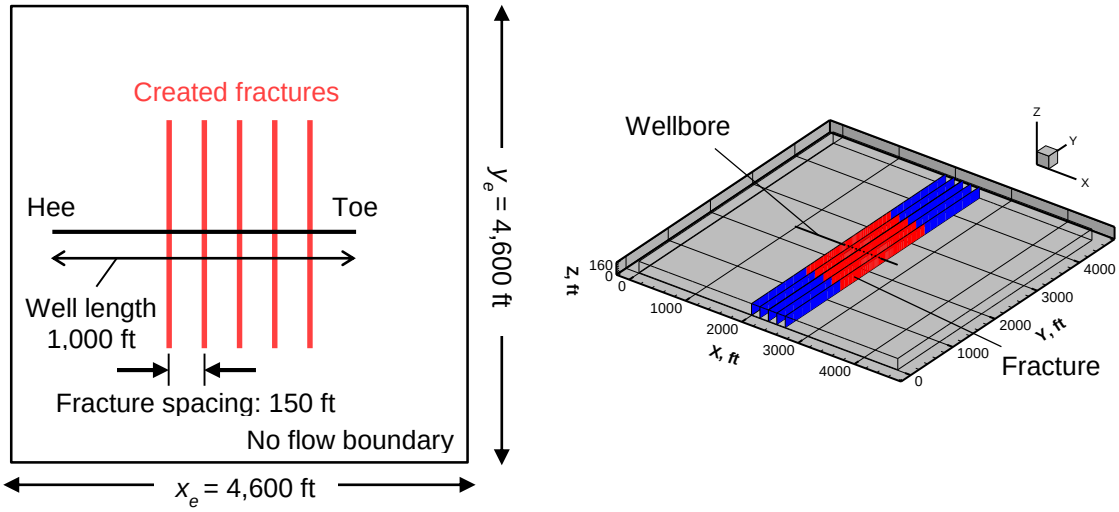

(a) *x-y* cross section (top view)

(b) Slice of fracture position in 3D view

Figure 3.16—Geometries of the single-stage case (identical fractures)

TABLE 3.2—INPUT DATA FOR THE CASE OF A HORIZONTAL WELL WITH FIVE IDENTICAL FRACTURES

Type	Property	Value
Reservoir	Reservoir size (*x*-dir) ft	4,600
	Reservoir size (*y*-dir) ft	4,600
	Net pay thickness, ft	160
	Matrix permeability, nD	583
	Matrix porosity, fraction	0.042
	Total thermal conductivity, Btu/(ft-hr-°F)	1.79
	Rock specific heat, Btu/(lbm-°F)	0.202
	Rock density, lbm/ft^3	148.58
	Initial water saturation, fraction	0.1
	Initial pressure, psi	4,500
	Initial temperature, °F	238.37
Fracture	Fracture width, in	0.24
	Fracture conductivity (injection), D-ft	10
	Fracture conductivity (shut-in/production), mD-ft	20
	Fracture spacing, ft	150
	Fracture porosity, fraction	0.2
	Fracture height, ft	160
	Created fracture half-length, ft	1,000
	Propped fracture half-length, ft	300
	Enhanced permeability, mD	5.83×10^{-3}
Wellbore	Wellbore diameter, inch	8.75
	Casing OD, inch	5.5
	Pipe-relative roughness, –	0.001
	Cement thermal conductivity, Btu/(hr-ft-°F)	4.021
	Casing thermal conductivity, Btu/(hr-ft-°F)	6.993

Figure 3.17 shows simulated DTS response (sandface temperature) of the horizontal well with identical fractures. During the injection, the sandface temperature is cooled down by the injected fluid as shown in the blue color region in the **Figure 3.17a**. Once the shut-in starts, the entire sandface is heated by the surrounding formation. According to the simulated DTS response map during shut-in (**Figure 3.17a**), the created fracture locations can be detected clearly because, at the fracture locations, the temperature recovery is slower than the non-perforated zone. The fracture positions are also detected

in the simulated DTS response during production periods (**Figure 3.17b**) while those temperature signals are not so obvious than those during the shut-in period.

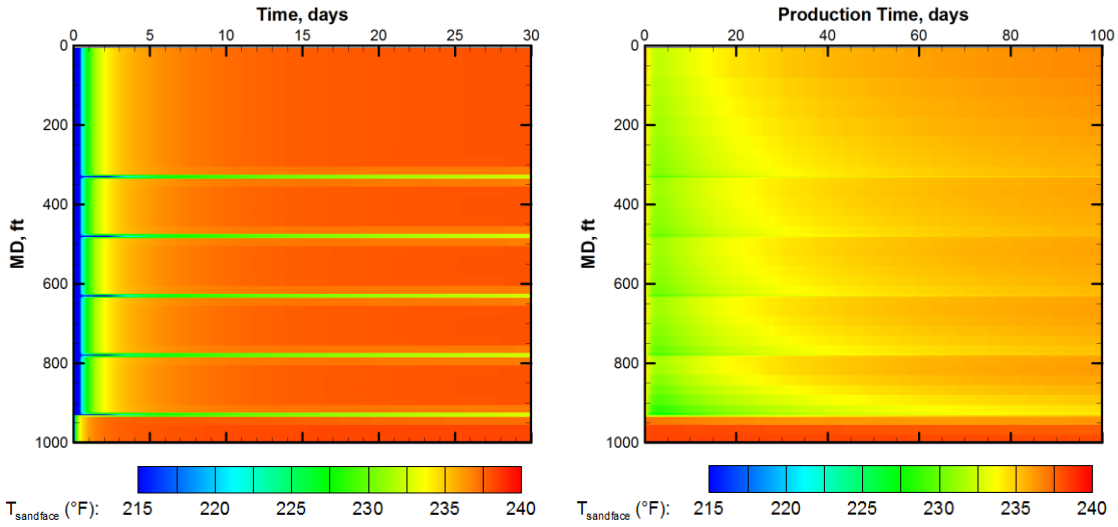

(a) During stimulation and shut-in (b) During production

Figure 3.17—Simulated DTS response (sandface temperature) of the horizontal well with identical fractures

Figure 3.18 shows sandface temperature profiles at selected time during shut-in and production. Even after 30 days of shut-in, the sandface temperature does not reach the initial geothermal temperature near those fracture locations, while the sandface temperature of the non-perforated region is close to the geothermal temperature (**Figure 3.18a**). During production, the sandface temperature profiles keep increasing with time (**Figure 3.18b**), which is caused by reduction of Joule-Thomson cooling effect associated with decrease of gas inflow rate as mentioned in the single fracture case. At all fracture locations, same magnitude of gas cooling effect can be seen in the sandface temperature profile because the fractures are identical and have the same gas inflow rate. The non-

symmetric sandface temperature profile results from the heat transfer between the wellbore and reservoir.

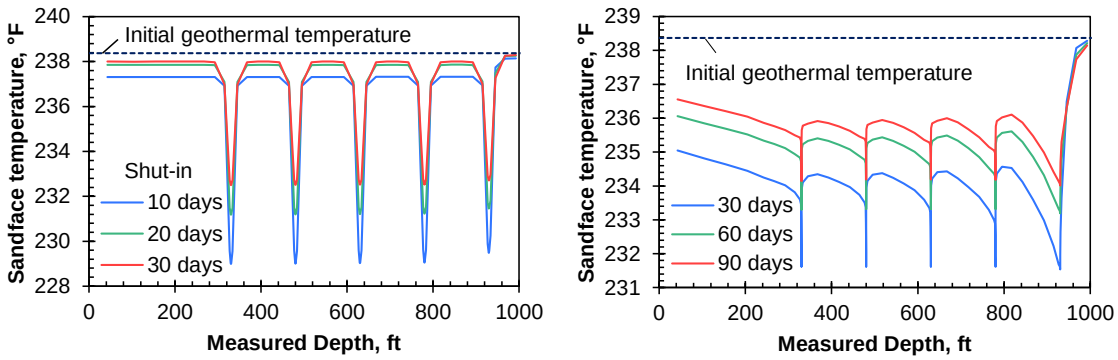

(a) During shut-in (b) During production

Figure 3.18—Sandface temperature profile during shut-in and production (identical fractures)

Figure 3.19 shows wellbore flowing temperature and flow rate profiles along the horizontal well at 30 days, 60 days and 90 days of production. While the inflow temperatures and the inflow rates are same at all of the fracture locations, temperature changes at the fracture position become smaller as fluid moves to the heel side. It results from the fluid mixing between inflow and wellbore streams (Hill 1990), and it makes it difficult to use wellbore flowing temperature for interpretation of flow rate profile along the horizontal well with multiple fractures (Yoshida et al. 2014).

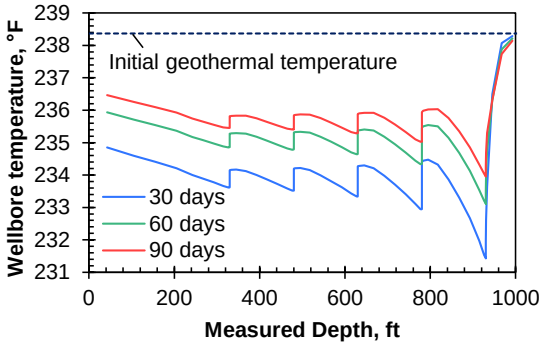

(a) Wellbore flowing temperature

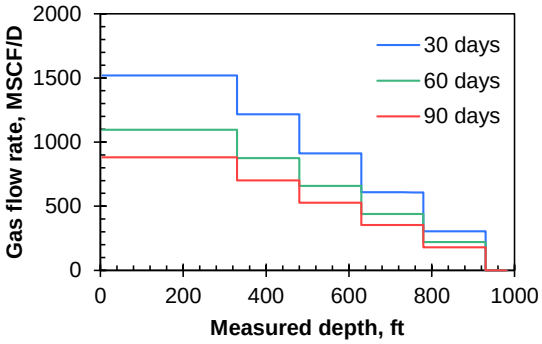

(b) Gas flow rate

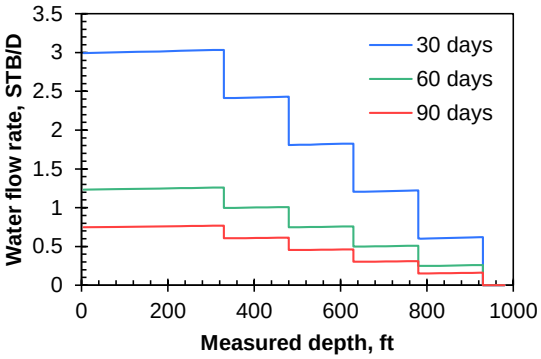

(c) Water flow rate

Figure 3.19—Wellbore flowing temperature and flow rate profiles during production (identical fractures)

Figure 3.20 compares wellbore temperature profiles and gas flow rate profiles by gas-water model and single phase gas model. The wellbore temperature profile given by gas-water model is around 1-2 °F lower than that by single phase gas model on average. In these cases, the gas flow rates are similar and the temperature changes at fracture positions are also similar. Therefore, when the single phase gas model is used to obtain same magnitude of temperature with gas-water case, it requires more gas flow rate; it may overestimate gas production rate from those fractures.

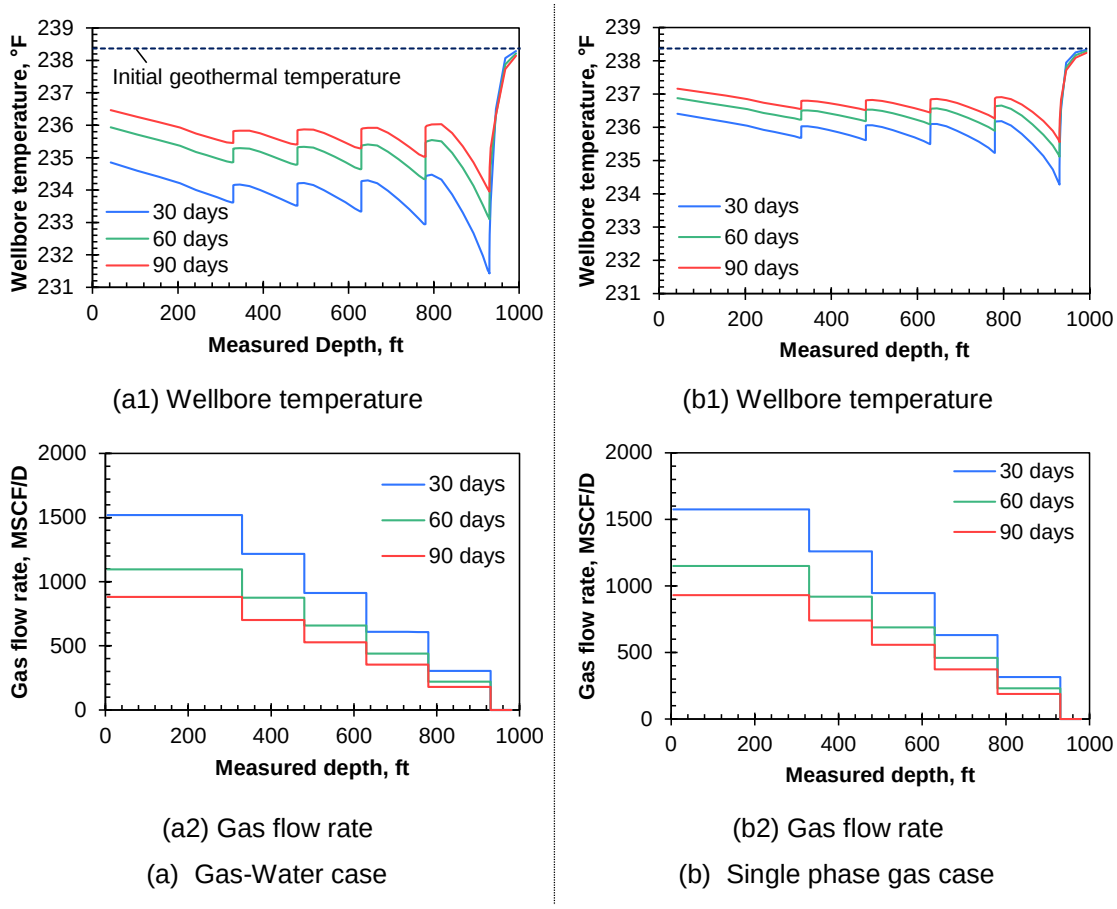

Figure 3.20—Comparison of wellbore temperature and gas rate profile between gas-water case and single phase gas case

Non identical fractures

With use of the plug-and-perf completion, local injection rate at each perforation cannot be controlled in field operations. In this case, non-identical fractures are considered; the created fracture half-length may not be evenly distributed as shown in **Figure 3.21**. The input data for this case is summarized in **TABLE 3.3**. The created fracture half-length are 750 ft, 0 ft (no fracture), 1,500 ft, 350 ft and 1,000 ft, and the propped fracture half-length are around 30% of the created fractures (200 ft, 0 ft, 500 ft, 100 ft and 300 ft) as shown in **Figure 3.22**. The conductivity of these fractures and enhancement effects due to natural

fractures are assumed to be the same with the case of identical fractures. The treatment pressure is 8,500 psi in this case during injection, and rate allocations of the injected fluid into fractures are linearly proportional to the created fracture half-length (18.75 bpm, 0 bpm, 37.5 bpm, 8.75 bpm and 25.0 bpm, respectively).

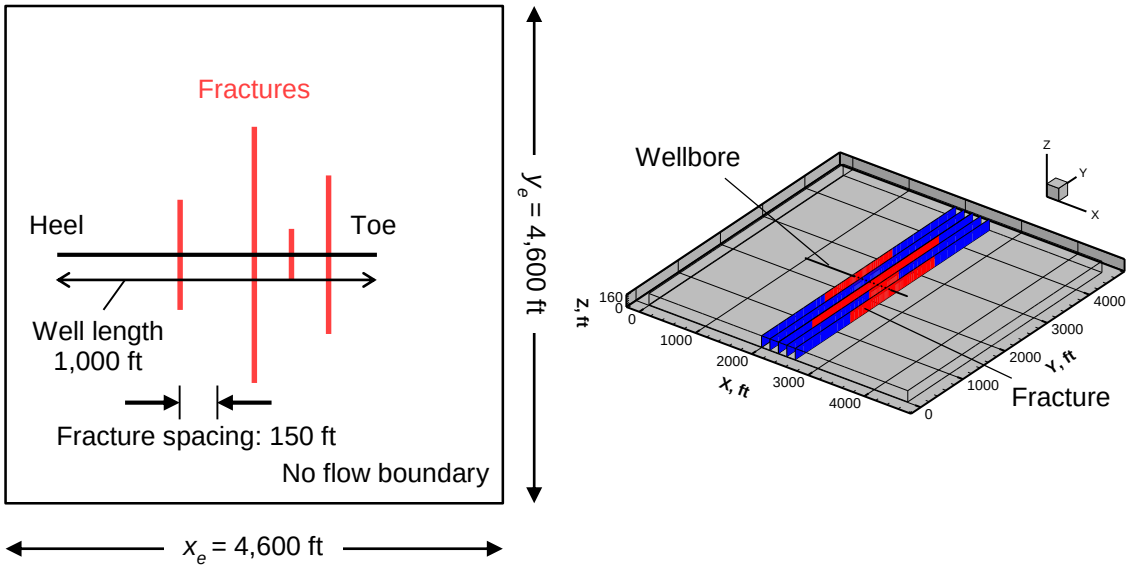

(a) *x-y* cross section (top view) (b) Slice of fracture position in 3D view

Figure 3.21—Geometries of the single-stage case (non-identical fractures)

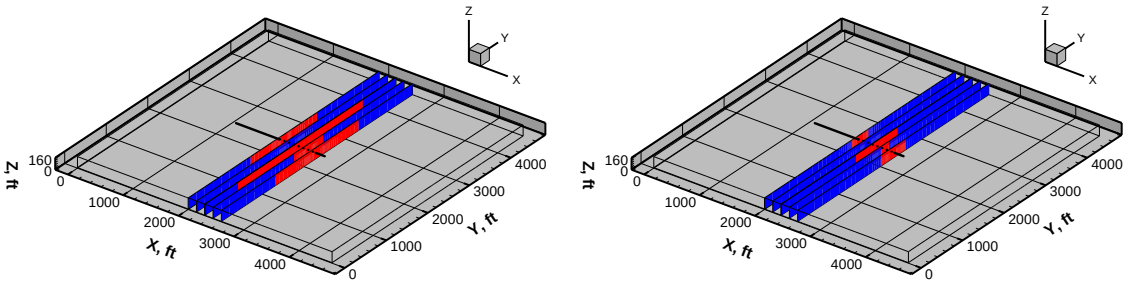

(a) Created fractures (b) Propped fractures for production

Figure 3.22—Created and propped fracture distributions of the single-stage with non-identical fractures

TABLE 3.3—INPUT DATA FOR THE CASE OF A HORIZONTAL WELL WITH FIVE NON-IDENTICAL FRACTURES

Type	Property	Value
Reservoir	Reservoir size (*x*-dir) ft	4,600
	Reservoir size (*y*-dir) ft	4,600
	Net pay thickness, ft	160
	Matrix permeability, nD	583
	Matrix porosity, fraction	0.042
	Total thermal conductivity, Btu/(ft-hr-°F)	1.79
	Rock specific heat, Btu/(lbm-°F)	0.202
	Rock density, lbm/ft^3	148.58
	Initial water saturation, fraction	0.1
	Initial pressure, psi	4,500
	Initial temperature, °F	238.37
Fracture	Fracture width, in	0.24
	Fracture conductivity (injection), D-ft	10
	Fracture conductivity (shut-in/production), mD-ft	20
	Fracture spacing, ft	150
	Fracture porosity, fraction	0.2
	Fracture height, ft	160
	Enhanced permeability, mD	5.83×10^{-3}
Wellbore	Wellbore diameter, inch	8.75
	Casing OD, inch	5.5
	Pipe-relative roughness, –	0.001
	Cement thermal conductivity, Btu/(hr-ft-°F)	4.021
	Casing thermal conductivity, Btu/(hr-ft-°F)	6.993

Figure 3.23 shows simulated DTS response (sandface temperature) of the horizontal well with non-identical fractures. According to the DTS response during stimulation and shut-in, the non-fractured location can be easily detected (no temperature signal during shut-in). In the qualitative interpretation of the simulated DTS response, it seems difficult to use the temperature map during injection and shut-in to determine the relative size or created volume of fractures. The simulated DTS response during production looks helpful to determine the relative contributions for the flow rate. For all of the three larger fracture positons, the gas cooling effects can be seen (**Figure 3.23b**).

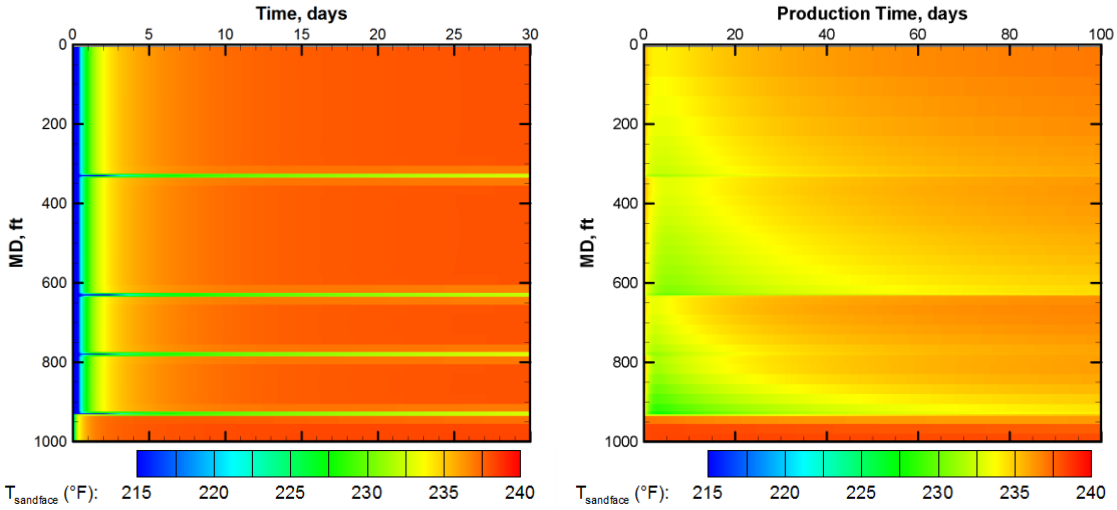

(a) During stimulation and shut-in (b) During production

Figure 3.23—Simulated DTS response (sandface) of the horizontal well with non-identical fractures

Figure 3.24 shows sandface temperature profiles at selected times during shut-in and production. According to the temperature profile during production (**Figure 3.24b**), the difference of fracture size can be clearly seen as the difference of the gas cooling effect at fracture locations.

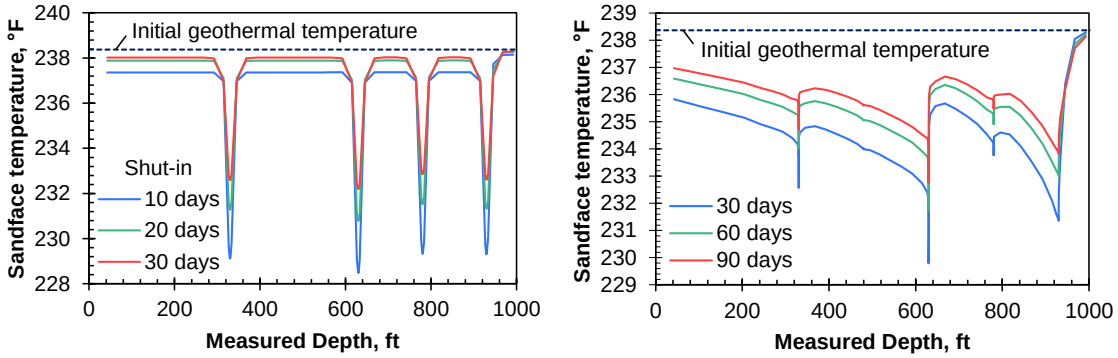

(a) During shut-in (b) During production

Figure 3.24—Sandface temperature profile during shut-in and production (non-identical fractures)

Figure 3.25 shows wellbore temperature and flow rate profiles, and it masks the temperature signals due to the mixing effect. In addition, when we have large amount of flowing fluid inside the wellbore, fracture spacing also affects the wellbore temperature behavior. If the spacing is not long enough to warm up the flowing fluid, the cooling effect cannot be detected. In this case study, the spacing is 150 ft and the cool anomalies are distinct, but, some field cases use shorter fracture spacing such as 75 ft or less.

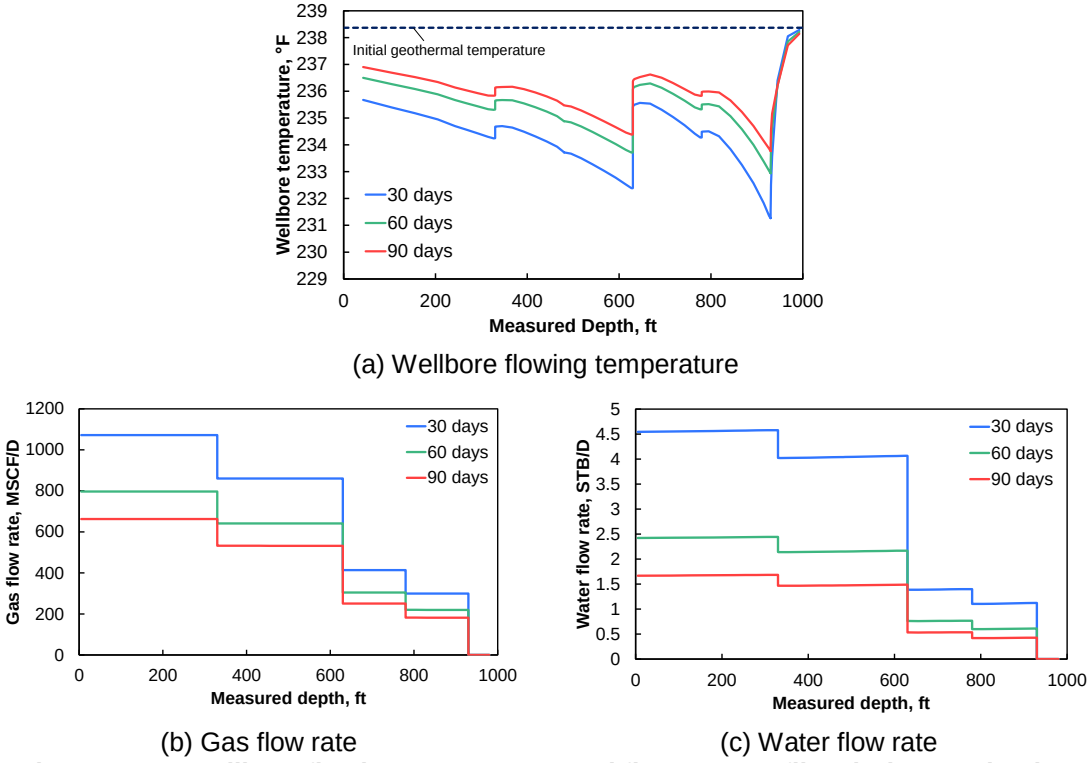

(a) Wellbore flowing temperature

(b) Gas flow rate

(c) Water flow rate

Figure 3.25—Wellbore flowing temperature and flow rate profiles during production (non-identical fractures)

3.2.3 A Three Stage-fractured Horizontal Well

This case considers three stage fracturing treatment (5 clusters per stage) and production to evaluate if the stair-step initial temperature distribution affects temperature profile

during production. **Figure 3.26** shows schematics of reservoir, fracture and wellbore geometry of this case. Each stage has five clusters, and the cluster and stage spacing are 150 ft. Identical fractures are assumed to be created in this case.

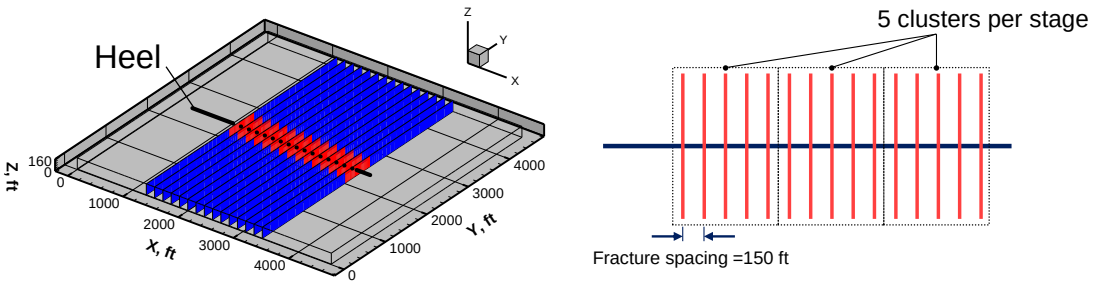

(a) Fracture distribution and well position (b) Near wellbore

Figure 3.26—Geometries of three stage-fractured well

Figure 3.27 shows treatment design of the three stage fracturing case. The injection rate is 90 bpm for 100 min per stage, and it is followed by 60 min shut-in to prepare for injection of next stage. The shut-in time between stages depends on actual field operations and it can be several hours. The shut-in time used in this study is thought to be the minimum possible time in field operations. This injection and shut-in cycle is repeated for all three stages. The change of the fracture distribution for each treatment is shown in **Figure 3.28**. It is noted that, at the beginning of injection, the velocity field in the wellbore is set to steady state condition, and, at the beginning of shut-in, the velocity becomes zero as discussed in the previous case. After the treatment, the well is shut-in for 10 days to prepare for production.

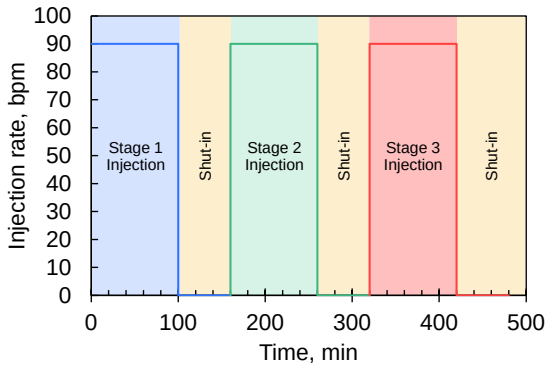

Figure 3.27—Treatment design of the three stage fracturing

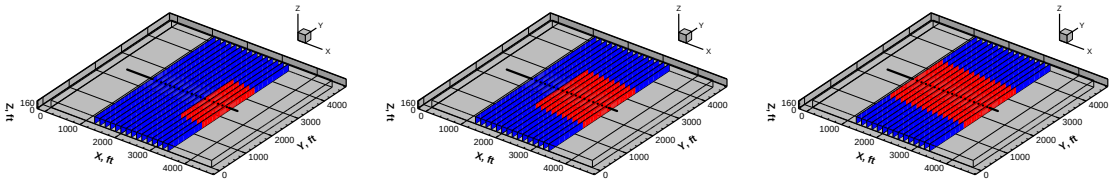

(a) Stage 1 (b) Stage 2 (c) Stage 3

Figure 3.28—Change of fracture distribution for multi-stage treatment

Figure 3.29 shows simulated DTS responses with time along the measure depth. The simulated DTS response shows the stair-step temperature profile as observed in field data, and it supports the effective zonal isolation in the simulation as well. Since the fractures are assumed to be identical, the temperature signals by each fracture are almost identical during production.

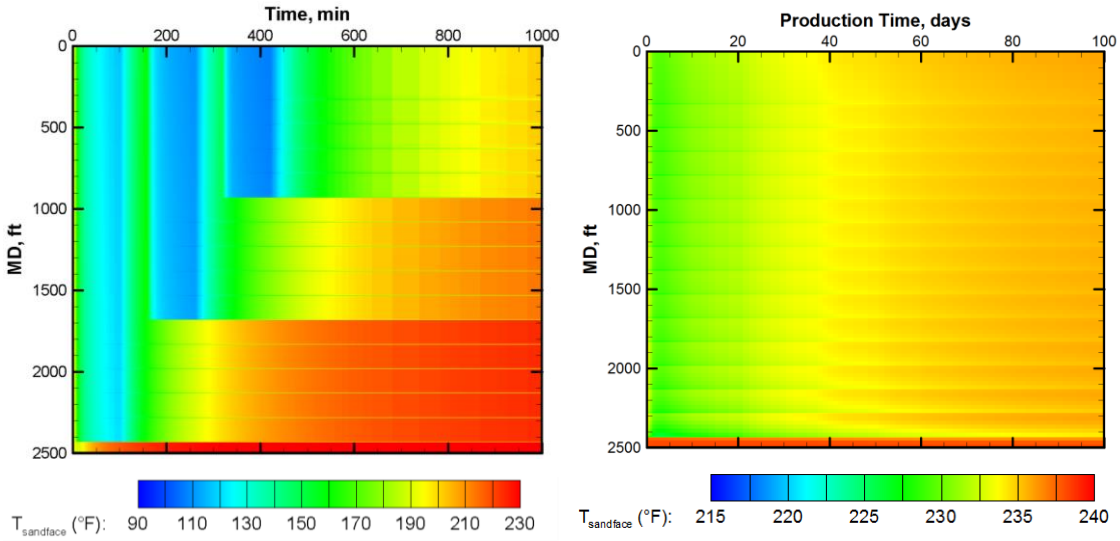

(a) During stimulation and early shut-in (b) During production

Figure 3.29—Simulated DTS response (sandface) of the horizontal well with three-stage fracturing treatment

Figure 3.30 shows a comparison of wellbore and sandface temperature during production. As expected, with increase a number of fractures and total flow rate in the wellbore, wellbore temperature changes associated with fracture inflow get smaller. It is noted that the sandface temperature change near the heel is limited only at the fracture locations while the sandface temperature change near the toe is more smeared. This difference results from the wellbore temperature distribution in these regions. **Figure 3.31** shows comparison of the wellbore temperature by gas-water case and single phase gas case. While the average temperature in the gas-water case is lower than that in the single phase case, the difference becomes smaller with time.

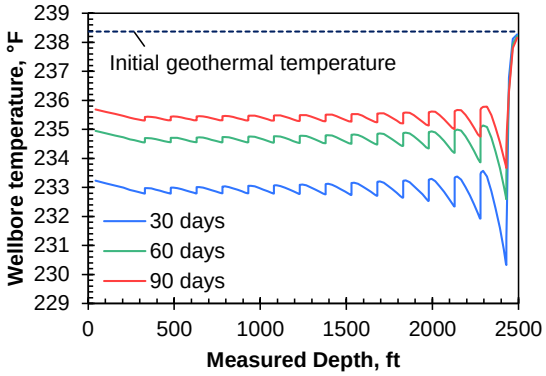

(a) Wellbore temperature

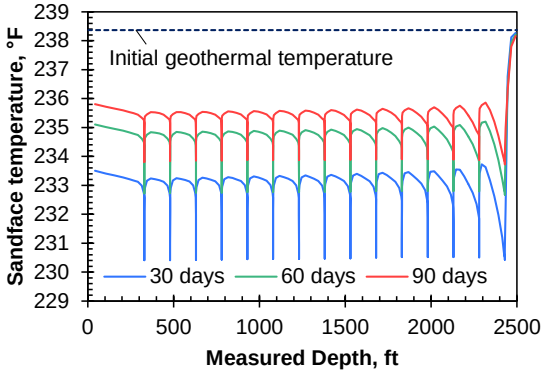

(b) Sandface temperature

Figure 3.30—Comparison of wellbore and sandface temperature (three stage case)

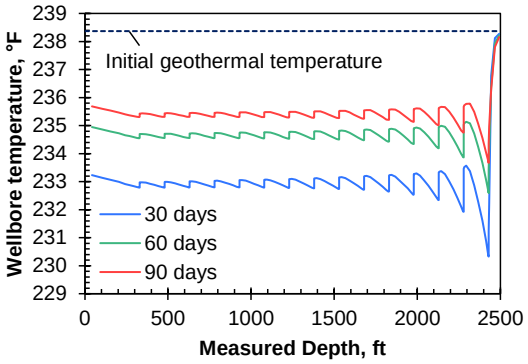

(a1) Wellbore temperature

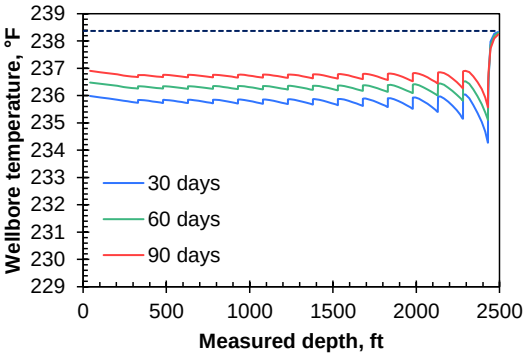

(b1) Wellbore temperature

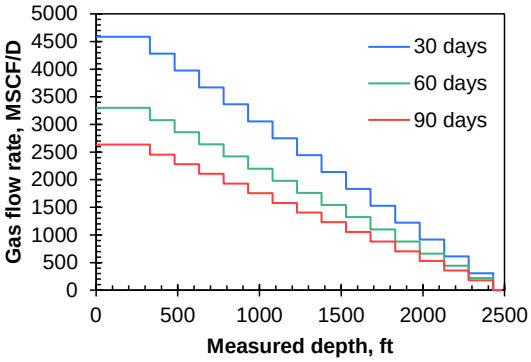

(a2) Gas flow rate

(a) Gas-Water case

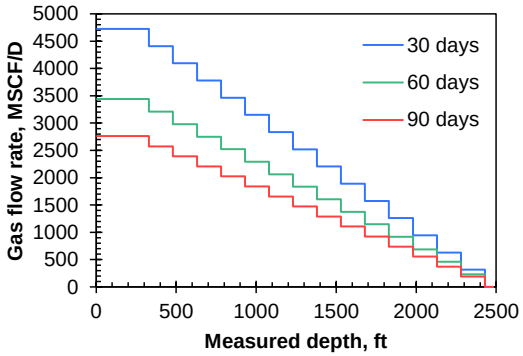

(b2) Gas flow rate

(b) Single phase gas case

Figure 3.31—Comparison of wellbore temperature and gas rate profile between gas-water case and single phase gas case (three stage case)

3.3 Sensitivity Study

The case studies provide ideas on the downhole temperature behavior in the single fracture and in the horizontal well with multiple fractures. This section further investigates sensitivity of inflow temperature on key parameters in evaluation of the fracture flow performance: propped fracture half-length and fracture conductivity. In this sensitivity study, we treat these parameters as independent to investigate their effects separately.

The problem geometry in the sensitivity study is the same with the single fracture case study. To obtain profiles of the pressure, temperature and saturation at the onset of production, the injection and shut-in simulations are run. The water is injected at the fracture position with injection rate at 18 bbl/min for 100 minutes. The injection fluid temperature is fixed at 80 °F. After the injection, the well is in shut-in for 30 days and the well starts to produce for 100 days. The input data for this case is summarized in **TABLE 3.4**. The rock density, thermal conductivity and specific heat are values of a shale read from Lake (2010).

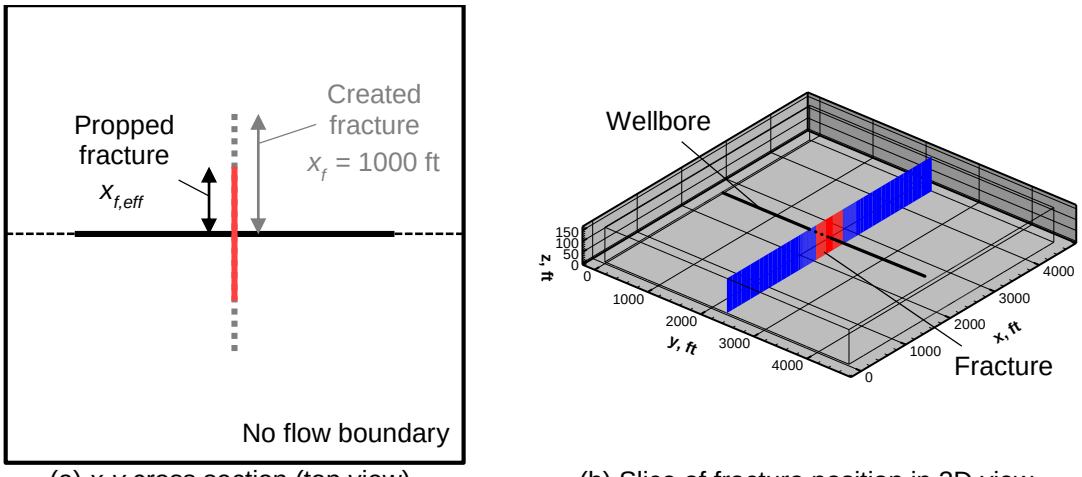

(a) *x-y* cross section (top view) (b) Slice of fracture position in 3D view

Figure 3.32—Geometries for sensitivity study of the single fracture

TABLE 3.4—INPUT DATA FOR SINGLE FRACTURE SENSITIVITY STUDY		
Type	Property	Value
Reservoir	Reservoir size (*x*-dir) ft	4,600
	Reservoir size (*y*-dir) ft	4,600
	Net pay thickness, ft	160
	Matrix permeability, nD	583
	Matrix porosity, fraction	0.042
	Thermal conductivity (dry), Btu/(ft-hr-°F)	0.571
	Thermal conductivity (saturated), Btu/(ft-hr-°F)	0.924
	Rock specific heat, Btu/(lbm-°F)	0.202
	Rock density, lbm/ft^3	148.58
	Initial water saturation, fraction	0.1
	Initial pressure, psi	4,500
	Initial temperature, °F	238.37
Fracture	Fracture width, in	0.24
	Fracture porosity, fraction	0.2
	Fracture height, ft	160
	Created fracture half-length, ft	1,000
	Enhanced permeability, mD	5.83×10^{-3}

3.3.1 Propped Fracture Half-length

The propped fracture half-length is changed from 100 ft to 500 ft. **Figure 3.33** shows simulated inflow temperature and gas production profiles with time using different fracture half-length sizes. When the fracture length increases, the inflow temperature becomes lower at a certain time after the initial flow-back water production. This results from the increase of the gas production because of the increase of the fracture contact area to the formation.

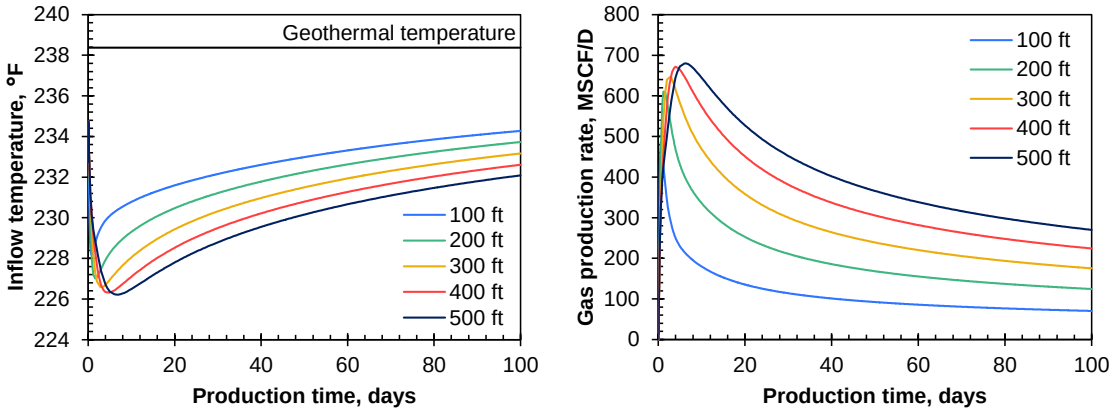

(a) Inflow temperature (b) Gas production rate

Figure 3.33—Simulated inflow temperature and gas production rate with time using different propped fracture half-length size

3.3.2 Fracture Conductivity

The fracture conductivity is changed from 2 mD-ft to 200 mD-ft. In this case, we only changed the permeability of the fracture to change the conductivity values (fracture width is 0.02 ft). **Figure 3.34** shows simulated inflow temperature and gas production profiles with time using different fracture conductivity values. With increase of the fracture conductivity, the inflow temperature becomes higher at a certain time after the initial flow-back water production. The increase of the fracture conductivity leads to significant increase of the gas production rate, but, at the same time, the pressure drop inside the fracture also becomes quite small. It leads to the reduction of the Joule-Thomson cooling effect inside the fracture with a higher conductive fracture.

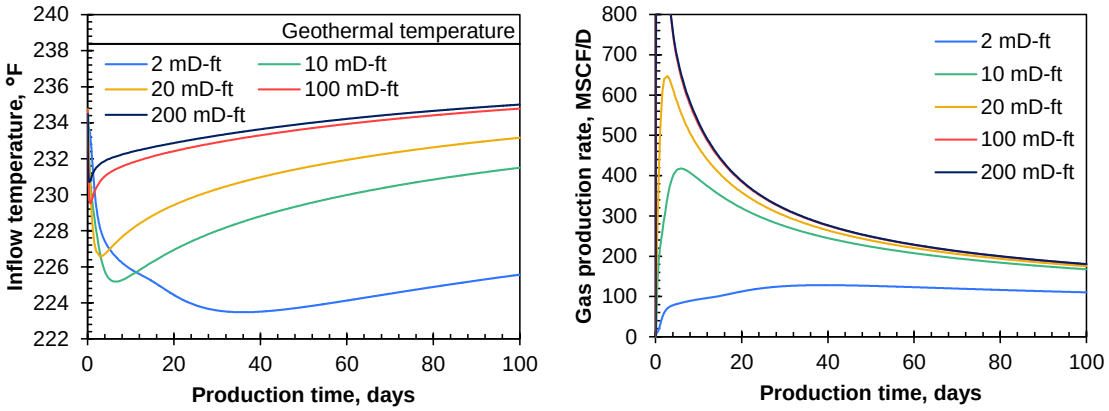

(a) Inflow temperature (b) Gas production rate

Figure 3.34—Simulated inflow temperature and gas production rate with time using different fracture conductivity

3.3.3 Formation Thermal Conductivity

The temperature sensitivity on the thermal conductivity is also studied. The value range of the shale rock thermal conductivity is reported by researchers (Schön 1996, Eppelbaum et al. 2014). We use the range by Eppelbaum et al. (2014) (1.1 W/m-K to 2.1 W/m-K), and the mean value (1.6 W/m-K) is equal to the value shown in Lake (2010) as water saturated thermal conductivity.

Figure 3.35 shows simulated inflow temperature and gas flow rate with time using three different thermal conductivities (min, mean and max are 1.1, 1.6 and 2.1 W/m-K, respectively). The gas production rate plots given by these three cases are overlain in **Figure 3.35b**. With the increase of the thermal conductivity, the inflow temperature slightly increases. This is caused by the increase of the thermal diffusivity in the formation, and it leads to relatively faster warm up by the surrounding formation.

With change of the value of the thermal conductivity, the inflow temperature behavior changes, but the change seems to be much smaller than the effects of the fracture half-length and fracture conductivity within the range discussed in this work.

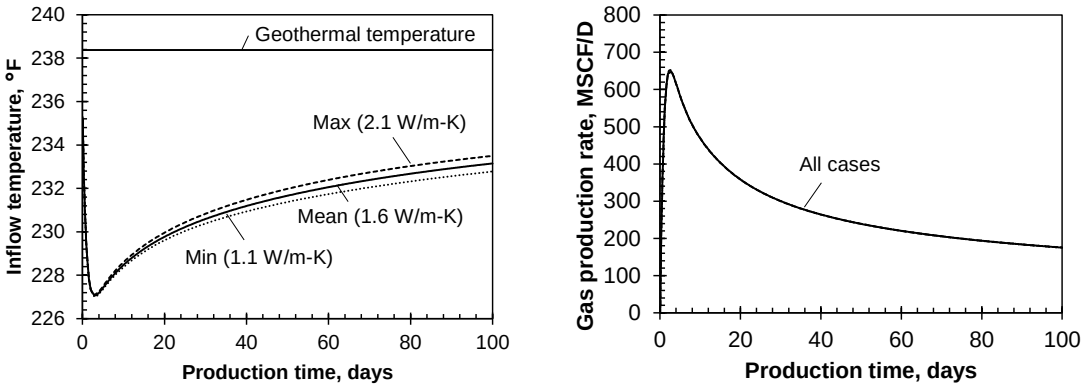

(a) Inflow temperature (b) Gas production rate

Figure 3.35—Simulated inflow temperature and gas production rate with time using different formation thermal conductivity

CHAPTER IV

FIELD APPLICATIONS: INTERPRETATION OF DOWNHOLE TEMPERATURE BEHAVIORS IN A HORIZONTAL WELL WITH MULTIPLE FRACTURES

4.1 Chapter Summary

This chapter applies the developed temperature model to field cases. This field application tries to justify the qualitative interpretations from the theoretical modeling perspective. And, the developed model is also used to quantitatively interpret the downhole temperature to predict flow profiles during production. The quantitatively interpreted flow profile is compared with the results by single phase gas model and the other measurement methods.

4.2 Introduction

This work shows two field cases. First, the model is applied to a field case presented by Ugueto et al. (2016). They showed the DTS and the DAS responses of a horizontal well with multiple fractures. The horizontal well has 11 stages with multiple clusters, and the DTS and DAS data of the stage 11 is presented for injection, shut-in and production period. Secondly, the model is used for the quantitative interpretation of the horizontal well with multiple fractures (15 stages) in the Eagle Ford shale, which is presented in Cui et al (2015). The downhole temperature data was measured with a production logging tool, and the surface production rate is available.

4.3 Qualitative Interpretation: A Field Case Study

4.3.1 Descriptions of the Field Data

Ugueto et al. (2015) showed DTS temperature maps for several wells, and Ugueto et al. (2016) further discussed the DTS profiles of one of those wells. The target well is a horizontal well with eleven stages of plug-and-perf completions. In their work, detailed DTS profiles are provided for the stage 11 close to the heel of the well. The stage has six perforation clusters and the cluster spacing is around 50 m. **Figure 4.1** shows DTS profiles provided in their work at stage 11 a few days after the fracturing treatment and after 30 days of production. The data of the plots is read from the plots in the work by Ugueto et al. (2016).

According to the DTS response during warm-back (**Figure 4.1a**), all of the perforation clusters show cooler temperature than the non-perforated region, while, during the fracturing treatment of the stage, the perforations 11.2 and 11.3 have little DAS activity (Ugueto et al. 2016). On the other hand, the DTS response during production clearly shows the cooler signals at perforations 11.1, 11.4, 11.5 and 11.6 while the other two perforations do not show any signals. These four clusters are thought to produce gas from the DTS responses qualitatively, and it is supported by the DAS response as well in their work.

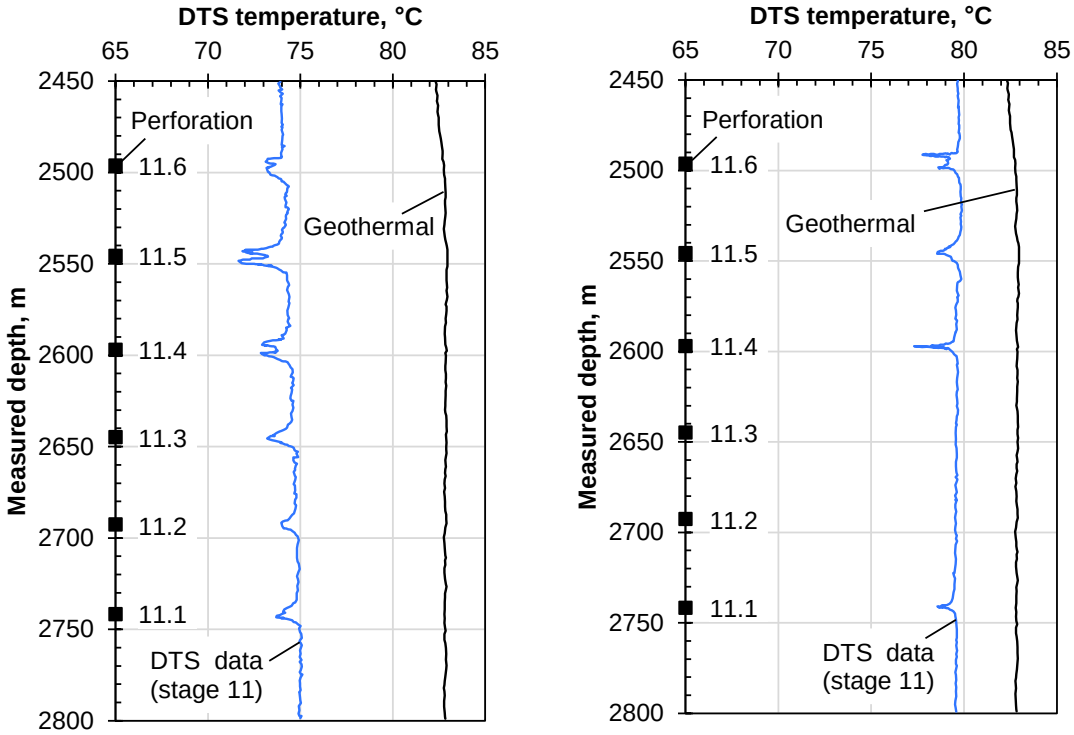

(a) DTS profile of the stage 11 few days after the fracturing treatment

(b) DTS profile of the stage 11 after 30 days of production

Figure 4.1—DTS profile of the stage 11 during warm-back and production (data read from Ugueto et al. (2016))

4.3.2 Model Setup

In this work, we try to replicate these DTS responses with the developed model to obtain better understanding of the temperature behaviors. The provided treatment data is limited in the work by Ugueto et al. (2016) (only for stage 4 and stage 11 are available), and we assume the treatment design and shut-in time from those provided data. For stage 11, the injection rate, duration and operating bottom-hole pressure are assumed to be 75 bpm, 105 min and 7832 psi (54 MPa). Other stages are assumed to be treated with 75 bpm for 2 hours, and the well is shut-in for 10 hours between the stages.

Figure 4.2 shows geometries of the reservoir and wellbore with the slices of the fracture plane before stage 11 treatment (**Figure 4.2a**) and after the beginning of the stage 11 treatment with uniform created fractures (**Figure 4.2b**). **TABLE 4.1** summarized the input used in this study. For the treatments of the stage 1 to stage 10, the injection and shut-in are repeated for the reservoir without any fractures (**Figure 4.2a**).

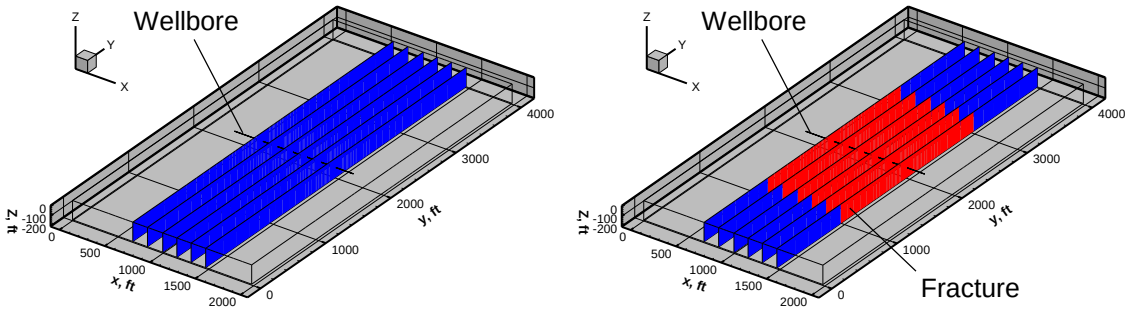

(a) Before stage 11 treatment (treatments and shut-in for other 10 stages)

(b) After the beginning of the stage 11 treatment (with uniform fractures)

Figure 4.2—Geometry for the stage 11

Figure 4.3 shows simulated DTS response with corresponding injection rate during the treatments of the stage 1 to stage 10. The repeated processes of the injection and shut-in make the warm-back slower as the treatment progresses. The final reservoir and wellbore temperature profiles are used for the treatment of the target stage.

TABLE 4.1—INPUT DATA FOR QUALITATIVE INTERPRETATION OF THE FIELD DATA IN UGUETO ET AL. (2016)

Type	Property	Value
Reservoir	Reservoir size (*x*-dir) ft	2,000
	Reservoir size (*y*-dir) ft	4,000
	Net pay thickness, ft	200
	Matrix permeability, nD	583
	Matrix porosity, fraction	0.042
	Rock specific heat, Btu/(lbm-°F)	0.202
	Rock density, lbm/ft^3	148.58
	Initial water saturation, fraction	0.1
	Initial pressure, psi	3,560
	Initial temperature, °F	180.0
Fracture	Fracture width, in	0.24
	Fracture conductivity (injection), D-ft	10
	Fracture conductivity (shut-in/production), mD-ft	20
	Fracture porosity, fraction	0.2
	Fracture height, ft	200
	Enhanced permeability, mD	583 × 10^{-2}
Wellbore	Wellbore diameter, inch	8.75
	Casing OD, inch	5.5
	Pipe-relative roughness, –	0.001
	Cement thermal conductivity, Btu/(hr-ft-°F)	4.021
	Casing thermal conductivity, Btu/(hr-ft-°F)	6.993

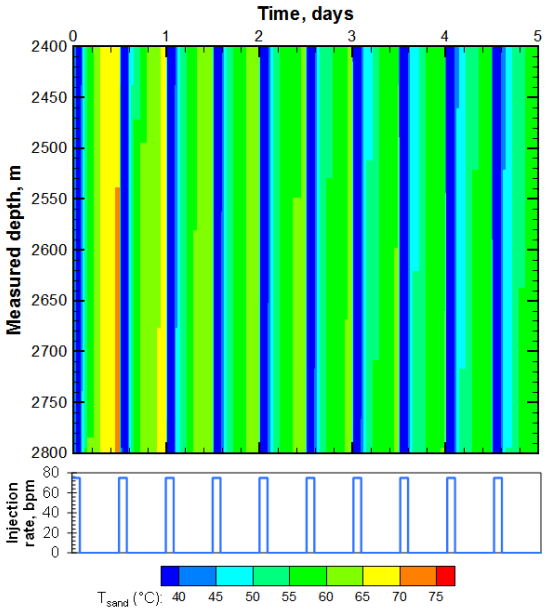

Figure 4.3—Simulated DTS response and corresponding injection rate during the treatments of the stage 1 to the stage 10

4.3.3 Results: Temperature Matching for the Qualitative Interpretation

For the field data, we try to match simulated DTS response to the measured shut-in DTS response obtained few days after the injection. In the temperature matching process, at first, we changed formation thermal conductivity values within the range shown by Eppelbaum et al. (2014) to match the temperature at the non-perforated region. We assume that identical fractures are created with 1,000 ft fracture half-length as initial guess.

Next, the created fracture half-length of each fracture is changed to obtain improved matched temperature profile. Since this work needs to assume the fracture length before the injection, the corresponding rate allocation also needs to be adjusted (Eq. 3.1). The rate into each perforation is estimated by the ratio of each fracture volume to sum of the fracture volume. The thickness of this reservoir is assumed to be 200 ft, so, if the fracture half-length becomes less than 100 ft, the fracture shape is changed to penny shape radial fracture. The temperature profile in the wellbore depends on the rate allocation. With multiple injection points, the well flow rate decreases progressively, and it leads to the changes in slope in the temperature profile (Ribeiro and Horne 2016).

Figure 4.4 shows an example wellbore temperature profile at the end of injection into the stage 11. The red shaded zones are perforation positions, and solid line and dashed line denote temperature profiles by uniform rate allocation and non-uniform rate allocation, respectively. In the uniform rate allocation case, each perforation took 12.5 bpm (17% of the total injection rate). However, in the non-uniform rate allocation case, the first three perforations took more than 99 % (74.5 bpm) of the total flow amount, and it leads to significantly small amount of flow inside wellbore. The small amount of

wellbore flow is easily heated up by the surrounding formation. The example plot shows an extreme case, but, this temperature deviation due to the rate allocation likely leads to slightly higher temperature near the toe side in shut-in temperature profile as shown in field data (**Figure 4.1a**).

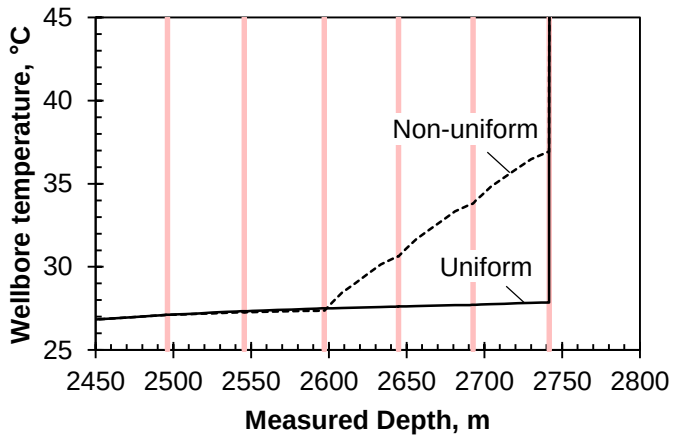

Figure 4.4—An example plot of wellbore temperature profile at the end of injection of stage 11 with uniform rate allocation and non-uniform rate allocation

Figure 4.5a shows the simulated DTS response with the measured DTS data after the calibration of the thermal conductivity with uniform fractures (no change in the rate allocations). In this case, the water-saturated thermal conductivity value is 1.6 W/m-K. By changing thermal conductivity, the temperature at non-perforated regions is matched slightly. **Figure 4.5b** shows the final matched temperature profile. The temperature profile at non-perforated region shows good matching, and, the temperature profiles at the perforations of 11.1, 11.2 and 11.3 show fairly good agreement. However, the measured temperature profile at the perforations 11.4, 11.5 and 11.6 show different temperature

shape compared with the simulated DTS response. Therefore, the temperature matching for these fractures were terminated when the simulated DTS temperature of the bottom three perforations are matched with the DTS temperature data. The temperature matching offers some insights on the rate allocation for the target stage and relative volume of the created fractures. The estimated fracture half-lengths and injection rates are summarized in **TABLE 4.2**.

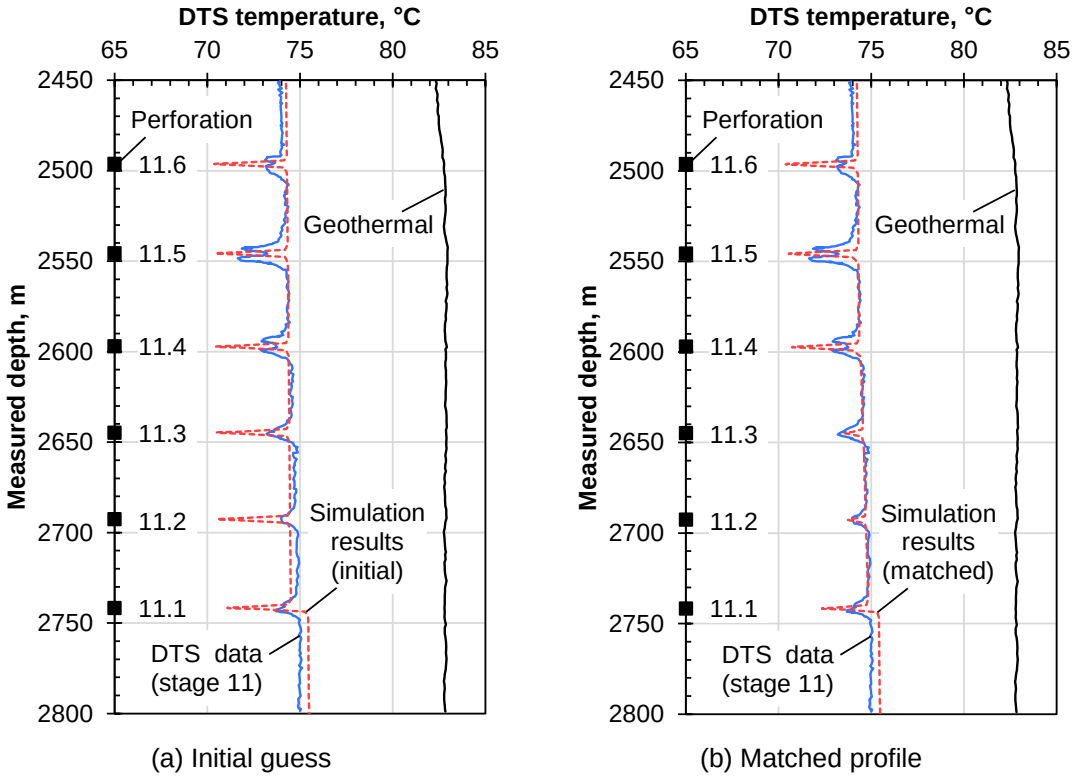

Figure 4.5—Measured DTS temperature and simulated DTS temperature for shut-in period (initial guess and matched profile)

TABLE 4.2—ESTIMATED FRACTURE LENGTH AND RATE ALLOCATION		
Perforation	Fracture-length, ft	Injection rate, bpm
11.6	1000	24.8
11.5	1000	24.8
11.4	1000	24.8
11.3	5	0.0049
11.2	5	0.0049
11.1	50	0.488

4.3.4 Discussion

In the above matching, the perforations 11.4, 11.5 and 11.6 show different temperature shape comparing with the simulated DTS response in this work. The measured DTS shows small warm temperature anomalies at the center of the perforations. These warm anomalies can only be seen at perforations which show larger DAS signal during injection and DAS/DTS signal during production (Ugueto et al. 2016). However, the DTS response during production (**Figure 4.1a**) shows no such warm anomalies except for the perforation 11.6 where the perforation still shows the warm anomaly at the center of the perforation. The sudden temperature change at the center of the perforation seems to result from the fluid movement between the fracture and wellbore systems by fracture closure (cross-flow fracture to wellbore) (Ribeiro and Horne 2016) or by fluid moving into the fracture from the wellbore due to the decrease of fluid density in the well associated with steep temperature increase during warm-back. One of the other possibilities to explain the temperature signal is the frictional heating when the injected fluid moves through perforations because the perforation pressure drop can be several hundred psi with high rate injection. To clearly explain the deviations, further investigations are required.

In addition, the estimated fracture half-length is based on the assumptions of the shape of the transverse fracture at each perforation. In reality, the shape of the fracture is altered by the stress changes near the wellbore, and, if we use slickwater for the fracturing, the fracture shape becomes more complex. Therefore, the estimated fracture half-length is thought to be total representative fracture length with the assumption of the transverse fracture, and the fracture diagnostics should be integrated and justified with the other method such as micro-seismic mapping.

4.4 Quantitative Interpretation: Well EF-2

4.4.1 Descriptions of the Field Data

This section discusses quantitative interpretation of the downhole temperature data for flow profiling during production. The target well (EF-2) is located in Eagle Ford shale, and the well was investigated by Cui et al. (2015b) using the single phase gas model. Well EF-2 is a gas well, and the surface production rates of gas, water and oil are 1,700 MSCF/D, 60 STB/D and 125 STB/D, respectively, at the time of production logging. The downhole temperature was measured by production logging temperature tool. The obtained production logging data for the same well is analyzed by Liao et al. (2013). According to them, the bottom-hole pressure is higher than the dew point pressure, and, at the downhole condition, the gas-water condition is anticipated. The well is completed with a plug-and-perf completion for 15 stages. Each stage has 4 clusters, and the cluster spacing is around 75 ft. The well trajectory and perforation positions are shown in **Figure 4.6**.

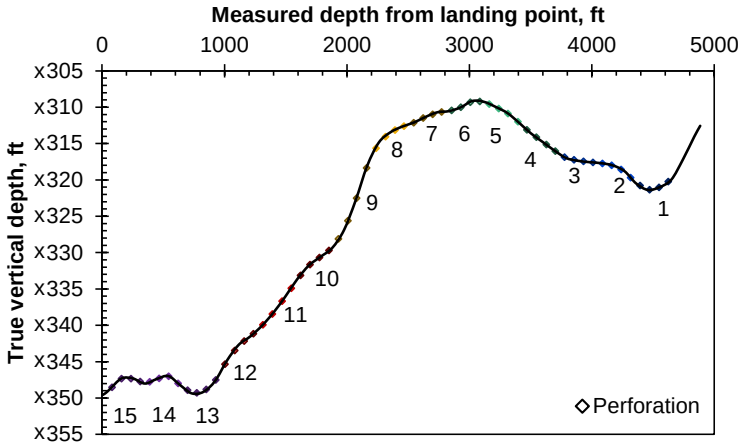

Figure 4.6—Well trajectory and perforation locations for Well EF-2

There are six sets of production logging data obtained by three up passes and three down passes, and the temperature data sets are plotted in **Figure 4.7**. In this work, we pick the first down pass data as the measurement data. During the production logging operation, the tool movement itself may smear the temperature measurement along the well. With use of the dataset of the first down pass data, we expect less smearing effects on the measurement. Cui et al. (2015b) also showed the geothermal temperature along the well, and the measured wellbore temperature near the toe is around 2-3 °F higher than the geothermal temperature in some of the dataset. They explained the higher temperature near the toe by the tool-traveling effect which generates heat near the toe, and they exclude the data in this region in their interpretation. In this work, we assume that the geothermal temperature itself has the uncertainty and we use the shifted temperature profile to match the geothermal temperature and the toe temperature measured by the production logging (**Figure 4.8**).

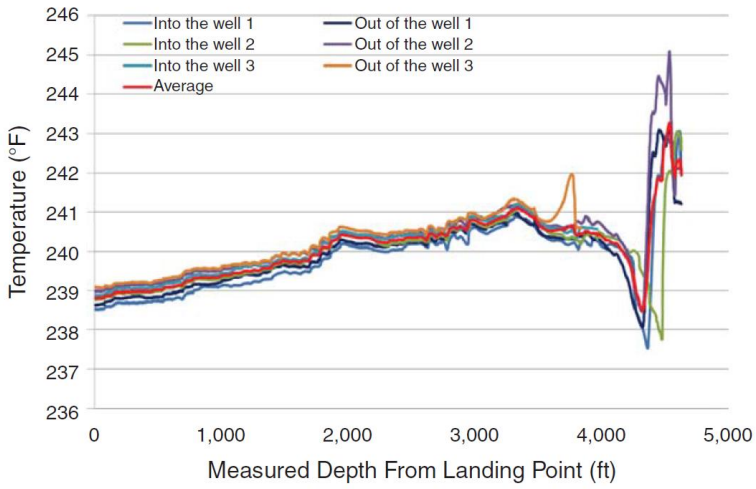

Figure 4.7—Temperature data set for Well EF-2 (from Cui et al. (2015b))

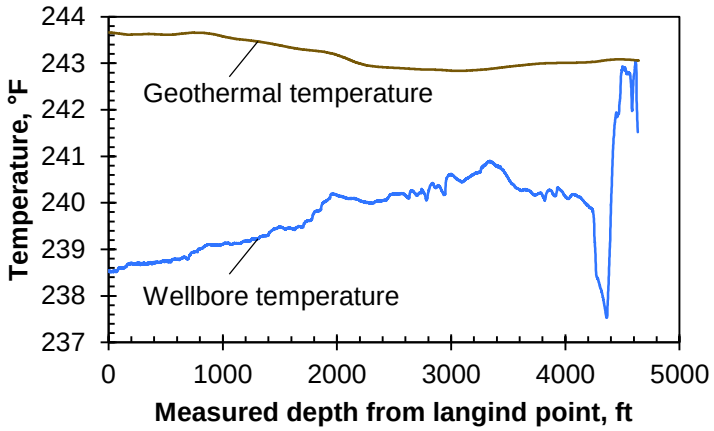

Figure 4.8—Wellbore and geothermal temperature profiles used in this work (Well EF-2)

4.4.2 Model Setup

The reservoir model is constructed in 2D domain and the wellbore is placed at the reservoir center. As discussed in one of the synthetic case studies, the high permeability fracture zones are sequentially assigned to the reservoir domain. **Figure 4.9** shows reservoir and wellbore geometries at the treatment of stage 4 and at the shut-in period after all of the

fracturing job is done. The reservoir is discretized into 794 × 49 × 1, and the reservoir cell which contains the wellbore is locally refined with 7 concentric cylinder grids.

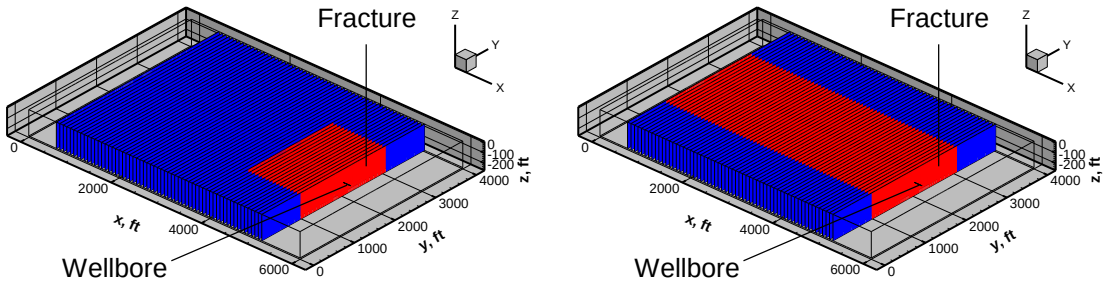

(a) Treatment period of the stage 4 (b) Shut-in period before production

Figure 4.9—Geometries of the field case (Well EF-2)

We assume the treatment design as follows: 2 hours injection and 7 hours shut-in for each stage and 60 bpm injection rate. After the treatment of the all of the stages, the well is shut-in for 30 days. Since we do not have any shut-in temperature data, the fractures are assumed to be created uniformly. **TABLE 4.3** summarizes input data for this case study. **Figure 4.10** shows the simulated DTS response during injection and early shut-in period. Because of the assumptions of the uniform created fractures and complete zonal isolations, the simulated DTS response shows the stair-step profile with uniform signals at all the created fractures. After the late shut-in period, profiles of pressure, temperature and saturation are obtained, and they are used as the initial condition at the onset of the production.

TABLE 4.3—INPUT DATA FOR QUANTITATIVE INTERPRETATION OF THE FIELD DATA (WELL EF-2)

Type	Property	Value
Reservoir	Reservoir size (*x*-dir) ft	6,000
	Reservoir size (*y*-dir) ft	4,000
	Net pay thickness, ft	200
	Matrix permeability, nD	583
	Matrix porosity, fraction	0.042
	Thermal conductivity (dry), Btu/(ft-hr-°F)	0.571
	Thermal conductivity (saturated), Btu/(ft-hr-°F)	0.924
	Rock specific heat, Btu/(lbm-°F)	0.202
	Rock density, lbm/ft^3	148.58
	Initial water saturation, fraction	0.1
	Initial pressure, psi	3560
	Initial temperature, °F	180.0
Fracture	Fracture width, in	0.24
	Fracture conductivity (injection), D-ft	10
	Fracture porosity, fraction	0.2
	Fracture height, ft	200
	Enhanced permeability (injection), mD	583×10^{-2}
Wellbore	Wellbore diameter, inch	8.75
	Casing OD, inch	5.5
	Pipe-relative roughness, –	0.001
	Cement thermal conductivity, Btu/(hr-ft-°F)	4.021
	Casing thermal conductivity, Btu/(hr-ft-°F)	6.993

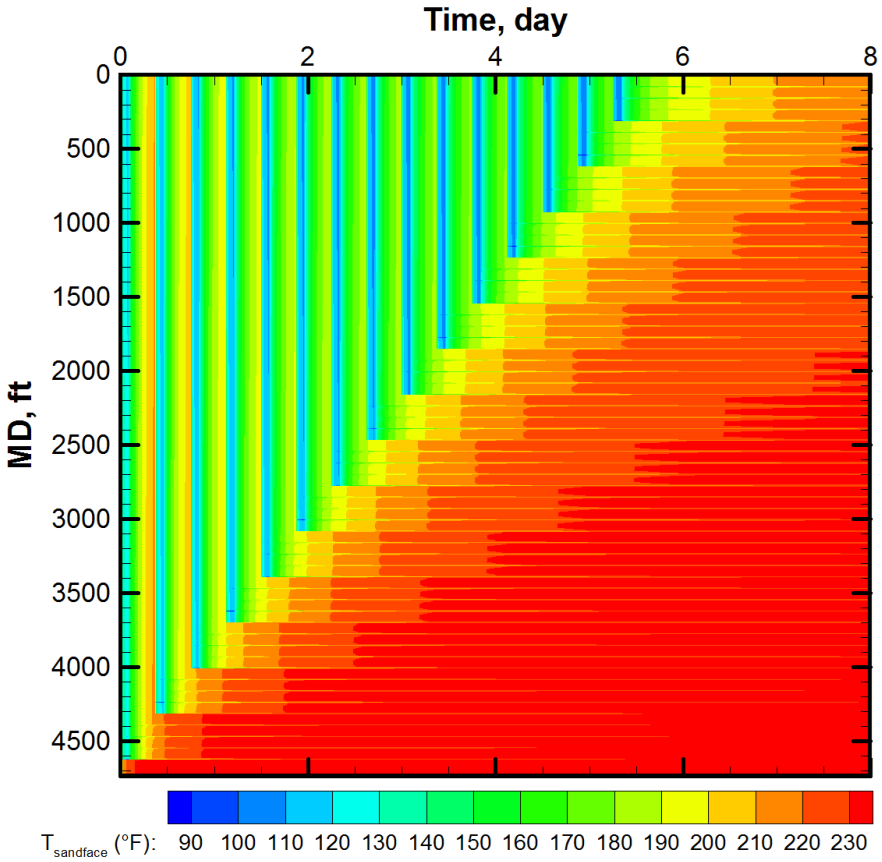

Figure 4.10—Simulated DTS response of the field case during injection and early shut-in with uniform created fractures (Well EF-2)

4.4.3 Results: Temperature Matching for the Quantitative Interpretation

With the obtained initial profiles at the onset of production, the temperature matching is performed by changing the propped fracture half-length and fracture conductivity. **Figure 4.11** shows results of the temperature matching. The simulated temperature profile is fairly well matched with the measured data. As noticed, the simulated temperature profile shows small temperature signals at all of the perforations. This is caused by the cooling effects of the injected fluid. Even if the fractures are assumed to be closed during shut-in period, the injected water is not heated up well, and it leads to the small cool anomalies.

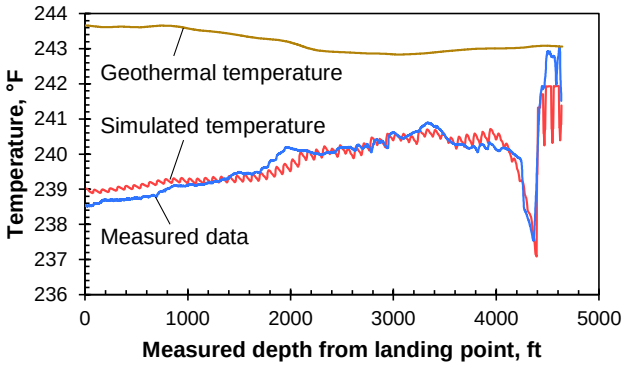

Figure 4.11—Measured wellbore temperature and simulated wellbore temperature at the time of production logging (30 days production)

Figure 4.12 compares the gas flow profiling given by this work and the other method (single phase gas temperature model and PLT interpretation by Cui et al. (2015b)). The results given by this work show consistent gas production with the other method except for the region near the toe. The overestimation of the gas flow near the toe comparing to the others results from the changed geothermal temperature profile.

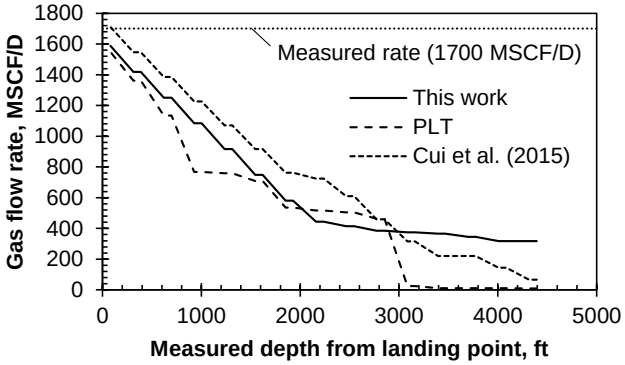

Figure 4.12—Comparison of gas flow profiles (Well EF-2)

Figure 4.13 shows improved temperature matching, and **Figure 4.14** compares gas flow profiles by the improved temperature matching. The simulated temperature profile is consistent with the measured temperature profile while deviations get larger near the heel region. Then, it leads to the difference of the gas flow profiles near the heel region in these improved temperature matching case as well.

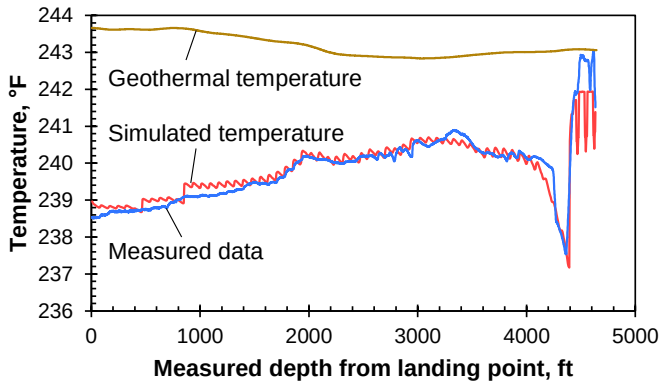

Figure 4.13—Improved temperature matching at the time of production logging (30 days production)

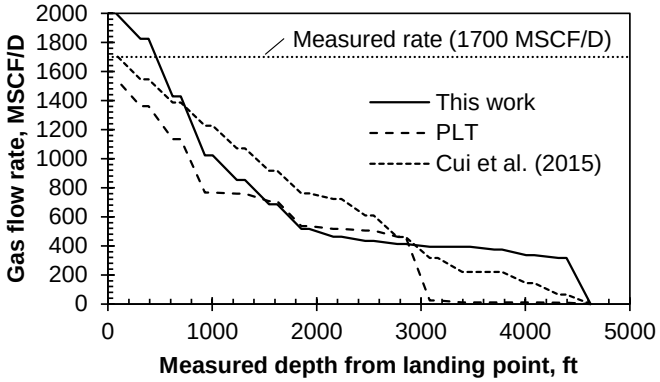

Figure 4.14—Comparison of gas flow profiles with improved temperature matching (Well EF-2)

4.4.4 Discussion

The simulated temperature profile in this study shows small cool anomalies even if the fracture is completely closed. The large amount of the water injected to the position based on the assumption of the uniform fracture is not heated up during shut-in period. As studied in the previous field case, if the created fracture size is quite small such as 5 ft penny-shaped fracture, the fracture temperature is easily heated up compared with the long created fractures. To obtain further improved matching results, the initial temperature profiles need to be modified.

In addition, this work overestimates the gas flow rate near the toe region because of the geothermal temperature. According to the completion design of the well, the stage 1 is located at the position where the trajectory is switched from downward direction to upward direction. At the location, water circulation may happen as shown by the negative velocity in the interpretation of the array spinner tool (Liao et al. 2013). The complex flow characteristics near the toe region provides more uncertainty of the measurement near the toe region. To obtain reliable estimation, accurate geothermal temperature is required.

In addition, this work only shows two matched cases, but, in reality, it seems to have multiple possible solutions. As discussed in the sensitivity study, the fracture half-length and fracture conductivity have opposite temperature sensitivity with respect to the inflow rate. In order to investigate the non-uniqueness of the solution, assisted history matching will be possible options. If we can estimate uncertainty of the estimation, it will be helpful in the evaluation of the completion effectiveness and flow performance evaluation.

CHAPTER V

CONCLUSIONS

In this study, comprehensive numerical flow and thermal models for a horizontal well with multiple fractures was presented. The models are formulated for the reservoir and wellbore domain using mass, momentum and energy conservation in transient conditions. The numerical model is developed with the integral finite difference method, and these models are coupled to obtain profiles of wellbore and sandface temperature as one of the solutions. With use of the mixed coordinate system, the sandface temperature is calculated directory in the reservoir model. The transient and coupled models enable us to simulate field operations in multistage fracturing treatments; injection and shut-in occur alternately for each stage from toe to heel with sufficient zonal isolation. Following the stimulation treatments, these models are used to simulate temperature behavior during production in gas-water two phase flow. The implemented models are verified against several simple cases which have analytical/semi-analytical solutions.

The developed model is applied for several synthetic cases. These case studies show capabilities of the developed model to simulate downhole temperature behavior during processes of injection, shut-in and production. A single fracture case shows injected fluid lowers temperature in the fracture below the geothermal temperature even after one month of shut-in. The further investigation was performed on the single fracture study, and it was concluded that the temperature profile at the onset of production is important for the fracture inflow temperature during production period. A synthetic case with five

fractures show capabilities of detection of fracture locations by shut-in temperature profile. The temperature profiles obtained during production show different characteristics of the wellbore temperature and sandface temperature due to fluid mixing in the wellbore.

The developed model was also applied to field cases. One of the field cases shows possibility to evaluate relative fracture length based on the shut-in temperature behavior, and the results are consistent with other measurements such as DAS qualitatively. We can estimate the short fractures with the shut-in temperature model, but we need to further investigate perforations which seem to take large amount of injected fluid. Their temperature profile shows warm anomalies at the center of perforations, but the implemented model could not capture the signal. The model was also applied for flow profiling of a field case. The estimated flow profile by this work is consistent with the interpretation by production logging measurements and the semi-analytical temperature model for single phase gas. These field cases show capabilities of the temperature interpretation to obtain further understanding of the downhole conditions in a horizontal well with multiple fractures.

NOMENCLATURE

A = cross-sectional area of a well segment, ft^2 [m^2]

A_r = surface area of a well segment, ft^2 [m^2]

C_0 = distribution parameter, dimensionless

C_p = specific heat, Btu/(lbm-°F) [J/(kg-°C)]

f_m = mixture friction factor on a wall of a well segment, dimensionless

$\mathbf{g}$ = acceleration vector of gravity, ft/D^2 [m/s^2]

$\mathbf{F}^{\kappa}$ = mass flux of component κ per unit area, lbm/(ft^2-D) [kg/(m^2-s)]

$\mathbf{F}^{\theta}$ = heat flux per unit area, Btu/(ft^2-D) [J/(m^2-s)]

H = specific enthalpy, Btu/lbm [J/kg]

h_l = heat transfer coefficient, Btu/(hr-ft^2-°F) [J/(s-m^2-°C)]

H_{β}^{κ} = specific enthalpy of mass component κ in phase β, Btu/lbm [J/kg]

H^g = Henry's coefficient, psi [Pa]

H_M = molar enthalpy, Btu/mol [J/mol]

j = volumetric flux of gas-liquid mixture in wellbore, ft/D [m/s]

j_{β} = superficial velocity (volumetric flux) of phase β in wellbore, ft/D [m/s]

k = intrinsic permeability, md [m^2]

k_{dry} = dry rock thermal conductivity, Btu-ft/(hr-ft^2-°F) [J-m/(s-m^2-°C)]

k_f = fluid thermal conductivity, Btu-ft/(hr-ft^2-°F) [J-m/(s-m^2-°C)]

k_{wet} = water-saturation rock thermal conductivity, Btu-ft/(hr-ft^2-°F) [J-m/(s-m^2-°C)]

$k_{r\beta}$ = relative permeability of phase β, dimensionless

k_{Tt} = total thermal conductivity, Btu-ft/(hr-ft^2-°F) [J-m/(s-m^2-°C)]

M^{κ} = mass accumulation of component κ per unit volume, lbm/ft^3 [kg/m^3]

M^{θ} = thermal accumulation per unit volume, Btu/ft^3 [J/m^3]

N_f = number of perforations, dimensionless

p = pressure, psia [Pa]

p_G^{κ} = partial pressure of component κ in gaseous phase, psia [Pa]

p_{sat}^{w} = water saturation pressure, psia [Pa]

q_{β} = mass flow rate of phase β per unit volume, lbm/(ft^3-D) [kg/(m^3-s)]

$\dot{q}_{\beta}$ = mass flow rate of phase β, lbm/D [kg/s]

q^{κ} = mass sink/source of component κ per unit volume, lbm/(ft^3-D) [kg/(m^3-s)]

q^{θ} = thermal sink/source per unit volume, Btu//(ft^3-D) [J/(m^3-s)]

q_{wb} = conductive heat transfer rate per unit volume, Btu/(ft^3-D) [J/(m^3-s)]

$\dot{q}_{wb}$ = conductive heat transfer rate, Btu/D [J/s]

r = radial direction in wellbore coordinate system , ft [m]

r_i = completion inner radius (radius for wellbore flow path), ft [m]

r_w = wellbore radius, ft [m]

R = gas constant per mole, Btu/(mol-R) [J/(mol-K)]

$\overline{S}$ = effective saturation, dimensionless

S_{β} = saturation of phase β, dimensionless

$S_{r\beta}$ = residual saturation of phase β, dimensionless

t = time, D [s]

T = temperature, °F [°C]

T_D = dimensionless temperature, dimensionless

t_D = dimensionless time, dimensionless

U = specific internal energy, Btu/lbm [J/kg]

U_T = overall heat transfer coefficient, Btu/(hr-ft^2-°F) [J/(s-m^2-°C)]

$\mathbf{v}$ = Darcy velocity (volumetric flux in reservoir), ft/D [m/s]

v_β = in-situ phase velocity of phase β, ft/D [m/s]

v_m = mean mixture velocity of center of mass, ft/D [m/s]

V_d = drift velocity of gas phase, ft/D [m/s]

V_M = molar volume, ft^3/mol [m^3/mol]

w = fracture width, ft [m]

x, X = x-directional coordinate, ft [m]

X_β^κ = mass fraction of component κ in phase β, dimensionless

y, Y = y-directional coordinate, ft [m]

Y_β^κ = mole fraction of component κ in phase β, dimensionless

z = axial direction in wellbore coordinate system, ft [m]

Z = compressibility factor, dimensionless

Greek

α = thermal diffusivity, ft^2/hr [m^2/s]

α_β = volume fraction of phase β, dimensionless

γ = pipe open ratio, dimensionless

Γ = perimeter of a well segment, ft [m]

θ = radial direction in wellbore coordinate system, radian

μ = viscosity, cP [Pa-s]

ρ = density, lbm/ft^3 [kg/m^3]

ϕ = porosity, dimensionless

φ = well inclination to horizontal line, radian

Superscripts and Subscripts

ann = annulus

β = phase

c = casing

cem = cement

eibh = initial earth bottom hole

f = fluid

fr = fracture

I = inflow property

i = inside

init = initial

inj = injection

IG = ideal gas

κ = component

l = liquid

mix = fluid mixture

r = rock

s = solid

t = tubing

REFERENCES

Adenekan, A.E., Patzek, T.W. and Pruess, K. 1993. Modeling of Multiphase Transport of Multicomponent Organic Contaminants and Heat in the Subsurface: Numerical Model Formulation. *Water Resources Research* **29** (11): 3727-3740. doi: 10.1029/93WR01957.

Al-Hussainy, R., Ramey, H.J. and Crawford, P. B. 1966. The Flow of Real Gases through Porous Media. *Journal of Petroleum Technology* **18** (5): 624-636. SPE-1243-A-PA. doi: 10.2118/1243-A-PA.

App, J. 2013. Influence of Hydraulic Fractures on Wellbore/Sandface Temperatures During Production. Presented at the SPE Annual Technical Conference and Exhibition, New Orleans, Louisiana, USA, 30 September-2 October. SPE-166298-MS. doi: 10.2118/166298-MS.

App, J. and Yoshioka, K. 2013. Impact of Reservoir Permeability on Flowing Sandface Temperatures: Dimensionless Analysis. *SPE Journal* **18** (4): 685-694. SPE-146951-PA. doi: 10.2118/146951-PA.

App, J. 2015. Influence of Flow Geometry on Sandface Temperatures During Single-Phase Oil Production: Dimensionless Analysis. *SPE Journal* Preprint. SPE-166298-PA. doi: 10.2118/166298-PA.

Aziz, K., Arababi, S. and Hewett, T.A. 1997. Productivity and Injectivity of Horizontal Wells. Technical Report DOE Contract No. FG22-93BC14862, Federal Energy Technology Center, Morgantown, West Virginia, and Pittsburgh, Pennsylvania (29 April 1997). doi: 10.2172/2157.

Bahonar, M., Azaiez, J. and Chen, Z. 2011. Transient Nonisothermal Fully Coupled Wellbore/Reservoir Model for Gas-Well Testing, Part 1: Modelling. *Journal of Canadian Petroleum Technology* **50** (9): 37-50. SPE-149617-PA. doi: 10.2118/149617-PA.

Bazan, L.W., Larkin, S.D., Lattibeaudiere, M.G. and Palisch, T.T. 2010. Improving Production in the Eagle Ford Shale with Fracture Modeling, Increased Conductivity and Optimized Stage and Cluster Spacing along the Horizontal Wellbore. Presented at the Tight Gas Completions Conference, San Antonio, Texas, USA, 2-3 November. SPE-138425-MS. doi: 10.2118/138425-MS.

Biot, M.A., Masse, L. and Medlin, W.L. 1987. Temperature Analysis in Hydraulic Fracturing. *Journal of Petroleum Technology* **39** (11): 1389-1397. SPE-13228-PA. doi: 10.2118/13228-PA.

Bird, R.B., Stewart, W.E. and Lightfoot, E.N. 2002. *Transport Phenomena*, John Wiley & Sons, Inc., New York. (Reprint).

Blasingame, T.A. 1993. Development and Application of Analytical Solutions for Fractured and Unfractured Wells in a Bounded Circular Reservoir - Constant Flow Rate Case. Presented at the SPE Production Operations Symposium, Oklahoma City, Oklahoma, USA, 21-23 March. SPE-25479.

Brennen, C.E. 2005. *Fundamentals of Multiphase Flow*, Cambridge University Press, Cambridge, UK.

Brown, G.A., Kennedy, B. and Meling, T. 2000. Using Fibre-Optic Distributed Temperature Measurements to Provide Real-Time Reservoir Surveillance Data on Wytch Farm Field Horizontal Extended-Reach Wells. Presented at the SPE Annual Technical Conference and Exhibition, Dallas, Texas, USA, 1-4 October. SPE-62952-MS. doi: 10.2118/62952-MS.

Carey, M.A., Mondal, S. and Sharma, M.M. 2015. Analysis of Water Hammer Signatures for Fracture Diagnostics. Presented at the SPE Annual Technical Conference and Exhibition, Houston, Texas, USA, 28-30 September. SPE-174866-MS. doi: 10.2118/174866-MS.

Carnahan, B.D., Clanton, R.W., Koehler, K.D., Harkins, G.O. and Williams, G.R. 1999. Fiber Optic Temperature Monitoring Technology. Presented at the SPE Western Regional Meeting, Anchorage, Alaska, USA, 26-27 May. SPE-54599-MS. doi: 10.2118/54599-MS.

Carslaw, H.S. and Jaeger, J.C. 1959. *Conduction of Heat in Solids*, Clarendon Press, Oxford, UK.

Chen, C.-Y. and Horne, R.N. 2006. Two-Phase Flow in Rough-walled Fractures: Experiments and a Flow Structure Model. *Water Resources Research* **42** (3). doi: 10.1029/2004WR003837.

Chen, C.-Y., Horne, R.N. and Fourar, M. 2004. Experimental Study of Liquid-Gas Flow Structure Effects on Relative Permeabilities in a Fracture. *Water Resources Research* **40** (8). doi: 10.1029/2004WR003026.

Chen, N.H. 1979. An Explicit Equation for Friction Factor in Pipe. *Industrial & Engineering Chemistry Fundamentals* **18** (3): 296-297. doi: 10.1021/i160071a019.

Cheshire, I.M. and Henriquez, A. 1992. Local Grid Refinement. In *The Mathematics of Oil Recovery*, ed. P. R. King, 337-357. Oxford University Press, New York, USA.

Choi, J., Pereyra, E., Sarica, C., Park, C. and Kang, J. 2012. An Efficient Drift-Flux Closure Relationship to Estimate Liquid Holdups of Gas-Liquid Two-Phase Flow in Pipes. *Energies* **5** (12): 5294-5306. doi: 10.3390/en5125294.

Class, H., Helmig, R. and Bastian, P. 2002. Numerical Simulation of Non-Isothermal Multiphase Multicomponent Processes in Porous Media.: 1. An efficient Solution Technique. *Advances in Water Resources* **25** (5): 533-550. doi: 10.1016/S0309-1708(02)00014-3.

Coats, K.H. 1977. Geothermal Reservoir Modelling. Presented at the SPE Annual Fall Technical Conference and Exhibition, Denver, Colorado, USA, 9-12 October. SPE-6892-MS. doi: 10.2118/6892-MS.

Corey, A.T. 1954. The Interrelation Between Gas and Oil Relative Permeabilities. *Producers Monthly* **19** (November): 38-41.

Cui, J., Yang, C., Zhu, D. and Datta-Gupta, A. 2015a. Fracture Diagnosis in Multiple Stage Stimulated Horizontal Well by Temperature Measurements Using Fast Marching Method. Presented at the SPE Annual Technical Conference and Exhibition, Houston, Texas, USA, 28-30 September. SPE-174880-MS. doi: 10.2118/174880-MS.

Cui, J., Zhu, D. and Jin, M. 2014. Diagnosis of Multi-Stage Fracture Stimulation in Horizontal Wells by Downhole Temperature Measurements. Presented at the SPE Annual Technical Conference and Exhibition, Amsterdam, The Netherlands, 27-29 October. SPE-170874-MS. doi: 10.2118/170874-MS.

Cui, J., Zhu, D. and Jin, M. 2015b. Diagnosis of Production Performance after Multistage Fracture Stimulation in Horizontal Wells by Downhole Temperature Measurements. *SPE Production & Operations* Preprint. SPE-170874-PA. doi: 10.2118/170874-PA.

Dake, L.P. 1978. *Fundamentals of Reservoir Engineering*, Elsevier Science BV, Amsterdam.

Davis, E.R., Zhu, D. and Hill, A.D. 1997. Interpretation of Fracture Height from Temperature Logs - The Effect of Wellbore/Fracture Separation. *SPE Formation Evaluation* **12** (02): 119-124. SPE-29588-PA. doi: 10.2118/29588-PA.

Dawkrajai, P., Lake, L.W., Yoshioka, K., Zhu, D. and Hill, A.D. 2006. Detection of Water or Gas Entries in Horizontal Wells from Temperature Profiles. Presented at the SPE/DOE Symposium on Improved Oil Recovery, Tulsa, Oklahoma, USA, 22-26 April. SPE-100050-MS. doi: 10.2118/100050-MS.

Dawkrajai, P., Romero, A.A., Yoshioka, K., Zhu, D., Hill, A.D. and Lake, L.W. 2004. A Comprehensive Statiscally-Based Method to Interpret Real-time Flowing Measurements. Technical Report DOE Contract No. FC26-03NT15402, The University Of Texas At Austin, Austin, Texas (05 January 2007). doi: 10.2172/902505.

Duru, O.O. and Horne, R.N. 2010. Modeling Reservoir Temperature Transients and Reservoir-Parameter Estimation Constrained to the Model. *SPE Reservoir Evaluation & Engineering* **13** (6): 873-883. SPE-115791-PA. doi: 10.2118/115791-PA.

Economides, M.J., Hill, A.D., Ehlig-Economides, C. and Zhu, D. 2012. *Petroleum Production Systems*, 2nd edition, Prentice Hall, Upper Saddle River, New Jersey.

Ehlig-Economides, C.A. 1979. Well Analysis for Wells Produced at a Constant Pressure. PhD Dissertation, Stanford University, Stanford, California (June 1979).

Eppelbaum, L.V., Kutasov, I.M. and Pilchin, A. 2014. *Applied Geothermics*, Springer, Berlin, Heidelberg. 10.1007/978-3-642-34023-9.

Everdingen, A.F.V. and Hurst, W. 1949. The Application of the Laplace Transformation to Flow Problems in Reservoirs. *Journal of Petroleum Technology* **1** (12): 305-324. SPE-949305-G. doi: 10.2118/949305-G.

Faust, C.R. and Mercer, J.W. 1976. An Analysis of Finite-Difference and Finite-Element Techniques for Geothermal Reservoir Simulation. Presented at the SPE Symposium on Numerical Simulation of Reservoir Performance, Los Angeles, California, 19-20 February. SPE-5742-MS. doi: 10.2118/5742-MS.

Faust, C.R., Mercer, J.W. and Miller, W.J. 1980. Geothermal Reservoir Engineering Computer Code Comparison and Validation. Technical Report DOE Contract No. AC03-80SF11452, GeoTrans, Inc., Reston, Virginia (12 November 1980). doi: 10.2172/6726252.

Fernández-Prini, R., Alvarez, J.L. and Harvey, A.H. 2003. Henry's Constants and Vapor–Liquid Distribution Constants for Gaseous Solutes in H2O and D2O at High Temperatures. *Journal of Physical and Chemical Reference Data* **32** (2): 903-916. doi: 10.1063/1.1564818.

Fisher, M.K., Heinze, J.R., Harris, C.D., Davidson, B.M., Wright, C.A. and Dunn, K.P. 2004. Optimizing Horizontal Completion Techniques in the Barnett Shale Using Microseismic Fracture Mapping. Presented at the SPE Annual Technical Conference and Exhibition, Houston, Texas, USA, 26-29 September. SPE-90051-MS. doi: 10.2118/90051-MS.

Fisher, M.K., Wright, C.A., Davidson, B.M., Steinsberger, N.P., Buckler, W.S., Goodwin, A. and Fielder, E.O. 2005a. Integrating Fracture-Mapping Technologies to Improve Stimulations in the Barnett Shale. *SPE Production & Operations* **20** (2): 85-93. SPE-77441-PA. doi: 10.2118/77441-PA.

Fisher, M.K., Wright, C.A., Davidson, B.M., Steinsberger, N.P., Buckler, W.S., Goodwin, A. and Fielder, E.O. 2005b. Integrating Fracture Mapping Technologies To Improve Stimulations in the Barnett Shale. *SPE Production & Facilities* **20** (2): 85-93. SPE-77441-PA. doi: 10.2118/77441-PA.

França, F. and Lahey Jr, R.T. 1992. The Use of Drift-Flux Techniques for the Analysis of Horizontal Two-Phase Flows. *International Journal of Multiphase Flow* **18** (6): 787-801. doi: 10.1016/0301-9322(92)90059-P.

Fryer, V.I., Dong, S., Otsubo, Y., Brown, G.A. and Guilfoyle, P. 2005. Monitoring of Real-Time Temperature Profiles Across Multizone Reservoirs During Production and Shut in Periods Using Permanent Fiber-Optic Distributed Temperature Systems. Presented at the SPE Asia Pacific Oil and Gas Conference and Exhibition, Jakarta, Indonesia, 5-7 April. SPE-92962-MS. doi: 10.2118/92962-MS.

Furui, K., Zhu, D. and Hill, A.D. 2003. A Rigorous Formation Damage Skin Factor and Reservoir Inflow Model for a Horizontal Well (Includes Associated Papers 88817 and 88818). *SPE Production & Operations* **18** (3): 151-157. SPE-84964-PA. doi: 10.2118/84964-PA.

Gildin, E., Valko, P. and Fuentes-Cruz, G. 2013. Analyzing Production Data from Hydraulically Fractured Wells: the Concept of Induced Permeability Field. Presented at the SPE Hydraulic Fracturing Technology Conference, The Woodlands, Texas, USA, 4-6, February. SPE-163843-MS. doi: 10.2118/163843-MS.

Glasbergen, G., Gualtieri, D., Domelen, M.S.V. and Sierra, J. 2009. Real-Time Fluid Distribution Determination in Matrix Treatments Using DTS. *SPE Production & Operations* **24** (1): 135-146. SPE-107775-PA. doi: 10.2118/107775-PA.

Han, J.-C. 2012. *Analytical Heat Transfer*, CRC Press, Boca Raton, Florida.

Hannah, R.R., Harrington, L.J. and Anderson, R.W. 1977. Stimulation Design Applications of a Technique to Locate Successive Fluid Segments in Fractures. Presented at the SPE Annual Fall Technical Conference and Exhibition, Denver, Colorado, USA, 9-12 October. SPE-6815-MS. doi: 10.2118/6815-MS.

Harrington, L.J., Hannah, R.R. and Robert, B. 1978. Post Fracturing Temperature Recovery and Its Implication for Stimulation Design. Presented at the SPE Annual Fall Technical Conference and Exhibition, Houston, Texas, USA, 1-3 October. SPE-7560-MS. doi: 10.2118/7560-MS.

Hasan, A.R. and Kabir, C.S. 1991. Heat Transfer During Two-Phase Flow in Wellbores; Part I--Formation Temperature. Presented at the SPE Annual Technical Conference and Exhibition, Dallas, Texas, USA, 6-9 October. SPE-22866-MS. doi: 10.2118/22866-MS.

Hasan, A.R. and Kabir, C.S. 1994. Aspects of Wellbore Heat Transfer During Two-Phase Flow (Includes Associated Papers 30226 and 30970). *SPE Production & Operations* **9** (3): 211-216. SPE-22948-PA. doi: 10.2118/22948-PA.

Hasan, A.R. and Kabir, C.S. 2002. *Fluid Flow and Heat Transfer in Wellbores*, Society of Petroleum Engineers, Richardson, Texas.

Hasan, A.R., Kabir, C.S. and Sayarpour, M. 2007. A Basic Approach to Wellbore Two-Phase Flow Modeling. Presented at the SPE Annual Technical Conference and Exhibition, Anaheim, California, USA, 11-14 November. SPE-109868-MS. doi: 10.2118/109868-MS.

Hasan, A.R., Kabir, C.S. and Wang, X. 1997. Development and Application of a Wellbore/Reservoir Simulator for Testing Oil Wells. *SPE Formation Evaluation* **12** (3): 182-188. SPE-29892-PA. doi: 10.2118/29892-PA.

Hibiki, T. and Ishii, M. 2003. One-Dimensional Drift-Flux Model and Constitutive Equations for Relative Motion Between Phases in Various Two-Phase Flow Regimes. *International Journal of Heat and Mass Transfer* **46** (25): 4935-4948. doi: 10.1016/S0017-9310(03)00322-3.

Hill, A.D. 1990. *Production Logging: Theoretical and Interpretive Elements*, Henry L. Doherty Memorial Fund of AIME, Society of Petroleum Engineers, Richardson, Texas.

Hoang, H.N., Mahadevan, J. and Lopez, H. 2012. Injection Profiling During Limited-Entry Fracturing Using Distributed-Temperature-Sensor Data. *SPE Journal* **17** (3): 752-767. SPE-140442-PA. doi: 10.2118/140442-PA.

Holley, E.H., Molenaar, M.M., Fidan, E. and Banack, B. 2013. Interpreting Uncemented Multistage Hydraulic-Fracturing Completion Effectiveness by Use of Fiber-Optic DTS Injection Data. *SPE Drilling & Completion* **28** (3): 243-253. SPE-153131-PA. doi: 10.2118/153131-PA.

Huber, M.L., Perkins, R.A., Friend, D.G., Sengers, J.V., Assael, M.J., Metaxa, I.N., Miyagawa, K., Hellmann, R. and Vogel, E. 2012. New International Formulation for the Thermal Conductivity of H2O. *Journal of Physical and Chemical Reference Data* **41** (3): 033102-1:23. doi: 10.1063/1.4738955.

Huber, M.L., Perkins, R.A., Laesecke, A. et al. 2009. New International Formulation for the Viscosity of H2O. *Journal of Physical and Chemical Reference Data* **38** (2): 101-125. doi: 10.1063/1.3088050.

Huckabee, P.T. 2009. Optic Fiber Distributed Temperature for Fracture Stimulation Diagnostics and Well Performance Evaluation. Presented at the SPE Hydraulic Fracturing Technology Conference, The Woodlands, Texas, USA, 19-21 January. SPE-118831-MS. doi: 10.2118/118831-MS.

Huebsch, H.T., Moss, M., Trilsbeck, T.C., Brown, G.A., Rogers, S.J. and Bouchard, T. 2008. Monitoring Inflow Distribution in Multi-Zone, Velocity String Gas Wells Using Slickline Deployed Fiber Optic Distributed Temperature Measurements. Presented at the SPE Annual Technical Conference and Exhibition, Denver, Colorado, USA, 21-24 September. SPE-115816-MS. doi: 10.2118/115816-MS.

Ishii, M. 1977. One-Dimensional Drift-Flux Model and Constitutive Equations for Relative Motion Between Phases in Various Two-Phase Flow Regimes. Technical Report ANL-77-47, DOE Contract No. W-31-109-ENG-38, Argonne National Laboratory, Argonne, Illinois (01 October 1977). doi: 10.2172/6871478.

Ishii, M. and Hibiki, T. 2011. *Thermo-Fluid Dynamics of Two-Phase Flow*, Springer, New York.

Izgec, B., Kabir, C.S., Zhu, D. and Hasan, A.R. 2007. Transient Fluid and Heat Flow Modeling in Coupled Wellbore/Reservoir Systems. *SPE Reservoir Evaluation & Engineering* **10** (3): 294-301. SPE-102070-PA. doi: 10.2118/102070-PA.

Johnson, D.O., Sierra, J.R., Kaura, J.D. and Gualtieri, D. 2006. Successful Flow Profiling of Gas Wells Using Distributed Temperature Sensing Data. Presented at the SPE Annual Technical Conference and Exhibition, San Antonio, Texas, USA, 24-27 September. SPE-103097-MS. doi: 10.2118/103097-MS.

Kabir, C.S., Hasan, A.R., Jordan, D.L. and Wang, X. 1996. A Wellbore/Reservoir Simulator for Testing Gas Wells in High-Temperature Reservoirs. *SPE Formation Evaluation* **11** (2): 128-134. SPE-28402-PA. doi: 10.2118/28402-PA.

Kamphuis, H., Davies, D.R. and Roodhart, L.P. 1993. A New Simulator For the Calculation of the In-Situ Temperature Profile During Well Stimulation Fracturing Treatments. *Journal of Canadian Petroleum Technology* **32** (5): 38-47. PETSOC-93-05-03. doi: 10.2118/93-05-03.

Kinney, R.B. 1968. Fully Developed Frictional and Heat-Transfer Characteristics of Laminar Flow in Porous Tubes. *International Journal of Heat and Mass Transfer* **11** (9): 1393-1401. doi: 10.1016/0017-9310(68)90184-1.

Kragas, T.K., Williams, B.A. and Myers, G.A. 2001. The Optic Oil Field: Deployment and Application of Permanent In-Well Fiber Optic Sensing Systems for Production and Reservoir Monitoring. Presented at the SPE Annual Technical Conference and Exhibition, New Orleans, Louisiana, USA, 30 September-3 October. SPE-71529-MS. doi: 10.2118/71529-MS.

Lake, L.W. 2010. *Enhanced Oil Recovery*, Society of Petroleum Engineers, Richardson, Texas. (Reprint).

Li, L. and Lee, S.H. 2008. Efficient Field-Scale Simulation of Black Oil in a Naturally Fractured Reservoir through Discrete Fracture Networks and Homogenized Media. *SPE Reservoir Evaluation & Engineering* **11** (4): 750-758. SPE-103901-PA. doi: 10.2118/103901-PA.

Li, Z. and Zhu, D. 2010. Predicting Flow Profile of Horizontal Well by Downhole Pressure and Distributed-Temperature Data for Waterdrive Reservoir. *SPE Production & Operations* **25** (3): 296-304. SPE-124873-PA. doi: 10.2118/124873-PA.

Liao, L., Zhu, D., Yoshida, N., Hill, A.D. and Jin, M. 2013. Interpretation of Array Production Logging Measurements in Horizontal Wells for Flow Profile. Presented at the SPE Annual Technical Conference and Exhibition, New Orleans, Louisiana, USA, 30 September- 2 October. SPE-166502-MS. doi: 10.2118/166502-MS.

Livescu, S., Durlofsky, L. and Aziz, K. 2010a. A Semianalytical Thermal Multiphase Wellbore-Flow Model for Use in Reservoir Simulation. *SPE Journal* **15** (3): 794-804. SPE-115796-PA. doi: 10.2118/115796-PA.

Livescu, S., Durlofsky, L.J., Aziz, K. and Ginestra, J.C. 2010b. A Fully-Coupled Thermal Multiphase Wellbore Flow Model for Use in Reservoir Simulation. *Journal of Petroleum Science and Engineering* **71** (3–4): 138-146. doi: 10.1016/j.petrol.2009.11.022.

Marquardt, D. 1963. An Algorithm for Least-Squares Estimation of Nonlinear Parameters. *Journal of the Society for Industrial and Applied Mathematics* **11** (2): 431-441. doi: 10.1137/0111030.

Mayerhofer, M.J., Lolon, E.P., Youngblood, J.E. and Heinze, J.R. 2006. Integration of Microseismic Fracture Mapping Results with Numerical Fracture Network Production Modeling in the Barnett Shale. Presented at the SPE Annual Technical Conference and Exhibition, San Antonio, Texas, USA, 24-27 September. SPE-102103-MS. doi: 10.2118/102103-MS.

Mayerhofer, M.J., Stegent, N.A., Barth, J.O. and Ryan, K.M. 2011. Integrating Fracture Diagnostics and Engineering Data in the Marcellus Shale. Presented at the SPE Annual Technical Conference and Exhibition, Denver, Colorado, USA, 30 October-2 November. SPE-145463-MS. doi: 10.2118/145463-MS.

McClure, M.W., Jung, H., Cramer, D.D. and Sharma, M.M. 2016. The Fracture-Compliance Method for Picking Closure Pressure from Diagnostic Fracture-Injection Tests. *SPE Journal* Preprint. SPE-179725-PA. doi: 10.2118/179725-PA.

Medeiros, F., Ozkan, E. and Kazemi, H. 2008. Productivity and Drainage Area of Fractured Horizontal Wells in Tight Gas Reservoirs. *SPE Reservoir Evaluation & Engineering* **11** (5): 902-911. SPE-108110-PA. doi: 10.2118/108110-PA.

Meyer, B.R. 1989. Heat Transfer in Hydraulic Fracturing. *SPE Production Engineering* **4** (4): 423-429. SPE-17041-PA. doi: 10.2118/17041-PA.

Moinfar, A., Varavei, A., Sepehrnoori, K. and Johns, R.T. 2014. Development of an Efficient Embedded Discrete Fracture Model for 3D Compositional Reservoir Simulation in Fractured Reservoirs. *SPE Journal* **19** (2): 289-303. SPE-154246-PA. doi: 10.2118/154246-PA.

Moridis, G.J., Blasingame, T.A. and Freeman, C.M. 2010. Analysis of Mechanisms of Flow in Fractured Tight-Gas and Shale-Gas Reservoirs. Presented at the SPE Latin American and Caribbean Petroleum Engineering Conference, Lima, Peru, 1-3 December. SPE-139250-MS. doi: 10.2118/139250-MS.

Mukherjee, H. and Economides, M.J. 1991. A Parametric Comparison of Horizontal and Vertical Well Performance. *SPE Formation Evaluation* **6** (2): 209-216. SPE-18303-PA. doi: 10.2118/18303-PA.

Narasimhan, T.N. and Witherspoon, P.A. 1976. An Integrated Finite Difference Method for Analyzing Fluid Flow in Porous Media. *Water Resources Research* **12** (1): 57-64. doi: 10.1029/WR012i001p00057.

Oddie, G., Shi, H., Durlofsky, L.J., Aziz, K., Pfeffer, B. and Holmes, J.A. 2003. Experimental Study of Two and Three Phase Flows in Large Diameter Inclined Pipes. *International Journal of Multiphase Flow* **29** (4): 527-558. doi: 10.1016/S0301-9322(03)00015-6.

Ouyang, L.-B., Arbabi, S. and Aziz, K. 1998. General Wellbore Flow Model for Horizontal, Vertical, and Slanted Well Completions. *SPE Journal* **3** (2): 124-133. SPE-36608-PA. doi: 10.2118/36608-PA.

Özisik, M.N. 1977. *Basic Heat Transfer*, McGraw-Hill, New York.

Pan, L., Oldenburg, C.M., Wu, Y.S. and Pruess, K. 2011a. T2Well/ECO2N Version 1.0: Multiphase and Non-Isothermal Model for Coupled Wellbore-Reservoir Flow of Carbon Dioxide and Variable Salinity Water. Technical Report LBNL-4191E, DOE Contract No. AC02-05CH11231, Lawrence Berkeley National Laboratory, Berkeley, California (14 February 2011). doi: 10.2172/1007233.

Pan, L., Webb, S.W. and Oldenburg, C.M. 2011d. Analytical Solution for Two-Phase Flow in a Wellbore Using the Drift-Flux Model. *Advances in Water Resources* **34** (12): 1656-1665. doi: 10.1016/j.advwatres.2011.08.009.

Peaceman, D.W. 1978. Interpretation of Well-Block Pressures in Numerical Reservoir Simulation (Includes Associated Paper 6988). *Society of Petroleum Engineers Journal* **18** (3): 183-194. SPE-6893-PA. doi: 10.2118/6893-PA.

Peaceman, D.W. 1983. Interpretation of Well-Block Pressures in Numerical Reservoir Simulation with Nonsquare Grid Blocks and Anisotropic Permeability. *Society of Petroleum Engineers Journal* **23** (3): 531-543. SPE-10528-PA. doi: 10.2118/10528-PA.

Pedrosa Jr., O.A. and Aziz, K. 1986. Use of a Hybrid Grid in Reservoir Simulation. *SPE Reservoir Engineering* **1** (6): 611-621. SPE-13507-PA. doi: 10.2118/13507-PA.

Peng, D.-Y. and Robinson, D.B. 1976. A New Two-Constant Equation of State. *Industrial and Engineering Chemistry: Fundamentals* **15** (1): 59-64. doi: 10.1021/i160057a011.

Poling, B.E., Prausnitz, J.M. and O'Connell, J.P. 2000. *The Properties of Liquids and Gases*, 5th Edition edition, McGraw-Hill, New York.

Pope, C.D., Palisch, T. and Saldungaray, P. 2012. Improving Completion and Stimulation Effectiveness in Unconventional Reservoirs- Field Results in the Eagle Ford Shale of North America. Presented at the SPE/EAGE European Unconventional Resources Conference and Exhibition, Vienna, Austria, 20-22 March. SPE-152839-MS. doi: 10.2118/152839-MS.

Prats, M. 1969. The Heat Efficiency of Thermal Recovery Processes. *Journal of Petroleum Technology* **21** (3): 323-332. SPE-2211-PA. doi: 10.2118/2211-PA.

Prats, M. 1992. The Heat Efficiency of Thermal Recovery Processes Resulting from Non-Uniform Vertical Temperature Profiles. Presented at the SPE Latin America Petroleum Engineering Conference, Caracas, Venezuela, 8-11 March. SPE-23744-MS. doi: 10.2118/23744-MS.

Prosperetti, A.T.G. 2007. *Computational Methods for Multiphase Flow*, Cambridge University Press, Cambridge.

Pruess, K., Oldenburg, C. and Moridis, G. 1999. *TOUGH2 User's Guide*, Version 2.0. Lawrence Berkeley National Laboratory, Berkeley, California.

Ramey, H.J. 1962. Wellbore Heat Transmission. *Journal of Petroleum Technology* **14** (4): 427-435. SPE-96-PA. doi: 10.2118/96-PA.

Ribeiro, P.M. and Horne, R.N. 2013. Pressure and Temperature Transient Analysis: Hydraulic Fractured Well Application. Presented at the SPE Annual Technical Conference and Exhibition, New Orleans, Louisiana, USA, 30 September-2 October. SPE-166222-MS. doi: 10.2118/166222-MS.

Ribeiro, P.M. and Horne, R.N. 2014. Detecting Fracture Growth Out of Zone Using Temperature Analysis. Presented at the SPE Annual Technical Conference and Exhibition, Amsterdam, The Netherlands, 27-29 October. SPE-170746-MS. doi: 10.2118/170746-MS.

Ribeiro, P.M. and Horne, R.N. 2016. Detecting Fracture Growth Out of Zone by Use of Temperature Analysis. *SPE Journal* Preprint. SPE-170746-PA. doi: 10.2118/170746-PA.

Richter, H.J. 1981. Flooding in Tubes and Annuli. *International Journal of Multiphase Flow* **7** (6): 647-658. doi: 10.1016/0301-9322(81)90036-7.

Sandler, S.I. 2006. *Chemical, Biochemical, and Engineering Thermodynamics*, 4th Edition, John Wiley, Hoboken, New Jersey.

Schlesinger, S., Crosbie, R.E., Gagné, R.E., Innis, G.S., Lalwani, C.S., Loch, J., Sylvester, R.J., Wright, R.D., Kheir, N. and Bartos, D. 1979. Terminology for Model Credibility. *Simulation* **32** (3): 103-104. doi: 10.1177/003754977903200304.

Schön, J. 1996. *Physical Properties of Rocks : Fundamentals and Principles of Petrophysics*, Vol. 18, Pergamon, Oxford, UK; Tarrytown, New York, USA.

Seth, G., Reynolds, A.C. and Mahadevan, J. 2010. Numerical Model for Interpretation of Distributed-Temperature-Sensor Data During Hydraulic Fracturing. Presented at the SPE Annual Technical Conference and Exhibition, Florence, Italy, 19-22 September. SPE-135603-MS. doi: 10.2118/135603-MS.

Shi, H., Holmes, J., Diaz, L., Durlofsky, L.J. and Aziz, K. 2005a. Drift-Flux Parameters for Three-Phase Steady-State Flow in Wellbores. *SPE Journal* **10** (2): 130-137. SPE-89836-PA. doi: 10.2118/89836-PA.

Shi, H., Holmes, J.A., Durlofsky, L.J., Aziz, K., Diaz, L., Alkaya, B. and Oddie, G. 2005b. Drift-Flux Modeling of Two-Phase Flow in Wellbores. *SPE Journal* **10** (1): 24-33. SPE-84228-PA. doi: 10.2118/84228-PA.

Shirdel, M. and Sepehrnoori, K. 2012. Development of a Transient Mechanistic Two-Phase Flow Model for Wellbores. *SPE Journal* **17** (3): 942-955. SPE-142224-PA. doi: 10.2118/142224-PA.

Sierra, J.R., Kaura, J.D., Gualtieri, D., Glasbergen, G., Sarkar, D. and Johnson, D. 2008. DTS Monitoring Data of Hydraulic Fracturing: Experiences and Lessons Learned. Presented at the SPE Annual Technical Conference and Exhibition, Denver, Colorado, USA, 21-24 September. SPE-116182-MS. doi: 10.2118/116182-MS.

Somerton, W.H., El-Shaarani, A.H. and Mobarak, S.M. 1974. High Temperature Behavior of Rocks Associated with Geothermal Type Reservoirs. Presented at the SPE California Regional Meeting, San Francisco, California, USA, 4-5 April. SPE-4897-MS. doi: 10.2118/4897-MS.

Stehfest, H. 1970. Numerical Inversion of Laplace Transforms. *Communications of the ACM* **13** (1): 47-49. doi: 10.1145/361953.361969.

Sui, W., 2009. Determining Multilayer Formation Properties from Transient Temperature and Pressure Measurements. PhD Dissertation, Texas A&M University, College Station, Texas (August 2009).

Sui, W., Ehlig-Economides, C., Zhu, D. and Hill, A.D. 2012. Determining Multilayer Formation Properties from Transient Temperature and Pressure Measurements in Gas Wells with Commingled Zones. *Journal of Natural Gas Science and Engineering* **9**: 60-72. doi: 10.1016/j.jngse.2012.05.010.

Sui, W., Zhu, D., Hill, A.D. and Economides-Economides, C.A. 2008a. Model for Transient Temperature and Pressure Behavior in Commingled Vertical Wells. Presented at the SPE Russian Oil and Gas Technical Conference and Exhibition, Moscow, Russia, 28-30 October. SPE-115200-MS. doi: 10.2118/115200-MS.

Sui, W., Zhu, D., Hill, A.D. and Economides-Economides, C.A. 2008b. Determining Multilayer Formation Properties from Transient Temperature and Pressure Measurements. Presented at the SPE Annual Technical Conference and Exhibition, Denver, Colorado, USA, 21-24 September. SPE-116270-MS. doi: 10.2118/116270-MS.

Sun, X. and Mohanty, K.K. 2005. Simulation of Methane Hydrate Reservoirs. Presented at the SPE Reservoir Simulation Symposium, The Woodlands, Texas, USA, 31 January-2 February. SPE-93015-MS. doi: 10.2118/93015-MS.

Tabatabaei, M. and Zhu, D. 2012. Fracture-Stimulation Diagnostics in Horizontal Wells through Use of Distributed-Temperature-Sensing Technology. *SPE Production & Operations* **27** (4): 356-362. SPE-148835-PA. doi: 10.2118/148835-PA.

Tan, X., Tabatabaei, M., Zhu, D. and Hill, A.D. 2012. Diagnosis of Acid Placement from Temperature Profiles. *SPE Production & Operations* **27** (3): 284-293. SPE-144194-PA. doi: 10.2118/144194-PA.

Thacker, B.H., Doebling, S.W., Hemez, F.M., Anderson, M.C., Pepin, J.E. and Rodriguez, E.A. 2004. Concepts of Model Verification and Validation. Technical Report LA-14167, DOE Contract No. W-7405-ENG-36, Los Alamos National Laboratory, Los Alamos, New Mexico (30 October 2004). doi: 10.2172/835920.

Thompson, J., Fan, L., Grant, D., Martin, R.B., Kanneganti, K.T. and Lindsay, G.J. 2011. An Overview of Horizontal-Well Completions in the Haynesville Shale. *Journal of Canadian Petroleum Technology* **50** (6): 22-35. SPE-136875-PA. doi: 10.2118/136875-PA.

Ugueto, G.A., Huckabee, P.T. and Molenaar, M.M. 2015. Challenging Assumptions about Fracture Stimulation Placement Effectiveness Using Fiber Optic Distributed Sensing Diagnostics: Diversion, Stage Isolation and Overflushing. Presented at the SPE Hydraulic Fracturing Technology Conference, The Woodlands, Texas, USA, 3-5 February. SPE-173348-MS. doi: 10.2118/173348-MS.

Ugueto, G.A., Huckabee, P.T., Molenaar, M.M., Wyker, B. and Somanchi, K. 2016. Perforation Cluster Efficiency of Cemented Plug and Perf Limited Entry Completions; Insights from Fiber Optics Diagnostics. Presented at the SPE Hydraulic Fracturing Technology Conference, The Woodlands, Texas, USA, 9-11 February. SPE-179124-MS. doi: 10.2118/179124-MS.

van Genuchten, M.T. 1980. A Closed-Form Equation for Predicting the Hydraulic Conductivity of Unsaturated Soils. *Soil Sci. Soc. Am. J.* **44** (5): 892-898. doi: 10.2136/sssaj1980.03615995004400050002x.

Wagner, W., Cooper, J.R., Dittmann, A., Kijima, J., Kretzschmar, H.J., Kruse, A., Mareš, R., Oguchi, K., Sato, H., Stöcker, I., Šifner, O., Takaishi, Y., Tanishita, I., Trübenbach, J. and Willkommen, T. 2000. The IAPWS Industrial Formulation 1997 for the Thermodynamic Properties of Water and Steam. *Journal of Engineering for Gas Turbines and Power* **122** (1): 150-184. doi: 10.1115/1.483186.

Wang, X., Lee, J., Thigpen, B., Vachon, G.P., Poland, S.H. and Norton, D. 2008. Modeling Flow Profile using Distributed Temperature Sensor (DTS) System. Presented at the Intelligent Energy Conference and Exhibition, Amsterdam, The Netherlands, 25-27 February. SPE-111790-MS. doi: 10.2118/111790-MS.

Yaws, C.L. 1995. *Handbook of Transport Property Data: Viscosity, Thermal Conductivity, and Diffusion Coefficients of Liquids and Gases*, Gulf Pub. Co., Houston Texas.

Yaws, C.L. 2008. *Thermophysical Properties of Chemicals and Hydrocarbons*, Elsevier Science BV, Amsterdam.

Yin, J., Xie, J., Datta-gupta, A. and Hill, A.D. 2011. Improved Characterization and Performance Assessment of Shale Gas Wells by Integrating Stimulated Reservoir Volume and Production Data. Presented at the SPE Eastern Regional Meeting, Columbus, Ohio, USA, 17-19 August. SPE-148969-MS. doi: 10.2118/148969-MS.

Yoshida, N., Zhu, D. and Hill, A.D. 2014. Temperature-Prediction Model for a Horizontal Well With Multiple Fractures in a Shale Reservoir. *SPE Production & Operations* **29** (4): 261-273. SPE-166241-PA. doi: 10.2118/166241-PA.

Yoshioka, K. 2007. Detection of Water or Gas Entry into Horizontal Wells by Using Permanent Downhole Monitoring Systems. PhD Dissertation, Texas A&M University, College Station, Texas (May 2007).

Yoshioka, K., Zhu, D., Hill, A.D., Dawkrajai, P. and Lake, L.W. 2005. A Comprehensive Model of Temperature Behavior in a Horizontal Well. Presented at the SPE Annual Technical Conference and Exhibition, Dallas, Texas, USA, 9-12 October. SPE-95656-MS. doi: 10.2118/95656-MS.

Yoshioka, K., Zhu, D., Hill, A.D., Dawkrajai, P. and Lake, L.W. 2007. Prediction of Temperature Changes Caused by Water or Gas Entry into a Horizontal Well. *SPE Production & Operations* **22** (4): 425-433. SPE-100209-PA. doi: 10.2118/100209-PA.

Yoshioka, K., Zhu, D., Hill, A.D. and Lake, L.W. 2009. A New Inversion Method to Interpret Flow Profiles from Distributed Temperature and Pressure Measurements in Horizontal Wells. *SPE Production & Operations* **24** (4): 510-521. SPE-109749-PA. doi: 10.2118/109749-PA.

Zhang, J., Kamenov, A., Hill, A.D. and Zhu, D. 2014. Laboratory Measurement of Hydraulic-Fracture Conductivities in the Barnett Shale. *SPE Production & Operations* **29** (3): 216-227. SPE-163839-PA. doi: 10.2118/163839-PA.

Zhang, J., Zhu, D. and Hill, A.D. 2015. Water-Induced Damage to Propped-Fracture Conductivity in Shale Formations. *SPE Production & Operations* Preprint. SPE-173346-PA. doi: 10.2118/173346-PA.

Zhang, X., Du, C., Deimbacher, F., Crick, M. and Harikesavanallur, A. 2009. Sensitivity Studies of Horizontal Wells with Hydraulic Fractures in Shale Gas Reservoirs. Presented at the International Petroleum Technology Conference, Doha, Qatar, 7-9 December. IPTC-13338-MS. doi: 10.2523/13338-MS.

Zhao, J. and Tso, C.P. 1993. Heat Transfer by Water Flow in Rock Fractures and the Application to Hot Dry Rock Geothermal Systems. *International Journal of Rock Mechanics and Mining Sciences & Geomechanics Abstracts* **30** (6): 633-641. doi: 10.1016/0148-9062(93)91223-6.

Zuber, N. and Findlay, J.A. 1965. Average Volumetric Concentration in Two-Phase Flow Systems. *Journal of Heat Transfer* **87** (4): 453-468. doi: 10.1115/1.3689137.

APPENDIX A

CONSERVATION EQUATIONS

This appendix describes derivations of flow and thermal models in reservoir and wellbore. The differential form of the equations is derived from the integral form of the conservation equations. In the wellbore model, once the equations are obtained, they are integrated over the cross-sectional area to get the one-dimensional form of the conservation equations.

A.1 Reservoir Model

Mass and energy conservations in reservoir are expressed in the integral form (Pruess et al. 1999) as:

$$\frac{d}{dt}\int_{V_m} M^\kappa dV = \int_{\Gamma_m} \mathbf{F}^\kappa \bullet \mathbf{n} d\Gamma + \int_{V_m} q^\kappa dV \quad \text{..... (A.1)}$$

$$\frac{d}{dt}\int_{V_m} M^\theta dV = \int_{\Gamma_m} \mathbf{F}^\theta \bullet \mathbf{n} d\Gamma + \int_{V_m} q^\theta dV \quad \text{..... (A.2)}$$

where M^κ, $\mathbf{F}^\kappa$ and q^κ are mass accumulation, mass flux, mass sink/source of component κ, respectively, and M^θ, $\mathbf{F}^\theta$ and q^θ are heat accumulation, heat flux and thermal sink/source, respectively. V_m and Γ_m are control volume of an element m and boundary of the element m, respectively. **n** is the inward normal vector on the boundary.

Suppose the control volume is fixed in the reservoir domain (Lake 2010), and the acccumulation terms become

$$\frac{d}{dt}\int_{V_m} M^\kappa dV = \int_{V_m} \frac{\partial M^\kappa}{\partial t} dV \quad \text{..... (A.3)}$$

$$\frac{d}{dt}\int_{V_m} M^{\theta} dV = \int_{V_m} \frac{\partial M^{\theta}}{\partial t} dV \quad \text{..... (A.4)}$$

The flux terms are rearraged into following form with the divergence theorem:

$$\int_{\Gamma_m} \mathbf{F}^{\kappa} \bullet \mathbf{n} d\Gamma = -\int_{\Gamma_m} \mathbf{F}^{\kappa} \bullet \mathbf{n}_{out} d\Gamma = -\int_{V_m} \nabla \bullet \mathbf{F}^{\kappa} dV \quad \text{..... (A.5)}$$

$$\int_{\Gamma_m} \mathbf{F}^{\theta} \bullet \mathbf{n} d\Gamma = -\int_{\Gamma_m} \mathbf{F}^{\theta} \bullet \mathbf{n}_{out} d\Gamma = -\int_{V_m} \nabla \bullet \mathbf{F}^{\theta} dV \quad \text{..... (A.6)}$$

where $\mathbf{n}_{out}$ is outward normal vector. Then, the reservoir flow and thermal models are expressed in differential form as

$$\int_{V_m} \left[\frac{\partial M^{\kappa}}{\partial t} + \nabla \bullet \mathbf{F}^{\kappa} - q^{\kappa} \right] dV = 0 \quad \text{..... (A.7)}$$

$$\int_{V_m} \left[\frac{\partial M^{\theta}}{\partial t} + \nabla \bullet \mathbf{F}^{\theta} - q^{\theta} \right] dV = 0 \quad \text{..... (A.8)}$$

or

$$\frac{\partial M^{\kappa}}{\partial t} = -\nabla \bullet \mathbf{F}^{\kappa} + q^{\kappa} \quad \text{..... (A.9)}$$

$$\frac{\partial M^{\theta}}{\partial t} = -\nabla \bullet \mathbf{F}^{\theta} + q^{\theta}. \quad \text{..... (A.10)}$$

A.1.1 Reservoir Flow Model

The accumulation, flux and sink/source for the reservoir flow model are given by Eq. 2.41, 2.42 and 2.43, respectively. Finally, the reservoir flow model is expressed as

$$\frac{\partial}{\partial t}\left(\phi \sum_{\beta} S_{\beta} \rho_{\beta} X_{\beta}^{\kappa} \right) = -\nabla \bullet \left[\sum_{\beta} \left(X_{\beta}^{\kappa} \rho_{\beta} \mathbf{v}_{\beta} \right) \right] + \sum_{\beta} X_{\beta}^{\kappa} q_{\beta}. \quad \text{..... (A.11)}$$

A.1.2 Reservoir Thermal Model

The reservoir thermal model is derived from conservation of total energy. The accumulation for the total energy balance contains both thermal energy and kinetic energy (Lake 2010):

$$M^{\theta} = \rho U + \frac{1}{2}\sum_{\beta}\rho_{\beta}\left|\mathbf{v}_{\beta}\right|^{2} \quad \text{..... (A.12)}$$

$$\rho u = \phi\sum_{\beta}\rho_{\beta}S_{\beta}U_{\beta} + (1-\phi)\rho_{s}U_{s} \quad \text{..... (A.13)}$$

The total energy flux is expressed as the sum of the advective energy flux, the rate of work done by molecular mechanisms and the rate of transporting heat by molecular mechanisms (conduction) (Bird et al. 2002). It is expressed as

$$\mathbf{F}^{\theta} = \sum_{\beta}\rho_{\beta}\mathbf{v}_{\beta}\left[U_{\beta} + \frac{1}{2}\left|\mathbf{v}_{\beta}\right|^{2}\right] + \mathbf{q}_{c} + \sum_{\beta}\left(p_{\beta}\mathbf{I} + \boldsymbol{\tau}_{\beta}\right)\bullet\mathbf{v}_{\beta} \quad \text{..... (A.14)}$$

where $\mathbf{q}_c$ is the conductive energy transport and $\boldsymbol{\tau}_\beta$ is the viscous stress tensor. By ignoring viscous stress tensor and assuming the isotropic thermal conductivity, the total energy flux is reduced into

$$\mathbf{F}^{\theta} = \sum_{\beta}\rho_{\beta}\mathbf{v}_{\beta}\left(H_{\beta} + \frac{1}{2}\left|\mathbf{v}_{\beta}\right|^{2}\right) - k_{Tt}\nabla T\,. \quad \text{..... (A.15)}$$

Therefore, we have the following equation for the total energy conservation:

$$\frac{\partial}{\partial t}\left(\rho U + \frac{1}{2}\sum_{\beta}\rho_{\beta}\left|\mathbf{v}_{\beta}\right|^{2}\right) = -\nabla\bullet\left[\sum_{\beta}\rho_{\beta}\mathbf{v}_{\beta}\left(H_{\beta} + \frac{1}{2}\left|\mathbf{v}_{\beta}\right|^{2}\right) - k_{Tt}\nabla T\right] + q_{wb} + \sum_{\beta}H_{\beta}q_{\beta} + \sum_{\beta}\rho_{\beta}\mathbf{v}_{\beta}\bullet\mathbf{g} \quad \text{..... (A.16)}$$

where the second and third terms in the right-hand-side denote thermal sink/source at

wellbore and reservoir contact, and the fourth term is work done by gravity (Lake 2010). The thermal energy balance equation is obtained by ignoring the kinetic and potential energy terms. Therefore, we have

$$\frac{\partial}{\partial t}\left[\phi\sum_{\beta}\rho_{\beta}S_{\beta}U_{\beta}+(1-\phi)\rho_{s}U_{s}\right]=-\nabla\bullet\left(\sum_{\beta}\rho_{\beta}\mathbf{v}_{\beta}H_{\beta}\right)+\nabla\bullet\left(k_{Tt}\nabla T\right)+q_{wb}+\sum_{\beta}H_{\beta}q_{\beta} \quad \text{. .... (A.17)}$$

A.2 Wellbore Model

General balance equation for single-phase and single component system can be expressed as (Ishii and Hibiki 2011)

$$\frac{d}{dt}\int_{V_m}\rho\psi dV=-\int_{\Gamma_m}\mathbf{n}_{out}\bullet\mathbf{J}d\Gamma+\int_{V_m}\rho\chi dV \quad \text{..... (A.18)}$$

where **J** is efflux term, χ is the body source of any quantity ψ defined for a unit mass. This equation is rearranged, with use of the Reynolds transport theorem and the divergence theorem, into

$$\int_{V_m}\left[\frac{\partial}{\partial t}(\rho\psi)+\nabla\bullet(\rho\mathbf{v}\psi)+\nabla\bullet\mathbf{J}-\rho\chi\right]dV=0 \quad \text{..... (A.19)}$$

or

$$\frac{\partial}{\partial t}(\rho\psi)+\nabla\bullet(\rho\mathbf{v}\psi)=-\nabla\bullet\mathbf{J}+\rho\chi. \quad \text{..... (A.20)}$$

In the two-phase flow problem, we also need to consider interphase contribution on each conservation properties: interphase mass, momentum and energy transfer. The final form

of the general balance equation under multiphase condtions is given as (Ishii and Hibiki 2011)

$$\frac{\partial \alpha_\beta \rho_\beta \psi_\beta}{\partial t} + \nabla \bullet \left(\alpha_\beta \rho_\beta \psi_\beta \mathbf{v}_\beta\right) = -\nabla \bullet \left(\alpha_\beta \mathbf{J}_\beta\right) + \alpha_\beta \rho_\beta \chi_\beta + I_\beta \quad \text{..... (A.21)}$$

where I_β represents the interphase transfer term of the property ψ_β. In the equation, the turbulence effect is ignored. By setting the quantity of ψ_β and corresponding $\mathbf{J}_\beta$ and χ_β, we obtain conservation equations of mass, momentum and total energy.

A.2.1 Wellbore Flow Model

Conservation of Component Mass

The continuity equation for each phase is given by

$$\frac{\partial}{\partial t}\left(\alpha_\beta \rho_\beta\right) + \nabla \bullet \left(\alpha_\beta \rho_\beta \mathbf{v}_\beta\right) = m_\beta \quad \text{..... (A.22)}$$

where m_β is interfacial mass transfer term of phase β satisfying

$$\sum_\beta m_\beta = 0. \quad \text{..... (A.23)}$$

Then, the continuity equation of component mass is expressed by taking sum of the phases considering mutual solubility:

$$\frac{\partial}{\partial t}\left(\sum_\beta \alpha_\beta \rho_\beta X_\beta^\kappa\right) + \nabla \bullet \left(\sum_\beta \alpha_\beta \rho_\beta X_\beta^\kappa \mathbf{v}_\beta\right) = 0. \quad \text{..... (A.24)}$$

This equation is expressed in the cylindrical coordinate system as

$$\frac{\partial}{\partial t}\left(\sum_{\beta}\alpha_{\beta}\rho_{\beta}X_{\beta}^{\kappa}\right)+\frac{1}{r}\frac{\partial}{\partial r}\left(r\sum_{\beta}\alpha_{\beta}\rho_{\beta}X_{\beta}^{\kappa}v_{\beta,r}\right)+\frac{\partial}{\partial z}\left(\sum_{\beta}\alpha_{\beta}\rho_{\beta}X_{\beta}^{\kappa}v_{\beta,z}\right)=0 \quad \text{..... (A.25)}$$

where the θ-directional component is ignored. Integrate this equation over the cross-section of the wellbore segment as

$$\frac{\partial}{\partial t}\left(\sum_{\beta}\alpha_{\beta}\rho_{\beta}X_{\beta}^{\kappa}\right)+\frac{\partial}{\partial z}\left(\sum_{\beta}\alpha_{\beta}\rho_{\beta}X_{\beta}^{\kappa}v_{\beta,z}\right)+\frac{2}{r_i^2}\int_0^{r_i}\left[\frac{\partial}{\partial r}\left(r\sum_{\beta}\alpha_{\beta}\rho_{\beta}X_{\beta}^{\kappa}v_{\beta,r}\right)\right]dr=0 \quad \text{. ..... (A.26)}$$

The last term in the left-hand-side is contribution of the component mass at the contact of the wellbore and reservoir. It can be rearranged using the inflow velocity notation into

$$\frac{\partial}{\partial t}\left(\sum_{\beta}\alpha_{\beta}\rho_{\beta}X_{\beta}^{\kappa}\right)+\frac{\partial}{\partial z}\left(\sum_{\beta}\alpha_{\beta}\rho_{\beta}X_{\beta}^{\kappa}v_{\beta}\right)=\frac{2\gamma}{r_i}\left(\sum_{\beta}\alpha_{\beta,I}\rho_{\beta,I}X_{\beta,I}^{\kappa}v_{\beta,I}\right). \quad \text{..... (A.27)}$$

Conservation of Combined-phase Momentum

The conservation of the combined-phase momentum is given by

$$\frac{\partial}{\partial t}\left(\sum_{\beta}\alpha_{\beta}\rho_{\beta}\mathbf{v}_{\beta}\right)+\nabla\bullet\left(\sum_{\beta}\alpha_{\beta}\rho_{\beta}\mathbf{v}_{\beta}\mathbf{v}_{\beta}\right)=-\nabla p-\nabla\bullet\boldsymbol{\tau}+\rho_m\mathbf{g} \quad \text{..... (A.28)}$$

where $\boldsymbol{\tau}$ is the viscous stress tensor, and $\mathbf{g}$ is the gravitational body force per unit mass. In the equation, the interfacial momentum transfer is ignored, and phase pressures are assumed to be same.

This equation is expressed in the cylindrical coordinate system as

$$\frac{\partial}{\partial t}\left(\sum_{\beta}\alpha_{\beta}\rho_{\beta}v_{\beta,z}\right)+\frac{\partial}{\partial z}\left(\sum_{\beta}\alpha_{\beta}\rho_{\beta}v_{\beta,z}v_{\beta,z}\right)=-\frac{\partial p}{\partial z}-\frac{1}{r}\frac{\partial}{\partial r}(r\tau_{rz})+\rho_m g_z \quad \text{... (A.29)}$$

where the θ-directional component is ignored. Integrate this equation over the cross-section of the wellbore segment as

$$\frac{\partial}{\partial t}\left(\sum_{\beta}\alpha_{\beta}\rho_{\beta}v_{\beta,z}\right)+\frac{\partial}{\partial z}\left(\sum_{\beta}\alpha_{\beta}\rho_{\beta}v_{\beta,z}v_{\beta,z}\right)=-\frac{\partial p}{\partial z}+\rho_m g_z - \frac{1}{\pi r_i^2}\int_0^{r_i}\int_0^{2\pi}\left[\frac{1}{r}\frac{\partial}{\partial r}(r\tau_{rz})\right]r\,d\theta\,dr \quad \text{..... (A.30)}$$

The integral term is expressed as

$$\frac{1}{\pi r_i^2}\int_0^{r_i}\int_0^{2\pi}\left[\frac{1}{r}\frac{\partial}{\partial r}(r\tau_{rz})\right]r\,d\theta\,dr=\frac{2}{r_i}\tau_{rz}\big|_{r=r_i}=\frac{\Gamma}{2A}\rho_m v_m|v_m|f_m \quad \text{..... (A.31)}$$

where Γ is inner perimeter of the well, A is well cross-sectional area, and f_m is mixture friction factor at the wall. Hence, we obtain the one-dimensional combined-phase momentum balance equation as

$$\frac{\partial}{\partial t}\left(\sum_{\beta}\alpha_{\beta}\rho_{\beta}v_{\beta}\right)+\frac{\partial p}{\partial z}+\frac{\partial}{\partial z}\left(\sum_{\beta}\alpha_{\beta}\rho_{\beta}v_{\beta}v_{\beta}\right)=-\frac{\Gamma}{2A}\rho_m v_m|v_m|f_m+\rho_m g_z. \quad \text{... (A.32)}$$

A.2.2 Wellbore Thermal Model

The conservation of the total energy is given by

$$\frac{\partial}{\partial t}\left[\sum_{\beta}\alpha_{\beta}\rho_{\beta}\left(U_{\beta}+\frac{v_{\beta}^2}{2}\right)\right]=-\nabla\bullet\left(\sum_{\beta}\alpha_{\beta}\rho_{\beta}\left(H_{\beta}+\frac{v_{\beta}^2}{2}\right)\mathbf{v}_{\beta}+\mathbf{q}_c\right)+\sum_{\beta}\alpha_{\beta}\rho_{\beta}\mathbf{g}_{\beta}\bullet\mathbf{v}_{\beta} \quad \text{..... (A.33)}$$

where $\mathbf{q}_c$ denotes heat conduction.

This equation is expressed in the cylindrical coordinate system as

$$\frac{\partial}{\partial t}\left[\sum_{\beta}\alpha_{\beta}\rho_{\beta}\left(U_{\beta}+\frac{v_{\beta}^{2}}{2}\right)\right]=-\frac{1}{r}\frac{\partial}{\partial r}\left[r\sum_{\beta}\alpha_{\beta}\rho_{\beta}\left(H_{\beta}+\frac{v_{\beta}^{2}}{2}\right)v_{\beta,r}\right]$$
$$-\frac{\partial}{\partial z}\left[\sum_{\beta}\alpha_{\beta}\rho_{\beta}\left(H_{\beta}+\frac{v_{\beta}^{2}}{2}\right)v_{\beta,z}\right]-\frac{1}{r}\frac{\partial}{\partial r}\left(rq_{c,r}\right)-\frac{\partial q_{c,z}}{\partial z}+\sum_{\beta}\alpha_{\beta}\rho_{\beta}g_{\beta,z}v_{\beta,z} \quad \text{... (A.34)}$$

where the θ-directional component is ignored. Integrate this equation over the cross-section of the wellbore segment as

$$\frac{\partial}{\partial t}\left[\sum_{\beta}\alpha_{\beta}\rho_{\beta}\left(U_{\beta}+\frac{v_{\beta}^{2}}{2}\right)\right]+\frac{\partial}{\partial z}\left[\sum_{\beta}\alpha_{\beta}\rho_{\beta}\left(H_{\beta}+\frac{v_{\beta}^{2}}{2}\right)v_{\beta,z}\right]$$
$$+\frac{\partial q_{c,z}}{\partial z}-\sum_{\beta}\alpha_{\beta}\rho_{\beta}g_{\beta,z}v_{\beta,z} \quad \text{..... (A.35)}$$
$$+\frac{2}{r_{i}^{2}}\int_{0}^{r_{i}}\left\{\frac{\partial}{\partial r}\left[r\sum_{\beta}\alpha_{\beta}\rho_{\beta}\left(h_{\beta}+\frac{v_{\beta}^{2}}{2}\right)v_{\beta,r}\right]+\frac{\partial}{\partial r}\left(rq_{c,r}\right)\right\}dr=0$$

where the integration term is rearranged into

$$\frac{2}{r_{i}^{2}}\int_{0}^{r_{i}}\left\{\frac{\partial}{\partial r}\left[r\sum_{\beta}\alpha_{\beta}\rho_{\beta}\left(H_{\beta}+\frac{v_{\beta}^{2}}{2}\right)v_{\beta,r}\right]+\frac{\partial}{\partial r}\left(rq_{c,r}\right)\right\}dr$$
$$=\frac{2}{r_{i}^{2}}\left\{\left[r\sum_{\beta}\alpha_{\beta}\rho_{\beta}\left(H_{\beta}+\frac{v_{\beta}^{2}}{2}\right)v_{\beta,r}\right]_{r=0}^{r=r_{i}}+\left[rq_{c,r}\right]_{r=0}^{r=r_{i}}\right\}. \quad \text{..... (A.36)}$$
$$=\frac{2}{r_{i}}\left[\sum_{\beta}\alpha_{\beta}\rho_{\beta}\left(H_{\beta}+\frac{v_{\beta}^{2}}{2}\right)v_{\beta,r}\right]_{r=r_{i}}+\frac{2}{r_{i}}q_{c,r}\Big|_{r=r_{i}}$$

Then, we obtain

$$\frac{\partial}{\partial t}\left[\sum_{\beta}\alpha_{\beta}\rho_{\beta}\left(U_{\beta}+\frac{v_{\beta}^{2}}{2}\right)\right]=-\frac{\partial}{\partial z}\left[\sum_{\beta}\alpha_{\beta}\rho_{\beta}\left(H_{\beta}+\frac{v_{\beta}^{2}}{2}\right)v_{\beta,z}\right]-\frac{\partial q_{c,z}}{\partial z}$$
$$+\sum_{\beta}\alpha_{\beta}\rho_{\beta}g_{\beta,z}v_{\beta,z}-\frac{2}{r_{i}}\left[\sum_{\beta}\alpha_{\beta}\rho_{\beta}\left(H_{\beta}+\frac{v_{\beta}^{2}}{2}\right)v_{\beta,r}\right]_{r=r_{i}}-\frac{2}{r_{i}}q_{c,r}\Big|_{r=r_{i}} \quad \text{. ..... (A.37)}$$

Here, the last two terms denote the energy transport across the contact of the wellbore and reservoir. They can be expressed with the inflow velocity and overall heat transfer coefficient. This can be further rearranged into

$$\frac{\partial}{\partial t}\left[\sum_{\beta}\alpha_{\beta}\rho_{\beta}\left(U_{\beta}+\frac{v_{\beta}^{2}}{2}\right)\right]=-\frac{\partial}{\partial z}\left[\sum_{\beta}\alpha_{\beta}\rho_{\beta}\left(H_{\beta}+\frac{v_{\beta}^{2}}{2}\right)v_{\beta,z}\right]$$
$$+\frac{\partial}{\partial z}\left(k_{f}\frac{\partial T}{\partial z}\right)+\sum_{\beta}\alpha_{\beta}\rho_{\beta}g_{\beta,z}v_{\beta,z} \quad \text{. ..... (A.38)}$$
$$+\frac{2}{r_{i}}U_{T}\Big|_{r=r_{i}}\left(T_{res}-T\right)+\frac{2}{r_{i}}\left\{\sum_{\beta}j_{\beta,I}\rho_{\beta,I}\left[H_{\beta,I}+\frac{v_{\beta,I}^{2}}{2}\right]\right\}$$

APPENDIX B

CONSTITUTIVE EQUATIONS AND THERMOPHYSICAL PROPERTIES

Governing equations presented in this work are solved with respect to selected primary variables, and rest of the variables needs to be estimated by the primary variables. Those variables determined by the primary variables are called secondary variables. Constitutive equations and equations of state describe those relations.

B.1 Constitutive Equations

B.1.1 Friction Factor with Influx/Outflux

Ouyang et al. (1998) proposed correlations of friction factor with inflow/outflow along the wellbore using nonlinear regression method. Their friction factor model depends on both of Reynolds number in the well and wall Reynolds number which are defined as (Kinney 1968)

$$N_{\mathrm{Re}} = \frac{Dv\rho}{\mu} \quad \text{..... (B.1)}$$

$$N_{\mathrm{Re},w} = \frac{Dv_I\rho_I}{\mu_I} = \frac{q_I}{\pi\mu_I} \quad \text{..... (B.2)}$$

where D is diameter of the wellbore, v is axial velocity in wellbore, q is mass flow rate, and the subscript I denotes the conditions of inflow (at wall). Let us focus on the production case ($N_{\mathrm{Re},w} > 0$) here. For laminar flow in wellbore, the friction factor does not depend on completion designs, and it is given as (Ouyang et al. 1998)

$$f = \frac{16}{N_{\mathrm{Re}}}\left(1 + 0.04304 N_{\mathrm{Re},w}^{0.6142}\right). \quad \text{..... (B.3)}$$

For turbulent flow in wellbore, the friction factor also depends on the completion design. Under open-hole completion, friction factor is given by

$$f_{open} = f_0\left[1 - 29.03\left(\frac{N_{\mathrm{Re},w}}{N_{\mathrm{Re}}}\right)^{0.8003}\right]. \quad \text{..... (B.4)}$$

Ouyang et al. (1998) mentioned this model overpredicts the friction factor by analyzing the data in experimental work of Aziz et al. (1997) under normal-wellbore flow condition. Therefore, they also proposed a local friction factor model as

$$f_{comp} = f_0\left[1 - 0.0153 N_{\mathrm{Re},w}^{0.3978}\right]. \quad \text{..... (B.5)}$$

In the turbulent model, f_0 denotes the friction factor without wall inflow, and it can be estimated using the correlation by Chen (1979)

$$\frac{1}{\sqrt{f_0}} = -4\log\left\{\frac{\varepsilon}{3.7065} - \frac{5.0452}{N_{\mathrm{Re}}}\log\left[\frac{\varepsilon^{1.1098}}{2.8257} + \left(\frac{7.149}{N_{\mathrm{Re}}}\right)^{0.8981}\right]\right\} \quad \text{..... (B.6)}$$

where ε is relative pipe roughness.

B.1.2 Kinematic Relations of Drift-velocity

The drift-flux model for two-phase flow correlates the gas phase velocity with volumetric flux of gas-liquid mixture using the drift-velocity. Zuber and Findlay (1965) proposed a kinematic relationship with consideration of the effect of nonuniform flow/concentration profiles and the effect of the local relative (slip) velocity. In following part, we omitted

the notation of the cross-sectional average and the volume-fraction weighted average which are used in the work by Ishii (1977).

The in-situ gas velocity is given by Zuber and Findlay (1965) as

$$v_G = C_0 j + V_d \quad \text{..... (B.7)}$$

where C_0 is the distribution parameter to account for the nonuniform flow/concentration profiles and V_d is the drift-velocity of gas phase to express the slip between the phases. The definition of the volumetric flux for gas-liquid two phase system

$$j \equiv j_L + j_G = (1-\alpha_G)v_L + \alpha_G v_G \quad \text{..... (B.8)}$$

gives the liquid velocity as function of gas volume fraction, volumetric flux of mixture and drift-velocity of gas phase:

$$v_L = \frac{1-\alpha_G C_0}{1-\alpha_G} j - \frac{\alpha_G}{1-\alpha_G} V_d . \quad \text{..... (B.9)}$$

In the drift-flux model, the conservation equations are solved in terms of the mixture velocity of the center of mass, and gas volume fraction. These are considered as the primary variables of the numerical simulation. The phasic velocities need to be formulated as function of these primary variables.

Mean drift-velocity is defined by (Ishii 1977)

$$\overline{V}_d \equiv v_G - j , \quad \text{..... (B.10)}$$

and the drift-velocity is rearranged into

$$\overline{V}_d = V_d + (C_0 - 1) j . \quad \text{..... (B.11)}$$

Then, the phase velocities are expressed by the mixture velocity of center of mass and the mean drift-velocity in the following forms (Ishii 1977):

$$v_G = v_m + \frac{\rho_L}{\rho_m}\overline{V}_d \quad \text{..... (B.12)}$$

$$v_L = v_m - \frac{\alpha_G}{1-\alpha_G}\frac{\rho_G}{\rho_m}\overline{V}_d \quad \text{..... (B.13)}$$

and

$$j = v_m + \frac{\alpha_G(\rho_L - \rho_G)}{\rho_m}\overline{V}_d . \quad \text{..... (B.14)}$$

The mean drift-flux is rearranged into, using Eq. B.11,

$$\overline{V}_d = \frac{\rho_m}{C_0\alpha_G\rho_G + (1-C_0\alpha_G)\rho_L}\left[(C_0-1)v_m + V_d\right] = \frac{\rho_m}{\rho_m^*}\left[(C_0-1)v_m + V_d\right] \quad \text{.. (B.15)}$$

where ρ_m^* is the profile adjusted average density given by (Pan et al. 2011d)

$$\rho_m^* = C_0\alpha_G\rho_G + (1-C_0\alpha_G)\rho_L . \quad \text{..... (B.16)}$$

Therefore, the phase velocities and the volumetric flux of mixture are rearranged into

$$v_G = C_0\frac{\rho_m}{\rho_m^*}v_m + \frac{\rho_L}{\rho_m^*}V_d \quad \text{..... (B.17)}$$

$$v_L = \frac{(1-C_0\alpha_G)}{(1-\alpha_G)}\frac{\rho_m}{\rho_m^*}v_m - \frac{\alpha_G}{(1-\alpha_G)}\frac{\rho_L}{\rho_m^*}V_d \quad \text{..... (B.18)}$$

and

$$j = \frac{\rho_m}{\rho_m^*}v_m + \alpha_G\frac{\rho_L - \rho_G}{\rho_m^*}V_d . \quad \text{..... (B.19)}$$

B.1.3 Correlations for Parameters in Drift-flux Model

The phase velocities and the volumetric flux are expressed as the function of mixture velocity of center of mass, distribution parameter C_0 and drift-velocity. Since the primary

variables of the drift-flux model are the gas phase volume fraction and the mixture velocity, the distribution parameter and the drift-velocity need to be estimated by these primary variables.

Several researchers proposed models to estimate these parameters to reproduce wide range of experimental measurements (Ishii 1977, Hibiki and Ishii 2003, Zuber and Findlay 1965, Hasan et al. 2007, França and Lahey Jr 1992, Shi et al. 2005a, Shi et al. 2005b). In the view of mechanics modeling, the constitutive equations have different forms to account for the different flow regimes. However, at the same time, the use of different correlations gives the difficulties in the numerical implementation; the discontinuities of correlations between the flow regimes bring the convergence issues in the solution procedure. To avoid the issues, several interpolation methods are used in the modeling works. Shi et al. (2005b) considered two extreme cases for gas-liquid two phase flow system: gas bubble rising through a stagnant liquid (low α_G) and liquid film flooding which supports a thin annular film of liquid and prevents it from falling back against the gas flow (high α_G). These two conditions are interpolated with smoothing function.

Shi et al. (2005b) proposed functional forms of the distribution parameter and the drift-velocity with optimized parameter values in the functions through the optimization process minimizing the error between model prediction and experimental data given by Oddie et al. (2003). The profile parameter for gas and liquid is written in the form of (Shi et al. 2005b)

$$C_0 = \frac{A}{1+(A-1)\gamma^2}. \quad \text{..... (B.20)}$$

where A is the profile parameter for low gas fraction in liquid, and the profile parameter reduction term γ is given by

$$\gamma = \frac{\beta - B}{1 - B} \quad \text{subject to the limits} \quad 0 \le \gamma \le 1 \quad \text{..... (B.21)}$$

where B is the profile parameter term (gas volume fraction) where the distribution parameter begins to reduce with expression of β:

$$\beta = \max\left(\alpha_G, F_V \frac{\alpha_G |j|}{v_{sGf}}\right). \quad \text{..... (B.22)}$$

The F_V is the velocity sensitivity parameter which makes the profile flatting more or less sensitive to the velocity by changing from unity (Shi et al. 2005b). The parameter v_{sGf} is the gas superficial velocity at the "flooding" condition which is at the condition of gas flow with zero liquid penetration (Shi et al. 2005b, Richter 1981), and it is in the form:

$$v_{sGf} = \mathrm{Ku}\left(\frac{\rho_L}{\rho_G}\right)^{1/2} v_c \quad \text{..... (B.23)}$$

where the critical velocity v_c is

$$v_c = \left[\frac{g\sigma_{GL}(\rho_L - \rho_G)}{\rho_L^2}\right]^{1/4}, \quad \text{..... (B.24)}$$

σ_{GL} is surface tension between gas and liquid phases, and Ku is the Kutateladze number given by

$$\mathrm{Ku} = \frac{\rho_G^{1/2} v_{sG}}{\left[g\sigma_{GL}(\rho_L - \rho_G)\right]^{1/4}}. \quad \text{..... (B.25)}$$

The Kutateladze number is rearranged into (Richter 1981)

$$\mathrm{Ku} = \frac{\rho_G^{1/2} v_{sG}}{\left[gD(\rho_L - \rho_G)\right]^{1/2}} \left[\frac{g(\rho_L - \rho_G)}{\sigma_{GL}}\right]^{1/4} D^{1/2} = v_{sG}^{*} \sqrt{D^{*}} \quad \text{..... (B.26)}$$

where the dimensionless gas superficial velocity and the dimensionless pipe diameter are given by

$$v_{sG}^{*} = \frac{\rho_G^{1/2} v_{sG}}{\left[gD(\rho_L - \rho_G)\right]^{1/2}} \quad \text{..... (B.27)}$$

$$D^{*} = \left[\frac{g(\rho_L - \rho_G)}{\sigma_{GL}}\right]^{1/2} D \quad \text{..... (B.28)}$$

where D is the pipe diameter. Richter (1981) proposed a correlation to predicts the flooding superficial gas velocity given by

$$\left(v_{sG}^{*}\right)^2 = \frac{75}{N_B}\left[\sqrt{1 + \frac{N_B}{75^2 C_w}} - 1\right] \quad \text{..... (B.29)}$$

where N_B is Bond number ($N_B = (D^{*})^2$), and the constant '75' is used in the Richter's original work approximately, but, according to Pan et al. (2011a), it overestimates the value of Ku in the rage of smaller dimensionless diameter. Then, Pan et al. (2011a) used the following formulation for the estimation of the Kutateladze number:

$$\mathrm{Ku} = \left(\frac{C_{ku}}{N_B}\right)^{1/2}\left[\sqrt{1 + \frac{N_B}{C_{ku}^2 C_w}} - 1\right]^{1/2} \sqrt{D^{*}} = \left[\frac{C_{ku}}{\sqrt{N_B}}\left(\sqrt{1 + \frac{N_B}{C_{ku}^2 C_w}} - 1\right)\right]^{1/2} \text{... (B.30)}$$

where C_{ku} is set to 142 and C_w is set to 0.008 to obtain satisfactory matching to the measurement given by the work of Richter (1981). In the estimation of the distribution profile parameter, the parameters A and B were optimized.

For the estimation of drift-velocity, Shi et al. (2005b) proposed the following equation:

$$V_d = \frac{(1-\alpha_G C_0)K(C_0,\alpha_G)v_c}{\alpha_G C_0\sqrt{\frac{\rho_G}{\rho_L}}+1-\alpha_G C_0}\, m(\theta) \quad \text{..... (B.31)}$$

where $K(\alpha_G)$ is the smooth function for the transition between the two cases defined by

$$K(C_0,\alpha_G)=\begin{cases}1.53 & (\alpha_G \le a_1)\\ 1.53+\left[C_0(a_2)\mathrm{Ku}(D^*)-1.53\right]\dfrac{\alpha_G-a_1}{a_2-a_1} & (a_1<\alpha_G<a_2)\\ C_0(\alpha_G)\mathrm{Ku}(D^*) & (a_2 \le \alpha_G)\end{cases} \quad \text{.... (B.32)}$$

or, Pan et al. (2011a) extended the smooth function to the following function to ensure the first derivative continuous at the switch points:

$$K(C_0,\alpha_G)=$$
$$\begin{cases}1.53 & (\alpha_G \le a_1)\\ 1.53+\dfrac{C_0(a_2)\mathrm{Ku}(D^*)-1.53}{2}\left[1-\cos\left(\pi\dfrac{\alpha_G-a_1}{a_2-a_1}\right)\right] & (a_1<\alpha_G<a_2)\\ C_0(\alpha_G)\mathrm{Ku}(D^*) & (a_2 \le \alpha_G)\end{cases} \quad \text{..... (B.33)}$$

where a_1, a_2 are the parameters to be optimized. The $m(\theta)$ is the function to account for the well inclination effect defined by

$$m(\theta)=m_0(\cos\theta)^{n_1}(1+\sin\theta)^{n_2} \quad \text{..... (B.34)}$$

where m_0, n_1 and n_2 are the parameters to be optimized.

Hence, the parameters to be optimized are listed as A, B, a_1, a_2, m_0, n_1 and n_2. Shi et al. (2005b) used the following values as initial condition: A = 1.2, B = 0.3, a_1 = 0.20, a_2 = 0.40. Finally, Shi et al. (2005b) concluded the optimized parameters for the water/gas system as summarized in **TABLE B.1**.

TABLE B.1—SUMMARY OF RECOMMENDED PARAMETERS FOR WATER/GAS SYSTEM (BASED ON SHI ET AL. (2005B))				
A	B	a_1	a_2	$m(\theta)$
1.00	—	0.06	0.21	$1.85(\cos\theta)^{0.21}(1+\sin\theta)^{0.95}$

It is noted that in the work of Shi et al. (2005b) they used the experimental data from vertial to near horizontal (88°) because they considered the experimental holdup data for 90° and 92° display relatively large errors due to the end effect. Choi et al. (2012) performed the comparison studies of the several modeling methods with a variety of dataset, and the model by Shi et al. (2005b) showed relatively higher error in the estimation of horizontal flow. Therefore, the model applicability on the horizontal flow needs to be validated with data given by horizontal flow experiments.

B.1.4 Heat Transfer Coefficient

The heat transfer coefficient, in general, is expressed by

$$h = \mathrm{Nu}\left(\frac{k_f}{D_H}\right) \quad \text{..... (B.35)}$$

where h is heat transfer coefficient, Nu is the Nusselt number, k_f is fluid thermal conductivity, and D_H is the hydraulic diameter. The Nusselt number depends on several factors such as flow condition and buoyant forces, and the Nusselt number is decomposed into forced convection and free convection. The heat transfer coefficient for forced convection is computed by Dittus-Boelter correlation as

$$h_{fc} = 0.023\,\mathrm{Re}^{0.8}\,\mathrm{Pr}^{n}\left(\frac{k_f}{D_H}\right) \quad \text{..... (B.36)}$$

where n is 0.4 for heating of fluid ($T_{wall} > T_f$) and 0.3 for cooling of fluid ($T_{wall} < T_f$). This heat transfer coefficient for forced convection is used for tubing or casing flow.

When the flow has large velocity in the tubing, the convective heat transfer has the dominant effects and the free convection effect can be neglected. However, when the fluid velocity decreases, the free convection effect needs to be considered. Bird et al. (2002) called the heat transfer coefficient with both of forced and free convention as mixed convection, and the area mean mixed convection Nusselt number is given by

$$\mathrm{Nu}_m^{\mathrm{total}} = \left[\left(\mathrm{Nu}_m^{\mathrm{free}}\right)^3 + \left(\mathrm{Nu}_m^{\mathrm{forced}}\right)^3\right]^{1/3}. \quad \text{..... (B.37)}$$

In this work, we approximate the local mixed convection Nusselt number using Eq. B.37 with assumption of the free convection in tubing or casing is considered by pure conduction. The Nusselt number of pure conduction is given by (Özisik 1977)

$$\mathrm{Nu}_m^{\mathrm{cond}} = 1, \quad \text{..... (B.38)}$$

and therefore, the local Nusselt number of mixed convection is approximated by

$$\mathrm{Nu}_{loc}^{\mathrm{total}} = \left[1 + \left(\mathrm{Nu}^{\mathrm{forced}}\right)^3\right]^{1/3}. \quad \text{..... (B.39)}$$

The heat transfer coefficient of tubing/casing is expressed using Dittus-Boelter correlation

$$h_{t,mixed} = \left[1 + \left(0.023\,\mathrm{Re}^{0.8}\,\mathrm{Pr}^{n}\right)^3\right]^{1/3}\left(\frac{k_f}{D_H}\right). \quad \text{..... (B.40)}$$

B.2 Fluid and Thermal Properties

B.2.1 Basic Thermodynamic Equations

Peng-Robinson Equation of State

Peng and Robinson (1976) proposed an analytic EOS in cubic form expressed by

$$p = \frac{RT}{V_M - b} - \frac{a_T}{V_M(V_M + b) + b(V_M - b)} \quad \text{..... (B.41)}$$

where V_M is molar volume defined by real gas equation of state, and coefficients are expressed by

$$V_M = \frac{ZRT}{p} \quad \text{..... (B.42)}$$

$$a_T = a_c(T_c) \cdot \alpha(T_r, \omega) \quad \text{..... (B.43)}$$

$$b = 0.07780 \frac{RT_c}{p_c} \quad \text{..... (B.44)}$$

$$a_c(T_c) = 0.45724 \frac{R^2 T_c^2}{p_c} \quad \text{..... (B.45)}$$

$$\alpha^{1/2} = 1 + \kappa\left(1 - T_r^{1/2}\right) \quad \text{..... (B.46)}$$

$$\kappa = 0.37464 + 1.54226\omega - 0.26992\omega^2 \quad \text{..... (B.47)}$$

$$T_r = \frac{T}{T_c} \quad \text{..... (B.48)}$$

where p_c and T_c are critical pressure and temperature, respectively, and ω is the acentric factor in dimensionless.

The compressibility factors are computed as the solution of the cubic EOS. The Peng-Robinson EOS (PR-EOS) can be rearranged, with the definition of real gas equation of state by eliminating molar volume in the PR-EOS, into

$$Z^3 - (1-B)Z^2 + (A - 2B - 3B^2)Z - (AB - B^2 - B^3) = 0 \quad \text{..... (B.49)}$$

with

$$A = \frac{a_T p}{R^2 T^2} \quad \text{..... (B.50)}$$

$$B = \frac{bp}{RT}. \quad \text{..... (B.51)}$$

Isothermal Compressibility

The isothermal compressibility, *c*, is defined by

$$c = \frac{1}{\rho}\frac{\partial \rho}{\partial p}\bigg|_T = -\frac{1}{V_M}\frac{\partial V_M}{\partial p}\bigg|_T . \quad \text{..... (B.52)}$$

Thermal Expansion Coefficient

The thermal expansion coefficient of fluids, β, is defined by

$$\beta = -\frac{1}{\rho}\frac{\partial \rho}{\partial T}\bigg|_p = \frac{1}{V_M}\frac{\partial V_M}{\partial T}\bigg|_p . \quad \text{..... (B.53)}$$

B.2.2 Thermophysical Properties of Water

Thermodynamic Properties – Region 1: Liquid Water

The Gibbs free energy equation for region 1 is given by (Wagner et al. 2000)

$$\frac{g}{RT} = \gamma(\pi,\tau) = \sum_{i=1}^{34} n_i (7.1-\pi)^{I_i} (\tau - 1.222)^{J_i} = \sum_{i=1}^{34} n_i \left(7.1 - \frac{p}{p^*}\right)^{I_i} \left(\frac{T^*}{T} - 1.222\right)^{J_i} \quad \text{..... (B.54)}$$

where g is specific Gibbs free energy, γ is dimensionless Gibbs free energy, n_i is the i-th coefficient of the equation, π is reduced pressure, τ is inverse reduced temperature, I_i and J_i are the i-th exponent of the equation, p is pressure and T is thermodynamic temperature (absolute temperature), and superscript * denotes reducing properties. The reducing pressure (p^*) and temperature (T^*) are 16.53 MPa and 1,386 K, respectively. The coefficients n_i and exponents I_i and J_i should be referred to the original work. Then, with use of the calculated Gibbs free energy, other fluid properties are calculated by following relations:

$$v(\pi,\tau)\frac{p}{RT} = \pi\gamma_\pi \quad \text{..... (B.55)}$$

$$\frac{h(\pi,\tau)}{RT} = \tau\gamma_\tau \quad \text{..... (B.56)}$$

$$\frac{c_p(\pi,\tau)}{R} = -\tau^2\gamma_{\tau\tau} \quad \text{..... (B.57)}$$

where v is specific volume in m^3/kg, h is specific enthalpy in J/kg, c_p is specific isobaric heat capacity in J/(kg·K). It is noted that these unit system depends on the unit of the gas constant R because the left-hand-side of these equations should be dimensionless. The derivatives of the dimensionless Gibbs free energy are given

$$\gamma_\pi = \sum_{i=1}^{34} \left[-n_i I_i (7.1-\pi)^{I_i - 1} (\tau - 1.222)^{J_i} \right] \quad \text{..... (B.58)}$$

$$\gamma_{\tau} = \sum_{i=1}^{34} \left[n_i (7.1 - \pi)^{I_i} J_i (\tau - 1.222)^{J_i - 1} \right] \quad \text{..... (B.59)}$$

$$\gamma_{\tau\tau} = \sum_{i=1}^{34} \left[n_i (7.1 - \pi)^{I_i} J_i (J_i - 1)(\tau - 1.222)^{J_i - 2} \right]. \quad \text{..... (B.60)}$$

Hence, the density and internal energy of the liquid water is given by

$$\rho = \frac{1}{v(\pi, \tau)} \quad \text{..... (B.61)}$$

$$u = h(\pi, \tau) - \frac{p}{\rho} \quad \text{..... (B.62)}$$

where ρ is density in kg/m^3, and u is specific internal energy in J/kg.

Thermodynamic Properties – Region 2: Vapor Water

The Gibbs free energy equation for region 2 is given by (Wagner et al. 2000)

$$\frac{g(p,T)}{RT} = \gamma(\pi, \tau) = \gamma^o(\pi, \tau) + \gamma^r(\pi, \tau) \quad \text{..... (B.63)}$$

where γ^o is an ideal-gas part and γ^r is a residual part of the dimensionless Gibbs free energy. The equation for the ideal-gas part of the dimensionless Gibbs free energy is

$$\gamma^o = \ln \pi + \sum_{i=1}^{9} n_i^o \tau^{J_i^o} = \ln \frac{p}{p^*} + \sum_{i=1}^{9} n_i^o \left(\frac{T^*}{T} \right)^{J_i^o} \quad \text{..... (B.64)}$$

where the reducing pressure (p^*) is 1 MPa and the reducing temperature (T^*) is 540 K. The coefficients and exponents should be referred to the original work.

The equation for the residual part of the dimensionless Gibbs free energy is

$$\gamma^r = \sum_{i=1}^{43} n_i \pi^{I_i} (\tau - 0.5)^{J_i} = \sum_{i=1}^{43} n_i \left(\frac{p}{p^*} \right)^{I_i} \left(\frac{T^*}{T} - 0.5 \right)^{J_i} \quad \text{..... (B.65)}$$

where the reducing pressure (p^*) is 1 MPa and the reducing temperature (T^*) is 540 K. Then, with use of the calculated Gibbs free energy, other fluid properties are calculated by following relations:

$$v(\pi,\tau)\frac{p}{RT} = \pi\left(\gamma_\pi^o + \gamma_\pi^r\right) \quad \text{..... (B.66)}$$

$$\frac{h(\pi,\tau)}{RT} = \tau\left(\gamma_\tau^o + \gamma_\tau^r\right) \quad \text{..... (B.67)}$$

$$\frac{c_p(\pi,\tau)}{R} = -\tau^2\left(\gamma_{\tau\tau}^o + \gamma_{\tau\tau}^r\right) \quad \text{..... (B.68)}$$

where v is specific volume in m^3/kg, h is specific enthalpy in J/kg, and c_p is specific isobaric heat capacity in J/(kg·K). The derivatives of the dimensionless Gibbs free energy are given

$$\gamma_\pi^o = \frac{1}{\pi} \quad \text{..... (B.69)}$$

$$\gamma_\tau^o = \sum_{i=1}^{9} n_i^o J_i^o \tau^{J_i^o - 1} \quad \text{..... (B.70)}$$

$$\gamma_{\tau\tau}^o = \sum_{i=1}^{9} n_i^o J_i^o \left(J_i^o - 1\right)\tau^{J_i^o - 2} \quad \text{..... (B.71)}$$

$$\gamma_\pi^r = \sum_{i=1}^{43} n_i I_i \pi^{I_i - 1}(\tau - 0.5)^{J_i} \quad \text{..... (B.72)}$$

$$\gamma_\tau^r = \sum_{i=1}^{43} n_i \pi^{I_i} J_i (\tau - 0.5)^{J_i - 1} \quad \text{..... (B.73)}$$

$$\gamma_{\tau\tau}^r = \sum_{i=1}^{43} n_i \pi^{I_i} J_i (J_i - 1)(\tau - 0.5)^{J_i - 2} \quad \text{..... (B.74)}$$

Hence, the density and internal energy of the vapor can be computed in the same way.

Thermodynamic Properties – Region 4: Saturation-pressure Equation

The explicit form of the saturation-pressure equation is given as (Wagner et al. 2000)

$$\frac{p_{sat}}{p^*} = \left[\frac{2C}{-B + \left(B^2 - 4AC\right)^{0.5}} \right]^4 \quad \text{..... (B.75)}$$

where

$$A = \theta^2 + n_1\theta + n_2 \quad \text{..... (B.76)}$$

$$B = n_3\theta^2 + n_4\theta + n_5 \quad \text{..... (B.77)}$$

$$C = n_6\theta^2 + n_7\theta + n_8 \quad \text{..... (B.78)}$$

$$\theta = \frac{T_{sat}}{T^*} + \frac{n_9}{\left(T_{sat}/T^*\right) - n_{10}}, \quad \text{..... (B.79)}$$

p^* is 1 MPa and T^* is 1 K. The coefficients of the saturation line should be referred to the original work. It is noted that the correlation is valid within the temperature range of 273.15 K $\leq T \leq$ 647.096 K.

Water Viscosity (Huber et al. 2009)

The formulation for the thermal conductivity of ordinary water has the general form as (Huber et al. 2009)

$$\overline{\mu} = \overline{\mu}_0\left(\overline{T}\right) \times \overline{\mu}_1\left(\overline{T}, \overline{\rho}\right) \times \overline{\mu}_2\left(\overline{T}, \overline{\rho}\right) \quad \text{..... (B.80)}$$

where the first factor of the product represents the viscosity in the zero-density limit, and the second factor and the third factor represent contributions to viscosity due to increasing density. The third factor represents an enhancement of the viscosity near the critical point

(Huber et al. 2009). The viscosity and arguments of the factor are written in the dimensionless form, and they are defined as follows:

$$\bar{\mu} = \frac{\mu}{\mu^*} \quad \text{..... (B.81)}$$

$$\bar{T} = \frac{T}{T^*} \quad \text{..... (B.82)}$$

$$\bar{\rho} = \frac{\rho}{\rho^*} \quad \text{..... (B.83)}$$

where μ^* is 1×10^{-6} Pa·s, T^* is 647.096 K, and ρ^* is 322.0 kg/m^3. The first factor is given by (Huber et al. 2009)

$$\bar{\mu}_0(\bar{T}) = \frac{100\sqrt{\bar{T}}}{\sum_{i=0}^{3} \frac{H_i}{\bar{T}^i}} \quad \text{..... (B.84)}$$

where H_i is the i-th coefficient of the function. The second factor is given by (Huber et al. 2009)

$$\bar{\mu}_1(\bar{T}, \bar{\rho}) = \exp\left[\bar{\rho}\sum_{i=0}^{5}\left\{\left(\frac{1}{\bar{T}} - 1\right)^i \sum_{j=0}^{6} H_{ij}(\bar{\rho} - 1)^j\right\}\right] \quad \text{..... (B.85)}$$

where coefficients H_{ij} are referred to the original work.

The critical enhancement effect, $\bar{\mu}_2$, can be computed with a series of equations, but it is only significant around the critical point (645.91 K < T < 650.77 K, 245.8 kg/m^3 < ρ < 405.3 kg/m^3) (Huber et al. 2009). Therefore, to avoid computational time with certain accuracy as studied in detain in the work by Huber et al. (2009), this term is simply omitted by setting $\bar{\mu}_2$ = 1.

Water Thermal Conductivity (Huber et al. 2012)

The formulation for the thermal conductivity of ordinary water has the general form as (Huber et al. 2012)

$$\bar{\lambda} = \bar{\lambda}_0\left(\bar{T}\right) \times \bar{\lambda}_1\left(\bar{T}, \bar{\rho}\right) + \bar{\lambda}_2\left(\bar{T}, \bar{\rho}\right) \quad \text{..... (B.86)}$$

where the first factor of the product represents the thermal conductivity in the zero-density limit, and the second factor and the third factor represent contributions to thermal conductivity due to increasing density. The third factor represents an enhancement of thermal conductivity near the critical point (Huber et al. 2012). The thermal conductivity and arguments of the factor are written in the dimensionless form, and they are defined as follows:

$$\bar{\lambda} = \frac{\lambda}{\lambda^*} \quad \text{..... (B.87)}$$

$$\bar{T} = \frac{T}{T^*} \quad \text{..... (B.88)}$$

$$\bar{\rho} = \frac{\rho}{\rho^*} \quad \text{..... (B.89)}$$

where λ^* is 1.00 mW/(m·K), T^* is 647.096 K, and ρ^* is 322.0 kg/m^3. The first factor is given by (Huber et al. 2012)

$$\bar{\lambda}_0\left(\bar{T}\right) = \frac{\sqrt{\bar{T}}}{\sum_{k=0}^{4} \frac{L_k}{\bar{T}^k}} \quad \text{..... (B.90)}$$

where L_k is the k-th coefficient of the function. The second factor is given by (Huber et al. 2012)

$$\bar{\lambda}_1(\bar{T},\bar{\rho}) = \exp\left[\bar{\rho}\sum_{i=0}^{4}\left\{\left(\frac{1}{\bar{T}}-1\right)^i\sum_{j=0}^{5}L_{ij}(\bar{\rho}-1)^j\right\}\right] \quad \text{..... (B.91)}$$

where coefficients $L_{ij.}$

B.2.3 Thermophysical Properties of Gas

Density: Real Gas Equation of State

Gas density is estimated by real gas equation of state given by

$$\rho = \frac{M_w}{V_M} = \frac{pM_w}{ZRT}, \quad \text{..... (B.92)}$$

where M_W is the molecular weight of the component.

Gas Viscosity: Empirical Correlation by Sun and Mohanty (2005)

Sun and Mohanty (2005) used the following gas viscosity correlation:

$$\begin{aligned}\mu_G &= 2.4504\times10^{-3} + 2.8764\times10^{-5}T + 3.279\times10^{-9}T^2 \\ &\quad - 3.7838\times10^{-12}T^3 + 2.0891\times10^{-5}\rho_G + 2.5127\times10^{-7}\rho_G^2 \\ &\quad - 5.822\times10^{-10}\rho_G^3 + 1.8378\times10^{-13}\rho_G^4\end{aligned} \quad \text{..... (B.93)}$$

where T is in K, ρ_G is gas density in kg/m^3, and μ_G is in cp.

Thermal Conductivity: Empirical Correlation by Yaws (1995)

According to Yaws (2008), the thermal conductivity of gas is computed by

$$\lambda_G = -0.00935 + 1.4028\times10^{-4}T + 3.3180\times10^{-8}T^2 \quad \text{..... (B.94)}$$

where λ_G is in W/(m·K), and T is in K.

Henry's Coefficient

The Henry's coefficient can be estimated by (Fernández-Prini et al. 2003):

$$\ln\left(\frac{H^g}{p_1^*}\right) = \frac{A}{T_R} + \frac{B\tau^{0.355}}{T_R} + C(T_R)^{-0.41}\exp(\tau) \quad \text{..... (B.95)}$$

where $\tau = 1 - T_R$, $T_R = T/T_{c1}$, T_{c1} is the critical temperature of the solvent (647.096 K for H_2O), and p_1^* is the vapor pressure of the solvent at the temperature of interest. The coefficients of the *A*, *B* and *C* are determined by fitting to the experimental data set in their work. Especially for the CH_4 solubility in H_2O is given by the following constants (Fernández-Prini et al. 2003): $A = -10.44708$, $B = 4.66491$ and $C = 12.12986$ with temperature range between 275.46 K and 633.11 K.

APPENDIX C

SPACE AND TIME DISCRETIZATION

This section discusses discretization of the governing equation. The spatial discretization is conducted by the integral finite difference. In the Chapter II, the final form of the residual equations are shown. This section describes the derivations of the final form.

C.1 Reservoir Model

The spatial and temporal discretization of the reservoir model follows the work by Pruess et al. (1999). As discussed, the general conservation equation is expressed in integral form:

$$\frac{d}{dt}\int_{V_m} M dV = \int_{\Gamma_m} \mathbf{F}\bullet\mathbf{n} d\Gamma + \int_{V_m} q dV \,. \quad \text{..... (C.1)}$$

The accumulation term and sink/source term are evaluated as volume average in the control volume:

$$\int_{V_m} M dV = M_m V_m \quad \text{..... (C.2)}$$

$$\int_{V_m} q dV = q_m V_m \quad \text{..... (C.3)}$$

where M_m and q_m are volume-averaged value of M and q, respectively. The flux term is approximated as a discrete sum of averages over surface segments A_{ml}:

$$\int_{\Gamma_m} \mathbf{F}\bullet\mathbf{n} d\Gamma = \sum_l A_{ml} F_{ml} \quad \text{..... (C.4)}$$

where F_{ml} is average value of the normal component of F over the surface semgent A_{ml} between element m and l (Pruess et al. 1999). Then, the general balance equation becomes

$$\frac{dM_m}{dt} = \frac{1}{V_m}\sum_l A_{ml}F_{ml} + q_m . \quad \text{..... (C.5)}$$

For the time discretization, a first-order finite difference is used. Let current time step be n, and the final form of the difference equation is

$$\frac{M_m^{n+1} - M_m^n}{\Delta t} = \frac{1}{V_m}\sum_l A_{ml}^{n+1}F_{ml}^{n+1} + q_m^{n+1} \quad \text{..... (C.6)}$$

where the spatial terms are evaluated at the new time-step (fully-implcit scheme). Hence, residual equations of the component mass and thermal energy are expressed as

$$R_m^{\kappa,n+1} = M_m^{\kappa,n+1} - M_m^{\kappa,n} - \frac{\Delta t}{V_m}\left(\sum_l A_{ml}F_{ml}^{\kappa,n+1} + V_m q_m^{\kappa,n+1}\right) = 0 \quad \text{..... (C.7)}$$

$$R_m^{\theta,n+1} = M_m^{\theta,n+1} - M_m^{\theta,n} - \frac{\Delta t}{V_m}\left(\sum_l A_{ml}F_{ml}^{\theta,n+1} + V_m q_m^{\theta,n+1}\right) = 0 . \quad \text{..... (C.8)}$$

C.2 Wellbore Model

The major difference in the wellbore model formulation is that the wellbore model is formulated for one-dimensional space with averaging over the cross-section of the wellbore. At first, the one-dimensional conservation equations are integrated over the target control volume, and the difference equations are derived in similar manner as discussed in the reservoir model.

The component mass balance and total energy balance equations are integrated over the control volume of the element m in **Figure 2.5**. The accumulation term and

sink/source terms of the mass balance equations are taken as the volume average:

$$\int_{V_m}\left[\frac{\partial}{\partial t}\left(\sum_{\beta}\alpha_{\beta}\rho_{\beta}X_{\beta}^{\kappa}\right)\right]dV = V_m\frac{\partial}{\partial t}\left(\sum_{\beta}\alpha_{\beta,m}\rho_{\beta,m}X_{\beta,m}^{\kappa}\right) \quad \text{..... (C.9)}$$

$$\int_{V_m}\left[\frac{2\gamma}{r_i}\left(\sum_{\beta}\alpha_{\beta,I}\rho_{\beta,I}X_{\beta,I}^{\kappa}v_{\beta,I}\right)\right]dV = \sum_{\beta}X_{\beta,I}^{\kappa}q_{\beta,I} \quad \text{..... (C.10)}$$

The flux term is also evaluated in the similar manner with the reservoir model:

$$-\int_{V_m}\left[\frac{\partial}{\partial z}\left(\sum_{\beta}\alpha_{\beta}\rho_{\beta}X_{\beta}^{\kappa}v_{\beta,z}\right)\right]dV = \sum_{l}\left(\sum_{\beta}A_{ml}\alpha_{\beta,ml}X_{\beta,ml}^{\kappa}\rho_{\beta,ml}v_{\beta,ml}\right). \quad \text{..... (C.11)}$$

The mass balance equations are spatially discretized into

$$\frac{d}{dt}\left(\sum_{\beta}\alpha_{\beta,m}\rho_{\beta,m}X_{\beta,m}^{\kappa}\right) = \frac{1}{V_m}\left[\sum_{l}\left(\sum_{\beta}A_{ml}\alpha_{\beta,ml}X_{\beta,ml}^{\kappa}\rho_{\beta,ml}v_{\beta,ml}\right)+\sum_{\beta}X_{\beta,I,m}^{\kappa}q_{\beta,I,m}\right] \quad \text{.... (C.12)}$$

With use of the first-order finite difference under fully implicit scheme, the residual equation becomes:

$$R_{v,m}^{\kappa,n+1} = \sum_{\beta}\alpha_{\beta,m}^{n+1}\rho_{\beta,m}^{n+1}X_{\beta,m}^{\kappa,n+1} - \sum_{\beta}\alpha_{\beta,m}^{n}\rho_{\beta,m}^{n}X_{\beta,m}^{\kappa,n} - \frac{\Delta t}{V_m}\left[\sum_{\beta}X_{\beta,I,m}^{\kappa,n+1}q_{\beta,I,m}^{n+1}\right] - \frac{\Delta t}{V_m}\left[\sum_{l}\left(\sum_{\beta}A_{ml}\alpha_{\beta,ml}^{n+1}X_{\beta,ml}^{\kappa,n+1}\rho_{\beta,ml}^{n+1}v_{\beta,ml}^{n+1}\right)\right] = 0 \quad \text{. .... (C.13)}$$

According to the geometry shown in **Figure 2.5**, this is equal to

$$R_{v,m}^{\kappa,n+1} = \sum_{\beta}\alpha_{\beta,m}^{n+1}\rho_{\beta,m}^{n+1}X_{\beta,m}^{\kappa,n+1} - \sum_{\beta}\alpha_{\beta,m}^{n}\rho_{\beta,m}^{n}X_{\beta,m}^{\kappa,n} - \frac{\Delta t}{V_m}\left[\sum_{\beta}X_{\beta,I,m}^{\kappa,n+1}q_{\beta,I,m}^{n+1}\right] - \frac{\Delta t}{V_m}\left[\sum_{\beta}A_p\alpha_{\beta,p}^{n+1}X_{\beta,p}^{\kappa,n+1}\rho_{\beta,p}^{n+1}v_{\beta,p}^{n+1} - \sum_{\beta}A_q\alpha_{\beta,q}^{n+1}X_{\beta,q}^{\kappa,n+1}\rho_{\beta,q}^{n+1}v_{\beta,q}^{n+1}\right] = 0 \quad \text{. .... (C.14)}$$

In similar manner, the total energy balance equation is also discretized into

$$
\begin{aligned}
R_{T,m}^{\kappa,n+1} = & \sum_{\beta} \alpha_{\beta,m}^{n+1} \rho_{\beta,m}^{n+1} \left\{ U_{\beta,m}^{n+1} + \frac{\left(v_{\beta,m}^{n+1}\right)^2}{2} \right\} - \sum_{\beta} \alpha_{\beta,m}^{n} \rho_{\beta,m}^{n} \left\{ U_{\beta,m}^{n} + \frac{\left(v_{\beta,m}^{n}\right)^2}{2} \right\} \\
& - \frac{\Delta t}{V_m} \left[A_p \left\{ \left[\sum_{\beta} \alpha_{\beta,p}^{n+1} \rho_{\beta,p}^{n+1} \left(H_{\beta,p}^{n+1} + \frac{\left(v_{\beta,p}^{n+1}\right)^2}{2} \right) v_{\beta,p}^{n+1} \right] - k_{f,p}^{n+1} \left. \frac{\partial T}{\partial z} \right|_{p}^{n+1} \right\} \right. \\
& \qquad \left. - A_q \left\{ \left[\sum_{\beta} \alpha_{\beta,q}^{n+1} \rho_{\beta,q}^{n+1} \left(H_{\beta,q}^{n+1} + \frac{\left(v_{\beta,q}^{n+1}\right)^2}{2} \right) v_{\beta,q}^{n+1} \right] - k_{f,q}^{n+1} \left. \frac{\partial T}{\partial z} \right|_{q}^{n+1} \right\} \right] \qquad \text{.... (C.15)} \\
& - \Delta t \sum_{\beta} \left(\alpha_{\beta,m}^{n+1} \rho_{\beta,m}^{n+1} g_z v_{\beta,m}^{n+1} \right) - \frac{\Delta t}{V_m} \left\{ \sum_{\beta} q_{\beta,I,m}^{n+1} \left[H_{\beta,I,m}^{n+1} + \frac{\left(v_{\beta,I,m}^{n+1}\right)^2}{2} \right] \right\} \\
& - \frac{\Delta t}{V_m} A_{in,m} \left(1 - \gamma_m\right) U_{T,\mathrm{m}}^{n+1} \left(T_{res,m}^{n+1} - T_m^{n+1} \right) = 0
\end{aligned}
$$

The control volume of the momentum balance equation is shifted to node *p*. Then, the momentum balance equation is integrated over the control volume (V_p) between node $m-1$ and m. We have

$$
\int_{V_p} \frac{\partial}{\partial t} \left(\sum_{\beta} \alpha_{\beta} \rho_{\beta} v_{\beta} \right) dV = V_p \frac{\partial}{\partial t} \left(\sum_{\beta} \alpha_{\beta,p} \rho_{\beta,p} v_{\beta,p} \right) \qquad \text{..... (C.16)}
$$

$$
\begin{aligned}
& \int_{V_p} \left[-\rho_m g_z + \frac{\Gamma}{2A} \rho_{m,p} v_{m,p} \left| v_{m,p} \right| f_{m,p} \right] dV \\
& \qquad = -\rho_{m,p} g_z V_p + V_p \frac{\Gamma}{2A} \rho_{m,p} v_{m,p} \left| v_{m,p} \right| f_{m,p}
\end{aligned}
\qquad \text{..... (C.17)}
$$

The flux term is also evaluated in the similar manner with the reservoir model:

$$
\begin{aligned}
& - \int_{V_p} \left[\frac{\partial}{\partial z} \left(\sum_{\beta} \alpha_{\beta,p} \rho_{\beta,p} v_{\beta,p}^2 \right) + \frac{\partial p}{\partial z} \right] dV \\
& \qquad = \sum_{l} A_{pl} \left(\left[\sum_{\beta} \alpha_{\beta,pl} \rho_{\beta,pl} v_{\beta,pl}^2 \right] + p_{pl} \right)
\end{aligned}
\qquad \text{..... (C.18)}
$$

where subscripts *pl* denotes properties at the interface between subdomain *p* and *l*. The momentum balance equation is spatially discretized into

$$\frac{d}{dt}\left(\sum_{\beta}\alpha_{\beta,p}\rho_{\beta,p}v_{\beta,p}\right)=\frac{1}{V_p}\sum_{l}A_{pl}\left(\left[\sum_{k}\alpha_{\beta,pl}\rho_{\beta,pl}v_{\beta,pl}^{2}\right]+p_{pl}\right) \\ -\frac{\Gamma}{2A}\rho_{m,p}v_{m,p}\left|v_{m,p}\right|f_{m,p}+\rho_{m,p}g_z \quad \text{..... (C.19)}$$

With use of the first-order finite difference under fully implicit scheme, the residual equation becomes:

$$R_{P,p}^{n+1}=\sum_{\beta}\alpha_{\beta,p}^{n+1}\rho_{\beta,p}^{n+1}v_{\beta,p}^{n+1}-\sum_{k}\alpha_{\beta,p}^{n}\rho_{\beta,p}^{n}v_{\beta,p}^{n}-\rho_{m,p}^{n+1}g_z\Delta t \\ +\frac{\Gamma}{2A}\rho_{m,p}^{n+1}v_{m,p}^{n+1}\left|v_{m,p}^{n+1}\right|f_{m,p}^{n+1}\Delta t \\ +\frac{\Delta t}{V_p}\left[A_m\left(\sum_{\beta}\alpha_{\beta,m}^{n+1}\rho_{\beta,m}^{n+1}v_{\beta,m}^{n+1}v_{\beta,m}^{n+1}\right)\right. \\ \left.-A_{m-1}\left(\sum_{\beta}\alpha_{\beta,m-1}^{n+1}\rho_{\beta,m-1}^{n+1}v_{\beta,m-1}^{n+1}v_{\beta,m-1}^{n+1}\right)\right] \\ +\frac{\Delta t}{V_p}\left[A_m p_m^{n+1}-A_{m-1}p_{m-1}^{n+1}\right]=0 \quad \text{..... (C.20)}$$

APPENDIX D

MODEL VERIFICATIONS

This section shows a series of verification cases for the developed numerical code by comparing simulation results with those given by analytical or semi-analytical solutions. Some verification cases related with the main topic of this work are shown in the Chapter II. This section focuses on the verification of the numerical code as the general purpose reservoir and wellbore simulator.

D.1 Reservoir Model

D.1.1 Case 1: 1D Radial Diffusivity Equation (Pressure Transient Testing)

Under isothermal condition, the radial diffusivity equation is formulated as (Dake 1978)

$$\frac{1}{r}\frac{\partial}{\partial r}\left(\frac{k\rho}{\mu}r\frac{\partial p}{\partial r}\right)=\phi c_t\rho\frac{\partial p}{\partial t} \quad \text{..... (D.1)}$$

where ρ is the fluid density, ϕ is the porosity, c_t is the total compressibility of the reservoir, μ is the viscosity of the fluid and k is intrinsic permeability of the reservoir. For slightly compressible fluid, with some assumptions, this partial differential equation is linearized with no special treatment, and it can be solved with associated initial and boundary conditions. For compressible fluid, the nonlinearity of the fluid properties has an important role in the diffusivity equation. To linearize the diffusivity equation, the pseudo-pressure is introduced (Al-Hussainy et al. 1966):

$$m(p) = 2\int_{p_{ref}}^{p} \frac{p}{\mu Z}\, dp \quad \text{..... (D.2)}$$

where p_{ref} is the reference pressure. With use of the pseudo-pressure, the radial diffusivity equation is rearranged into

$$\frac{1}{r}\frac{\partial}{\partial r}\left(r\frac{\partial m}{\partial r}\right) = \frac{\phi c_t \mu}{k}\frac{\partial m}{\partial t}. \quad \text{..... (D.3)}$$

It is noted that this equation is not fully linearized because of the non-linerarity of the total compressibility. To obtain same form of the dimensionless diffusivity equation, the total compressibility and fluid viscosity are assumed to be constant, or small change from the initial value.

This verification study investigates finite acting no flow boundary condition at the outer boundary of the domain. The reservoir is cylindrical reservoir with a single layer (fully-penetrated completion), and the reservoir is assumed to be isotropic and homogeneous.

Slightly Compressible Fluid: Water

For slightly compressible fluid with constant discharge (q_d) at the wellbore face ($r = r_w$), the Laplace space solution is given by Everdingen and Hurst (1949), and it can be expressed in terms of dimensionless numbers as follows:

$$\bar{p}_D(r_D, u_l) = \frac{K_0\left(\sqrt{u_l}\, r_D\right) I_1\left(\sqrt{u_l}\, r_{eD}\right) + K_1\left(\sqrt{u_l}\, r_{eD}\right) I_0\left(\sqrt{u_l}\, r_D\right)}{u_l\left[\sqrt{u_l} K_1\left(\sqrt{u_l}\right) I_1\left(\sqrt{u_l}\, r_{eD}\right) - \sqrt{u_l} I_1\left(\sqrt{u_l}\right) K_1\left(\sqrt{u_l}\, r_{eD}\right)\right]} \quad \text{..... (D.4)}$$

where u_l is the Laplace space variable, $\bar{p}_D$ is dimensionless pressure in the Laplace space, K_n is the modified Bessel function of zero kind, I_n is the modified Bessel function of first

kind), and dimensionless parameters are expressed with reservoir outer radius, r_e, and initial reservoir pressure, p_i, as

$$p_D = \frac{2\pi kh}{q_d \mu}\left(p_i - p(r,t)\right) \quad \text{..... (D.5)}$$

$$r_D = \frac{r}{r_w} \quad \text{..... (D.6)}$$

$$r_{eD} = \frac{r_e}{r_w}. \quad \text{..... (D.7).}$$

The real space pressure solutions are obtained by numerical Laplace inversion algorithm proposed by Stehfest (1970). For slightly compressible fluid with constant bottom-hole pressure at the wellbore face, the Laplace space solution is given as (Ehlig-Economides 1979)

$$\bar{p}_{cpD}(r_D, u_l) = \frac{K_1\left(\sqrt{u_l} r_{eD}\right) I_0\left(\sqrt{u_l} r_D\right) + K_0\left(\sqrt{u_l} r_D\right) I_1\left(\sqrt{u_l} r_{eD}\right)}{u_l\left[K_0\left(\sqrt{u_l}\right) I_1\left(\sqrt{u_l} r_{eD}\right) + I_0\left(\sqrt{u_l}\right) K_1\left(\sqrt{u_l} r_{eD}\right)\right]} \quad \text{..... (D.8)}$$

where the dimensionless properties are expressed as

$$p_{cpD}(r_D, t_D) = \frac{p_i - p(r,t)}{p_i - p_{wf}} \quad \text{..... (D.9)}$$

$$t_D = \frac{kt}{\phi \mu c_t r_w^2}. \quad \text{..... (D.10)}$$

TABLE D.1 summarizes input data for the slightly compressible fluid case. This case assumes constant density (702.5 kg/m^3), constant viscosity (4.23 × 10^{-4} Pa-s), and constant fluid compressibility (10^{-10} 1/Pa). A cylindrical reservoir (1D) is discretized into 400 grids with logarithmic spacing to account for the diffusive nature of the pressure

solution. For the constant rate condition, the rate is set to 0.25 kg/s (production). On the other hand, the constant bottom-hole pressure condition is operated at 5 MPa.

TABLE D.1—INPUT DATA
(RESERVOIR MODEL CASE 1: SLIGHTLY-COMPRESSIBLE FLUID)

Parameter	Value
Permeability, mD	180
Porosity, fraction	0.18
Initial reservoir pressure, MPa	25
Initial reservoir temperature, °C	42
Pore compressibility, 1/Pa	1.00×10^{-9}
Outer radius, m	10,000

Figure D.1 shows comparisons of pressure distributions given by the above analytical solutions and the numerical simulations with constant rate and constant bottom-hole pressure condition for the slightly compressible fluid. The pressure profiles are shown for four different time (10 day, 100 day, 365 day and 730 day), and these results show satisfactory agreement.

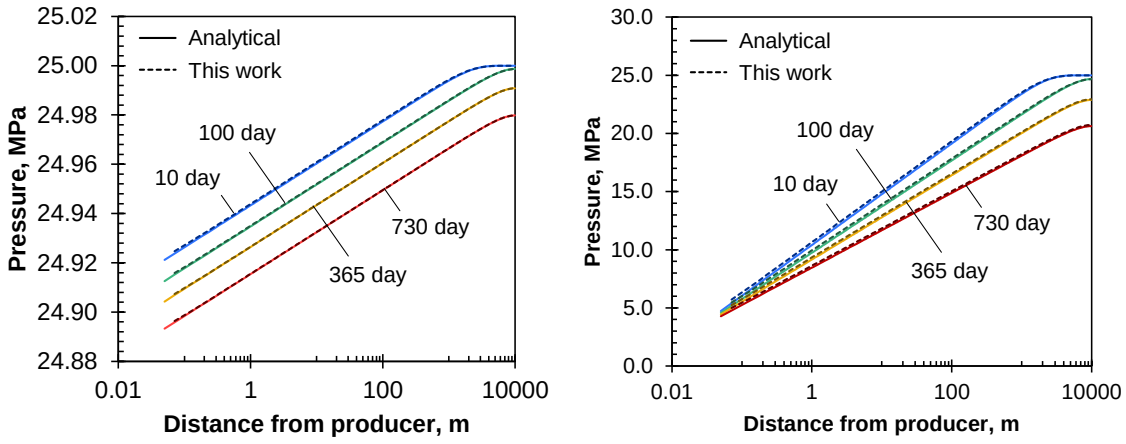

(a) Constant rate (b) Constant bottom-hole pressure

Figure D.1—Comparison of pressure distribution
(reservoir model case 1: slightly compressible fluid)

Compressible Fluid: Non-condensable Gas

For compressible fluids, the radial diffusivity equations is expressed in terms of the pseudo-pressure. In analogous to slightly compressible fluids, the Laplace space solution for compressible fluids with constant discharge can be given as (Blasingame 1993):

$$\overline{m}_D(r_D,u_l)=\frac{K_0\left(\sqrt{u_l}r_D\right)I_1\left(\sqrt{u_l}r_{eD}\right)+K_1\left(\sqrt{u_l}r_{eD}\right)I_0\left(\sqrt{u_l}r_D\right)}{u_l\left[\sqrt{u_l}K_1\left(\sqrt{u_l}\right)I_1\left(\sqrt{u_l}r_{eD}\right)-\sqrt{u_l}I_1\left(\sqrt{u_l}\right)K_1\left(\sqrt{u_l}r_{eD}\right)\right]} \quad \text{..... (D.11)}$$

where $\overline{m}_D$ is dimensionless pseudo-pressure in the Laplace space and, in real space, the dimensionless pseudo-pressure is

$$m_D=\frac{\mu_i Z_i}{2p_i}\frac{2\pi kh}{q\mu_i}\left(m(p_i)-m(p(r,t))\right) \quad \text{..... (D.12)}$$

where μ_i and Z_i are initial viscosity and initial compressibility factor, respectively. Once the pseudo-pressure is obtained, the pressure is inversely calculated with the relation in Eq. D.2. In similar manner, the constant pressure solution is given based on Ehlig-Economides (1979) as

$$\overline{m}_{cpD}(r_D,u_l)=\frac{K_1\left(\sqrt{u_l}r_{eD}\right)I_0\left(\sqrt{u_l}r_D\right)+K_0\left(\sqrt{u_l}r_D\right)I_1\left(\sqrt{u_l}r_{eD}\right)}{u_l\left[K_0\left(\sqrt{u_l}\right)I_1\left(\sqrt{u_l}r_{eD}\right)+I_0\left(\sqrt{u_l}\right)K_1\left(\sqrt{u_l}r_{eD}\right)\right]} \quad \text{..... (D.13)}$$

where

$$m_{cpD}(r_D,t_D)=\frac{m(p_i)-m(p(r,t))}{m(p_i)-m(p_{wf})}. \quad \text{..... (D.14)}$$

For the compressible fluid case, the reservoir set up is same with the slightly compressible fluid case (**TABLE D.1**). The reservoir fluid is assumed as methane, and fluid properties are calculated with the critical properties summarized in **TABLE D.2**. The

boundary conditions are same: constant rate (0.25 kg/s production) and constant bottom-hole pressure (5 MPa).

TABLE D.2—CRITICAL PROPERTIES OF METHANE	
Parameter	Value
Molecular weight, g/g-mol	16.043
Critical pressure, Pa	4,599,200
Critical temperature, K	190.564
Acentric factor, -	0.01142

Figure D.2 shows comparisons of pressure distributions given by the above analytical solutions and the numerical simulations with constant rate and constant bottom-hole pressure condition. These results show satisfactory agreement. The **Figure D.2a** shows slight deviations near producer visually, but the magnitude is quite small because the pressure change itself is quite small compared with the case with constant bottom-hole pressure. It is noted that, at the high pressure change regions, the deviation seem to get larger because the assumption of the constant compressibility is not valid.

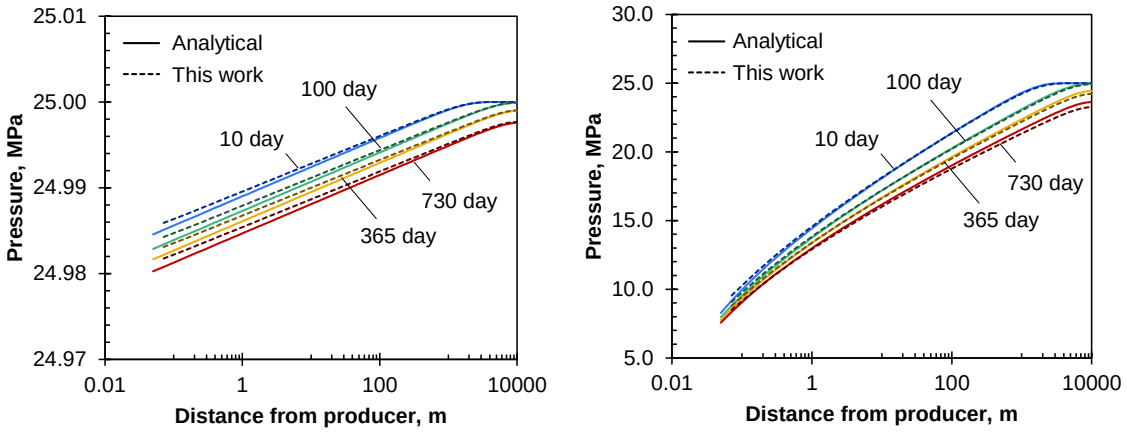

(a) Constant rate (b) Constant bottom-hole pressure

Figure D.2—Comparison of pressure distribution (reservoir model case 1: compressible fluid)

These results verify the transient reservoir flow model under the isothermal condition, and it also verifies the implementation to account for the radial flow geometry.

D.1.2 Case 2: 1D Transient Heat Conduction

This case considers 1D heat conduction in the reservoir domain to verify thermal accumulation term and conductive heat transport term. This case assumes that that there is no fluid flow in the reservoir, single phase water exists in the pore space, and the total thermal conductivity is constant and isotropic. **Figure D.3** shows a schematic of the problem domain.

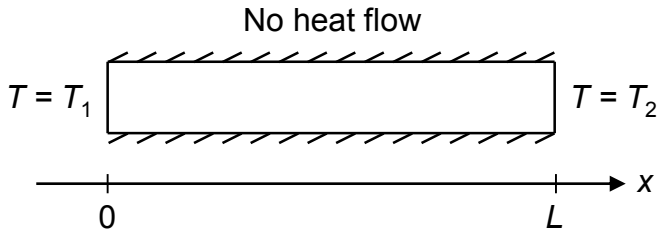

Figure D.3—Schematic of 1D reservoir for heat conduction problem

The reservoir thermal model is reduced into:

$$\left[\phi\rho_A C_{p,A} + (1-\phi)\rho_s C_{p,s}\right]\frac{\partial T}{\partial t} = k_{Tt}\frac{\partial^2 T}{\partial x^2}. \quad \text{..... (D.15)}$$

When all of the fluid properties are assumed to be constant, this equation is further rearranged into

$$\frac{\partial T}{\partial t} = \alpha_{th}\frac{\partial^2 T}{\partial x^2} \quad (x \in [0, L]) \text{..... (D.16)}$$

where α_{th} is thermal diffusivity defined as

$$\alpha_{th} = \frac{k_{Tt}}{\phi\rho_A C_{p,A} + (1-\phi)\rho_s C_{p,s}}. \quad \text{..... (D.17)}$$

Initial and boundary conditions are:

$$T(x,0) = T_0 \quad (x \in [0, L]) \quad \text{..... (D.18)}$$

$$T(0,t) = T_1 \quad \text{..... (D.19)}$$

$$T(L,t) = T_2. \quad \text{..... (D.20)}$$

The analytical solution is given by Carslaw and Jaeger (1959):

$$T(x,t) = T_1 + \frac{x}{L}(T_2 - T_1) + \frac{2}{\pi}\sum_{m=1}^{\infty}\frac{1}{m}\left[(-1)^m(T_2 - T_0) + T_0 - T_1\right]\sin\left(\frac{m\pi}{L}x\right)e^{-\left(\frac{m\pi}{L}\right)^2\alpha_{th}t}. \quad \text{..... (D.21)}$$

Under steady-state condition ($t \to \infty$), the temperature distribution leads to

$$T(x,t) = T_1 + \frac{x}{L}(T_2 - T_1). \quad (x \in [0, L]) \quad \text{..... (D.22)}$$

TABLE D.3 summarises reservoir and fluid properties used in this case. The initial temperature (T_0) is set to 122 °F. The left boundary temperature (T_1) is suddenly changed to 212 °F and the temperature is fixed for the entire simulation time. The right boundary temperature (T_2) is fixed to the initial resevoir temperature, 122 °F.

Figure D.4a shows temperature profiles at initial condition, 50 days, 100 day and 300 days, and the numerical simulation results by this work show satisfactory agreement on the transient temperature profile. **Figure D.4b** shows temperature profiles given by analytical solution under steady-state condition with the simulated temperature profile at 1,000 days. These results show satisfactory agreements against analytical solutions.

TABLE D.3—RESERVOIR AND FLUID PROPERTIES (RESERVOIR MODEL CASE 2)		
Type	Property	Value
Reservoir	Length, ft	50
	Width, ft	50
	Height, ft	50
	Total thermal conductivity, Btu/(hr-ft-°F)	2.5
	Rock density, lbm/ft^3	148.58
	Porosity, fraction	0.2
	Rock heat capacity, Btu/(lbm-°F)	0.202
Fluid	Fluid density, lbm/ft^3	63.04
	Fluid specific heat, Btu/(lbm-°F)	1.002

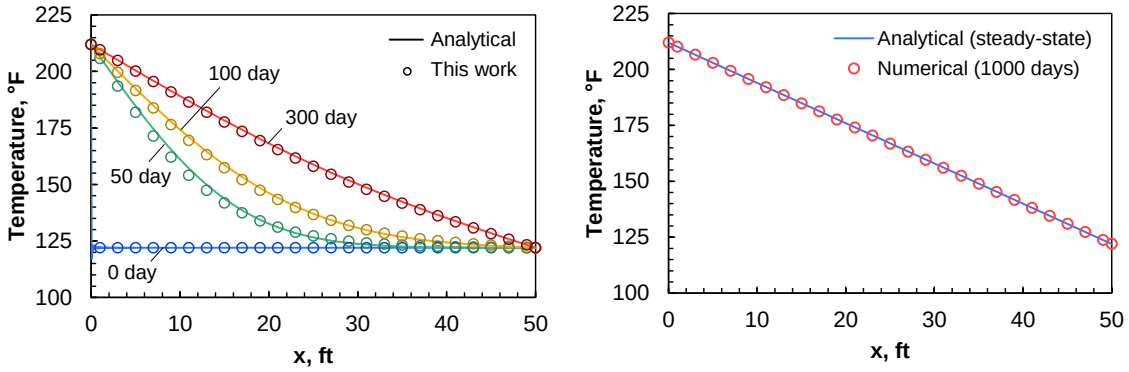

(a) Transient solution (b) Steady-state solution

Figure D.4—Comparison of temperature distribution (reservoir model case 2)

This verificaiton successfully verified the implementation of the one of the transient term and also the conductive heat transfer in the reservoir.

D.1.3 Case 3: 1D Steady-state Mass Flow and Transient Heat Flow Problem

This problem considers one-dimensional, radial, steady-state flow and transient heat transport in a single-phase liquid water. The purpose is to verify terms of the conductive and advective energy transport under single-phase flow condition.

This case considers a cylindrical reservoir with one layer. The inner boundary condition is constant rate with constant temperature (smaller than initial reservoir temperature), and the outer boundary is fixed to the initial condition for the entire simulation. Faust and Mercer (1976) showed analytical solutions developed by Avdonin for one-dimensional, radial flow with heat conduction in the orthogonal direction.

TABLE D.4 summarises properties used in this verification cases based on the code comparison study by Faust et al. (1980). The inner boundary condition is constaint injection rate at 10 kg/s with fixed temperature 160°C, and the outer boundary condition is constant pressure (50 bars) and constant temperature (170 °C).

TABLE D.4—RESERVOIR PROPERTIES (RESERVOIR MODEL CASE 3)

Property	Value
Reservoir outer radius, m	1,000
Reservoir inner radius, m	0
Initial pressure, bar	50
Initial temperature, °C	170
Thickness, m	100
Permeability, m2	1.0×10^{-12}
Density, kg/m3	2,500
Specific heat, J/(kg-°C)	1,000
Thermal conductivity, W/(m-°C)	20
Porosity, fraction	0.2

Figure D.5 shows comparisons of temperature profiles given by the Avdonin solution and the numerical simulation at 10^9 seconds. As shown, the injected fluid is heated up within around 500 m from the injection point. These results are showing satisfactory agreements to verify the implementation of the code on the terms of thermal accumulation, and advective and conductive heat fluxes.

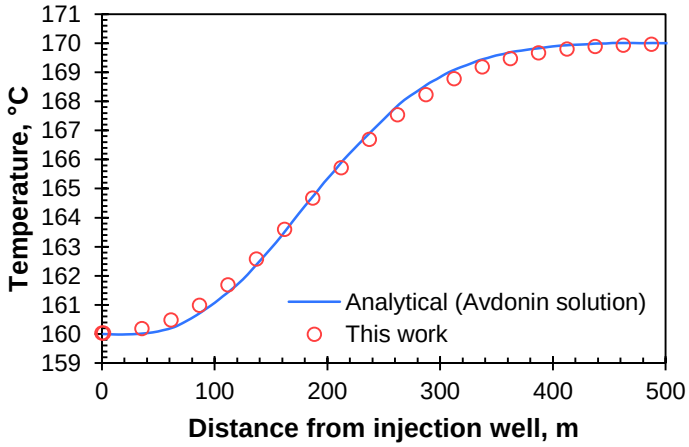

Figure D.5—Comparison of temperature distribution at time = 10^9 seconds (reservoir model case 3)

D.1.4 Case 4: 1D Steady-state Solution of Single Phase Flow and Thermal Model

Yoshioka et al. (2007) showed the analytical temperature solution for steady state single phase flow and heat transfer problem. In their model, they considered box-shaped reservoir geometry with a horizontal wellbore placed at the center. The side of the reservoir is supported by the constant pressure boundary condition, and the pressure distribution is computed based on the radial and linear flow path proposed by Furui et al. (2003). This case verifies spatial terms including the Joule-Thomson effects and the mixed coordinate system.

The general form of the governing equation for the reservoir thermal model is expressed as (Yoshioka et al. 2005)

$$\rho C_p \mathbf{v} \bullet \nabla T - \beta T \mathbf{v} \bullet \nabla p - \nabla \bullet (\mathbf{K}_T \bullet \nabla T) + \mathbf{v} \bullet \nabla p = 0 \quad \text{..... (D.23)}$$

where $\mathbf{K_T}$ is the total thermal conductivity tensor. In their model, the reservoir flow geometry is separated into a linear flow region and a radial flow region. In the linear flow

region, by considering the 1D linear flow model in the *y*-direction, the reservoir thermal model is reduced into the following form:

$$\rho C_p v_l \frac{dT}{dy} - \beta T v_l \frac{dp}{dy} + v_l \frac{dp}{dy} - k_{Tt} \frac{d^2T}{dy^2} = 0 \quad \text{..... (D.24)}$$

where y is coordiante, v_l is Darcy velocity in linear flow region. The solution of the second-order ordinary differential equation is given by

$$T(y) = L_1 e^{m_+ y} + L_2 e^{m_- y} + \frac{1}{\beta} \quad \text{..... (D.25)}$$

where L_1 and L_2 are integration constants to be determined by boundary conditions, and

$$m_{\pm} = \frac{q}{4hL}\left[\frac{\rho C_p}{k_{Tt}} \pm \sqrt{\left(\frac{\rho C_p}{k_{Tt}}\right)^2 + \frac{4\beta\mu}{k k_{Tt}}}\right]. \quad \text{..... (D.26)}$$

The reservoir thermal model in the radial flow region is also simplified into

$$\rho C_p v_r \frac{dT}{dr} - \beta T v_r \frac{dp}{dr} + v_r \frac{dp}{dr} - k_{Tt} \frac{1}{r} \frac{d}{dr}\left(r \frac{dT}{dr}\right) = 0 \quad \text{..... (D.27)}$$

where r is coordinate in radial flow region and v_r is Darcy velocity in radial flow region. The solution of the second-order ordinary differential equation is given by

$$T(r) = R_1 e^{n_+} + R_2 e^{n_-} + \frac{1}{\beta} \quad \text{..... (D.28)}$$

where R_1 and R_2 are integration constants to be determined by boundary conditions, and

$$n_{\pm} = \frac{q}{4\pi L}\left[\frac{\rho C_p}{K_T} \pm \sqrt{\left(\frac{\rho C_p}{K_T}\right)^2 + \frac{4\beta\mu}{k K_T}}\right]. \quad \text{..... (D.29)}$$

The boundary conditions of their model are

$$T\Big|_{y=\frac{Y}{2}} = T_0 \quad \text{..... (D.30)}$$

$$T\Big|_{r=\frac{h}{2}} = T\Big|_{y=\frac{h}{2}} \quad \text{..... (D.31)}$$

$$\left.\frac{dT}{dr}\right|_{r=\frac{h}{2}} = \left.\frac{dT}{dy}\right|_{y=\frac{h}{2}} \quad \text{..... (D.32)}$$

$$K_T \left.\frac{dT}{dr}\right|_{r=r_w} = U_T\left(T\Big|_{r=r_w} - T_b\right) \quad \text{..... (D.33)}$$

Finally, with the boundary conditions, the integration constants are determined in the form:

$$L_1 = \frac{l_1 + l_2}{\psi_+ + \psi_-} \quad \text{..... (D.34)}$$

$$L_2 = \frac{l_3 + l_4}{\psi_+ + \psi_-} \quad \text{..... (D.35)}$$

$$R_1 = \frac{\theta_1 + \theta_2}{\psi_+ + \psi_-} \quad \text{..... (D.36)}$$

$$R_2 = \frac{\theta_3 + \theta_4}{\psi_+ + \psi_-} \quad \text{..... (D.37)}$$

where

$$l_1 = r_w^{n_-} e^{\frac{h}{2}m_-}\left(-K_T n_- + U_T r_w\right)\left(\beta T_0 - 1\right)\left(\frac{h}{2}\right)^{n_+}\left(\frac{h}{2}m_- - n_+\right) \quad \text{..... (D.38)}$$

$$l_2 = \left(\frac{h}{2}\right)^{n_-}\left[e^{\frac{h}{2}m_-} r_w^{n_+}\left(-\frac{h}{2}m_- + n_-\right)\left(-K_T n_+ + U_T r_w\right)\left(\beta T_0 - 1\right) + e^{\frac{Y}{2}m_-} U_T r_w\left(\frac{h}{2}\right)^{n_+}\left(\beta T_b - 1\right)\left(n_+ - n_-\right)\right] \quad \text{..... (D.39)}$$

$$l_3 = r_w^{n_+} e^{\frac{h}{2}m_-} \left(K_T n_- - U_T r_w\right)\left(\beta T_0 - 1\right)\left(\frac{h}{2}\right)^{n_+}\left(\frac{h}{2}m_+ + n_+\right) \quad \text{..... (D.40)}$$

$$l_4 = \left(\frac{h}{2}\right)^{n_-}\left[e^{\frac{h}{2}m_+} r_w^{n_+}\left(\frac{h}{2}m_+ - n_-\right)\left(-K_T n_+ + U_T r_w\right)\left(\beta T_0 - 1\right) - e^{\frac{Y}{2}m+} U_T r_w \left(\frac{h}{2}\right)^{n_+}\left(\beta T_b - 1\right)\left(n_+ - n_-\right)\right] \quad \text{..... (D.41)}$$

$$\theta_1 = e^{\frac{h}{2}(m_+ + m_-)}\frac{h}{2} r_w^{n_-}\left(m_+ - m_-\right)\left(K_T n_- - U_T r_w\right)\left(\beta T_0 - 1\right) \quad \text{..... (D.42)}$$

$$\theta_2 = \left(\frac{h}{2}\right)^{n_-}\left(\beta T_b - 1\right) U_T r_w \left[e^{\frac{h}{2}m_+ + \frac{Y}{2}m_-}\left(\frac{h}{2}m_+ - n_-\right) + e^{\frac{Y}{2}m_+ + \frac{h}{2}m_-}\left(-\frac{h}{2}m_- + n_-\right)\right] \quad \text{..... (D.43)}$$

$$\theta_3 = e^{\frac{h}{2}(m_+ + m_-)}\frac{h}{2} r_w^{n_+}\left(m_+ - m_-\right)\left(-K_T n_+ + U_T r_w\right)\left(\beta T_0 - 1\right) \quad \text{..... (D.44)}$$

$$\theta_4 = \left(\frac{h}{2}\right)^{n_+}\left(\beta T_b - 1\right) U_T r_w \left[e^{\frac{h}{2}m_- + \frac{Y}{2}m_+}\left(\frac{h}{2}m_- - n_+\right) + e^{\frac{Y}{2}m_- + \frac{h}{2}m_+}\left(-\frac{h}{2}m_+ + n_+\right)\right] \quad \text{..... (D.45)}$$

$$\psi_\pm = \beta r_w^{n_\pm}\left(\frac{h}{2}\right)^{n_\mp}\left(K_T n_\pm - U_T r_w\right)\left[e^{\frac{Y}{2}m_\pm + \frac{h}{2}m_\mp}\left(\frac{h}{2}m_\mp - n_\mp\right) + e^{\frac{h}{2}m_\pm + \frac{Y}{2}m_\mp}\left(-\frac{h}{2}m_\pm + n_\mp\right)\right]. \quad \text{..... (D.46)}$$

It is noted that the thermodynamic temperature in K needs to be used in the analytical solution because their thermal model is expressed in temperature by decomposing the enthalpy difference by contributions of pressure and temperature (Bird et al. 2002).

TABLE D.5 and **TABLE D.6** summarize properties of reservoir and wellbore and fluid properties, respectively. The wellbore pressure is fixed, and the drawdown is 400 psi.

TABLE D.5—PROPERTIES OF RESERVOIR AND WELLBORE (RESERVOIR MODEL CASE 4)

Type	Property	Value
Reservoir	Length, ft	50
	Width, ft	3,000
	Height, ft	50
	Permeability, mD	50
	Pressure at outer boundary, psi	4,000
	Temperature at outer boundary, °F	180.0
Wellbore	Wellbore radius, ft	0.25
	Bottom-hole pressure, psi	3,600

TABLE D.6—FLUID PROPERTIES (RESERVOIR MODEL CASE 4)

Property	Fluid Type		
	Oil	Water	Gas
Density, lbm/ft^3	40	63.044	13
Viscosity, cP	0.38	0.48	0.0257
Thermal expansion coefficient, 1/°F	0.000679	0.000311	0.00236
Specific heat, Btu/(lbm-°F)	0.524	1.002	0.587
Total thermal conductivity, Btu/(hr-ft-°F)	2	2.5	1.3

Figure D.6 shows pressure distributions given by the analytical solution (Furui et al. 2003) and the numerical simulation (this work) from the wellbore to the reservoir outer boundary. The profiles are shown in both of the Cartesian coordinate (**Figure D.6a**) and the semi-log scale to elevate the near wellbore region (**Figure D.6b**). The results show satisfactory agreement in both linear flow region and radial flow region. **Figure D.7** shows temperature distributions by the analytical solution (Yoshioka et al. 2007) and the numerical simulation (this work) in the Cartesian coordinate and the semi-log coordinate.

The different fluids are expressed in different colors (oil: green, water: blue and gas: red). These results show satisfactory agreement on all three fluid types.

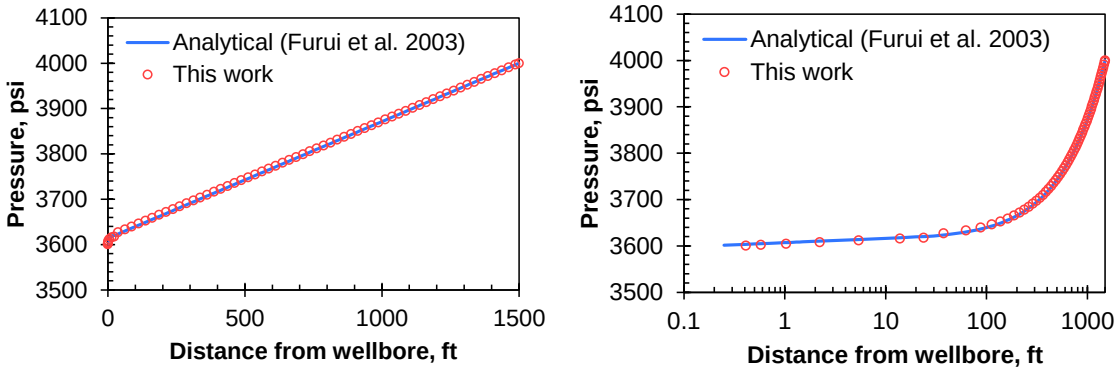

Figure D.6—Comparison of pressure distribution (reservoir model case 3)

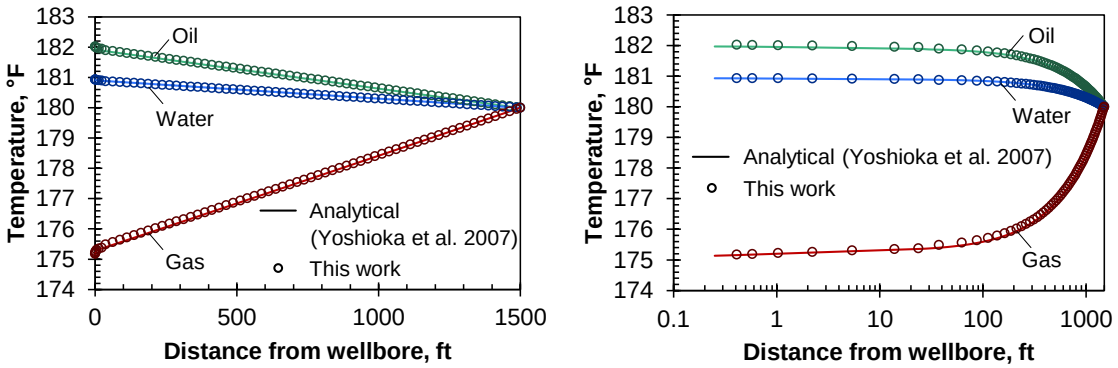

Figure D.7—Comparison of temperature distribution (reservoir model case 3)

This case verifies the successful implementation of the spatial terms in both reservoir flow and thermal model, and the validity of the local grid refinement near the wellbore region to account for the radial flow convergence.

D.2 Wellbore Model

D.2.1 Case 1: Steady-state Single Phase Flow and Thermal Model in a Horizontal Well

Under steady state condition, the wellbore flow/thermal models are reduced into set of ordinary differential equations with respect to spatial coordinates. These can be solved with considerations of boundary conditions.

This study considers one-dimensional horizontal well (**Figure D.8**) under steady-state condition with single phase flow. Three scenarios are considered: injection into a non-perforated cased well, production from a non-perforated cased well, and production from an open-hole well. While boundary conditions for each scenario are defined at edges in the axial direction of the well, we also need to determine the conditions at the contact between the reservoir and the wellbore. These are related to terms of the inflow/outflow velocity and the heat transfer between the domains.

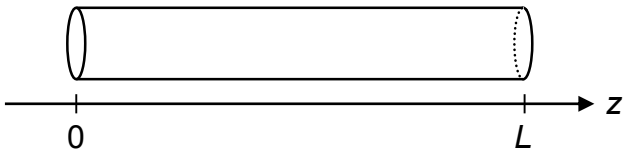

Figure D.8—Schematic of 1D horizontal well

Water Injection into a Non-perforated Cased Horizontal Well

Let us assume following conditions:

- constant fluid properties and single phase flow
- constant geothermal temperature (T_{res})
- no slip condition at the wall

– negligible kinetic energy contribution in energy balance equation

– no outflux at the contact of the wellbore and the reservoir ($v_I = 0$ and $\gamma = 0$)

Under these assumptions, the wellbore model is reduced into:

$$\frac{dv}{dz} = 0 \quad \text{..... (D.47)}$$

$$\frac{dp}{dz} = -\rho \frac{d}{dz}(vv) + \rho g_z - \frac{\rho v|v| f}{r_i} \quad \text{..... (D.48)}$$

$$\rho \frac{d}{dz}(Hv) = k_f \frac{d^2T}{dz^2} + \rho g_z v + \frac{2}{r_i} U_T\big|_{r=r_i}(T_{res} - T) \quad \text{..... (D.49)}$$

and boundary conditions are expressed as

$$v(z=0) = v_{inj} \quad \text{..... (D.50)}$$

$$p(z=0) = p_{inj} \quad \text{..... (D.51)}$$

$$T(z=0) = T_{inj} \quad \text{..... (D.52)}$$

$$\left.\frac{dT}{dz}\right|_{z=L} = 0 \quad \text{..... (D.53)}$$

where L is the length of the well and subscript *inj* denotes properties of injected fluid at inlet position. The first three boundary conditions denote constant rate, pressure and temperature at the inlet. The fourth boundary condition denotes the no heat flux condition in the axial direciton at the toe of the well.

Velocity profile is obtained by integrating the continuity equation over the domain of $z \in [0, z]$ with the boundary condition as:

$$v(z) = v_{inj}. \quad \text{..... (D.54)}$$

The velocity is constant in the domain, and the derivative of the velocity with respect to z becomes zero. Substitute this into the momentum balance equation, and the pressure profile is obtained by integrating it as

$$p(z) = p_{inj} + \left(\rho g_z - \frac{\rho v_{inj}^2 \overline{f}}{r_i} \right) z \quad \text{..... (D.55)}$$

where $\overline{f}$ is average friction factor:

$$\overline{f} = \frac{1}{z} \int_{z=0}^{z} f dz \,. \quad \text{..... (D.56)}$$

With these relations, the energy balance equation is rearranged into

$$k_f \frac{d^2T}{dz^2} - \rho v_{inj} C_p \frac{dT}{dz} - \left[\frac{2}{r_i} U_T \Big|_{r=r_i} - v_{inj} \beta \left(\rho g_z - \frac{\rho v_{inj}^2 \overline{f}}{r_i} \right) \right] T + \frac{2}{r_i} U_T \Big|_{r=r_i} T_{res} + \frac{\rho v_{inj}^3 \overline{f}}{r_i} = 0 \quad \text{.... (D.57)}$$

where the following thermodynamic relation of specific enthalpy on pressure and temperature (Bird et al. 2002) is used:

$$dH = \left(\frac{\partial H}{\partial T} \right)_p dT + \left(\frac{\partial H}{\partial p} \right)_T dp = C_p dT + \frac{1}{\rho} (1 - \beta T) dp \,. \quad \text{..... (D.58)}$$

The Eq. D.57 is rearranged into a second order liner ordinary equation:

$$\frac{d^2T}{dz^2} + b_1 \frac{dT}{dz} + c_1 T + d_1 = 0 \quad \text{..... (D.59)}$$

where

$$b_1 = -\frac{\rho v_{inj} C_p}{k_f} \quad \text{..... (D.60)}$$

$$c_1 = -\frac{1}{k_f}\left[\frac{2}{r_i}U_T\big|_{r=r_i} - v_{inj}\beta\left(\rho g_z - \frac{\rho v_{inj}^2 \overline{f}}{r_i}\right)\right] \quad \text{..... (D.61)}$$

$$d_2 = \frac{1}{k_f}\left(\frac{2}{r_i}U_T\big|_{r=r_i} T_{res} + \frac{\rho v_{inj}^3 \overline{f}}{r_i}\right). \quad \text{..... (D.62)}$$

Therefore, the general solution of the second order linear ordinary differential equation is given by

$$T(z) = C_1 \exp\left[\frac{z}{2}\left(-\sqrt{b_1^2 - 4c_1} - b_1\right)\right] + C_2 \exp\left[\frac{z}{2}\left(\sqrt{b_1^2 - 4c_1} - b_1\right)\right] - \frac{d_1}{c_1} \quad \text{..... (D.63)}$$

where C_1 and C_2 are integration constants, and they are determined by the boundary conditions. The integration constants are given by

$$C_1 = \frac{B_1 e^{B_1 L}}{B_1 e^{B_1 L} - A_1 e^{A_1 L}}\left(T_{inj} + \frac{d_1}{c_1}\right) \quad \text{..... (D.64)}$$

$$C_2 = -\frac{A_1 e^{A_1 L}}{B_1 e^{B_1 L} - A_1 e^{A_1 L}}\left(T_{inj} + \frac{d_1}{c_1}\right) \quad \text{..... (D.65)}$$

where

$$A_1 = -\frac{\sqrt{b_1^2 - 4c_1} + b_1}{2} \quad \text{..... (D.66)}$$

$$B_1 = \frac{\sqrt{b_1^2 - 4c_1} - b_1}{2}. \quad \text{..... (D.67)}$$

Eventually, the temperture profile becomes

$$T(z) = \xi(z) T_{inj} + [\xi(z) - 1]\frac{d_1}{c_1} \quad \text{..... (D.68)}$$

where $\xi(z)$ is expressed as

$$\xi(z)=\frac{B_1 e^{B_1 L}e^{A_1 z}-A_1 e^{A_1 L}e^{B_1 z}}{B_1 e^{B_1 L}-A_1 e^{A_1 L}}=\frac{Be^{A_1 z}-A_1 e^{A_1 L}e^{B_1(z-L)}}{B_1-A_1 e^{(A_1-B_1)L}}. \quad \text{..... (D.69)}$$

TABLE D.7 summarizes input data used for the injection case. The wellbore is discretized into 80 grids. The inlet velocity, pressure and temperature are 4.7 m/s, 6,000 psi and 80 °F. The reservoir temperature is 180 °F.

TABLE D.7—INPUT DATA (WELLBORE MODEL CASE 1: INJECTION)

Type	Property	Value
Wellbore	Inner radius, inch	2.335
	Length, ft	4,000
	Average friction factor, –	0.001
	Overall heat transfer coefficient, Btu/(hr-ft^2-°F)	37.00
Fluid	Density, lbm/ft^3	63.1
	Viscosity, cP	0.350
	Specific heat, Btu/(lbm-°F)	0.976
	Thermal conductivity, Btu/(hr-ft-°F)	0.393
	Thermal expansion coefficient, 1/°F	3.50×10^{-4}

Figure D.9 shows comparisons of velocity, pressure and temperature profiles given by the analytical solution and the numerical simulation (this work). These results show almost perfect matches. The injected fluid temperature increases as the fluid moves to the toe direction. The increase of the temperature is mainly driven by the warm-up by the surrounding formation.

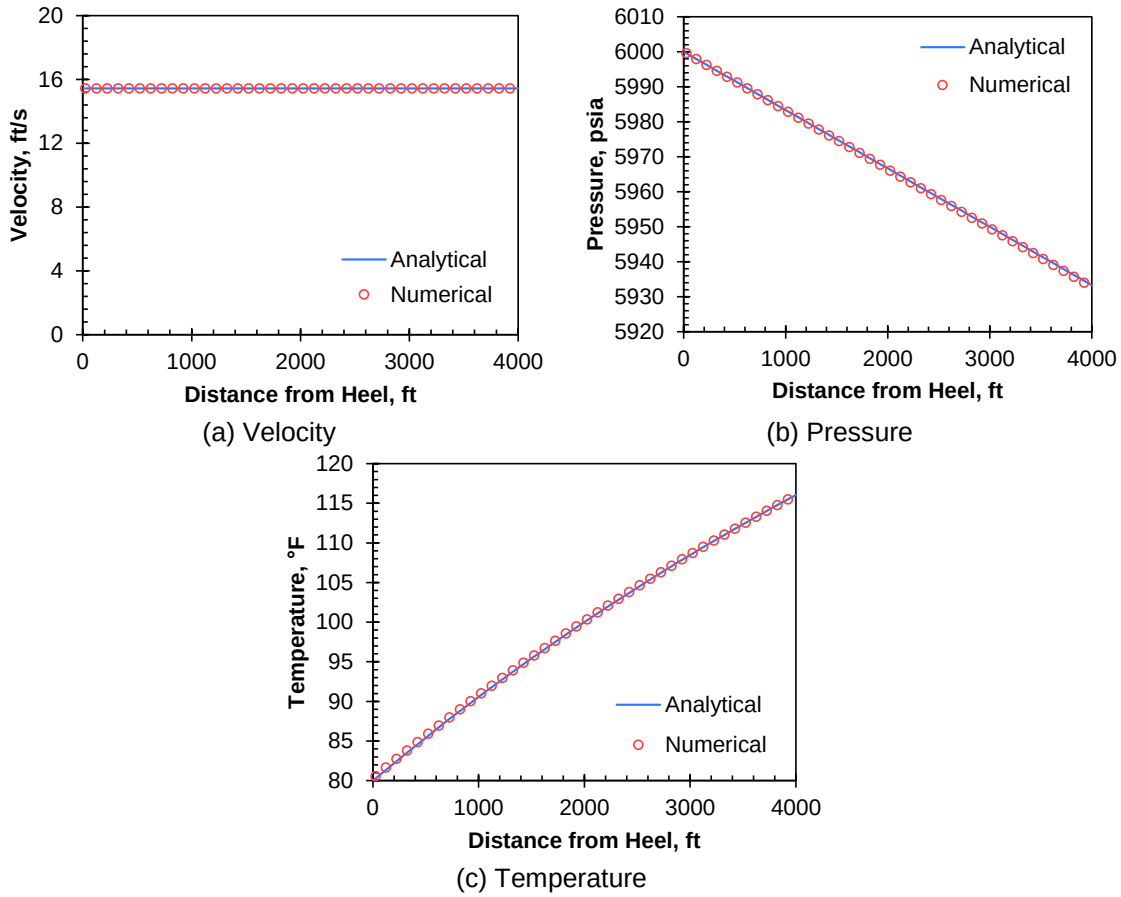

Figure D.9—Comparison of velocity, pressure and temperature distribution (wellbore model case 1: injection)

Production from a Non-perforated Cased Horizontal Well

Let us assume following conditions:

- constant fluid properties and single phase flow
- constant geothermal temperature (T_{res})
- no slip condition at the wall
- negligible kinetic energy contribution in energy balance equation
- no influx at the contact of the wellbore and the reservoir ($v_I = 0$ and $\gamma = 0$)

Under these assumptions, the wellbore model is reduced into:

$$\frac{dv}{dz} = 0 \quad \text{..... (D.70)}$$

$$\frac{dp}{dz} = -\rho \frac{d}{dz}(vv) + \rho g_z - \frac{\rho v|v| f}{r_i} \quad \text{..... (D.71)}$$

$$\rho \frac{d}{dz}(Hv) = k_f \frac{d^2 T}{dz^2} + \rho g_z v + \frac{2}{r_i} U_T\big|_{r=r_i}(T_{res} - T) \quad \text{..... (D.72)}$$

and boundary conditions are expressed as

$$v(z=0) = -v_0 \quad \text{..... (D.73)}$$

$$p(z=0) = p_0 \quad \text{..... (D.74)}$$

$$T(z=L) = T_I \quad \text{..... (D.75)}$$

$$\left.\frac{dT}{dz}\right|_{z=0} = 0. \quad \text{..... (D.76)}$$

The first and second boundary conditions denote constant production rate and constant outlet pressure, respectively. The third condition is constant inflow temperature at the inlet. The fourth boundary condition is the no heat flux in the axial direciton at the outlet.

The velocity profile is obtained by integrating the Eq. D.70 over $z \in [0, z]$ as

$$v(z) = -v_0. \quad \text{..... (D.77)}$$

This means that the velocity is constant in the entire domain. Substitute this into the Eq. D.71, and the pressure profile is obtained by integrating it as

$$p(z) = p_0 + \rho g_z z + \frac{\rho v_0^2 \overline{f}}{r_i} z = p_0 + \left(\rho g_z + \frac{\rho v_0^2 \overline{f}}{r_i}\right) z. \quad \text{..... (D.78)}$$

Substitution of the Eq. D.77 and Eq. D.78 into Eq. D.72 provides

$$k_f \frac{d^2T}{dz^2} + \rho v_0 C_p \frac{dT}{dz} - \left[\frac{2}{r_i} U_T\big|_{r=r_i} + v_0 \beta \left(\rho g_z + \frac{\rho v_0^2 \overline{f}}{r_i} \right) \right] T + \frac{2}{r_i} U_T\big|_{r=r_i} T_{res} + \frac{\rho v_0^3 \overline{f}}{r_i} = 0 \quad \text{..... (D.79)}$$

where the thermodynamic relation of specific enthalpy on pressure and temperature (Eq. D.58) is used. The Eq. D.79 is rearranged into a second order liner ordinary equation:

$$\frac{d^2T}{dz^2} + b_2 \frac{dT}{dz} + c_2 T + d_2 = 0 \quad \text{..... (D.80)}$$

where

$$b_2 = \frac{\rho v_0 C_p}{k_f} \quad \text{..... (D.81)}$$

$$c_2 = -\frac{1}{k_f} \left[\frac{2}{r_i} U_T\big|_{r=r_i} + v_0 \beta \left(\rho g_z + \frac{\rho v_0^2 \overline{f}}{r_i} \right) \right] \quad \text{..... (D.82)}$$

$$d_2 = \frac{1}{k_f} \left(\frac{2}{r_i} U_T\big|_{r=r_i} T_{res} + \frac{\rho v_0^3 \overline{f}}{r_i} \right). \quad \text{..... (D.83)}$$

Therefore, the general solution of the second order linear ordinary differential equation is given by

$$T(z) = C_3 \exp\left[\frac{z}{2} \left(-\sqrt{b_2^2 - 4c_2} - b_2 \right) \right] + C_4 \exp\left[\frac{z}{2} \left(\sqrt{b_2^2 - 4c_2} - b_2 \right) \right] - \frac{d_2}{c_2}. \quad \text{... (D.84)}$$

where C_3 and C_4 are integration constants, and they are determined by the boundary conditions. The integration constants are given by

$$C_3 = \frac{B_2}{B_2 e^{-A_2 L} + A_2 e^{B_2 L}} \left(T_I + \frac{d_2}{c_2} \right) \quad \text{..... (D.85)}$$

$$C_4 = \frac{A_2}{B_2 e^{-A_2 L} + A_2 e^{B_2 L}} \left(T_I + \frac{d_2}{c_2} \right) \quad \text{..... (D.86)}$$

where

$$A_2 = \frac{\sqrt{b_2^2 - 4c_2} + b_2}{2} \quad \text{..... (D.87)}$$

$$B_2 = \frac{\sqrt{b_2^2 - 4c_2} - b_2}{2}. \quad \text{..... (D.88)}$$

Eventually, the temperture profile becomes

$$T(z) = \eta(z) T_I + [\eta(z) - 1] \frac{d_2}{c_2} \quad \text{..... (D.89)}$$

where $\xi(z)$ is expressed as

$$\eta(z) = \frac{B_2 e^{-A_2 z} + A_2 e^{B_2 z}}{B_2 e^{-A_2 L} + A_2 e^{B_2 L}}. \quad \text{..... (D.90)}$$

TABLE D.8 summarizes input data used for the production case. The wellbore is discretized into 25 grids. The outlet velocity, outlet pressure and inlet temperature are −5.0 m/s, 3200 psi and 180 °F. The reservoir temperature is 180 °F.

TABLE D.8—INPUT DATA
(WELLBORE MODEL CASE 1: PRODUCTION WITH NO INFLOW)

Type	Property	Value
Wellbore	Inner radius, inch	2.335
	Length, ft	12,000
	Average friction factor, –	0.001
	Overall heat transfer coefficient, Btu/(hr-ft^2-°F)	37.00
Fluid	Density, lbm/ft^3	47.9
	Viscosity, cP	0.856
	Specific heat, Btu/(lbm-°F)	0.524
	Thermal conductivity, Btu/(hr-ft-°F)	0.0797
	Thermal expansion coefficient, 1/°F	5.76×10^{-4}

Figure D.10 shows comparisons of velocity, pressure and temperature profiles given by the analytical solution and the numerical simulation (this work). These results show satisfactory agreement on production from the non-perforated cased horizontal well. The temperature increases near heel location associated with the pressure drop along the well because the value of the thermal expansion coefficient used in this study provides the Joule-Thomson heating.

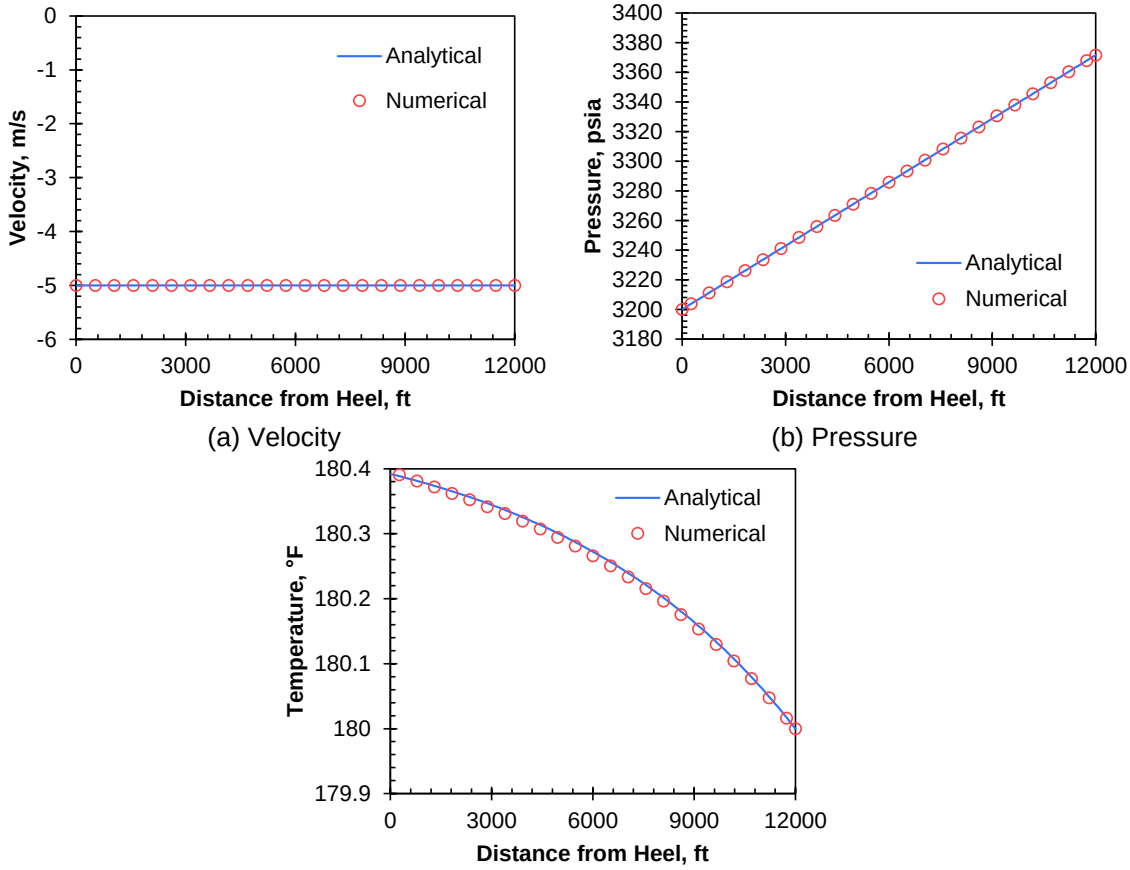

Figure D.10—Comparison of velocity, pressure and temperature distribution (wellbore model case 1: production with no influx)

Production from an Open-hole Horizontal Well with Uniform Influx

The analytical solutions of velocity, pressure and temperature distribution for the wellbore with constant influx are derived in this section. The derivation of this work follows the work done by Dawkrajai et al. (2004). Let us assume following conditions:

- constant fluid properties and single phase flow
- constant geothermal temperature (T_{res})
- no slip condition at the wall
- negligible kinetic energy contribution in energy balance equation
- negligible conductive heat in the axial direction
- uniform influx at the contact of the wellbore and the reservoir (v_I = const.)

Under these assumptions, the wellbore model is reduced into:

$$\frac{dv}{dz} = \frac{2}{r_i} v_I \quad \text{..... (D.91)}$$

$$\frac{dp}{dz} = -2\rho v \frac{dv}{dz} + \rho g_z - \frac{\rho v|v| f}{r_i} \quad \text{..... (D.92)}$$

$$\rho \frac{d}{dz}(Hv) = \rho g_z v + \frac{2}{r_i} \rho_I h_I v_I + \frac{2}{r_i} U_T\big|_{r=r_i} (T_{res} - T) \quad \text{..... (D.93)}$$

and boundary conditions are expressed as

$$v(z = L) = 0 \quad \text{..... (D.94)}$$

$$p(z = 0) = p_0 \quad \text{..... (D.95)}$$

$$T(z = L) = T_I . \quad \text{..... (D.96)}$$

The velocity profile is obtained by integrating the Eq. D.91 over $z \in [0, z]$ as

$$v(z)=\frac{2}{r_i}v_I(z-L). \quad \text{..... (D.97)}$$

The inflow velocity v_I is constant, and the value is positive for production and negative for injection in terms of mass balance. Substitution of this into the momentum balance gives

$$\frac{\partial p}{\partial z}=\rho g_z-\frac{8\rho v_I^2}{r_i^2}(z-L)+\frac{4\rho\overline{f}}{r_i^3}v_I^2(z-L)^2. \quad \text{..... (D.98)}$$

Integrate this equation over the domain, and we have

$$p(z)=p_0+\rho g_z z-\frac{4\rho}{r_i^2}v_I^2\left[(z-L)^2-L^2\right]+\frac{4}{3}\frac{\rho\overline{f}}{r_i^3}v_I^2\left[(z-L)^3+L^3\right]. \quad \text{..... (D.99)}$$

When the well is perfectly horizontal, the energy balance equation is rearranged by substituing the Eq. D.97 and D.99 as (Dawkrajai et al. 2004):

$$\frac{dT}{dz}+p(z)T+q(z)=0 \quad \text{..... (D.100)}$$

where

$$p(z)=\left(\frac{U_T|_{r=r_i}}{\rho C_p v_I}+1\right)\frac{1}{z-L}=m_1\frac{1}{z-L} \quad \text{..... (D.101)}$$

$$\begin{aligned} q(z)=&-\frac{4K_{JT}\rho\overline{f}v_I^2}{r_i^3}(z-L)^2+\left(\frac{8K_{JT}\rho v_I^2}{r_i^2}+\frac{6v_I^2}{r_i^2C_p}\right)(z-L)\\ &-\left(\frac{U_T|_{r=r_i}}{\rho C_p v_I}T_{res}+\frac{v_I^2}{2C_p}+T_I\right)\frac{1}{z-L} \quad \text{..... (D.102)}\\ =&\,m_2(z-L)^2+m_3(z-L)+\frac{m_4}{z-L} \end{aligned}$$

$$K_{JT}=\frac{\beta T-1}{\rho C_p} \quad \text{..... (D.103)}$$

The solution of the Eq. D.100 is (Dawkrajai et al. 2004):

$$T(z) = T_I \left[\frac{m_1 m_2}{(m_1+3)m_4}(z-L)^3 + \frac{m_1 m_3}{(m_1+2)m_4}(z-L)^2 + 1 \right]. \quad \text{..... (D.104)}$$

TABLE D.9 summarizes input data used for the production case. The wellbore is discretized into 25 grids. The outlet velocity, outlet pressure and inlet temperature are −4.7 m/s, 3200 psi and 180 °F. The inflow velocity of this case is 3.83×10^{-5} m/s. The reservoir temperature is 180 °F.

TABLE D.9—INPUT DATA
(WELLBORE MODEL CASE 1: PRODUCTION WITH UNIFORM INFLOW)

Type	Property	Value
Wellbore	Inner radius, inch	2.335
	Length, ft	12,000
	Average friction factor, –	0.001
	Overall heat transfer coefficient, Btu/(hr-ft^2-°F)	37.00
Fluid	Density, lbm/ft^3	47.9
	Viscosity, cP	0.856
	Specific heat, Btu/(lbm-°F)	0.524
	Thermal conductivity, Btu/(hr-ft-°F)	0.0797
	Thermal expansion coefficient, 1/°F	5.76×10^{-4}

Figure D.11 shows comparisons of velocity, pressure and temperature profiles given by the analytical solution and the numerical simulation (this work). These results show satisfactory agreement on production from the open-hole horizontal well with uniform influx.

In this case, the fluid (negative) velocity increases because the uniform influx from the reservoir. The negative velocity means the flow in the heel direction: production flow.

The linear increase of the velocity leads to the non-linear change (cubic equation with respect to the position) of the pressure profile as expected.

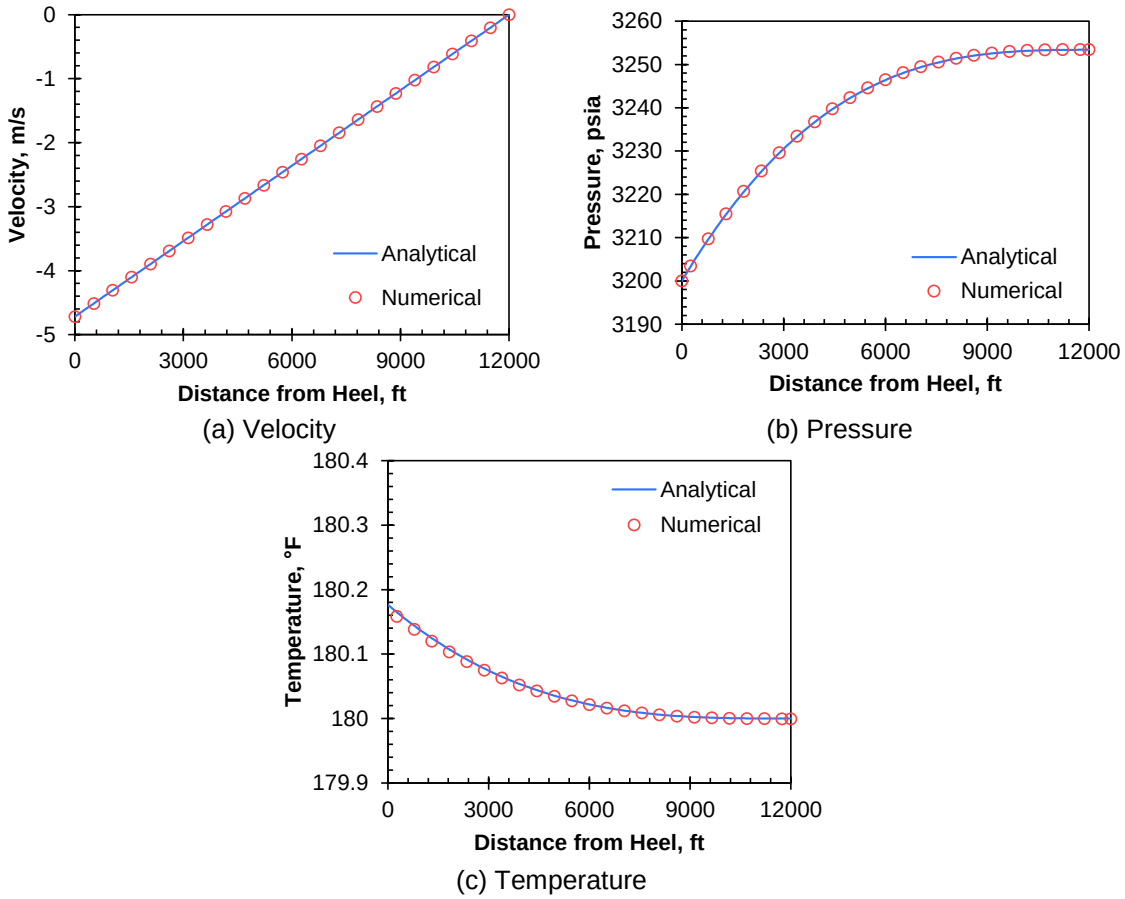

Figure D.11—Comparison of velocity, pressure and temperature distribution (wellbore model case 1: production with uniform flux)

These results verify the implementation of the spatial terms including the Joule-Thomson effects along the well.

D.2.2 Case 2: Steady-state Wellbore Thermal Model with Transient Rock Temperature

The pioneering work in the estimation of the wellbore temperature distribution during production or injection was conducted by Ramey (1962). This model considers a steady state temperature model in the wellbore with transient formation temperature. The heat transfer between wellbore and reservoir was incorporated with use of the overall transfer coefficient. The mathematical formulation for incompressible fluid during production is given by

$$T_f = T_{Ge} - g_G\left[(L-z) - A_R\left(1 - e^{-\frac{(L-z)}{A_R}}\right)\right] \quad \text{..... (D.105)}$$

where T_{Ge} is the sandface temperature (producing fluid temperature is assumed to be same with geothermal temperature) at bottomhole, g_G is the geothermal gradient, and L is the distance from the surface to the bottom hole (positive). The parameter A_R is defined as

$$A_R = \frac{q_v \rho_f C_{p,f}\left[k_{Tt} + r_1 U_{T,1} f(t)\right]}{2\pi r_1 U_{T,1} k_{Tt}} \quad \text{..... (D.106)}$$

where q_v is volumetric flow rate along the wellbore, and $f(t)$ and thermal diffusivity α are

$$f(t) = -\ln\left[\frac{r_2}{2\sqrt{\alpha t}}\right] - 0.290 \quad \text{..... (D.107)}$$

$$\alpha = \frac{k_{Tt}}{\rho_s C_{p,s}}. \quad \text{..... (D.108)}$$

Figure D.12 shows the schematics of the problem. The overall heat transfer coefficient can be defined at either of r_1 and r_2. In this work, it is defined at r_1, and the parameter A is defined corresponding to it; $U_{T,1}$ is the overall heat transfer at r_1. The time function $f(t)$ is originally given as the line source solution of radial diffusivity equation, and it was

approximated by the log-linear form; this solution is applicable for the time region after certain time.

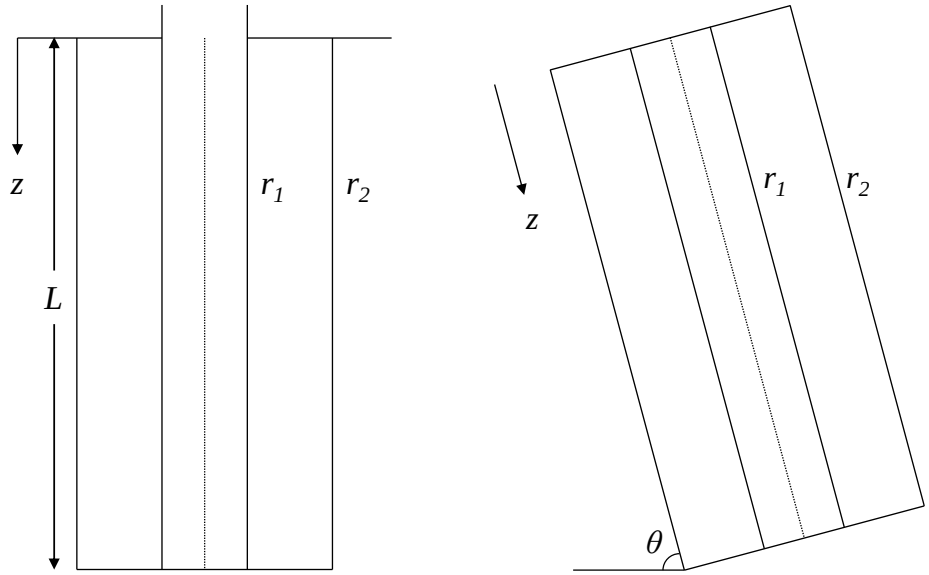

Figure D.12—Schematics of wellbore heat transfer problem (wellbore model case 2)

Recall that Ramey (1962) used the approximated log-linear function to account for the transient formation temperature with line-source approximation of the wellbore, and this is rigorously correct after sufficient time of production or injection. To account for the rigorous early transient formation temperature behavior, Hasan and Kabir (1991) relaxed this approximation by using more rigorous representation of the time function with consideration of finite size of wellbore unlike line-source solution. This is still based on the approximation because the rigorous temperature solution is expressed with Bessel functions in real domain or derived in Laplace space, but this model can capture transient behavior of the formation temperature at early time with higher accuracy to the Ramey's

solution. And, also, in their model, they extended the model for deviated wells with inclination of wellbores.

The model is formulated for incompressible fluids as (Hasan and Kabir 2002):

$$T_f = T_{eibh} - g_G \sin\theta \left[(L - z) - \frac{1 - e^{-(L-z)L_R}}{L_R} \right] \quad \text{..... (D.109)}$$

where T_{eibh} is the inflow temperature at the bottom hole (assumed to be geothermal temperature), θ is the inclination shown in **Figure D.12b**, and L_R is the relaxation parameter given as:

$$L_R = \frac{2\pi}{q_v \rho_f C_{p,f}} \left[\frac{r_1 U_{T,1} k_{Tt}}{k_{Tt} + r_1 U_{T,1} T_D(t)} \right]. \quad \text{..... (D.110)}$$

The dimensionless temperature T_D was derived in the work by Hasan and Kabir (1991), and it was extended to continuous expression in the form by Hasan and Kabir (2002):

$$T_D(t) = \ln\left[e^{-0.2 t_D} + \left(1.5 - 0.3719 e^{-t_D}\right) \sqrt{t_D} \right] \quad \text{..... (D.111)}$$

where the dimensionless time is given as

$$t_D = \frac{\alpha t}{r_w^2}. \quad \text{..... (D.112)}$$

For compressible fluid, the contribution of pressure on the determination of enthalpy is not negligible; Joule-Thomson effect is included in the temperature model. In the work by Hasan and Kabir (1994), the temperature model for compressible fluid is given by:

$$T_f = T_{eibh} - g_G (L - z) \sin\theta + \frac{1 - e^{(z-L)L_R}}{L_R} \left[g_G \sin\theta - \frac{g \sin\theta}{C_{p,f}} \right]. \quad \text{..... (D.113)}$$

In previous verification study, the pressure distribution in a horizontal pipe with and without inflow distribution ignores the potential energy contribution (Δp_{PE}) because of no depth change. This case needs to calculate the pressure distribution with considering Δp_{PE}. The total pressure drop is calculated by (Economides et al. 2012)

$$\Delta p = \Delta p_{PE} + \Delta p_{KE} + \Delta p_F \quad \text{..... (D.114)}$$

where the subscripts *PE*, *KE* and *F* denote potential energy, kinetic energy and friction, respectively. Each of the pressure drop terms is computed by

$$\Delta p_{PE} = \rho g \Delta z = \rho g \Delta L \sin\theta \quad \text{..... (D.115)}$$

$$\Delta p_{KE} = \frac{1}{2}\rho\left(\Delta u^2\right) \quad \text{..... (D.116)}$$

$$\Delta p_F = \frac{2 f \rho u^2 \Delta L}{D} \quad \text{..... (D.117)}$$

where Δz is the difference in elevation between two points, ΔL is the differential length along the well, Δu is difference of the superficial velocity between two points, and D is pipe diameter.

In this verification study, the coupled model (reservoir-wellbore) is used. Let us consider a cylindrical reservoir domain with large reservoir radius (r_e = 100,000 ft) to avoid effects by outer boundary. **Figure D.13a** shows the schematics of the reservoir/wellbore system. The target reservoir is located at 5350 ft from the surface. The outer boundary of the reservoir is set to fixed pressure (constant pressure boundary). The *r*–*z* directional cross-sectional view of the entire reservoir with simulation mesh is shown in **Figure D.13b**. The reservoir is discretized into logarithmically-spaced mesh in the *r*-direction to capture the diffusive nature of the thermal conduction in the reservoir. The

reference properties of each flowing fluid are summarized in **TABLE D.10**. It is noted that the gas fluid properties are estimated by the PR-EOS with critical properties of pure methane. And, formation properties are summarized in **TABLE D.11**.

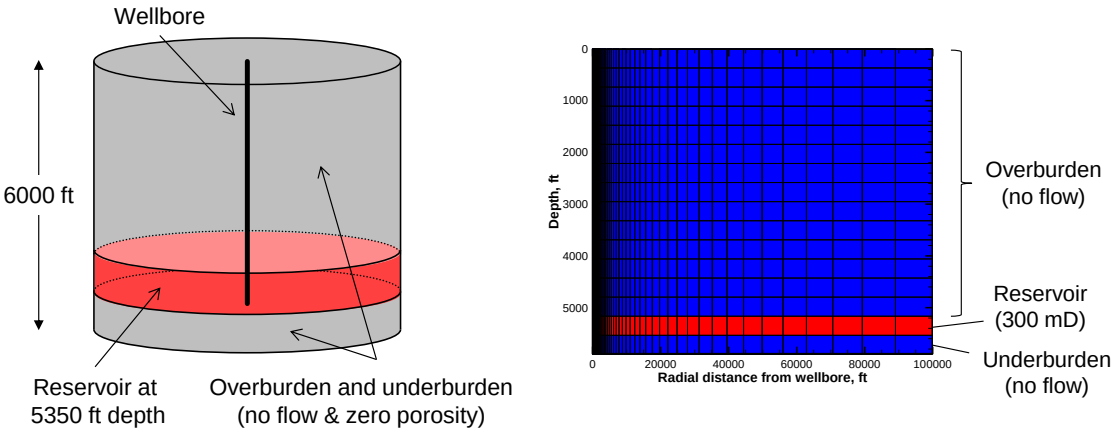

(a) Geometry of reservoir/wellbore (b) *r-z* cross section and simulation mesh

Figure D.13—Schematics of the reservoir/wellbore system and simulation mesh (wellbore model case 2)

TABLE D.10—REFERENCE PROPERTIES OF FLOWING FLUID (WELLBORE MODEL CASE 2)

Fluid	Property	Value
Oil	Density, lbm/ft^3	53.1
	Specific heat, Btu/(lbm-°F)	0.538
Water	Density, lbm/ft^3	61.3
	Specific heat, Btu/(lbm-°F)	0.990
Gas	Density, lbm/ft^3	10.2
	Specific heat, Btu/(lbm-°F)	0.787

TABLE D.11—FORMATION PROPERTIES (WELLBORE MODEL CASE 2)		
Region	Properties	Value
Reservoir	Outer radius, ft	100,000
	Thickness, ft	350
	Permeability, mD	300
	Porosity, fraction	0.18
	Density, lbm/ft^3	162.313
	Total thermal conductivity, Btu/(ft-hr-°F)	1.79
	Rock heat capacity, Btu/(lbm-°F)	0.239
Overburden	Outer radius, ft	100,000
Underburden	Permeability, mD	0
	Porosity, fraction	0
	Density, lbm/ft^3	162.313
	Total thermal conductivity, Btu/(ft-hr-°F)	1.79
	Rock heat capacity, Btu/(lbm-°F)	0.239

Before the well starts to produce reservoir fluids, we need to obtain the equilibrium conditions of the pressure and temperature for each fluid. After this initialization process, we start to produce fluid from the reservoir at constant mass flow rate at the surface. The completion properties and the surface flow rate of each fluid are summarized in **TABLE D.12**.

TABLE D.12—COMPLETION PROPERTIES AND SURFACE FLOW RATE (WELLBORE MODEL CASE 2)	
Parameters	Value
Wellbore radius, in	8.75
Casing inner radius, in	4.67
Overall heat transfer coefficient, Btu/(hr-ft^2-°F)	37.01
Friction factor, –	0.001
Oil flow rate (single phase), STB/d	959
Water flow rate (single phase), STB/d	830
Gas flow rate (single phase), MSCF/d	187
Water flow rate (two-phase), STB/d	403
Gas flow rate (two-phase), MSCF/d	1,163

Figure D.14, **Figure D.15** and **Figure D.16** show results of pressure and temperature distribution by this work for single phase oil, water and gas production, respectively, comparing to the available analytical solutions. Temperature distribution of the liquid phase (organic and aqueous) is given by the analytical solution for incompressible fluid, and, on the other hand, that of the gaseous phase is given by the model for compressible fluid. The pressure distributions are satisfactory agreement with the analytical solutions. It is clear that the dominant contribution of pressure drop is the potential energy term, and the density differences can be seen in the slope of the pressure distribution of all cases. The temperature distributions given by single phase flow show satisfactory agreements to verify this work.

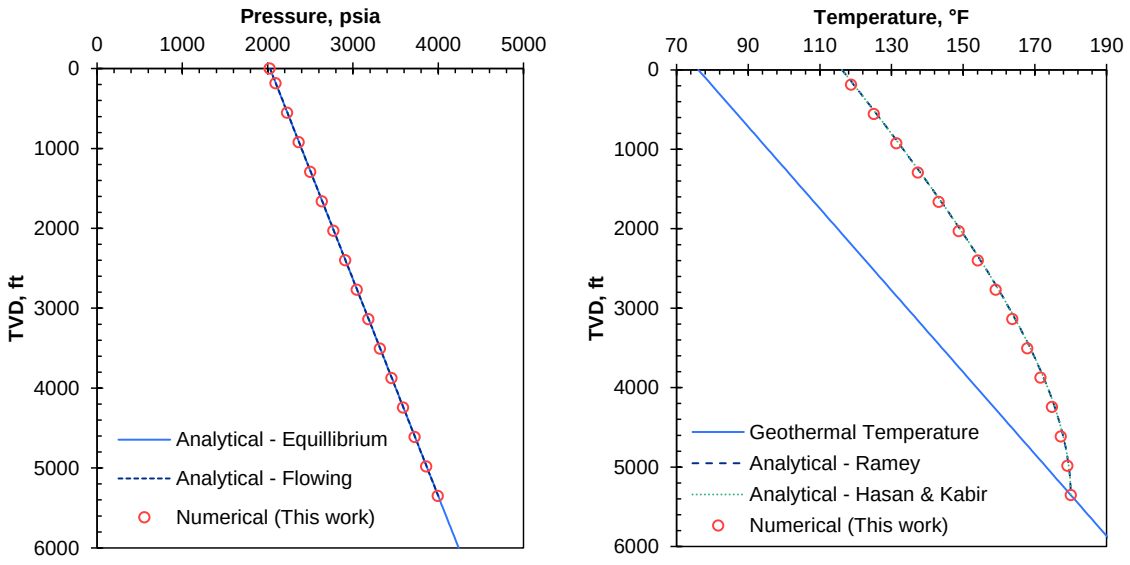

(a) Pressure (b) Temperature (at 100 days of production)

Figure D.14—Comparison of pressure and temperature distribution at 100 days if production with single phase oil production (wellbore model case 2)

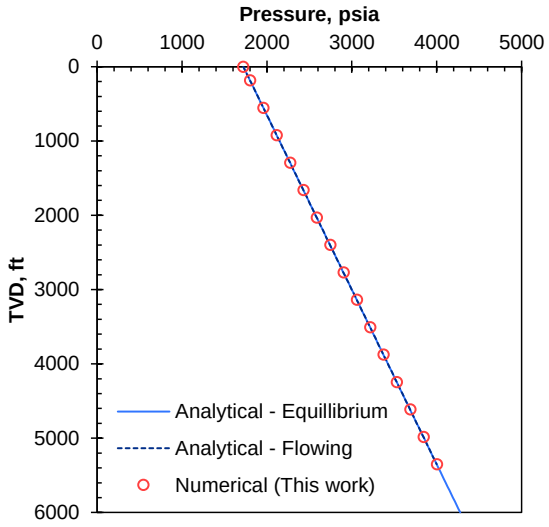

(a) Pressure

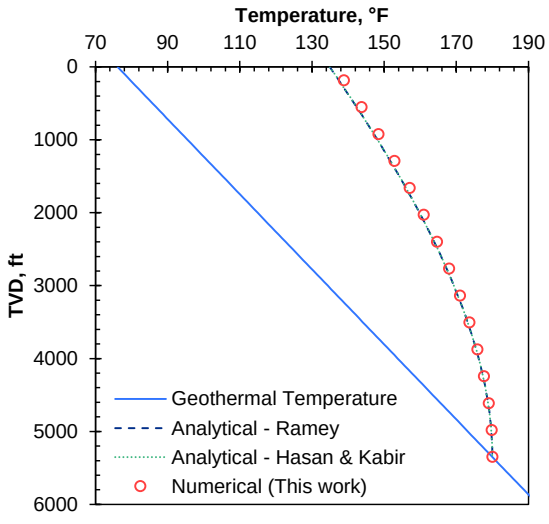

(b) Temperature (at 100 days of production)

Figure D.15—Comparison of pressure and temperature distribution at 100 days if production with single phase water production (wellbore model case 2)

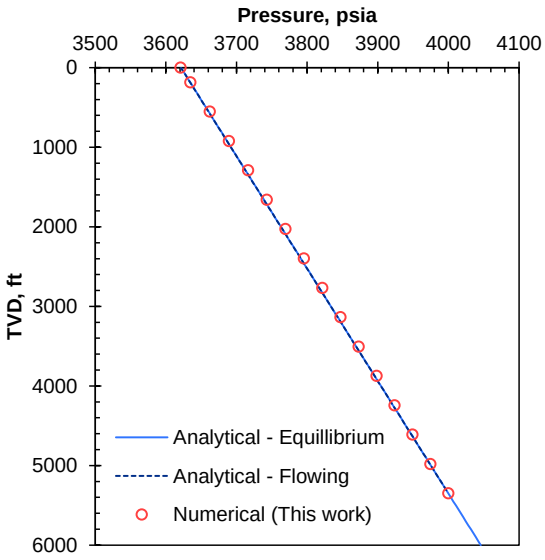

(a) Pressure

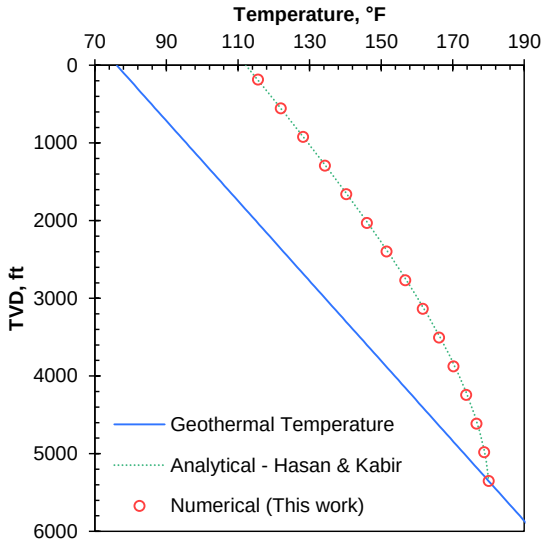

(b) Temperature (at 100 days of production)

Figure D.16—Comparison of pressure and temperature distribution at 100 days if production with single phase gas production (wellbore model case 2)